SELF–CONSISTENT CHARGE DENSITIES AT ISOLATED PLANAR DEFECTS IN METALS

by

SIMON CRAMPIN

Thesis submitted for the degree of

Doctor of Philosophy of the University of London
and the
Diploma of Imperial College

Solid State Theory Group
The Blackett Laboratory
Imperial College of Science, Technology and Medicine
London

September 1989

ABSTRACT

Deformation processes in materials are largely controlled by defects of the crystalline structure. Consequently, applications of quantum mechanics to systems of pertinence to mechanical behaviour are confronted with complex structures at the limits of the capabilities of current computational techniques, forcing a compromise between faithfulness of the structural representation and the accuracy with which the electronic structure is determined.

This Thesis concerns the development and application of a new method for determining the self–consistent electronic structure of planar defects in metals which goes beyond current techniques. Adopting the language of multiple–scattering theory, the scattering properties of isolated atomic layers are determined by a Fourier transform, and subsequently combined using a recursive algorithm to assemble the full structure of the solid. This approach alleviates the demands of three–dimensional periodicity imposed by traditional techniques, which force the adoption of artificial boundary conditions, leading to an elegant and computationally efficient solution of the one–electron properties of the solid. In the case of structures where atomic planes are closely spaced, a combined plane–wave / partial–wave solution to the layer assembly algorithm is developed.

Applications are presented which demonstrate the capabilities of the method. These include a study of stacking faults in face–centred metals, exploring the microscopic origins of the stacking fault energy, and with good agreement found between calculated and experimental energies. The modifying effects of small concentrations of impurities are also studied. The first self–consistent electronic structure calculation of an isolated transition metal is presented, with a study of the nickel $\Sigma 5$ (210) / [100] tilt boundary. Sulfur is known to induce intergranular brittleness in nickel, and we study the effects of substitutional sulfur in the grain–boundary geometry. On the basis of the local density of states a possible mechanism is proposed.

CONTENTS

FIGURE CAPTIONS

Figure 1.1 Γ point densities of states for various models of an intrinsic stacking fault in copper calculated with the LKKR technique. The density of states is evaluated about the atoms shaded in the diagrams, and structures included are an isolated fault, and supercells consisting of 5, 8 and 11 layers, for which adjacent faults are illustrated below.

Figure 2.1 Energy dependence of the atomic t–matrices for aluminium, nickel and niobium.

Figure 2.2 Schematic illustration of the assignment of atoms to plane, planes to layers and the left and right half spaces.

Figure 2.3 Illustration of the embedded layer problem.

Figure 2.4 Pictorial representation of the layer transmission and reflection matrices of equation (2.8.5), and those resulting from the composite scattering system of layer $1 + 2$. In all cases the origins of the expansions of the incident and scattered plane wave are indicated by the dark circle.

Figure 2.5 The structure discussed in the text which does not benefit from the partitioning of more planes to each layer.

Figure 2.6 The structure discussed in the text which does benefit from the partitioning of additional planes to each layer, due to the varying inter–layer separation. **a)**. Each layer consisting of a single plane, and the shortest scattering path treated in the plane wave basis. **b)**. Two planes assigned to each layer, and the resulting shortest scattering path to be treated in the plane wave basis.

Figure 2.7a). The embedded layer problem for the close–spaced layer case. **b)**. The location of the origins of the half spaces (indicated by black circles) for the close–spaced layer case.

Figure 2.8 Schematic representation of the four right half space reflection matrices in the close–spaced layer problem. The black circles indicate the position of the origins, solid arrows incident waves and dashed arrows reflected waves. The plane wave basis is used for scattering paths more distant than one layer, so is positioned

to the left of the origin, whilst the spherical wave basis is used for scattering between adjacent layers, and so is positioned between the half space and the origin.

Figure 2.9 Schematic illustration of the 16 matrices entering the layer "tripling" algorithm. See caption to figure 2.8 for more details.

Figure 2.10 Possible partitioning of close–spaced layers to optimise the two basis sets. a). one ,b). two and c). three atomic planes assigned to each layer.

Figure 3.1 Irreducible Brillouin zone and sampling sets for the square (upper) and hexagonal (lower) two dimensional lattices. The high symmetry points are labeled in the hexagonal case.

Figure 3.2 Free electron density of states $\varrho(\mathrm{E}, \mathbf{k}_{||})$ evaluated at E=0.5Ha projected onto the two dimensional momentum space $\mathrm{k_x}, \mathrm{k_y} > 0$. The data are truncated; $\varrho(\mathrm{E}, \mathbf{k}_{||}) = \min(\varrho(\mathrm{E}, \mathbf{k}_{||}), 0.05)$.

Figure 3.3 Schematic illustration of the form of the energy integral in equation (3.3.3), and the quantities entering.

Figure 3.4 Contour used in evaluating equation (3.3.5a).

Figure 3.5 Muffin–tin density of states for the 2p core level in aluminium evaluated at various imaginary energies.

Figure 3.6 a). Valence band density of states for bulk copper evaluated at various imaginary energies. Real energies quoted with respect to the Fermi energy. b). Valence band density of states for bulk copper taken from Moruzzi, Janak and Williams (1978).

Figure 3.7 Muffin–tin density of states of nickel evaluated in the complex plane out to an imaginary energy 0.06Ha.

Figure 3.8 Energy contour used in evaluating the total charge density.

Figure 3.9 Density of states across the Brillouin zone for Ni (100) a).$\mathrm{E} = 0.1 + 0.01i$ b). $\mathrm{E} = 0.1 + 0.1i$ c). $\mathrm{E} = 0.25 + 0.1i$ d).$\mathrm{E} = 0.25 + 0.01i$. (all energies in Ha)

Figure 3.10a). Energy dependence of the diagonal elements of the Green function integrated over the muffin–tin sphere, evaluated with imaginary energy 0.03Ha.

b). Muffin–tin density of states for nickel at imaginary energy 0.003Ha, obtained by extrapolation *via* a rational polynomial fit, with the original data evaluated at 0.03Ha. c. Muffin–tin density of states for bulk nickel taken from Moruzzi, Janak and Williams (1978).

Figure 3.11 a). Schematic illustration of the geometry as used in solving Poisson's equation, showing repeat lengths and expansion origins. The darker atoms are those whose potentials would be allowed to change during an interface calculation. b). "Dressing " the interface with bulk layers.

Figure 3.12 Lattice constant test for aluminium, with changes in energy and pressure monitored under a symmetry preserving scaling of the bulk unit cell.

Figure 3.13 Schematic illustration of the wavefields in the band structure problem.

Figure 3.14 A small part of the nickel band structure calculated from the eigenvalue problem (3.9.2).

Figure 3.15 Muffin–tin density of states evaluated at various constant $\mathbf{k}_{||}$ between the Γ and K points of the irreducible Brillouin zone of the (111) face of aluminium, illustrating the projected band structure.

Figure 3.16 Convergence of the elements of the reflection matrix with the number of passes through the layer doubling algorithm for nickel. Continuous line $E = 0.1 + 0.0i$ (all energies in Ha) where extended states exist. Long dash $E = 0.1 + 1 \times 10^{-5} i$ showing convergence. Short dash $E = 0.2 + 0.0i$ where no extended states exist.

Figure 3.17 a) Two–dimensional projected band structure for Al(111) evaluated by attempting to converge the bulk reflection matrix on the real energy axis. A square indicates the layer doubling procedure failed to converge at that $(E, \mathbf{k}_{||})$. b). Two–dimensional projected band structure for Al(111) from Caruthers, Kleinman and Alldredge (1974).

Figure 3.18 Localised states at the K point of a twin fault in copper appearing as singular peaks in the density of states at E=0.2193Ha and E=0.2365Ha.

Figure 3.19 Muffin–tin density of states for bulk copper evaluated with a plane wave basis set of 7, 13, and 19 **g** vectors.

Figure 3.20 Convergence of the density of states with the dimension of the plane wave basis. See text for explanation of a)–f).

Figure 3.21 Relative calculation times using the plane wave (normal) and plane wave/ partial wave (close–spaced) codes along the (210) direction of nickel.

Figure 4.1 Atomic positions of AA' (unshaded), BB' (shaded) and CC' (black) sites of the silicon lattice projected onto the (111) plane.

Figure 4.2 Bulk and stacking fault structures of the FCC and HCP lattices. The view is edge on to the (111) planes and taken in a [211] direction. Shaded atoms occupy positions one row back.

Figure 4.3 Muffin–tin density of states for bulk aluminium, and s, p and d decomposition.

Figure 4.4 Muffin–tin density of states for bulk copper, and s, p and d decomposition.

Figure 4.5 Muffin–tin density of states for bulk iridium, and s, p and d decomposition.

Figure 4.6 Twin fault structure as viewed in figure 4.2, with shading to indicate atoms whose potentials were allowed to relax.

Figure 4.7 Comparison of the muffin–tin density of states of the central two atoms at a twin fault in copper with the bulk.

Figure 4.8 Comparison of the muffin–tin density of states of the atom two layers from the twin fault plane in copper with the bulk.

Figure 4.9 The muffin–tin density of states within 1eV of the Fermi energy for the central atom in a twin fault in copper, and the bulk.

Figure 4.10 Comparison of the muffin–tin density of states of the central two atoms at a twin fault in aluminium with the bulk.

Figure 4.11 Comparison of the muffin–tin density of states of the atom four layers from the twin fault plane in aluminium with the bulk.

Figure 4.12 The muffin–tin density of states within 1eV of the Fermi energy for the central atom in a twin fault in aluminium, and the bulk.

Figure 4.13 Comparison of the muffin–tin density of states of the central two atoms at a twin fault in iridium with the bulk.

Figure 4.14 Comparison of the muffin–tin density of states of the atom two layers from the twin fault plane in iridium with the bulk.

Figure 4.15 The muffin–tin density of states within 1eV of the Fermi energy for the central atom in a twin fault in iridium, and the bulk.

Figure 4.16 Muffin–tin density of states for copper, iridium and aluminium evaluated in the HCP cystal structure using bulk FCC potentials (dotted line). The shaded region is the corresponding bulk FCC MTDOS.

Figure 4.17 Localised states visible in the MTDOS evaluated at the K point at the aluminium twin fault.

Figure 4.18 Structure and unit cell used in the impurity calculations.

Figure 4.19 Muffin–tin density of states for the aluminium stacking fault with magnesium impurity.

Figure 4.20 Muffin–tin density of states for the aluminium stacking fault with copper impurity.

Figure 5.1 Atomic structure of the $\Sigma 5$ (210) / [001] symmetric tilt boundary used in the calculations, with the atoms closest to the fault labeled. The dotted line indicates the conventional face–centred cubic cell, with shaded atoms lying one plane back. **Below.** Plan view of the interface layer (labeled 0 in main diagram) with one of the two adjacent layers (shaded).

Figure 5.2 MTDOS near a Ni (210) / [001] symmetric tilt boundary (shaded), compared with the MTDOS of bulk Ni (dashed line).

Figure 5.3 Comparison of the MTDOS calculated at the Ni (210) / [001] symmetric tilt boundary with the LKKR technique (dashed line), and a multiple–scattering $X\alpha$ cluster calculation (shaded). The cluster results have been rescaled to the LKKR peak height. The inset shows the cluster geometry in cross–section.

Figure 5.4 Non self–consistent MTDOS for the Ni (210) / [001] symmetric tilt boundary.

Figure 5.5 MTDOS of the indicated atoms near a Ni (210) / [001] symmetric tilt boundary (shaded), with sulfur substituted for the atom 0. For comparison the associated MTDOS from figure 5.2 are given (dashed line), except for the sulfur atom, where the comparison is with bulk nickel.

TABLE CAPTIONS

Table 2.1 Comparison of the basis vector attenuation at the adjacent layer for the FCC (111) and FCC (210) directions for selected numbers of vectors, N_g.

Table 3.1 Allowed values of special $k_{||}$ sampling points given by Cunningham's algorithm for the square and hexagonal lattices.

Table 3.2 Convergence of energy integrals using the Gaussian integration technique with the number of sampling points N_E, for core level and valence band muffin–tin charges. The core level calculations were performed with a contour of width 0.01Ha centred on the real eigenvalue, and the valence band integral extended from -0.100Ha to 0.314Ha relative to the muffin–tin zero.

Table 4.1 Selected interface energies γ (in ergs/cm^2) for various metals (sf = stacking fault, gb = grain boundary and s = surface). Data taken from Appendix 2 of Hirth and Lothe, 1982.

Table 4.2 Stacking fault energy of silver as determined in a variety of studies using the techniques listed (compiled from Gallagher, 1970). Energies in ergs/cm^2.

Table 4.3 Estimates of the stacking fault energy (in ergs/cm^2) of silicon.

Table 4.4 Calculated stacking fault energies and corresponding experimental values, taken from Gallagher (1970) and Murr (1975) (ergs/cm^2).

Table 4.5 The relative weights of the localised states at the twin fault in aluminium on the atoms in the interface region.

ACKNOWLEDGEMENTS

I would like to offer my deepest thanks to Dimitri Vvedensky for identifying a problem so suited to my character. His careful supervision and constant interest and enthusiasm are an example to all. I wish to acknowledge also the indispensible help of James MacLaren in the course of this work, and look forward to continuing collaboration.

The work has gained from the conversations I have had with many people, and I thank especially Mark Eberhart and Tony Gonis for their insight into various aspects of this work.

I appreciate greatly the friendship of all past and present members of the Solid State Theory Group who have made my time at Imperial so enjoyable, and I particularly thank Karl and Shaun for being ideal office mates, and Pav and John for numerous conversations. Dimitri's tireless efforts have enabled me to travel abroad on numerous occasions and I am very grateful for the opportunities that he has presented to me. During many visits I have been fortunate to fall in love with New Mexico, which is in no small way due to the hospitality of Mark, Cheryl and James on La Jacona Ranch.

Finally, I am greatly indebted to my family for their unquestioning support, and to Sarah whose friendship and affection have been a *sine qua non.*

Financial assistance was provided by the U.K. Science and Engineering Research Council, the Office of Naval Research and NATO.

Ah! don't say that you agree with me. When people agree with me I always feel that I must be wrong.

— OSCAR WILDE (1854-1900)

CHAPTER 1: INTRODUCTION

1.0 Introduction

Technological advances go hand in hand with the development of new materials, as new materials prompt new technologies (*e.g.* high–temperature superconductors) and advances in technology call for the development of materials with specified properties (*e.g.* microelectronics). Mechanical properties are an important characteristic of any material, in applications both structurally orientated and in non–structural areas. Thus, the development of new light–weight ductile alloys with good high–temperature performance will greatly benefit the aircraft industry, whilst an understanding of, and the ability to control, the brittle behaviour of the new superconducting ceramics will considerably aid their incorporation into electronic devices. As for the latter, it is often the case that a material exists with desirable or novel characteristics, but whose exploitation is prevented by some other detrimental properties, like excessive brittleness, which prevents fabrication, or has side effects which cannot be tolerated, as would be the case for an engine component with a tendency to fracture. The modification of mechanical properties – whilst retaining the desirable characteristics – is therefore a goal in a wide range of industries.

There are numerous approaches to the modification of the mechanical behaviour of crystals. Historically, this optimisation has been achieved by largely empirical techniques. However, increasingly powerful computers have in recent years enabled the application of quantum–mechanical theories to the study of realistic systems and suggest theory–assisted material design may one day be possible. We consider a few of the areas in which theory has provided hints at a possible predictive capability.

Deformation behaviour of materials is largely governed by defects within the crystal structure. Most important are the line defects and in particular dislocations, small regions of deformation which move under applied loads, migrating or

extending the deformation through the crystal. In real materials one finds dislocation loops, within which the material is slipped. Under stress, elastic forces result in the movement of the dislocations, contracting or expanding the slipped region, and in doing so altering the deformation energy stored in the loop. Dislocations also induce local elastic fields which interact with other dislocations, providing another mechanism for energy storage as well as a factor important to dislocation motion. Dislocation mobility is often a controlling factor in deformation processes, governing the extent to which stresses are relieved within the crystal, and is severely limited through interaction with other defects, not only neighbouring dislocations, but also, for example, voids, grain boundaries and stacking faults. Accurate quantum mechanical calculations are not yet possible on isolated dislocation structures, due their extended topological nature. However, continuum elasticity theory (Hirth and Lothe, 1982) may reasonably describe the interactions of dislocations, requiring as input such numbers as the stacking fault and grain–boundary energy. It is in the determination of these quantities, which depend fundamentally on atomic–scale interactions, that accurate electronic structure calculations are of utmost importance.

Microstructural design, where dislocation mobility is controlled through the variation of grain size and structures, has long been employed to alter the hardness and strength of metals. Work hardening, whereby dislocations are introduced into the metal to the extent that they greatly impede one another, was a phenomenon known, but presumably little understood, by the ancient Egyptians. More recently, microstructural design has progressed to the stage where optimisation of material properties is possible through the introduction of ceramic particles of *controlled* shapes and sizes into an intermetallic matrix, with the morphology and composition of the ceramic reinforcements allowing such properties as the fracture toughness, compressibility and failure modes to be manipulated (*e.g.* Christodoulou, Parrish and Crowe, 1988). An important factor in determining the influence of the reinforcement is the microchemistry at the metal–ceramic interface, the nature of the interface bond and abruptness of the interface, questions which may be answered through electronic structure calculations.

Alloying a material with additional elements can significantly alter its mechanical properties, even in the limits of a few parts per million, and provides an alternative means of optimising behaviour. Solid–solution softening and hardening and ductility enhancement by this mechanism have recently attracted theoretical attention. Masadu–Jindo and Terakura (1989) performed total energy calculations on aluminium-based alloys and, from the corresponding bulk moduli, accounted

for the experimentally observed changes in elastic moduli. Chubb, Papaconstantopoulos and Klein (1988) considered TiAl, which has the $L1_0$ structure with c/a ratio of about 1.02. They argued that the ductility of TiAl could be enhanced by a reduction in c/a ratio to 1, at which point all slip planes would be equivalent. Total energy calculations with vanadium substituted for aluminum indicated a reduced value of c/a, due to the vanadium donating electrons into bonding orbitals directed along the c–axis. This work also highlights the importance of *structure–property* relationships, where particular structures have a tendency to exhibit certain properties, such as the ductile behaviour of face–centred metals which is attributed to the large number of available slip systems. This behaviour has been utilised in an alternative approach to theoretical materials design, the use of "structure–maps" (Pettifor, 1986). Using a phenomenological ordering of the elements, structural separation of compounds with a given stoichiometry may be achieved, and so in reverse the appropriate stoichiometry of a binary compound with a given structure may be predicted.

Some solute atoms are found to segregate at defects such as stacking faults and anti–phase boundaries (APB's), significantly altering the corresponding defect energy, and consequently affecting dislocation formation energies and mobilities. Hong and Freeman (1989) have studied the effect of ternary additions on the anti–phase boundary energy of NiAl, finding the addition of various transition metal atoms reduced the energy. However, as in the work of Masadu–Jindo and Terakura (1989) and Chubb *et al.* (1988) these first–principles calculations are extremely demanding computationally and, for reasons described in the following Sections, restrict calculations to a small number of unique atoms and consequently unphysically high solute densities.

More dramatic impurity effects are found with changes in grain–boundary stoichiometry, which in some cases strongly influence grain boundary chemistry and consequently cohesive properties. A classic example is the addition of boron to the intrinsically brittle polycrystalline material Ni_3Al, (Aoki and Izumi, 1979) which significantly increases ductility, and the addition of sulfur to nickel, which has the opposite effect, and in large concentrations results in grain boundary embrittlement (Lassila and Birnbaum, 1987). Whilst a thermodynamic approach incorporating the interfacial energetics can account for the segregation behaviour of such alloying elements, the mechanisms for the intrinsic behaviour, and how the impurity–host bonding results in the macroscopically observed behaviour is still to be answered. On the basis of cluster calculations Eberhart and Vvedensky (1987) have suggested that intergranular fracture in polycrystalline materials may be

associated with localised states near the Fermi energy and a more isotropic distribution of charge. This results in a softer region within which bond rearrangement is more easily achieved and consequently large dislocation core regions will result, inhibiting the crossing of the interface, and causing a local build up of strain. An alternative approach to the study of impurity effects at grain–boundaries was taken by Goodwin, Needs and Heine (1988) on the basis of pseudopotential calculations on simplified structures of aluminium grain boundaries with arsenic or germanium impurities. These results indicated increased cohesion in the presence of the impurity, and subsequent studies (Goodwin *et al.*, 1989) indicated a decreased cleavage stress and increased ideal shear stress, favouring bond breaking but discouraging bond bending. These results are interesting in the light of continuum models of fracture due to Kelly, Tyson and Cottrell (1967), which emphasise the *competition* between cleavage and shear stress without providing the microscopic basis underlying the effect. Again, quantum mechanical calculations are being used to account for observed mechanical behaviour and offer a glimpse of future impact upon materials design.

In the remainder of this Chapter the foundations of our current approaches to the electronic structure of solids are outlined. Traditional techniques employed for the study of bulk solids will be briefly described, along with the difficulties in their use for the study of defect structures. The accuracy of these methods contrasts sharply with the alternative more approximate techniques which have been developed for the particular study of low symmetry defect systems, which will also be described. It will become clear that no technique addresses all aspects of the complex phenomena underlying the mechanical behaviour of materials. Against this background, the need for new methods such as that described in Chapters 2 and 3 of this Thesis will be argued, and the benefits highlighted. Chapters 4 and 5 describe applications of this new technique to stacking faults, including the calculation of twin fault energies, and the first self–consistent electronic structure calculation of an isolated grain–boundaries.

1.1 Electronic structure calculations

Our understanding of the observable properties of solids are, in principle, determined completely by quantum mechanics through the solutions of the many–body Schrödinger equation for the motion of the electrons and nuclei. Since the nuclear mass is considerable larger than the electron mass this equation may be considerably simplified through the Born–Oppenheimer approximation, which treats the electrons as moving in the potential arising from *static* nuclei. The result of this approximation is the separation of the electronic and nuclear coordinates, and we may focus on a reduced many–electron Schrödinger equation

$$\left\{ -\frac{\hbar^2}{2m_e} \sum_j \nabla^2_{\mathbf{r}_j} - \sum_{jj'} \frac{e^2 Z_{j'}}{|\mathbf{r}_j - \mathbf{R}_{j'}|} + \frac{1}{2} \sum_{j \neq j'} \frac{e^2}{|\mathbf{r}_j - \mathbf{r}_{j'}|} \right\} \psi(\mathbf{r}_1, \ldots, \mathbf{r}_n) = E\psi(\mathbf{r}_1, \ldots, \mathbf{r}_n) \tag{1.1.1}$$

where the $\mathbf{r}_j$ and $\mathbf{R}_j$ are the electronic and nuclear coordinates, $\hbar$ is Planck's constant, m_e is the electronic mass, e is the electronic charge and Z_j is the atomic number of the j'th nucleus. The terms on the left–hand side of (1.1.1) are the electronic kinetic energy, the electron–nucleus potential energy and the electron–electron potential energy. The solution $\psi(\mathbf{r}_1, \ldots, \mathbf{r}_n)$ is the n–electron wavefunction, which completely characterises the electron behaviour for the chosen nuclear configuration. The solution of (1.1.1) coupled with the Hellmann–Feynman theorum (Hellmann, 1937; Feynman, 1939) allows the determination of the forces on the nuclei which may then be moved accordingly, and the lowest energy nuclear configuration determined. Since the time scale of deformation of a material is considerably longer than the relaxation time of the electrons, the energy required for a particular deformation path may be in principle determined from a sequence of calculations with appropriate atomic coordinates. However, such a process requires huge computational resources and even determining the atomic structure of the initial configuration when, as is usually the case for defect structures, there is limited information, is a daunting task (see, however, the discussion of the embedded–atom method below).

Direct solution of (1.1.1) is impractical for a solid since there are typically of the order of 10^{23} electrons, each strongly interacting through a strong r^{-1} Coulomb interaction. In fact even if a solution was possible, the tabulation of a function of 10^{23} vector variables would not be a convenient or accessible way of understanding the behaviour of the electrons. A more suitable approach which

is almost universally employed in the field of solid state physics, particularly in the problems which concern the work in this thesis, is that known as density–functional theory (DFT). Formally justified through the work of Hohenberg and Kohn (1964), DFT is based upon the theorem that the ground state properties of the solid are functionals *only* of the charge density, $\varrho(\mathbf{r})$. Thus the energy corresponding to density ϱ may be written

$$E[\varrho] = E_0[\varrho] + \frac{1}{2}\int \frac{\varrho(\mathbf{r})\varrho(\mathbf{r}')}{|\mathbf{r}-\mathbf{r}'|}d\mathbf{r}d\mathbf{r}' + \frac{1}{2}\sum_{i\neq j}\frac{e^2 Z_i Z_j}{|\mathbf{R}_i - \mathbf{R}_j|} - \sum_i eZ_i \int \frac{\varrho(\mathbf{r})}{|\mathbf{r}-\mathbf{R}_i|}d\mathbf{r} + E_{XC}[\varrho] \tag{1.1.2}$$

where $E_0[\varrho]$ is the (known) energy of a system of noninteracting electrons with density ϱ, the second, third and fourth terms on the left of (1.1.2) are the classical electron–electron, nucleus–nucleus and electron–nucleus interaction energies respectively, and $E_{XC}[\varrho]$ is the exchange–correlation contribution, arising from the quantum mechanical behaviour of the electrons. This latter contribution is actually *defined* to be the difference between the exact energy and sum of other terms on the left of the equation. Minimising this energy with respect to the density one obtains an effective one–electron Schrödinger equation (Kohn and Sham, 1965)

$$\left[-\frac{\hbar^2}{2m_e}\nabla^2 + V(\mathbf{r})\right]\phi_i(\mathbf{r}) = E_i\phi_i(\mathbf{r}) \tag{1.1.3}$$

with

$$\varrho(\mathbf{r}) = e\sum_i |\phi_i(\mathbf{r})|^2 \tag{1.1.4}$$

and where the potential $V(\mathbf{r})$ is the sum of the electron–electron repulsion and the Coulomb potential due to the nuclei, plus an additional exchange–correlation potential

$$V_{XC}(\mathbf{r}) = \frac{\delta E_{XC}[\varrho]}{\delta\varrho(\mathbf{r})} \tag{1.1.5}$$

The E_i in (1.1.3) enter as Lagrange multipliers and *appear* to play the role of single–electron eigenvalues. However, their correspondance to the quasi–particle excitation spectra is only approximate (Moruzzi, Janak and Williams, 1987). The only limitation of this theory is that the functional $E_{XC}[\varrho]$ is not known exactly, and must be approximated. A particularly successful approach has been the local

density approximation (LDA), where the exchange–correlation energy functional is written

$$E_{XC}[\varrho] = \int \varepsilon_{XC}(\varrho(\mathbf{r}))\varrho(\mathbf{r})d\mathbf{r} \qquad (1.1.6)$$

with $\varepsilon_{XC}(\varrho(\mathbf{r}))$, the exchange–correlation energy density, taken to be that due to a homogeneous electron gas of the same local density, and for which a number of expressions exist (*e.g.* Slater and Johnson, 1972; Hedin–Lundquist, 1971). The LDA is easily implemented and has been demonstrated to give (*e.g.* Moruzzi, Janak and Williams, 1978) accurate lattice constants, phonon frequencies, bulk moduli, cohesive energies and predicts pressure induced structural transformations (*e.g.* Needs and Martin, 1984). Even the one–electron eigenvalues correspond very well with experimental excitation spectra (Thiry *et al.*, 1979). The LDA approaches the exact solution in the limit of slowly varying densities, and also in the limit of high densities, since the kinetic energy is given exactly by $E_0[\varrho]$. Indeed, recent calculations going beyond the LDA suggest the largest errors contributing to calculated cohesive energies arise from the isolated atom energies, where the density is less smoothly varying. This might have important consequences for the calculation of defect energies, such as grain–boundary energies, where electron densities can also be considerably more anisotropic than in the bulk.

Even within the LDA, accurate solution of the Kohn–Sham equations (1.1.4-5) presents a formidable task. In this regard symmetry is an important property of the system being studied. For perfect crystals, defined by a lattice of vectors $\mathbf{R}_{ijk} = i\mathbf{a}_1 + j\mathbf{a}_2 + k\mathbf{a}_3$ where i, j, k are integers and $\mathbf{a}_1, \mathbf{a}_2, \mathbf{a}_3$ map out a unit cell, the invariance of the crystal under any displacement $\mathbf{R}_{ijk}$ restricts wavefunctions to the form

$$\phi_{\mathbf{K}}(\mathbf{r}) = e^{i\mathbf{K}\cdot\mathbf{r}}u_{\mathbf{K}}(\mathbf{r}) \qquad (1.1.7)$$

where the function $u_{\mathbf{K}}$ has the periodicity of the lattice, $u_{\mathbf{K}}(\mathbf{r}) = u_{\mathbf{K}}(\mathbf{r}+\mathbf{R}_{ijk})$. $\mathbf{K}$, the crystal momentum, labels the state. This result, Bloch's theorem, is extremely powerful, reducing the problem of determining the wavefunctions of the solid to finding solutions within the unit cell, since the wavefunction outside this region may be constructed from (1.1.7). Further symmetry (*e.g.*, reflection, rotation, ...) may reduce the problem further. Bloch's theorem also enables one to use a Fourier basis for the expansion of the wavefunctions or, alternatively, allows one to use a localised basis centred about each unique atom. Thus the effect of structure on the complexity of the calculation may be clearly seen, since the larger the unit cell or the more symmetrically–unique atoms, the larger the dimension of the localised basis and the larger the region of space over which the solution

must be determined, since Bloch's theorem is not applicable *within* the unit cell. Typically, the calculation time scales as the cube of the number of unique atoms, realistically restricting applications to structures with 10–20 atoms in the unit cell.

Having adopted the LDA and invoked Bloch's theorem, one must next attempt to solve equation (1.1.4) within the unit cell. In this respect the nature of the electrons in a solid strongly influence the method of solution. The lowest energy solutions of (1.1.4) are the "core states", spatially localised around the nucleus, with no significant overlap with neighbouring atoms and which, to an excellent approximation, behave as though in an isolated atom, occupying $1s$,$2s$,$2p$,... levels and retaining spherically symmetric charge distributions. With increasing energy the wavefunctions become less localised, eventually interacting with electrons from neighbouring atoms to such an extent that the energy levels broaden into valence bands and the wavefunctions extend throughout the whole solid. It is with these two regimes that any electronic structure technique must come to terms.

1.2 First principles techniques

There have been a large number of methods developed for solving the one–electron Schrödinger equation from first–principles, the most important of which are briefly summarised here (for more details see the review by Koelling (1981)). The simplest basis for dealing with three–dimensional periodicity is the set of plane waves, but, due to the highly localised core states which induce rapid oscillation in the valence electrons (to maintain orthogonality), do not constitute a practical method, requiring many millions of plane waves. This difficulty may be overcome by replacing the actual crystal potential with a much weaker "pseudopotential" which traps no core levels and results in wavefunctions smoothly varying within the core region, but which match to the true solutions outside, thus permitting a representation with only a few plane waves. The pseudopotential method therefore focusses on the valence electrons, which are responsible for the binding of the solid and, by removing the core states from the picture, avoids many problems arising from their large energy contribution, which plays an unimportant role in determining structure. The pseudopotential method (Cohen, 1985) has been extremely successful in applications on many of the lighter materials, such as Si, GaAs and Al, but applications to transition–metals are inhibited by the large numbers of plane waves still required for the valence d-electrons, which retain some of their localised atomic character, and whose study is only now becoming feasible following advances in computational technology.

In close–packed solids, including many transition metals, the high coordination found in the crystal structure has motivated the "muffin–tin" approximation

to the potential, which forms the basis of the augmented plane wave (APW) (Loucks, 1967) and the Korringa–Kohn–Rostoker (KKR) (Ham and Segall, 1961) techniques. The solid is first divided into non–overlapping spheres centred upon the atomic sites, within which the potential is spherically–averaged. In the region between the spheres the potential is volume averaged. The Schrödinger equation is numerically integrated within the muffin–tin, where the wavefunction is strongly affected by the nuclear charge and retains much of its atomic character, and then matched to the solution in the interstitial regin. This matching leads to a secular equation, the solutions of which yield the one–electron energies and wavefunctions. The accuracy of the muffin–tin approximation increases with the isotropy of the atomic–site environment in the material, being most valid for close–packed metals and breaking down for covalently–bonded materials such as Si.

As mentioned above the calculation time for an electronic structure calculation scales with the cube of the number of unique atoms. For the APW and KKR methods the solution of the secular equation involves the location of the zeros of a large determinant as a function of energy, which are found by many evaluations at trial energies, due to the *non–linear* energy dependence and because there are no algorithms which can simultaneously yield all eigenvalues and eigenfunctions simultaneously. Andersen (1975) proposed a modification to the APW and KKR methods, introducing energy–independent basis functions at some reference energy which are then employed throughout a range of energies. Consequently the secular equation becomes a *linear* eigenvalue problem, with simultaneous evaluation of the eigenvalues and eigenfunctions at a given crystal momentum **K**. These new methods, the linear combination of muffin–tin–orbitals (LMTO) (Skriver, 1984) constructed from the KKR equations, and linearized APW (LAPW) (Koelling and Arbman, 1975), at the cost of slightly reduced accuracy, offer roughly an order of magnitude increase in computational efficiency and thus increase the complexity of system which may be studied. Recently both methods have been extended to include the full crystal potential (Wimmer, Krakauer, Weinert and Freeman, 1981; Weyrich, 1988), thus allowing the treatment of both semiconductors and transition metals within a common computational framework.

Having developed these techniques for solving Schrödinger's equation for perfect crystals, it is natural to ask whether thay can be employed in the study of defects. The answer, at least in principle, is yes. The major difficulty to be confronted is the reduced periodicity: a planar defect such as a stacking fault or grain boundary only has two–dimensional periodicity, whilst a dislocation has only one–dimensional periodicity. Thus, since Bloch's theorem cannot be applied

along the directions which lack translational symmetry, Schrödinger's equation must be integrated over an effectively infinite unit cell. However, in metals, perturbations in the electronic structure resulting from the presence of a defect are confined to within a few Ångstroms because of screening by the electrons. Beyond the screening length the electronic distribution is essentially bulk–like. Thus, a regularly–repeated array of, say, coincident grain boundaries, will possess translational periodicity in all three dimensions and, if the separation of adjacent defects is sufficiently large, each defect will behave as though isolated. This geometry is referred to as a supercell, and, because of the success and familiarity of workers with bulk electronic structure techniques, its use abounds in the literature of surface and interface calculations.

1.3 Approximate techniques

The computational demands of those techniques mentioned above which restrict their application to systems with but a few unique atoms are a direct consequence of the accuracy of the solutions produced. By allowing a more approximate solution of relevant equations, but without excluding the important physics, larger systems and more realistic structures may be studied. This approach to electronic structure and total energy calculations of reduced symmetry systems, rather than the extension and generalisation of the sophisticated band structure techniques, is desirable for a number of reasons:

- The development of even qualitative theories of complex phenomena such as mechanical behaviour requires many calculations, each of which may be time consuming if standard methods are used. One must therefore sacrifice some accuracy for computational feasibility. These initial calculations may act as a "fast screening" method, and once the trends have been identified more elaborate calculations may be used to develop further insight.
- Simplified approaches with a judicious choice of approximations may more easily clarify the essential underlying physics, identifying the fundamental parameters of the problem, and thus providing an important first step in the development of a more general theory.

Among the many approximate techniques used for studies of direct relevance to mechanical properties, the most important have been the tight–binding, cluster and embedded–atom methods.

Tight–binding. The tight–binding (TB) scheme was originally proposed by Slater and Koster (1954) as a means of obtaining solutions of Schrödinger's equation in solids away from the high symmetry directions of the Brillouin zone which,

at the time, were the only feasible calculations. Taking the results of accurate band structure calculations, bonding integrals (see below) could be determined empirically by some sort of fit, and the solutions along other directions of $\mathbf{K}$ could then be calculated. With the development of more powerful calculations, the need for such a scheme diminished and the method was largely discarded. However, the TB method has been revived recently (Bullett, 1980) in applications for crystal defects, where conventional techniques are often too computationally demanding.

Within the TB approximation the one–electron wavefunction is expanded as a sum of localised orbitals $\phi_\alpha(\mathbf{r}-\mathbf{R}_j)$ expressed about the atom at site j. When applied to perfect crystalline materials this may be written as a Bloch sum of localised orbitals $\phi_\alpha^\beta(\mathbf{r})$ centered about each atom β in the unit cell at lattice site j:

$$\psi_{\mathbf{K}}(\mathbf{r}) = \sum_{\alpha\beta j} \mathrm{C}_\alpha^\beta(\mathbf{K})\phi_\alpha^\beta(\mathbf{r}-\mathbf{R}_j)\mathrm{e}^{i\mathbf{K}\cdot\mathbf{R}_j} \tag{1.3.1}$$

where the $\mathrm{C}_\alpha^\beta(\mathbf{K})$ are $\mathbf{K}$–dependent expansion coefficients. Substituting this wavefunction into Schrödinger's equation results in a linear eigenvalue problem (since the basis is energy independent) whose solutions yield the band structure $\mathrm{E}(\mathbf{K})$:

$$[\mathbf{H}(\mathbf{K}) - \mathrm{E}(\mathbf{K})\mathbf{S}(\mathbf{K})]\,\mathbf{C}(\mathbf{K}) = 0 \tag{1.3.2}$$

where C is the vector with entries $\mathrm{C}_\alpha^\beta(\mathbf{K})$, and $\mathbf{H}$ and $\mathbf{S}$ are matrices with entries

$$\mathrm{H}_{\alpha'\alpha}^{\beta'\beta}(\mathbf{K}) = \sum_j \mathrm{e}^{i\mathbf{K}\cdot\mathbf{R}_j} \int \phi_{\alpha'}^{\beta'*}(\mathbf{r})\mathrm{H}(\mathbf{r})\phi_\alpha^\beta(\mathbf{r}-\mathbf{R}_j)\mathrm{d}\mathbf{r} \tag{1.3.3}$$

$$\mathrm{S}_{\alpha'\alpha}^{\beta'\beta}(\mathbf{K}) = \sum_j \mathrm{e}^{i\mathbf{K}\cdot\mathbf{R}_j} \int \phi_{\alpha'}^{\beta'*}(\mathbf{r})\phi_\alpha^\beta(\mathbf{r}-\mathbf{R}_j)\mathrm{d}\mathbf{r} \tag{1.3.4}$$

The elements in (1.3.3) are the "hopping" or "bonding" integrals, and those in (1.3.4) the overlap integrals. Further simplification is possible if the orbitals ϕ_α^β are represented as linear combinations of functions which are orthogonal when centred on different lattice sites. The problem then reduces to evaluating a few matrix elements in (1.3.3), by fitting to accurate band structures produced by first–principle techniques. Normally, terms no more distant than the second neighbour shell are included, hence the name tight–binding.

The total energy in the TB approximation may be written in terms of the band structure energy $\mathrm{E_{bs}}$, the ion–ion interaction energy $\mathrm{E_{ii}}$ and the electron–electron interaction energy $\mathrm{E_{ee}}$:

$$\mathrm{E} = \mathrm{E_{bs}} + \mathrm{E_{ii}} - \mathrm{E_{ee}} \tag{1.3.5}$$

In many applications E_{bs} provides the major contribution to the energy differences between different structures, particularly when there is no change in atomic volume (Pettifor, 1986). Thus by determining E_{bs} from the density of states $\varrho(E)$ (E_f is the Fermi energy)

$$E_{bs} = \int^{E_f} E\varrho(E)dE \qquad (1.3.6)$$

and, where necessary, modelling $E_{ii} - E_{ee}$ *via* some sort of short–ranged force–constant model, questions concerning the cohesive energy and structure of solids may be addressed (Pettifor, 1986).

An additional attractive feature of the TB method is the application of the *recursion method* (Haydock, 1980), in which the density of states is evaluated by means of a continued fraction, the elements of which are found by repeated operation of the Hamiltonian on some starting vector. Each application of the Hamiltonian may be viewed as coupling the initial state vector to successively more distant sites through the hopping elements, with the importance to the density of states diminishing as the n–th iterated state spreads out. The simplicity of the recursion method allows the study of arrangements of many thousands of atoms with no assumption as to the underlying periodicity.

The major difficulty within the tight–binding framework centres around the choice of values for the bonding integrals. When a first principles calculation exists these may be obtained by fitting (Papaconstantopoulos, 1986), though for many situations such calculations do not exist, and some assumption must be made about the "portability" of the bonding integrals from one environment to another. Even in those cases where first–principles results do exist, some assumptions must be made concerning the dependence of hopping integrals on bond length and bond angle if they are to be used to model defects, where such quantities can take quite different values for those of the perfect crystal. Despite these uncertainties there are many problems for which TB represents one of the few viable approaches currently available (*e.g.* the studies of grain boundaries in silicon by Paxton and Sutton (1988)).

Clusters. As mentioned above, there is a play off between the accuracy with which the electronic structure is calculated and the faithfulness of the structural representation of the system being modelled. Whereas the tight–binding approach, in conjunction with the recursion method, may be used to study systems containing of the order of one thousand atoms, including realistic geometries of grain–boundaries or crack tips, an alternative approach which some workers have adopted is to study clusters of 10–100 atoms in representative geometries, but for which accurate self–consistent solutions of Schrödinger's equation are found.

Since many features of electronic structure, particularly those involving defects or impurities, are spatially localised, the electronic structure of small clusters has achieved considerable popularity as a first step toward more detailed studies (*e.g.*, Briant and Messmer, 1980; Eberhart and Vvedensky, 1987; Painter and Averill, 1987, 1989). The benefits of cluster calculations are manifold, including

- the freedom from underlying translational symmetry, which permits any manner of deformation to be considered without significant increase in computational demand,
- the large number of calculations which may be performed, allowing the identification of gross trends,
- any first–principles method which employs a localised basis may be implemented within a cluster framework. Furthermore, alternative techniques from the field of quantum chemistry, such as the method of configuration–interaction, and which determine the solution of (1.1.1) without invoking the LDA, can be applied due to the small number of electrons. Thus there is the possibility of a large number of calculations making different approximations, which will help identify the essential components of any general theory.

Approaches based upon clusters have their drawbacks, such as the neglect of long range influences and the limited ability to check the effects of free boundaries. Consequently, subtle effects such as the small differences in total energy arising from small structural modifications are probably inaccessible to cluster calculations. However, gross features of the electronic structure can certainly be calculated with less effort than conventional methods, and chemical effects due to isolated impurities correctly identified. Used in conjunction with more elaborate methods, they are particularly useful as a "fast screening" method.

Embedded–atom. The embedded atom method (EAM) has recently been developed (Daw and Baskes, 1983, 1984) for the simulation of realistic problems of mechanical behaviour, and has largely superceded traditional methods, such as pair potentials and alternative phenomenological approaches, which suffer from a number of shortcomings. Pair potentials, describing the interaction energy between pairs of atoms, do not account well for elastic properties of metals without the addition of volume dependent corrections (for example, in order to satisfy the Cauchy discrepancy $C_{12} \neq C_{44}$) and neglect directionality in chemical bonding. Therefore in the case of defect structures, such as surfaces or grain boundaries, the question arises: how does one partition the volume and hence determine the volume–dependent energy term? Phenomenological approaches, such as those considering the interactions between larger entities like layers or dislocations, suffer

from the difficulties in determining interaction laws, are not good for alloy or impurity problems, and introduce many unknown parameters into the problem.

The major feature of the EAM is the introduction of an embedding energy, dependent only upon the charge density of the surrounding atoms. This justification follows from the work of Nørskov and Lang (1980) and Stott and Zaremba (1980), who showed the embedding energy of an isolated impurity in a homogeneous electron gas is dependent, to first order, upon the density of the gas at the position of the nucleus. This idea is generalised in the EAM by writing the cohesive energy of the solid as

$$E_{coh} = \sum_i F_i \left(\sum_{j \neq i} \varrho_j^{at}(R_{ij}) \right) + \frac{1}{2} \sum_{ij} \phi_{ij}(R_{ij}) \qquad (1.3.7)$$

that is, as an embedding energy and a pair interaction energy, the latter describing the electrostatic interaction of the atoms. The embedding energy, given by the embedding function F_i, is determined by the assumption that each atom interacts with a locally homogeneous electron gas, as in effective medium theory, and the density of which is determined by atomic charge densities centred upon each atomic site. This term provides a volume dependence which ensures the Cauchy discrepancy is satisfied. Once the energy is known, the EAM can be coupled with Monte Carlo or Molecular Dynamics techniques to simulate finite temperature dynamical systems or determine equilibrium structures.

Recently Daw (1989) has provided a formal justification of the EAM by deriving equation (1.3.7) from density–functional theory. In doing so, the underlying approximations were clarified, and in particular the method is shown to neglect Fermi surface/band structure effects and *d–d* hybridisation, which implies its use should be restricted to simple and early/late transition metals, and not used for BCC or more covalently bonded materials. However, the embedding functions Daw derived were of a restricted form. In practice these functions are parameterised, the basic form being dictated by qualitative behaviour and the requirement that the universal binding energy relation (Banerjea and Smith, 1988) be exactly satisfied, and with unknowns determined by a fitting procedure incorporating many experimentally determined properties of the material (Foiles, 1989). Consequently band structure effects and some degree of directionality may be indirectly incorporated. Applications to BCC metals have suggested reasonable accuracy (Adams and Foiles 1989), but should perhaps be treated with caution at present. Applications to FCC metals and alloys have demonstrated the accuracy of this technique

for a wide range of structures and problems, including surfaces (Daw, 1986), grain–boundaries (Foiles, 1988), phonons (Daw and Hatcher, 1985), crack propagation and fracture (Daw, Baskes, Bisson and Wolfer, 1985). However, some questions which are not well addressed are chemical effects, since the superposition of atomic charge densities neglects the response of the material to the embedded atom, and also absolute defect energies, which are sensitive to the potential cut–off radius. For example, in studying dislocations, the stacking fault energy *must* be one of the properties to which the embedding function is fitted, in order for the results to be realistic (Baskes, 1989).

1.4 Future directions – the LKKR method

It is evident from the above discussion of the techniques used in the study of questions of direct relevance to mechanical behaviour of materials, that no single approach incorporates and addresses all the important physical aspects of the problems. These factors may be broadly catagorised as

- **Chemistry** The assumptions underlying both the EAM and TB methods mean many questions concerning, for example, chemical effects at grain–boundaries and other defects cannot be addressed. Such questions require self–consistent solutions of the one–electron Schrödinger equation.
- **Structure** Cluster techniques and the use of first–principle electronic structure methods working within the slab or supercell approximation rely upon idealised and simplified representations of the atomic structure of complex defects.
- **Energy** Only the EAM, TB and pseudopotential methods have demonstrated the ability to determine the energetics of defects including deformation processes, and calculating corresponding stresses and fracture energies.
- **Temperature** The EAM is the only technique for which the temperature plays a role. All others assume 0°K.

In this respect the development of new techniques which may be employed to study realistic systems and which extend the bounds currently present will play an important role in future progress of our understanding of the underlying mechanisms responsible for mechanical behaviour. One such advance recently made is the novel approach of Carr and Parinello (1985), in which the electronic and nuclear coordinates of the solid are simultaneously relaxed. Introducing a fictitious Lagrangean and temperature, classical equations of motion for the wavefunctions and nuclear coordinates are derived which may be integrated in time, whilst simultaneously the temperature removed from the system (simulated annealing).

Thus, time–consuming matrix diagonalisation is avoided, and the one–electron Kohn–Sham equations only solved exactly once, when, at T=0, the equilibrium structure has been determined. The numerous solutions at non–equilibrium structures performed with energy minimisation *via* the Hellmann–Feynman theorem are thus avoided, and computational costs significantly reduced. The power of the technique has been demonstrated with several applications, including a twist boundary in germanium (Payne, Bristowe and Joannopoulos, 1987).

Another development is the concern of this Thesis, the layer KKR (LKKR) technique for the calculation of the self–consistent electronic structure of systems characterised by only two–dimensional periodicity, including such defects as stacking faults and grain boundaries, the primary motivation of this work, but also surfaces and interfaces in general, and in some cases complex bulk systems. In the discussion above, much was made of the compromise which must be made between accuracy and structural realism. As a consequence of the calculation time scaling with the cube of the number of unique atoms in the unit cell, first–principles techniques have been severely restricted in their applications to defects such as grain boundaries. Indeed there have been no studies of transition metal grain boundaries by "*ab–initio*" methods. In the case of the LKKR method, however, atoms of the system are assigned to layers. Within the layers multiple scattering ideas similar to those employed in the three–dimensional KKR method (Ham and Segall, 1961) are used, whilst a recursive algorithm is employed to assemble the layers into the full crystal. This algorithm requires the perturbations induced by the defect to be localised, as is the case as a consequence of screening, so that beyond a certain distance from the fault the *potential* is bulk–like. A number of important points concern the method

- Calculation times scale as $\sum_i n_i^3$, where the n_i is the number of atoms in the unit cell for layer i. Thus the time scales linearly with the number of layers, ideal for the study of intrinsically planar problems.
- **Only** the perturbations in the potential are truncated beyond some distance. The charge density is evaluated for the infinite system without truncation.
- The use of the supercell geometry is dispensed with and the correct boundary conditions placed upon the solutions.
- There is no need to perform troublesome convergence tests with respect to supercell dimension, although the size of the interface region must be checked. However, the correct boundary conditions **reduce** the number of atoms which must be explicitly considered, as compared to the corresponding supercell

which would be required, since there is no problem with adjacent defects interacting.

These last three points are clearly illustrated in figure 1.1, which displays the one–dimensional density of states evaluated at the Γ point for an intrinsic stacking fault in copper, the density of states being evaluated on the atom closest to the fault and all potentials taken to be bulk–like (more details concerning the quantities and structure may be found in the following Chapters). The four different results correspond to an isolated fault, requiring one unique atom in the calculation, and the corresponding results for 5, 8 and 11 atom supercells, all determined by the LKKR method. It is evident from these curves that, while the supercell results are converging to the isolated fault results, they do so slowly, with the 11 layer supercell displaying distinct differences. Furthermore, two localised states at about 0.208 Ha and 0.256 Ha, which appear as singular peaks in the density of states, are clearly split in the 5 layer supercell results due to interaction between adjacent faults. These particular states are *d*–like in character, and hence more strongly localised than similar states in free–electron–like metals, such as aluminium, which would require significantly larger supercells. Of course the effects of boundary conditions can be overstated, and integrated quantities such as the full density of states and total energy are significantly less sensitive than these **K** resolved density of states. For example, consider the case of a free electron gas of density n in a box or a sphere, both of which have the same Fermi energy and energy density, yet which have completely different eigenfunctions. However, such trust in the convergence with supercell dimensions should be supported by considerable testing, and, for magnetic systems, or those where localised states are close to the Fermi energy, much care must be taken. Stacking faults in face–centred crystals represent rather minor structural perturbations, and similar results as those shown in figure (1.1) for grain boundary geometries (Gonis, 1989) display even larger differences and poorer convergence between supercell and isolated fault calculations.

Thus the LKKR technique has features which allow the study of complex defect systems such as grain boundaries, providing results of similar accuracy to the standard bulk KKR electronic structure method. These results not only allow the possibility of judging the accuracy of more approximate techniques such as clusters or TB, and thereby provide justification for the approximations made, but also enable accurate studies of grain boundary electronic structure and chemistry. The technique is still, of course, more demanding computationally than TB or the EAM, and, for example, in the case of energy minimisation at grain boundaries it is envisaged that in the near future these more approximate techniques will

Figure 1.1 Γ point densities of states for various models of an intrinsic stacking fault in copper calculated with the LKKR technique. The density of states is evaluated about the atoms shaded in the diagrams, and structures included are an isolated fault, and supercells consisting of 5, 8 and 11 layers, for which adjacent faults are illustrated below.

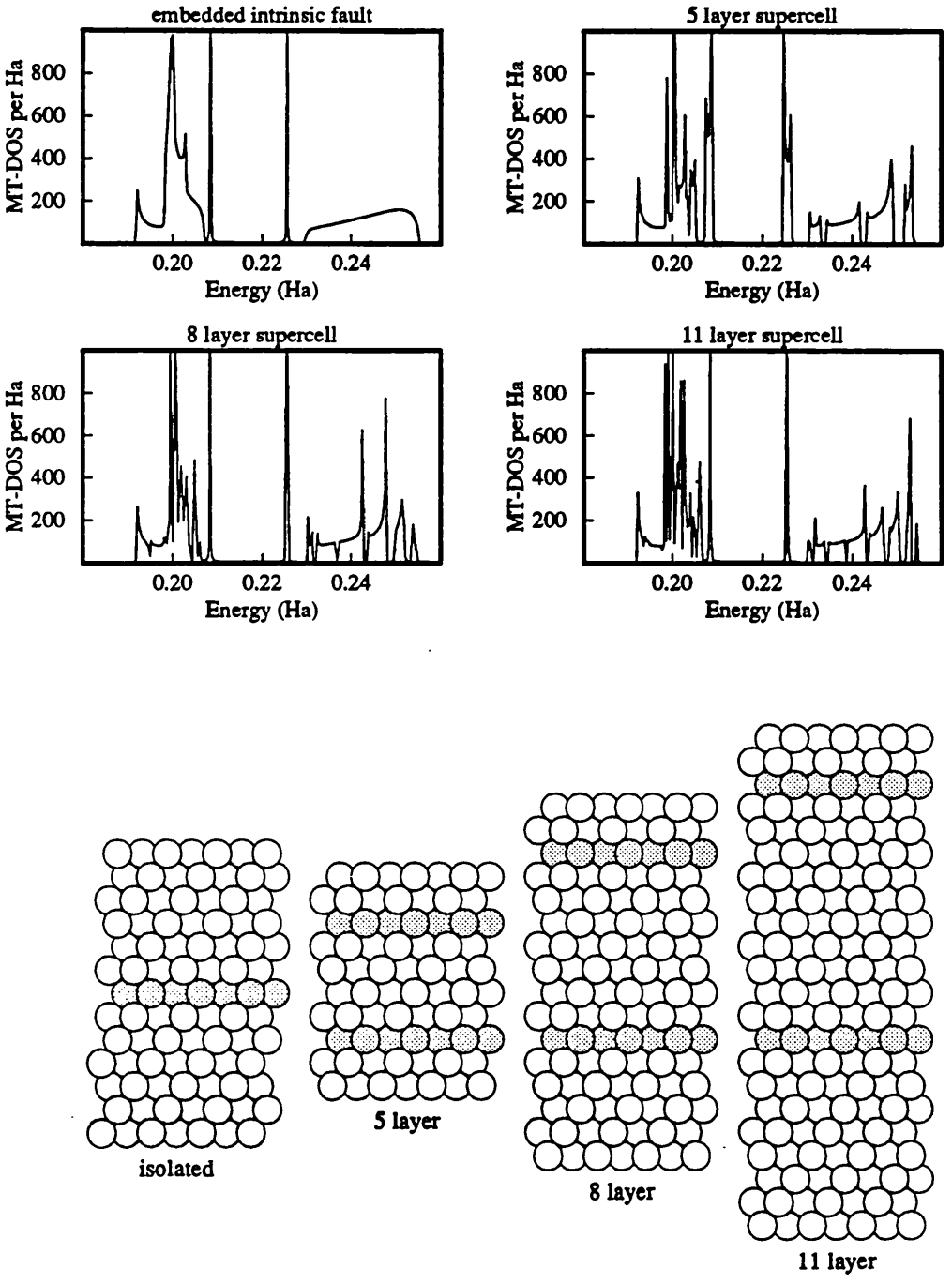

probably provide coordinates for subsequent studies of the electronic structure by the LKKR method. Such an approach was taken for the study of a twist boundary in silicon by DiVincenzo, Alerhand, Schlüter and Wilkins (1986), and illustrates how the various approaches to the energetics and electronic structure of defects can complement one another.

CHAPTER 2. LAYER KKR THEORY

2.0 Introduction

Beyond the application of conventional "bulk" techniques in the supercell or slab approach, there have been a number of techniques developed in the past for the study of isolated interfaces. This is particularly true for the case of surface electronic structure, where experimental results are more readily available for comparison to confirm the validity of model theories and new theoretical methods, and also to stimulate theoretical studies. Thus experimental techniques such as angle–resolved photoemission (Feuerbacher, Fitton and Willis, 1978), X–ray photoemission (Brennan, Stöhr, Jaeger and Rowe, 1980) and field emission (Plummer and Gadzuk, 1970) may provide direct evidence of the surface electronic structure through the identification of transition states or of the surface potential through energy loss analysis. Low energy electron diffraction (Pendry, 1974) can be used to determine surface atomic structure, both providing input to theoretical calculations and challenging theory to explain the observed reconstructions and relaxations. Only recently have experiments begun to probe the structure of internal interfaces with similar accuracy (Fitzsimmons and Sass, 1988,1989; Taylor, Majid, Bristowe and Balluffi, 1989; Majid, Bristowe and Balluffi, 1989).

The overriding difficulty to be overcome in theoretical calculations is the reduction in translational symmetry incurred by the interface. However, as a consequence of electronic screening, the distance over which the effective potential differs significantly from the bulk is usually small (typically a few atomic layers within a metal), and a number of approaches have taken advantage of this behaviour. In this Chapter the theory behind the layer KKR method for determining the electronic structure of systems characterised by two dimensional periodicity, such as isolated grain boundaries, surfaces, and stacking faults, will be presented.

Wavefunction matching was originally employed by Lang and Kohn (1970) in studies of the jellium surface. The crystal potential was replaced by a positive uniform background potential truncated at the surface and the free electron wavefunctions matched to vacuum solutions integrated through a self–consistently determined surface barrier. Various electron densities were studied as models for the simple metals and perturbation theory used to include the weak pseudopotentials. In their alternative wavefunction matching method Appelbaum and Hamann (1972) took proper account of the crystal potential using pseudopotential theory, matching the bulk Bloch states in amplitude and derivative at some plane within the solid to states integrated through the surface region and into the vacuum. This approach was also self–consistent, but neglected the presence of surface states and evanescent waves. Difficulties have been noted with this method (Wachutka, 1987; Inglesfield and Benesh, 1988) from the need to match an infinite number of Bloch states within the 2-d surface Brillouin zone. A similar wavefunction matching was followed by Holzwarth and Lee (1978a,b) with their spherical wave approach, capable of studying transition metals, where the coefficients of the spherical wave expansion were determined by requiring wavefunction and derivative to be everywhere continuous, matching to the normal modes within the solid. This method was not made self–consistent and is prone to the same difficulties as that of Appelbaum and Hamann.

Ultimately wavefunction matching is not a suitable basis for the study of surface and interfacial electronic structure due to the highly sensitive nature of the wavefunction to the crystal potential and boundary conditions and since it actually contains more information than is usually needed (Heine, 1980; Inglesfield, 1982). In this respect the Green function, being directly related to the local density of states, is a far more suitable quantity, and has been the focus of many studies.

A basis of localised orbitals has an advantage in the study of defects in that the matrix elements connecting sites have a natural cutoff with distance, limiting the effects of the defect to a small subspace of the Hamiltonian. A number of techniques have taken advantage of this, particularly for surface studies. Mele and Joannopoulos (1978) formulated a general solution to this problem for the case of a surface and demonstated its application within an empirical tight binding model of GaAs. Within the approach presented by Lee and Joannopoulos (1981a), matching of wavefunction across atomic layers is achieved through a transfer matrix, from which the electronic structure may be determined. The tight binding formulation was also adapted to give the Green function (Lee and Joannopoulos, 1981b). Pollmann and Pantelides (1978) and Schmeits, Mazur and Pollmann (1983) have

developed scattering theoretical Green–function–based methods for tight binding models of semiconductors. Also closely related to these latter approaches is the tight–binding muffin–tin orbital approach of Lambrecht and Andersen (1986), whilst a Green function-transfer matrix method for transition metals has been developed by Falicov and Yndurain (1975a,b) and used in a number of studies such as the magnetisation of Ni surfaces and interfaces with Cu (Tersoff and Falicov, 1982). The Green function may also be determined directly by the method of moments (Cyrot-Lackmann, 1969) and the recursion method (Haydock, 1980; Heine, 1980) without recourse to the wavefunction. However, none of these approaches are self consistent in a satisfactory way, as well as suffering from the usual problems of tight–binding studies of the choice of suitable matrix elements.

Inglesfield (1971,1978,1981) and García–Moliner and Rubio (1969) have developed a method by which the Green function for a composite system G_{A+B} is obtained from those of the isolated parts G_A and G_B *via* some matching conditions upon the plane separating A and B. Thus the Green function for a surface may be determined from that of the solid and the free space Green function. These ideas are independent of the basis set chosen, and Inglesfield and Benesh (1984; also Benesh and Inglesfield, 1984) have chosen to implement this method within the linearised augmented plane wave basis, enabling the full crystal potential to be incorporated, and where an energy–dependent, complex, non–local potential is added to the Hamiltonian for the surface region. This embedding correction takes the form of the bulk Green function evaluated on the surface separating the substrate from the surface region. Applications of this fully self-consistent method to Al(001) and Ni(001), where the embedding plane is taken to be one or two atomic layers from the vacuum, have illustated the benefits of correctly incorporating the surface boundary conditions.

Finally, two other defect calculations demonstrate the power of Greens function in studies of isolated defects. In studies of magnetic impurities (Podloucky, Zeller and Dederichs, 1980 and references therein) a KKR–based muffin–tin model has proven especially successful for studing 3d impurites in metal hosts, with the embedding Green function determined from the host atom scattering properties and structural Green function, which need only be determined once. This is important in terms of self–consistency, since for each subsequent iteration the defect Green function and charge density may be rapidly determined, and likewise when studying different impurities in the same host. Finally, Feibelman (1985) has presented a method for the study of isolated impurities adsorbed upon a substrate surface employing a localised basis coupling to the clean surface Green function.

The approach taken in this work is related to the multiple scattering theory of low energy electron diffraction (Pendry, 1974), a technique used for the determination of surface structure, where electron states within the solid are matched to an incident plane wave and the resultant scattered wavefield compared with experiment. The application of the technique in the area of electronic structure has previously been noted for determining band structures (Wood and Pendry, 1973) and studies of surface states (Gurman and Pendry, 1973). Green function multiple scattering formulations have been given by Noguerra, Spanjaard and Jepsen (1978) for the interstitial region at surfaces and Màca and Scheffler (1985) also for surfaces, but neither approach has included self–consistency nor been applied to the general interface problem. The formulation of Wachutka (1987) also has some similarities too with the layer theory presented here.

We consider in this Chapter the evaluation of the one–electron Green function for systems characterised by two–dimensional translational periodicity. Chapter 3 deals explicitly with the determination of the electronic structure from the Green function.

2.1 Notation

The following notation and conventions are observed in the remainder of this thesis. Atomic units are employed in which

$$\hbar^2 = m_e = e^2 = 1 \tag{2.1.1}$$

The units of energy are, unless stated, the Hartree (Ha) and of length the atomic unit (au) (Bohr radius)

$$1\text{Ha} = 27.2116\,\text{eV} \qquad 1\,\text{au} = 0.529177\text{Å} \tag{2.1.2}$$

The energy variable E is assumed to be complex and it is convenient to introduce $\kappa = \sqrt{2E}$.

Vectors are denoted in bold: $\mathbf{r} = (r, \theta, \phi) = (r, \Omega)$ with the volume element $d\mathbf{r} = r^2 dr \sin\theta d\theta d\phi$. Two dimensional vectors are further indicated with the parallel subscript , e.g. $\mathbf{k}_{||}$, where confusion may arise. Lattice vectors $\mathbf{R}_n$ may refer to a two or three dimensional lattice.

$Y_L(\mathbf{r}) = Y_L(\theta, \phi)$ is a complex spherical harmonic (Condon and Shortley phase — see Pendry, 1974) of order $L = (\ell, m)$ where ℓ is the principle and m the magnetic quantum number. The complex conjugate of the harmonic is denoted $Y_L^*(\mathbf{r})$ but should always be determined *via* $Y_L^*(\mathbf{r}) = (-1)^m Y_{\ell -m}(\mathbf{r})$. $j_\ell(z)$ ($n_\ell(z)$) is a spherical bessel (neumann) function and $h_\ell^{(1)}(z) = j_\ell(z) + i n_\ell(z)$ a spherical hankel function of the first kind. An undertilda denotes a matrix in the angular momentum representation which, for operator $\Lambda(\mathbf{r}, \mathbf{r}')$, is defined by

$$\Lambda_{LL'} = -2i\kappa \int Y_L^*(\mathbf{r}) j_\ell(\kappa r) \Lambda(\mathbf{r}, \mathbf{r}') j_{\ell'}(\kappa r') Y_{L'}(\mathbf{r}') d\mathbf{r} d\mathbf{r}' \tag{2.1.3}$$

The L label is also used to denote the partial wave basis which is (ℓ, m, n) with n a site label. The free space propagator $G_0(\mathbf{r}', \mathbf{r}; E)$, the solution of

$$(-\frac{1}{2}\nabla^2 - E) G_0(\mathbf{r}', \mathbf{r}; E) = -\delta(\mathbf{r}' - \mathbf{r}) \tag{2.1.4}$$

has the angular momentum expansion

$$G_0(\mathbf{r}', \mathbf{r}; E) = G_0(\mathbf{r}' - \mathbf{r}; E) = -2i\kappa \sum_L Y_L^*(\mathbf{r}') j_\ell(\kappa r_<) h_\ell^{(1)}(\kappa r_>) Y_L(\mathbf{r}) \tag{2.1.5}$$

where $r_< = \min(r, r')$, $r_> = \max(r, r')$ and the angular momentum representation of the translation operator $\underset{\sim}{G}(\mathbf{R})$ satisfies

$$h_\ell^{(1)}(\kappa(r - R))Y_L(\mathbf{r} - \mathbf{R}) = \sum_{L'} G_{LL'}(\mathbf{R}) j_{\ell'}(\kappa r) Y_{L'}(\mathbf{r})$$

$$G_{LL'}(\mathbf{R}) = 4\pi \sum_{L''} i^{\ell - \ell' - \ell''} h_{\ell''}(\kappa R) Y^*_{L''}(-\mathbf{R}) \int Y_L(\Omega) Y^*_{L'}(\Omega) Y_{L''}(\Omega) d\Omega \quad (2.1.6)$$

for $R > r$. Unit cell volumes are denoted by τ and the volume of the interstitial region outide the muffin–tin spheres is denoted by τ^{int}. The volume of the Brillouin zone is denoted by Ω_{bz} in three dimension and area Ω_{2bz} in two. The area of the two dimensional unit cell is represented by A.

2.2 Muffin–tin approximation

As in the original formulation of KKR theory this work adopts a simplification almost universally employed within multiple scattering theories, the muffin–tin (MT) approximation. In this approximation the crystal volume is partitioned into non-overlapping spheres, usually centred upon the atomic sites. In the case of elemental solids the radius of the sphere would normally be half the nearest neighbour distance, whilst for materials with many atom types, the choice of sphere radii is more arbritrary, and usually chosen to maximise the occupied volume or charge within them. Within the spheres the potential is replaced by its spherical average, and in the interstitial region by its volume average. Energies are defined with respect to this to constant, which is thus taken to be zero.

Scattering by a bounded potential region may be characterised by scattering phaseshifts, or a transition matrix, which for the general (non–relativistic) case may be determined from the solution of the $(\ell_{\max} + 1)^2$ coupled 2^{nd} order differential equations (Evans and Keller, 1971).

$$-\frac{1}{r^2}\frac{d}{dr}\left(r^2 \frac{d}{dr}\phi_L(r)\right) + \frac{\ell(\ell+1)}{r^2} - \kappa^2 \phi_L(r) + 2\frac{V_{00}(r)}{\sqrt{4\pi}}\phi_L(r) = -2 \sum_{L'L''} (1 - \delta_{L''00})\, C^L_{L'L''} V_{L''}(r) \phi_{L'}(r) \quad (2.2.1)$$

$$
\begin{aligned}
V(\mathbf{r}) &= \sum_{L} V_L(\mathbf{r}) Y_L(\mathbf{r}) \\
\Phi(\mathbf{r}) &= \sum_{L} \phi_L(\mathbf{r}) Y_L(\mathbf{r}) \\
C^{L}_{L'L''} &= \int Y^{*}_{L} Y_{L'} Y_{L''} d\Omega
\end{aligned}
\tag{2.2.2}
$$

Within the MT approximation the coupling term on the right of (2.2.1) is zero and the scattering properties may be determined from just $\ell_{max}+1$ uncoupled differential equations, a considerable simplification and correspondingly faster proposition than the full solution of (2.2.1). Despite the discontinuity in the potential within the MT approximation it may be shown that the wavefunctions and hence the charge density are continuous throughout all space (Treusch and Sandrock, 1966).

Constraints upon expansions of the free space translation operator (see equation 2.1.6 for example), lead to difficulties when attempting to generalise multiple scattering theories to full cell potentials, that is, those in which the potential takes its correct form throughout the unit cell. A number of studies (see Molenaar, 1988, and references therein) have attempted to address this point and formulate the solution to this problem, and there is some dispute as to whether or not such extensions retain the benefits of MT KKR theory, with a separation of potential and structure, or whether so called "near field corrections" exist when the bounding spheres of the full cell potential overlap. Recent work (Molenaar, 1988; Gonis, 1986, Gonis, Zhang and Nicholson, 1988) has swung the balance of opinion toward the absence of these corrections, and at the very least they have never been observed within the accuracy of current calculations. In the context of this work, the absence or negligible contribution from near-field corrections imply that the substitution for the atomic scattering operators t of non-diagonal cell t-matrices would effect a full potential solution to the interface Green function. The use of a non diagonal t-matrix but which only included any non–sphericity within the muffin–tin potential would not involve these uncertainties, but the largest error within the muffin–tin approximation arises from the poor treatment of the interstitial region (Williams and Morgan, 1974; Koelling, Freeman and Mueller, 1970).

The justification for the muffin–tin approximation lies with the accuracy of the results obtained with it. Fortunately the development of techniques incorporating the full crystal potential enable us to make this judgement without making recourse to experimental data, and we make make the comparison purely on the basis of the solution of the local density equations. It is clear from these comparisons that, as might be expected, the muffin–tin approximation is best for

materials where the crystal structure is close–packed and hence most isotropic. Thus for FCC, HCP and, to a slightly lesser degree, BCC the essential physics is captured with the muffin–tin approximation. For more open crystal structures such as the diamond structure the approximation is clearly inadequate. In the case of Si there is no band gap within the muffin–tin approximation, although for more heteropolar materials with a similarly open lattice structure such as ZnS and ZnTe the agreement of calculated band structures with those of full potential determinations is surprisingly good (Eckelt, 1967). However it is unlikely that total energy calculations employing the muffin–tin approximation would be sufficiently good for such materials since first order perturbation theory suggests shift of the order of $\langle\psi|\Delta V|\psi\rangle$ in the energy eigenvalues resulting from the interstitial region. A simple scheme for reducing the size of the interstitial region is to use "empty" spheres, not centred upon an atomic site, but since the overriding philisophy behind the LKKR method is the correct treatment of the boundary conditions for accuracy and reduced computation, this represents a largely unsatisfactory procedure. The calculation time scales rapidly with the number of empty spheres.

2.3 A single scattering centre

One of the useful features of multiple scattering theory is the ability to build the Green function for an arbitrary collection of atoms from the scattering properties of the isolated atoms. We start therefore by considering the Green function for an isolated muffin–tin potential. The atomic Green function $G_a(\mathbf{r}',\mathbf{r};E)$ satisfies the inhomogeneous Schrödinger equation for the muffin–tin potential $v(r)$

$$(-\frac{1}{2}\nabla^2 + v(r) - E)G_a(\mathbf{r}',\mathbf{r};E) = -\delta(\mathbf{r}'-\mathbf{r}) \tag{2.3.1}$$

which may also be cast in integral form

$$G_a(\mathbf{r}',\mathbf{r};E) = G_0(\mathbf{r}',\mathbf{r};E) + \int G_0(\mathbf{r}',\mathbf{r}_1;E)v(r_1)G_a(\mathbf{r}_1,\mathbf{r};E)d\mathbf{r}_1 \tag{2.3.2a}$$

$$= G_0(\mathbf{r}',\mathbf{r};E) + \int G_0(\mathbf{r}',\mathbf{r}_1;E)t(\mathbf{r}_1,\mathbf{r}_2)G_0(\mathbf{r}_2,\mathbf{r};E)d\mathbf{r}_1 d\mathbf{r}_2 \tag{2.3.2b}$$

$t(\mathbf{r},\mathbf{r}')$ is the t-matrix defined by

$$t(\mathbf{r},\mathbf{r}') = v(r)\delta(\mathbf{r}-\mathbf{r}') + v(r)\int G_0(\mathbf{r},\mathbf{r}_1;E)t(\mathbf{r}_1,\mathbf{r}')d\mathbf{r}_1 \tag{2.3.3}$$

and we note $t_{LL'} = t_\ell \delta_{LL'}$ is a consequence of the spherically symmetric potential.

Noting that from (2.3.3) $t(\mathbf{r},\mathbf{r}')$ is zero unless both arguments lie within the bounds of the potential, initially considering the domain $r > r' > R_{MT}$ in (2.3.2b) and then using continuity statements found by twice integrating the radial equation from (2.3.1), it is easily shown that the atomic Green function may be written

$$G_a(\mathbf{r}',\mathbf{r};E) = -4i\kappa \sum_L Y_L^*(\mathbf{r}')Z_\ell(r_<;E)S_\ell(r_>;E)Y_L(\mathbf{r}) \tag{2.3.4}$$

where Z_ℓ (S_ℓ) is the regular (irregular) radial wavefunction matching smoothly up to first derivative at the muffin–tin radius R_{MT} to the free space solution

$$\begin{aligned} Z_\ell(r;E) &= j_\ell(\kappa r) + t_\ell h_\ell^{(1)}(\kappa r) \\ S_\ell(r;E) &= h_\ell^{(1)}(\kappa r) \end{aligned} \tag{2.3.5}$$

A spin degeneracy factor of two is included in (2.3.4). It should also be noted that these equations apply to the non–relativistic Schrödinger equation. Relativistic corrections, important for the heavier elements, may be conveniently included by the method of Koelling and Harmon (1977) in which the Dirac equation is reduced by performing a j average over the radial equation (j is the total angular momentum). The spin–orbit interaction is thus omitted, but all other relativistic

kinematic effects are included, and shifts and band widths correctly modified. The inclusion of relativistic corrections, which were used for the calculations on iridium presented in Chapter 4, only has the effect of modifying the quantities t_ℓ above. These quantities are the (energy dependent) elements of the atomic t–matrix and are most conveniently found from the scattering phase shifts δ_ℓ:

$$t_\ell = i \sin \delta_\ell e^{i\delta_\ell} \tag{2.3.6}$$

These may be determined from the logarithmic derivative of the wavefunction $R_\ell(r)$ found by outward numerical integration of the radial Schrödinger equation for the muffin–tin potential.

$$e^{2i\delta_\ell} = \left. \frac{h_\ell^{(2)\prime}(\kappa r) - L_\ell(r) h_\ell^{(2)}(\kappa r)}{L_\ell(r) h_\ell^{(1)}(\kappa r) - h_\ell^{(1)\prime}(\kappa r)} \right|_{r=R_{MT}} \tag{2.3.7}$$

$$L_\ell(r) = \frac{R'_\ell(r)}{R_\ell(r)} \tag{2.3.8}$$

The prime denotes the derivative taken with respect to r. The definitions (2.3.5) differ slightly from those of other workers which usually include a phase resulting in real wavefunctions at real energies. As will be shown later it is both desirable and necessary that complex energies are employed within the layer formalism.

The t–matrix (2.3.6) characterises the scattering by the muffin–tin potential, and provides a natural truncation of the localised partial wave basis. Figure 2.1 illustrates the magnitude of the t-matrix at band energies for various metals determined from self-consistent bulk potentials. In each case it is evident that the magnitude drops rapidly beyond $\ell = 2$. For aluminium, typically considered a free–electron metal, the largest contribution arises in the s and p scattering channels, although $\ell = 2$ becomes increasingly important as the energy rises. In nickel we see the dominant contribution is due to the $\ell = 2$ electrons with a sharp resonance, typical of the transition metals, at about 0.275 Ha, and a significant contribution form the s scattering. Finally BCC niobium displays a much broader resonance in the d channel and has significant contributions from both s and p electrons. For all three metals it is sufficient (and necessary) to include s, p and d electrons in the computations to capture all the essential physics, that is, to be able to understand the origin of structural and electronic properties, although

Figure 2.1 Energy dependence of the atomic t-matrices for aluminium, nickel and niobium.

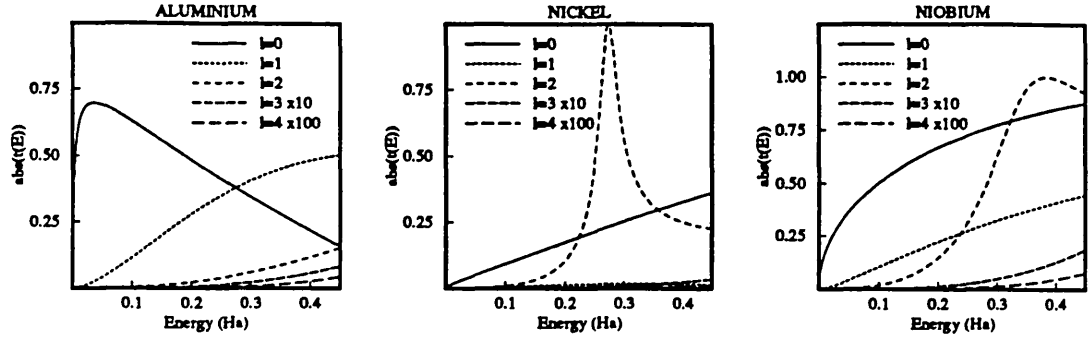

the wavefunctions and charge density require larger values of ℓ, maybe 4–7, to be continuous throughout the unit cell.

We now derive a general expression for the Green function of an arbritrary collection of muffin–tin scatterers, and which will be employed within the layer formalism. As in the atomic case the Green function is defined by the integral equation

$$G(\mathbf{r}',\mathbf{r};E) = G_0(\mathbf{r}',\mathbf{r};E) + \int G_0(\mathbf{r}',\mathbf{r}_1;E)v(\mathbf{r}_1)G(\mathbf{r}_1,\mathbf{r};E)d\mathbf{r}_1 \qquad (2.3.9)$$

but the potential now comprises a sum of non overlapping muffin–tin potentials $v(\mathbf{r}) = \sum_n v^n(|\mathbf{r}_n|)$ centred at the points $\mathbf{R}_n$. We define $\mathbf{r}_n = \mathbf{r} - \mathbf{R}_n$. We are interested primarily in so called "single site" properties such as the local density of states, as against non-site-diagonal properties which arise in alloy theory such as the successful Coherent Potential Approximation (CPA) (Faulkner and Stocks, 1980; Temmerman and Szotek, 1987), and we will restrict our attention to an expansion of $G(\mathbf{r}',\mathbf{r};E)$ where both $\mathbf{r}$,$\mathbf{r}'$ are centred upon some site α. We start by introducing the scattering path, operators which play a central role in the layer KKR theory and provide a convenient formalism for manipulating the multitude of scattering paths throughout the crystal. In much of the following we suppress the energy label for clarity.

2.4 The scattering path operator

The original idea to partition the scattering events *via* the scattering path operator can be traced to the work by Beeby (1968), although it was Györffy (Györffy and Stott, 1973; Györffy, 1972) who generalised the concept to the single site–operators used here, and we start by outlining the properties of these operators.

Adopting formal operator notation for clarity we may rewrite what may be taken as the defining equation for the atomic t-matrix (2.4.3) of site n as

$$t^n = v^n + v^n G_0 t^n = [1 - v^n G_0]^{-1} v^n \tag{2.4.1}$$

and by direct analogy the t-matrix for the multi-centred scattering cluster may be written

$$T = V + V G_0 T \qquad V = \sum_n v^n \tag{2.4.2}$$

It follows from (2.4.1) and (2.4.2) that we may express T as a sum over site operators τ^{nm} in the following manner:

$$T = \sum_n v^n + \sum_{npm} v^n G_0^{np} \tau^{pm} = \sum_{nm} [v^n \delta_{nm} + v^n \sum_p G_0^{np} \tau^{pm}] \equiv \sum_{nm} \tau^{nm} \tag{2.4.3}$$

G_0^{nm} denotes $G_0(\mathbf{r}_n, \mathbf{r}_m; E)$ and $G_0^{nn} = G_0$. The τ^{nm} operators introduced here are referred to as scattering path operators (SPO) and may be expressed completely in terms of the atomic t-matrices and the free particle propagator:

$$\begin{aligned}
\tau^{nm} &= v^n \delta_{nm} + v^n \sum_p G_0^{np} \tau^{pm} \\
&= v^n \delta_{nm} + v^n G_0^{nn} \tau^{nm} + v^n \sum_{p \neq n} G_0^{np} \tau^{pm} \\
&= [1 - v^n G_0^{nn}]^{-1} v^n \delta_{nm} + [1 - v^n G_0^{nn}]^{-1} v^n \sum_{p \neq n} G_0^{np} \tau^{pm} \\
&= t^n \delta_{nm} + t^n \sum_{p \neq n} G_0^{np} \tau^{pm}
\end{aligned} \tag{2.4.4a}$$

This equation has a simple interpretation within the scattering formalism. τ^{nm} is the operator which transforms a wave incident upon site n into an outgoing wave from site m, including all possible scattering paths in between. Equation (2.4.4a) is then simply a self-consistency requirement, that waves scattered from n to m are those scattered from p to m following scattering at n, plus a single scattering at n when n = m. Propagation between scattering events is given by G_0, the free particle propagator. An alternative form for (2.4.4a) which may be obtained by

repeated iteration and resummation and which is also useful in multiple scattering manipulations is

$$\tau^{nm} = t^n \delta_{nm} + \sum_{p \neq m} \tau^{np} G_0^{pm} t^m \tag{2.4.4b}$$

These two equations (2.4.4a,b) are commonly referred to as the equations of motion (EOM) of the SPO's.

In the presence of translational symmetry (in one, two or three dimensions) the site labels designating the positions of scatterers may be relabelled N_n with N labeling the unit cell and n the atom within it. This atom is then located at $\mathbf{R}_{N_n}$ with the unit cell origin at $\mathbf{R}_N$. It is clearly the case that the SPO $\tau^{N_n M_m}$ must depend only upon the relative difference of its unit cell labels N and M, since a displacement of both by some lattice vector results in an identical situation, and hence we may define a lattice Fourier transform and corresponding inverse transform

$$\tau^{N_n M_m} = \frac{1}{\Omega_{bz}} \int_{\Omega_{bz}} \tau^{nm}(\mathbf{K}) e^{i\mathbf{K}\cdot(\mathbf{R}_N - \mathbf{R}_M)} d\mathbf{K} \tag{2.4.5}$$

$$\tau^{nm}(\mathbf{K}) = \sum_{NM} \tau^{N_n M_m} e^{-i\mathbf{K}\cdot(\mathbf{R}_N - \mathbf{R}_M)} \tag{2.4.6}$$

where we use $\mathbf{K}$ as a generic variable to designate the appropriate reciprocal space variable for one (k), two ($\mathbf{k}_{||}$) or three ($\mathbf{K}$) dimensions. The EOM (2.4.4a) may then be Fourier transformed, yielding

$$\tau^{nm}(\mathbf{K}) = t^n \delta_{nm} + t^n \sum_p g^{np}(\mathbf{K}) \tau^{pm}(\mathbf{K}) \tag{2.4.7}$$

with $g^{nm}(\mathbf{K})$ the Bloch Green function given by

$$g^{nm}(\mathbf{K}) = \sum_M (1 - \delta_{0M}\delta_{nm}) G_0^{0_n M_m} e^{i\mathbf{K}\cdot\mathbf{R}_M} \tag{2.4.8}$$

We now consider the situation where the scattering sites may be partitioned into sub-spaces within which the scattering paths may themselves be summed. The situation we have in mind may be, for example, two layers whose scattering properties as isolated entities are known and which we wish to combine, thus forming a composite layer whose scattering properties we wish to know. We therefore relabel the sites i_J to indicate site i in subspace J, and assume N_I sites in subspace I. The EOM becomes

$$\tau^{i_I j_J} = t^{i_I} \delta_{ij} \delta_{IJ} + t^{i_I} \sum_{kK} (1 - \delta_{ik}\delta_{IK}) G_0^{i_I k_K} \tau^{k_K j_J} \tag{2.4.9}$$

where for each subspace

$$\tau_I^{ij} = \tau^{i_I j_I} = t^{i_I}\delta_{ij} + t^{i_I}\sum_k (1-\delta_{ik}) G_0^{i_I k_I} \tau^{k_I j_I} = \left(\left[(t_I)^{-1} - G_0^{II} \right]^{-1} \right)^{ij} \qquad (2.4.10)$$

with $(t_I)^i = t^{i_I}$ and

$$[G_0^{IJ}]^{ij} = (1-\delta_{ij}\delta_{IJ}) G_0^{i_I j_J} \qquad (2.4.11)$$

Then if τ^{IJ} is a sub-block of the full transition matrix of the composite system whose site dimensions are N_I by N_J we have

$$[\tau^{IJ}]^{ij} = (t_I)^i \delta_{ij}\delta_{IJ} + (t_I)^i \sum_k (1-\delta_{ik}) G_0^{i_I k_I} \tau^{k_I j_J} + (t_I)^i \sum_{\substack{k \\ K\neq I}} G_0^{i_I k_K} \tau^{k_K j_J}$$

$$\left(\left[1 - t_I G_0^{II} \right] \tau^{IJ} \right)^{ij} = (t_I)^i \delta_{ij}\delta_{IJ} + \left(t_I \sum_{K\neq I} G_0^{IK} \tau^{KJ} \right)^{ij} \qquad (2.4.12)$$

and hence we find that the subspace scattering path operators obey an identical equation of motion to the site SPO with the replacement of the site transition matrices with the isolated subspace SPO and the introduction of new propagators.

$$\tau^{IJ} = \tau_I \delta_{IJ} + \tau_I \sum_{K\neq I} G_0^{IK} \tau^{KJ} \qquad (2.4.13)$$

Finally we will find it useful in the course of this Chapter to also use the SPO's introduced by Beeby which we may write as

$$\tau_m = \sum_n \tau^{nm} \qquad (2.4.14)$$

and which may be viewed as an operator which sum all scattering paths **ending** with a scattering event at site m. One can simply show from (2.4.4a) that the EOM for this operator is

$$\tau_m = t^m + t^m \sum_{m\neq n} G_0^{mn} \tau_n \qquad (2.4.15)$$

In the presence of translational symmetry both (2.4.14) and (2.4.15) may be Fourier transformed along the lines of (2.4.5-8) to yield **K**–resolved EOM's.

2.5 Full Green function

We now use the SPO formalism of Section 2.4 to obtain an expression for the Green function of an arbritrary collection of scatterers. In particular, we wish to solve

$$G = G_0 + G_0 T G_0 \tag{2.5.1}$$

and find an expansion of G valid about the site α. Manipulating T in terms of the SPO and introducing

$$T^{\alpha\alpha} = \sum_{\substack{n\neq\alpha \\ m\neq\alpha}} \tau^{nm} \tag{2.5.2}$$

we obtain

$$\begin{aligned} T = \sum_{nm} \tau^{nm} &= \sum_{\substack{n\neq\alpha \\ m\neq\alpha}} \tau^{nm} + \sum_{n\neq\alpha} \tau^{n\alpha} + \sum_{m\neq\alpha} \tau^{\alpha m} + \tau^{\alpha\alpha} \\ &= T^{\alpha\alpha} + \sum_{\substack{n\neq\alpha \\ m\neq\alpha}} \tau^{nm} G_0^{m\alpha} t^{\alpha} + \sum_{\substack{n\neq\alpha \\ m\neq\alpha}} t^{\alpha} G_0^{\alpha n} \tau^{nm} + t^{\alpha} + t^{\alpha} \sum_{p\neq\alpha} G_0^{\alpha p} \tau^{p\alpha} \\ &= T^{\alpha\alpha} + T^{\alpha\alpha} G_0 t^{\alpha} + t^{\alpha} G_0 T^{\alpha\alpha} + t^{\alpha} + t^{\alpha} G_0 T^{\alpha\alpha} G_0 t^{\alpha} \\ &= t^{\alpha} + (1 + t^{\alpha} G_0) T^{\alpha\alpha} (1 + G_0 t^{\alpha}) \end{aligned} \tag{2.5.3}$$

Thus, combining (2.5.2) and (2.5.3) and identifying $G_0 + G_0 t^{\alpha} G_0$ as the atomic Greens function for the muffin-tin potential at site α we arrive at

$$G = G_{\alpha} + G_{\alpha} T^{\alpha\alpha} G_{\alpha} \tag{2.5.4}$$

A final expression convenient for calculating the Greens function can now be obtained using the the EOM's (2.5.4a,b) to express $T^{\alpha\alpha}$ in terms of the site diagonal elements of the SPO's.

$$\sum_{m\neq\alpha} \tau^{\alpha m} = t^{\alpha} \sum_{\substack{m\neq\alpha \\ p\neq\alpha}} G_0^{\alpha p} \tau^{pm} \qquad \tau^{\alpha\alpha} = t^{\alpha} + \sum_{p\neq\alpha} \tau^{\alpha p} G_0^{p\alpha} t^{\alpha} \tag{2.5.5}$$

and hence

$$G_0 T^{\alpha\alpha} G_0 = (t^{\alpha})^{-1} \sum_{m\neq\alpha} \tau^{\alpha m} G_0^{m\alpha} = (t^{\alpha})^{-1} [\tau^{\alpha\alpha} - t^{\alpha}] (t^{\alpha})^{-1} \tag{2.5.6}$$

We thus obtain the following expression for the Green function (including a spin degeneracy factor of 2)

$$\begin{aligned} G(\mathbf{r},\mathbf{r}';E) = &-4i\kappa \sum_{L} Y_L^*(\mathbf{r}) Z_{\ell}^{\alpha}(r) S_{\ell}^{\alpha}(r') Y_L(\mathbf{r}') \\ &-4i\kappa \sum_{LL'} Y_L^*(\mathbf{r}) Z_{\ell}^{\alpha}(r) \Gamma_{LL'}^{\alpha} Z_{\ell'}^{\alpha}(r') Y_{L'}(\mathbf{r}') \end{aligned} \tag{2.5.7}$$

with the matrix elements

$$\Gamma^{\alpha}_{LL'} = \left[(t^{\alpha}_{\ell})^{-1}\,\tau^{\alpha\alpha}_{LL'} - \delta_{LL'}\right](t^{\alpha}_{\ell'})^{-1} \tag{2.5.8}$$

This expression corresponds to equation 2.18 of Faulkner and Stocks (1980) with the differing definitions of wavefunctions and atomic t–matrix. The form of (2.5.7) makes it evident that Schrödingers equation is satisfied, whilst the presence of the atomic Green function evidently satisfies the additional requirements of the source term in the defining equation (2.3.1). The determination of the Green function is now reduced to evaluating $\underset{\sim}{\tau}^{\alpha\alpha}$, the site diagonal SPO.

2.6 Site diagonal elements of the scattering path operator

Manipulation of the EOM's (2.4.4a,b) yields an expression for the SPO in the form

$$\underset{\sim}{\tau}^{nm} = \left(\left[(\underset{\sim}{t})^{-1} - \underset{\sim}{G}\right]^{-1}\right)^{nm} \tag{2.6.1}$$

$$\underset{\sim}{\Gamma}^{\alpha} = ([1 - \underset{\sim}{G}\,\underset{\sim}{t}]\,\underset{\sim}{G})^{\alpha\alpha} \tag{2.6.2}$$

However, this matrix, which needs to be inverted, has the dimensions $N_S(\ell_{max}+1)^2$ by $N_S(\ell_{max}+1)^2$ which quickly becomes unmanageable for more than a few sites N_S, even after allowing for the use of symmetry to reduce its size. Hence this can only be used for small clusters of atoms (Durham, Pendry and Hodges, 1982), typically 10–20 depending upon the degree of symmetry present.

For bulk systems we can use instead the **K** resolved EOM (2.4.7) and (2.4.6) to obtain $\tau^{\alpha\alpha}$ since the site dimension is restriced to the number of atoms within the unit cell.

$$\underset{\sim}{\tau}^{nm}(\mathbf{K}) = \left(\left[(\underset{\sim}{t})^{-1} - \underset{\sim}{g}(\mathbf{K})\right]^{-1}\right)^{nm} \tag{2.6.3}$$

$$\underset{\sim}{\Gamma}^{\alpha} = \left[(\underset{\sim}{t}^{\alpha})^{-1}\,\frac{1}{\Omega_{bz}}\int_{\Omega_{bz}} \underset{\sim}{\tau}^{\alpha\alpha}(\mathbf{K})d\mathbf{K} - 1\right](\underset{\sim}{t}^{\alpha})^{-1} \tag{2.6.4}$$

This represents the complete solution in the presence of three dimensional periodicity.

The problem we have set out to solve is more demanding however. We have translational periodicity in two dimensions and so we may use the Fourier transformed EOM, but in the third dimension we have two semi-infinite half spaces and so the site dimension of the matrix to be inverted is still infinite. We will now obtain the solution to this problem by determining the site diagonal elements of the SPO for an embedded layer.

Figure 2.2 Schematic illustration of the assignment of atoms to planes, planes to layers and the left and right half spaces.

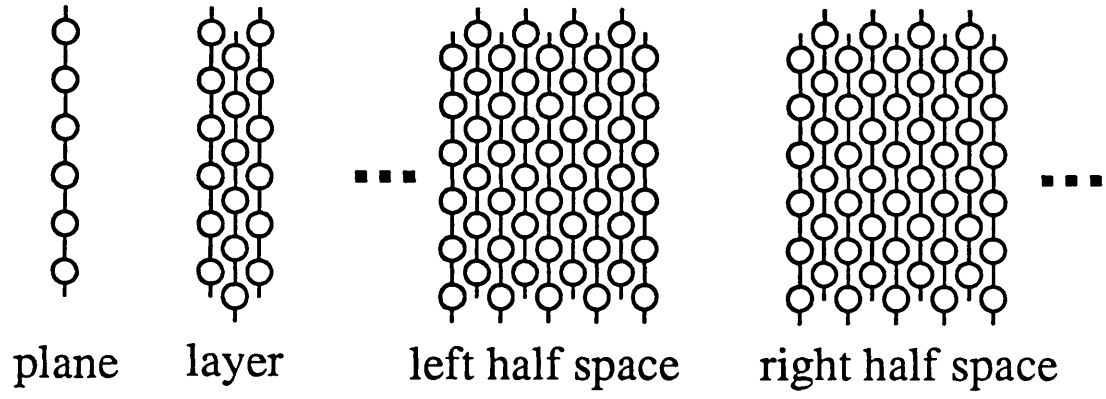

We consider the solid to be made up of parallel atomic planes, the plane passing through the centre of those atoms assigned to it. A layer, illustrated in figure 2.2, is a collection of one or more atomic planes which it is convenient to group together (and hence may include two or more symmetrically unique atoms). The scattering by a single layer may be determined from the Fourier transformed equation of motion (2.4.7) which may be solved immediately to give

$$\underset{\sim}{T}_I = \left[(\underset{\sim}{t})^{-1} - \underset{\sim}{g}(\mathbf{k}_{\|})\right]^{-1} \tag{2.6.5}$$

where the matrix elements of $\underset{\sim}{g}(\mathbf{k}_{\|})$ are given by (see equations (2.1.6) and (2.4.8))

$$\left[\underset{\sim}{g}(\mathbf{k}_{\|})\right]^{nm}_{LL'} = 4\pi \sum_{L''} \sum_{j} (1 - \delta_{j0}\delta_{nm})\, i^{\ell - \ell' - \ell''} h^1_{\ell''}(\kappa|\mathbf{R}_{0n} - \mathbf{R}_{jm}|) \times Y^*_{L''}(\mathbf{R}_{0n} - \mathbf{R}_{jm}) C^{L'}_{LL''} e^{i\mathbf{k}_{\|}\cdot\mathbf{R}_{j0}} \tag{2.6.6}$$

The summation over j is over unit cells within the layer. These matirx elements are closely related to the two dimensional analogs of the three dimensional structure constants of bulk KKR theory. As written this expression converges too slowly to be of practical use at band energies. More suitable expressions are given in Kambe (1967a,b;1968;1969) and Pendry (1974), where an Ewald split is used, partitioning the sum into two, one in real space and one in reciprocal space.

The embedded layer problem is such a layer sandwiched between two semi-infinite half spaces whose scattering properties as isolated objects may be determined (Figure 2.3). The matrices characterising these scattering properties are referred to as reflectivities, as they determine the reflected wave arising from the scattering of an initially incident wave. These half spaces themselves are assumed to be made up layers of atoms, and their scattering properties determined from the subspace equation of motion (2.4.13) where the individual layers acting as the subspaces. In the first instance we assume their scattering properties are known, and only after obtaining an expression for the scattering path operator we will proceed to determine them explicitly. Finally, from the SPO we may determine $\underset{\sim}{\Gamma}^{\alpha}$ *via*

$$\underset{\sim}{\Gamma}^{\alpha} = \left[(\underset{\sim}{t}^{\alpha})^{-1} \frac{1}{\Omega_{2bz}} \int_{\Omega_{2bz}} \underset{\sim}{\tau}^{\alpha\alpha}(\mathbf{k}_{||}) d\mathbf{k}_{||} - 1 \right] (\underset{\sim}{t}^{\alpha})^{-1} \tag{2.6.7}$$

For clarity we omit the $\mathbf{k}_{||}$ label from the operators in the subsequent Sections.

Figure 2.3 Illustration of the embedded layer problem.

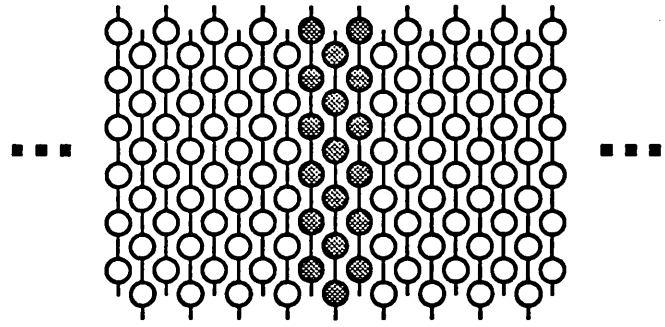

2.7 The embedded layer problem

To derive an expression for site diagonal elements of the SPO in the embedded layer problem we find it most convenient to introduce new scattering path operators, more in the spirit of those originally used by Beeby (2.4.14). We write the full transition matrix

$$T = \tau_L^{I-1} + \tau_I + \tau_R^{I+1} \tag{2.7.1}$$

where τ_I sums those paths which **end** with a scattering event within layer I and τ_L^{I-1} (τ_R^{I+1}) sums those which end with a scattering event within the left (right) half space, defined as layers $-\infty \ldots I-1$ ($I+1 \ldots \infty$). This is clearly equivalent to (2.4.3) as it accounts for all the scattering paths through the crystal. The SPO for the isolated layer I is denoted T_I and that of the individually isolated half spaces L^{I-1} and R^{I+1}. Subsequent Sections will detail the determination of the scattering matrices.

We may write out the EOM for the new SPO explicitly as

$$\tau_L^{I-1} = [1 + \tau_I g + \tau_R^{I+1} g] L^{I-1} \tag{2.7.2a}$$

$$\tau_I = [\tau_L^{I-1} g + 1 + \tau_R^{I+1} g] T_I \tag{2.7.2b}$$

$$\tau_R^{I+1} = [\tau_L^{I-1} g + \tau_I g + 1] R^{I+1} \tag{2.7.2c}$$

where we denote all propagators by g for clarity, their exact form dependent upon the SPO's between which they appear. Equation (2.7.2a) states that all paths which end with a scattering in the left half space comprise those which are wholly contained in it plus those which scatter there having scattered previously in layer I or the right half space.

These relations may be manipulated to give

$$\begin{aligned} \tau_L^{I-1}[1 - g T_I g L^{I-1}] &= [1 + \tau_R^{I+1} g][1 + T_I g] L^{I-1} \\ \tau_R^{I+1}[1 - g T_I g R^{I+1}] &= [1 + \tau_L^{I-1} g][1 + T_I g] R^{I+1} \end{aligned} \tag{2.7.3}$$

which, noting that SPO's for the isolated half spaces with and without layer I are related *via* the coupling equations to be derived in the following Section

$$\begin{aligned} L^I &= T_I + [1 + T_I g] L^{I-1} [1 - g T_I g L^{I-1}]^{-1} [1 + g T_I] \\ R^I &= T_I + [1 + T_I g] R^{I+1} [1 - g T_I g R^{I+1}]^{-1} [1 + g T_I] \end{aligned} \tag{2.7.4}$$

we can obtain the following expressions for the new half space SPO's.

$$\tau_L^{I-1} = [1 + T_I g]\left[1 + [1 - R^{I+1} g T_I g]^{-1} R^{I+1} g [1 + T_I g]\right] L^{I-1} [1 - g R^I g L^{I-1}]^{-1}$$
$$\tau_R^{I+1} = [1 + T_I g]\left[1 + [1 - L^{I-1} g T_I g]^{-1} L^{I-1} g [1 + T_I g]\right] R^{I+1} [1 - g L^I g R^{I+1}]^{-1}$$

(2.7.5)

Putting together the relations (2.7.1), (2.7.2b) and (2.7.5) we can thus write the full transition matrix for the system comprising a layer embedded between two semi infinite half spaces as

$$T = T_I + [1 + T_I g] R_{eff}^I [1 + g T_I] \tag{2.7.6}$$

where we define the effective "reflectivity" of the medium surrounding layer I as

$$R_{eff}^I = \left[1 + [1 - R^{I+1} g T_I g]^{-1} R^{I+1} g [1 + T_I g]\right] L^{I-1} [1 - g R^I g L^{I-1}]^{-1}$$
$$+ \left[1 + [1 - L^{I-1} g T_I g]^{-1} L^{I-1} g [1 + T_I g]\right] R^{I+1} [1 - g L^I g R^{I+1}]^{-1} \tag{2.7.7}$$

(Note this actually includes the scattering matrix of layer I, and so is not strictly speaking a reflection operator). The first term in (2.7.6) is the solution for an isolated layer (the solution for the usual slab problem), whilst the second term represents the correction for embedding in half spaces.

The final step is to identify those elements of the full transition matrix which correspond to the site diagonal elements of the SPO $\tau^{\alpha\alpha}$ appearing in the expression for the full Green function, and where α represents an atom within the embedded layer I. This SPO takes a wave incident upon site α and transforms it into a wave leaving site α, including all possible paths throughout the crystal. It thus starts and ends with a scattering event at atom α, and we can quickly identify this from (2.7.6) as the site diagonal block

$$\tau^{\alpha\alpha} = [T_I + T_I g R_{eff}^I g T_I]^{\alpha\alpha} \tag{2.7.8}$$

2.8 Half space reflectivities

We now consider the evaluation of the half space reflectivities and subsequent evaluation of the effective reflectivity R^I_{eff}. Starting with the scattering of a single layer, I, which treated in isolation may be obtained directly from the EOM

$$\underset{\sim}{T}_I(\mathbf{k}_{||}) = \left((\underset{\sim}{t})^{-1} - \underset{\sim}{g}(\mathbf{k}_{||}) \right)^{-1} \tag{2.8.1}$$

we can determine the scattering for the composite system of the two (different) layers I and $I-1$ *via* the relation (2.4.13). We may then view the resultant SPO as describing scattering by a single layer and again employ (2.4.13) to incorporate another layer $I-2$ into our composite system. Repeated application of this algorithm will serve to assemble a slab any number of layers thick and upon the assumption that more distant scattering paths are of diminishing importance to the electronic properties, we may expect this procedure to converge in the sense that the matrix elements of the reflection matrix are affected less and less by the addition of subsequent (more distant) layers.

There are some points of note with respect to this procedure. The first concerns the dimensions of the reflection matrix, which grow with the number of layers in a multicentre basis such as the angular momentum basis centred upon each atomic site. Clearly it is impractical to stack hundreds of layers with this sort of behaviour. We can get round this by adopting the techniques familiar from the standard theory of low energy electron diffraction (Pendry, 1974), transforming the localised angular momentum basis within each layer into a plane wave basis to treat scattering between the layers. Thus, the reflection matrix R^I_{eff} becomes an operator transforming an outgoing plane wave from layer I into one incident after including all possible scattering by the layers of the system. The number of origins is then independent of the number of layers within the stack. Defining the plane wave basis vectors as

$$e^{i\mathbf{K}^{\pm}_{\mathbf{g}}\cdot\mathbf{r}} \tag{2.8.2}$$

where

$$\begin{aligned} \mathbf{K}^{\pm}_{\mathbf{g}} &= \mathbf{k}_{||} + \mathbf{g} \pm \sqrt{\kappa^2 - |\,\mathbf{k}_{||} + \mathbf{g}\,|^2}\,\hat{\mathbf{z}} \qquad && \kappa^2 > |\,\mathbf{k}_{||} + \mathbf{g}\,|^2 \\ &= \mathbf{k}_{||} + \mathbf{g} \pm i\sqrt{|\,\mathbf{k}_{||} + \mathbf{g}\,|^2 - \kappa^2}\,\hat{\mathbf{z}} \qquad && \kappa^2 < |\,\mathbf{k}_{||} + \mathbf{g}\,|^2 \end{aligned} \tag{2.8.3}$$

and the $\pm$ refers to the direction of propagation, so that the forward travelling wave between layers I and I+1 may be written as

$$\Psi^+_I = \sum_{\mathbf{g}} a^{I+}_{\mathbf{g}} e^{i\mathbf{K}^+_{\mathbf{g}}\cdot(\mathbf{r}-\mathbf{c}_I)} \tag{2.8.4}$$

with c_I the origin of layer I, we can define for each layer four scattering operators illustrated schematically in figure 2.4

$$\begin{aligned} [T_I^{-+}]_{gg'} &= \left[\Gamma_{gL}^{-}\underset{\sim}{T}_I\Gamma_{Lg}^{+}\right]_{gg'} & [T_I^{++}]_{gg'} &= \left[1+\Gamma_{gL}^{+}\underset{\sim}{T}_I\Gamma_{Lg}^{+}\right]_{gg'} \\ [T_I^{+-}]_{gg'} &= \left[\Gamma_{gL}^{+}\underset{\sim}{T}_I\Gamma_{Lg}^{-}\right]_{gg'} & [T_I^{--}]_{gg'} &= \left[1+\Gamma_{gL}^{-}\underset{\sim}{T}_I\Gamma_{Lg}^{-}\right]_{gg'} \end{aligned} \qquad (2.8.5)$$

Figure 2.4 Pictorial representation of the layer transmission and reflection matrices of equation (2.8.5), and those resulting from the composite scattering system of layer 1 + 2. In all cases the origins of the expansions of the incident and scattered plane wave are indicated by the dark circle.

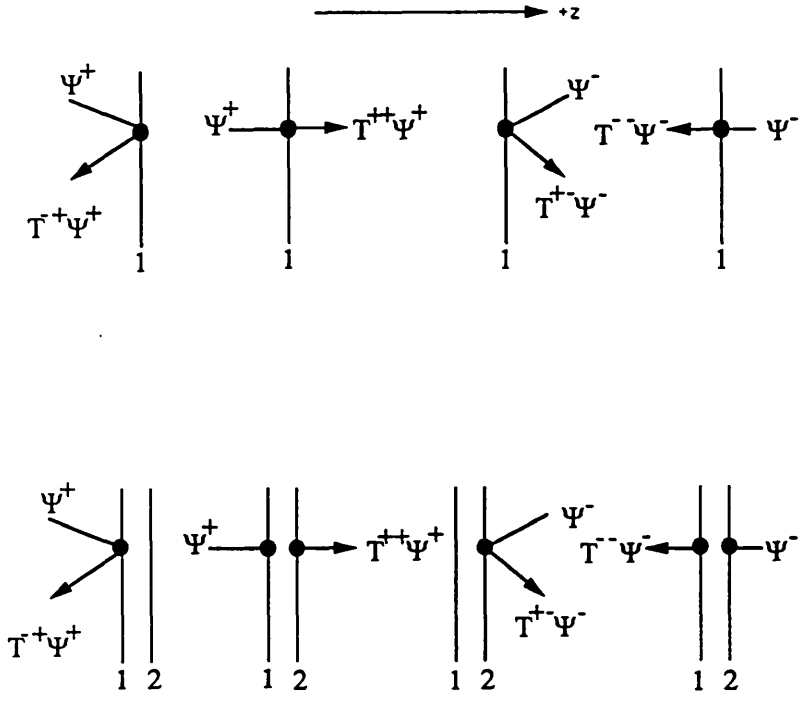

where $\Gamma^{\pm}_{gL}$ converts from the plane wave to the partial wave basis, and $\Gamma^{\pm}_{Lg}$ converts from the partial wave to plane wave basis:

$$\begin{aligned}\left[\Gamma^{\pm}\right]_{gLn} &= 4\pi i^{\ell} e^{i\mathbf{K}^{\pm}_{g}\cdot\mathbf{R}_{0n}} Y^{*}_{L}(\mathbf{K}^{\pm}_{g}) \\ \left[\Gamma^{\pm}\right]_{Lng} &= \frac{2\pi i^{-\ell}}{\kappa A(\mathbf{K}^{+}_{g})_{z}} e^{-i\mathbf{K}^{\pm}_{g}\cdot\mathbf{R}_{0n}} Y_{L}(\mathbf{K}^{\pm}_{g})\end{aligned} \tag{2.8.6}$$

$\mathbf{R}_{0n}$ corresponds to the displacement of site n in the origin at the unit cell. In terms of these matrices the layer coupling relation becomes the following four equations for the resultant scattering matrices of the composite layer $1+2$:

$$\begin{aligned}T^{++}_{1.2} &= T^{++}_{1}\left[1 - P^{+}_{1}T^{+-}_{2}P^{-}_{1}T^{-+}_{1}\right]^{-1}P^{+}_{1}T^{++}_{2} \\ T^{--}_{1.2} &= T^{--}_{1}\left[1 - P^{-}_{1}T^{-+}_{1}P^{+}_{1}T^{+-}_{2}\right]^{-1}P^{-}_{1}T^{--}_{2} \\ T^{+-}_{1.2} &= T^{+-}_{1} + T^{++}_{1}P^{+}_{1}T^{+-}_{2}\left[1 - P^{-}_{1}T^{-+}_{1}P^{+}_{1}T^{+-}_{2}\right]^{-1}P^{-}_{1}T^{--}_{1} \\ T^{-+}_{1.2} &= T^{-+}_{2} + T^{--}_{2}P^{-}_{1}T^{-+}_{1}\left[1 - P^{+}_{1}T^{+-}_{2}P^{-}_{1}T^{-+}_{1}\right]^{-1}P^{+}_{1}T^{++}_{2}\end{aligned} \tag{2.8.7}$$

where the propagators $P^{\pm}_{I}$ are the plane wave matrix elements of the Bloch Green function transfering between the origins $\mathbf{c}_I$ and $\mathbf{c}_{I+1}$ of the plane wave basis between layers I and $I+1$.

$$\left[P^{\pm}_{I}\right]_{gg'} = \delta_{gg'}e^{i\mathbf{K}^{\pm}_{g}\cdot(\mathbf{c}_{I+1}-\mathbf{c}_{I})} \tag{2.8.8}$$

Rather importantly, this propagator is diagonal. The reflection matrix T^{+-} transforms an incident plane wave travelling in the $+$ direction into an outgoing plane wave travelling in the $-$ direction, and thus has a **single** origin on the left most layer. Similarly T^{-+} has a single origin on the right–most layer and reflects an incident plane wave travelling in the $-$ direction into an outgoing plane wave traveling in the $+$ direction. The transmission matrices T^{++} and T^{--} have two origins on the outer layers.

At first sight it might appear that one could implement the above procedure, that is, employing a single origin for all incident waves and all outgoing waves, entirely within the angular momentum basis. Consequently, the site dimensions would not increase when the layer coupling algorithm is performed, as at most only a shift in the origin occurs to the last layer added. However, by iterative analysis, we can see that repeated application of the layer coupling equations (2.8.7) introduces the product of propagators which, in the case of the angular momentum basis, are not diagonal (see 2.1.6) and hence troublesome internal summations must be performed. Thus the dimension of the partial wave basis is no longer

determined by the scattering properties of the atoms but more by the geometrical structure, since the convergence of the internal summation is dependent upon the arguments, which are the vectors connecting origins. Although the site dimensions do not increase as the iterative layer coupling is performed, the actual angular momentum variable must range over larger values, and consequently the matrices become impractically large. Such a formulation would be very difficult to implement, and the convergence problems associated with the angular momentum basis in a single site representation have been noted in other multiple scattering problems. Geometrical propagators requiring up to $\ell = 14$ are needed at band energies within cluster codes (Durham, Pendry and Hodges, 1982) and chain scattering codes (Pinkava, 1989). In the case of the plane wave basis the propagator is diagonal and consequently no internal summations need be performed.

Having therefore developed a practical scheme for coupling the scattering properties of the layers, the reflectivity may be determined by repeated application of (2.8.7), the calculation being accelerated by the layer doubling algorithm. First the repeat unit of layers in the half space is assembled by individually coupling the layers *via* (2.8.7), and then this matrix is coupled to itself, or "doubled", a number of times, each time both $T_1^{\pm\pm}$ and $T_2^{\pm\pm}$ in (2.8.7) being set to the matrix $T_{1,2}^{\pm\pm}$ from the previous "double". Hence n applications of the procedure stacks 2^n layers rather than n by direct application to the individual layers. This procedure is essential for the practical implementation of the method and imposes the restriction upon the geometry of the systems which may be studied by the layer KKR technique that they possess semi-infinite periodicity, i.e. some repeat unit within each half space which enables the layer doubling algorithm to be applied. Of course once the reflectivity of this semi-infinite stack has been determined additional layers may then be coupled *via* (2.8.7) so that in the vicinity of the atom of interest one is free to incorporate any structure desired (with two dimensional periodicity). Again this is essential if we are to allow the relaxation of the potentials self–consistently in the vicinity of some internal interface, for example. Finally, we note that the layer doubling procedure does not necessarily converge at real energies since a contribution may arise from the last layer added when the scattering path involves propagation to the last layer *via* a Bloch state, a scattering event and propagation back *via* another Bloch state. Hence it is necessary to add a small but finite imaginary contribution to the energy. In the following Chapter use will be made of this non–convergent behaviour of the layer doubling procedure to determine the 2-dimensional band structure, and the properties of the Green function in the complex plane utilised in order to improve the efficiency of the calculations.

Returning to the reflectivity, if $T^{\pm\pm}_{I,J}$ represents the scattering matrix for the stack of layers I to J, then the reflectivities of the left and right half spaces in (2.7.7) are given by

$$L^I = T^{-+}_{-\infty,I} \qquad R^I = T^{+-}_{I,\infty} \tag{2.8.9}$$

and from (2.8.7) we see that

$$\begin{aligned} L^I =& T_I^{-+} + T_I^{--} P_{I-1}^{-} L^{I-1} \left[1 - P_{I-1}^{+} T_I^{+-} P_{I-1}^{-} L^{I-1}\right]^{-1} P_{I-1}^{+} T_I^{++} \\ R^I =& T_I^{+-} + T_I^{++} P_I^{+} R^{I+1} \left[1 - P_I^{-} T_I^{-+} P_I^{+} R^{I+1}\right]^{-1} P_I^{-} T_I^{--} \end{aligned} \tag{2.8.10}$$

which are the plane wave analogs of the formal expressions (2.7.4) presented in the previous Section. The effective reflectivity matrix (2.7.7) is given by the following expression whose origin is within the layer I

$$\begin{aligned} &\left[R^I_{\text{eff}}\right]^{\alpha\beta}_{LL'} = \\ &\Bigg[\left[\Gamma^{-}_{Lg} + \Gamma^{+}_{Lg} P^{+}_I \left[1 - R^{I+1} P^{-}_I T^{-+}_I P^{+}_I\right]^{-1} R^{I+1} P^{-}_I T^{--}_I\right] \times \\ &P^{-}_{I-1} L^{I-1} \left[1 - P^{+}_{I-1} R^I P^{-}_{I-1} L^{I-1}\right]^{-1} P^{+}_{I-1} \Gamma^{+}_{gL} + \\ &\left[\Gamma^{+}_{Lg} + \Gamma^{-}_{Lg} P^{-}_{I-1} \left[1 - L^{I-1} P^{+}_{I-1} T^{+-}_I P^{-}_{I-1}\right]^{-1} L^{I-1} P^{+}_{I-1} T^{++}_I\right] \times \\ &P^{+}_I R^{I+1} \left[1 - P^{-}_I L^I P^{+}_I R^{I+1}\right]^{-1} P^{-}_I \Gamma^{-}_{gL} \Bigg]^{\alpha\beta}_{LL'} \end{aligned} \tag{2.8.11}$$

so that

$$\underset{\sim}{\tau}^{\alpha\alpha} = \underset{\sim}{T}_I \left[1 + \underset{\sim}{R}^I_{\text{eff}} \underset{\sim}{T}_I\right]^{\alpha\alpha} \tag{2.8.12}$$

which completes the derivation of a practical expression for the Green function for the layer embedded in semi–infinite half–spaces (MacLaren, Crampin, Vvedensky and Pendry, 1989). The following Section details a difficulty with the use of this expression which calls for the use of more sophisticated algorithm for the determination of the half space reflectivities and embedded layer problem in the case of closely spaced atomic planes, such as high–Miller–index planes.

2.9 Close spaced layers

The plane wave basis used within the interstitial region (constant potential) to couple layers together generally consists of 10–30 beams. As g increases in magnitude the z component of the momentum of the basis vector, given by

$$\mathbf{K}_{\mathbf{g}}^{\pm} \cdot \hat{\mathbf{z}} = \pm i\sqrt{|\,\mathbf{k}_{||} + \mathbf{g}\,|^2 - \kappa^2} \qquad \kappa^2 < |\,\mathbf{k}_{||} + \mathbf{g}\,|^2 \tag{2.9.1}$$

has an increasing imaginary component which results in the amplitude of the basis vector on the adjacent layer becoming less significant, approaching $\exp(-c_z g)$ for large $|g|$ where c_z is the z displacement between adjacent layers.

When dealing with closely–spaced layers, however, two factors conspire to make the size of the plane wave basis set impractically large. Firstly the z spacing between adjacent planes is significantly reduced, so the exponential decay of the basis vectors is not so effective. Secondly, for high–Miller–index directions in crystals, the reduced spacing between atomic planes is accompanied by an increase in the size of the unit cell within the planes (consider, for example, that in elemental crystals the volume per atom is constant for all directions), and consequently the magnitude of the reciprocal space basis vectors is reduced. Thus the magnitude of the n^{th} reciprocal lattice vector (when arranged in order of their sizes) is smaller the closer the atomic planes, again conspiring to make the decay to the next atomic plane less effective.

We can see this very clearly by contrasting the (111) and (210) direction in the FCC crystal structure. For this structure the (111) direction has the most widely spaced planes and consequently the layer unit cell has the smallest area. The layer unit cell basis vectors may be taken to be $a/\sqrt{2}(1,0)$, $a/\sqrt{2}(1/2,\sqrt{3}/2)$ where a is the length of the cubic face, and the z separation of adjacent layers is $a/\sqrt{3}$. For the (210) direction which corresponds to the $\Sigma 5$ grain boundary which will be described later, the basis vectors are $a/2(\sqrt{5},1)$, $a/2(\sqrt{5},-1)$ with a z separation of $a/(2\sqrt{5})$. In table 2.1 the quantity $\exp(-c_z g_{max})$ is given for various basis set sizes. It is evident that while a basis set of 13 or 19 vectors may be sufficient in the case of the the (111) direction (as numerical evidence will illustrate in the following Chapter) this increases to near 100 for the (210) direction, and is even worse for (310) and other high miller index directions if a comparable degree of convergence is demanded. In fact, while the quantity $\exp(-g_{max} c_z)$ provides some measure of the basis set necessary, for a direction such as the (210) even more vectors, of the order of 500, are actually needed to converge the scattering, due to the increasing number of vectors contributing (the number of vectors of length |g|

Table 2.1

Comparison of the basis vector attenuation at the adjacent layer for the FCC (111) and FCC (210) directions for selected numbers of vectors, N_g.

	FCC (111)			FCC (210)	
N_g	$g_{max}/(2\pi/a)$	$\exp(-g_{max}c_z)$	N_g	$g_{max}/(2\pi/a)$	$\exp(-g_{max}c_z)$
1	0	$1.00 \times 10^{+0}$	1	0	$1.00 \times 10^{+0}$
7	$\sqrt{8}/\sqrt{3}$	2.67×10^{-3}	3	$2/\sqrt{5}$	2.84×10^{-1}
13	$\sqrt{8}$	3.50×10^{-5}	7	$\sqrt{6}/\sqrt{5}$	2.15×10^{-1}
19	$2\sqrt{8}/\sqrt{3}$	7.16×10^{-6}	11	$\sqrt{14}/\sqrt{5}$	9.53×10^{-2}
31	$2\sqrt{14}/\sqrt{3}$	1.56×10^{-7}	15	2	6.02×10^{-2}
37	$2\sqrt{6}$	1.91×10^{-8}	27	$6/\sqrt{5}$	2.31×10^{-2}
43	$4\sqrt{2}$	1.22×10^{-9}	57	$\sqrt{134}/\sqrt{5}$	6.94×10^{-4}
55	$2\sqrt{26}$	0.53×10^{-9}	103	$6\sqrt{14}/\sqrt{5}$	7.48×10^{-7}

scales as g). More numerical evidence for this behaviour will be presented in the next Chapter.

The layer doubling equations (2.8.6) involve matrix inversions and so the calculation time to determine the reflectivities and hence $\Gamma^{\alpha}_{LL'}$ (2.5.8) scales approximately with the cube of the number of plane wave basis vectors. An alternative approach which can reduce the size of this basis set can therefore extend the calculations which may be performed. Indeed it is in no way practical to look at structures such as grain boundaries with the conventional technique. One might naïvely assume that by assigning more planes to each layer, one can increase the distance between scattering events performed within the plane wave basis. Thus at the cost of a larger partial wave basis one can reduce the dimensions of the plane wave basis set. In figure 2.5 for example we have a situation in which all planes are identical. The simplest partitioning is to assign one plane to each layer, so that the distance between adjacent plane wave origins in the z direction is $\hat{\mathbf{z}} \cdot \mathbf{R}_{AB}$. In

the event that this results in a plane wave basis too large to be practical, we could instead assign two planes to each layer, doubling the z distance between plane wave origins to $\hat{\mathbf{z}}\cdot\mathbf{R}_{AC}$, and hence the basis set vectors will decay further. However, this is not the case, because we must consider the actual propagation of the **partial** wave from B to C. This is given by the product $\Gamma^{+}_{Lg}P^{+}\Gamma^{+}_{gL}$ and the exponential factors in the Γ's exactly cancel the benefits of this increased separation.

$$\begin{aligned}\Gamma^{+}_{Lg}P^{+}\Gamma^{+}_{gL} &\sim e^{-i\mathbf{K}^{+}_{g}\cdot\mathbf{R}_{BA}}e^{i\mathbf{K}^{+}_{g}\cdot(\mathbf{c}_{I+1}-\mathbf{c}_{I})} \\ &\sim e^{i\mathbf{K}^{+}_{g}\cdot\mathbf{R}_{CB}}\end{aligned} \tag{2.9.2}$$

where $\mathbf{R}_{BA}$ is the vector to site B from A, and $(\mathbf{c}_{I+1}-\mathbf{c}_{I})=\mathbf{R}_{CA}$. There is no benefit in assigning two planes to one layer in the form of a decrease in the required size of the plane wave basis; in fact, a consequence is the increased partial wave basis which significantly increases the time for the evaluation of the intralayer scattering matrix $\underset{\sim}{T}$.

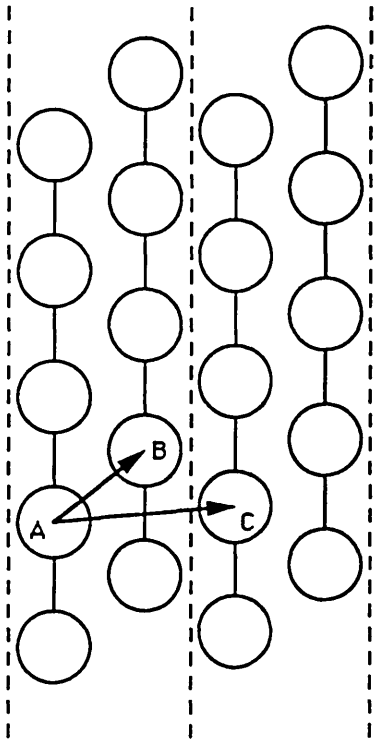

Figure 2.5 The structure discussed in the text which does not benefit from the partitioning of more planes to each layer.

In some cases the assignment of more planes to a layer is beneficial, when not all layer spacings are small. In this case those planes which are closely spaced may be assigned to a single layer and the shortest scattering performed within the plane wave basis will be across a layer spacing which is reasonably large. Hence in the situation illustrated in figure 2.6, assigning two planes to one layer is beneficial due to the increased plane wave scattering path. However, when all spacings are close such as the (210) direction of an fcc crystal, the non-coplanar layers or combined space methods (Van Hove and Tong, 1979) are not sufficient.

Figure 2.6 The structure discussed in the text which does benefit from the partitioning of additional planes to each layer, due to the varying inter–layer separation. a). Each layer consisting of a single plane, and the shortest scattering path treated in the plane wave basis b). Two planes assigned to each layer, and the resulting shortest scattering path to be treated in the plane wave basis.

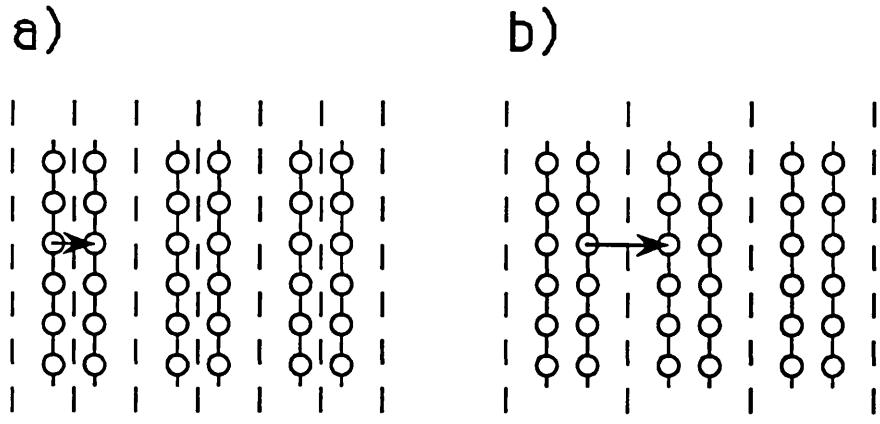

The solution to this problem presented below (MacLaren, Crampin and Vvedensky, 1989) is very simple in philosophy, although it will be evident that in practice the solution is somewhat complex. The plane wave basis is significantly reduced so that, for example, only 5 vectors are typically needed for the BCC (100) direction (previously about 30) and 15 for FCC (210) (previously about 500), and consequently an overall increase in efficiency in achieved. The fundamental idea is to treat scattering between adjacent layers within the localised partial wave basis and between more distant scatterers in the single site plane wave basis. This avoids any problems with uncontrolled internal summations within the angular

momentum basis since scattering paths across layers are assembled with a diagonal propagator.

As in the presentation of the conventional approach we first consider the embedded layer problem and then determine the reflectivities.

2.10 The embedded layer problem for close spaced layers

We first derive an expression for the site diagonal elements of the $\mathbf{k}_{||}$ resolved SPO about some atom embedded between semi–infinite half spaces. Once again we assume that we know the reflectivities characterising these half spaces, and leave the details of their calculation to subsequent Sections. However, we assume for convenience that the origin of the reflection matrix R^{I+1} which describes the reflectivity of the stack of layers $I+1, I+2, \ldots\ldots, \infty$ is upon layer I, as is that of the reflection matrix L^{I-1} of the stack of layers $-\infty, \ldots\ldots, I-2, I-1$ (figure 2.7). This results in a considerable simplification of notation.

Figure 2.7 a). The embedded layer problem for the close–spaced layer case. b). The location of the origins of the half spaces (indicated by black circles) for the close–spaced layer case.

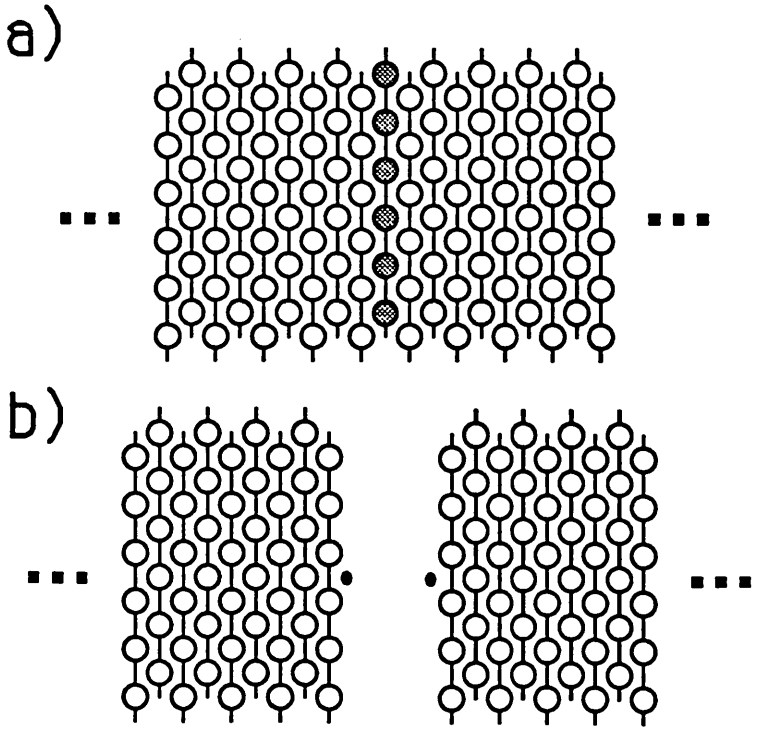

Previously the reflection matrices acted upon plane wave states, for example a wave leaving layer I $\sum_{\mathbf{g}} a_{\mathbf{g}} e^{i\mathbf{K}_{\mathbf{g}}^{+}\cdot(\mathbf{r}-\mathbf{c}_I)}$ was reflected into an incoming wave $\sum_{\mathbf{g}} b_{\mathbf{g}} e^{i\mathbf{K}_{\mathbf{g}}^{-}\cdot(\mathbf{r}-\mathbf{c}_I)}$ by the right half space, where $b_{\mathbf{g}} = \sum_{\mathbf{g}'} a_{\mathbf{g}'} P^{+}_{I\mathbf{g}} [R^{I+1}]_{\mathbf{g}\mathbf{g}'} P^{-}_{I\mathbf{g}'}$. We now include the additional possibility that the reflection matrix may convert an outgoing plane wave into a incoming partial wave, and *vice versa*. Consequently, we introduce the notation, that the operator $\Lambda_{L\mathbf{g}}$ acts to the left on a partial wave basis and to the right on a plane wave basis, and it should be noted that the subscripts L and g refer not to specific matrix elements but to the actual form of the operator. There are now four reflection matrices, illustrated schematically in figure 2.8.

Figure 2.8 Schematic representation of the four right half space reflection matrices in the close-spaced layer problem. The black circles indicate the position of the origins, solid arrows incident waves and dashed arrows reflected waves. The plane wave basis is used for scattering paths more distant than one layer, so is positioned to the left of the origin, whilst the spherical wave basis is used for scattering between adjacent layers, and so is positioned between the half space and the origin.

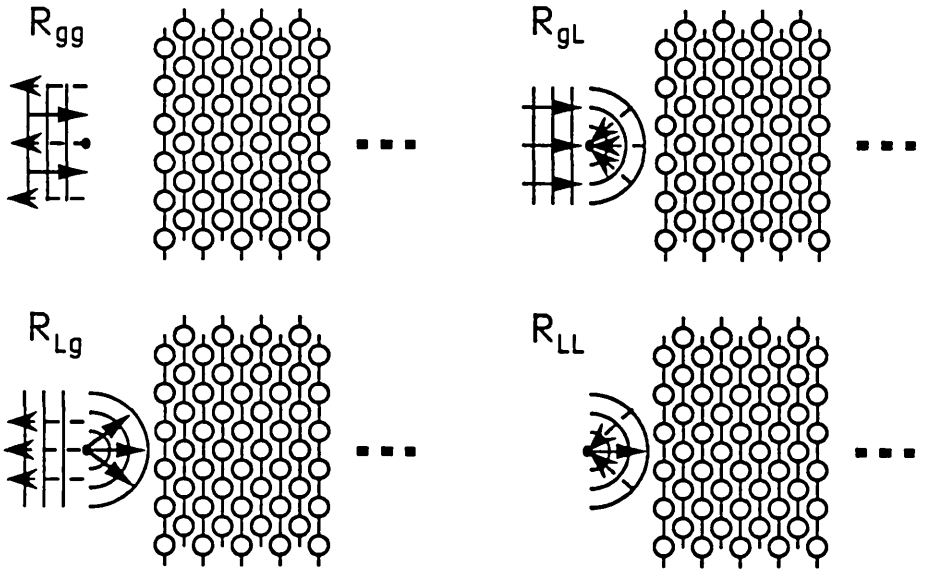

Using this new notation, we may solve the EOM for the three SPO's as in Section (2.7) *via* the formal expressions

$$\tau_L^{I-1} = \left[1 + \tau_I + \tau_R^{I+1}\right] L^{I-1} \tag{2.10.1a}$$

$$\tau_I = \left[\tau_L^{I-1} + 1 + \tau_R^{I+1}\right] T_I \tag{2.10.1b}$$

$$\tau_R^{I+1} = \left[\tau_L^{I-1} + \tau_I + 1\right] R^{I+1} \tag{2.10.1c}$$

Rather than following the previous procedure for the solution of these coupled EOM, an alternative route turns out to more transparent, and computationally more convenient. This is due to the need to explicitly separate scattering paths between adjacent and more distant scatterers so that they may be treated within the correct basis set. Manipulating (2.10.1a,c) we obtain

$$\begin{aligned}
\tau_L^{I-1} &= \left[1 + \tau_I + \left[\tau_L^{I-1} + \tau_I + 1\right] R^{I+1}\right] L^{I-1} \\
&= \left[1 + \tau_I\right]\left[1 + R^{I+1}\right] L^{I-1}\left[1 - R^{I+1}L^{I-1}\right]^{-1} \\
\tau_R^{I+1} &= \left[1 + \tau_I\right]\left[1 + L^{I-1}\right] R^{I+1}\left[1 - L^{I-1}R^{I+1}\right]^{-1}
\end{aligned} \tag{2.10.2}$$

which may be used with (2.10.1b) to obtain for τ_I

$$\begin{aligned}
\tau_I &= \Big[1 + \left[1 + \tau_I\right]\left[1 + R^{I+1}\right] L^{I-1}\left[1 - R^{I+1}L^{I-1}\right]^{-1} + \\
&\qquad \left[1 + \tau_I\right]\left[1 + L^{I-1}\right] R^{I+1}\left[1 - L^{I-1}R^{I+1}\right]^{-1}\Big] T_I \\
&= \left[1 + \left[1 + \tau_I\right] X\right] T_I \\
&= \left[1 + X\right] T_I \left[1 - XT_I\right]^{-1}
\end{aligned} \tag{2.10.3}$$

where we introduce X, which sums scattering by the composite system in the *absence* of layer I

$$\begin{aligned}
X = R^{I+1} + L^{I-1} + L^{I-1}\left[1 + R^{I+1}L^{I-1}\right]\left[R^{I+1} + R^{I+1}L^{I-1}\right] + \\
R^{I+1}\left[1 + L^{I-1}R^{I+1}\right]\left[L^{I-1} + L^{I-1}R^{I+1}\right]
\end{aligned} \tag{2.10.4}$$

Remembering that $\tau_I^{\alpha\alpha}$ sums scattering paths both beginning and ending with a scattering event at site α in layer I and noting that no paths in X have an initial

scattering within layer I, we obtain the diagonal element of the scattering path operator as

$$\tau_I^{\alpha\alpha} = \left[T_I \left[1 - X T_I \right]^{-1} \right]^{\alpha\alpha} \tag{2.10.5}$$

We now take matrix elements with the philosophy that no scattering between adjacent scattering planes may be permitted within the plane wave basis set and obtain the following expression

$$\begin{aligned} \underset{\sim}{\tau}_I^{\alpha\alpha} = \Bigg(\underset{\sim}{T}_I \Big[1 - \left[R_{LL}^{I+1} + L_{LL}^{I-1} \right] \underset{\sim}{T}_I \\ - L_{Lg}^{I-1} \left[1 - R_{gg}^{I+1} L_{gg}^{I-1} \right]^{-1} \left[R_{gL}^{I+1} + R_{gg}^{I+1} L_{gL}^{I-1} \right] \underset{\sim}{T}_I \\ - R_{Lg}^{I+1} \left[1 - L_{gg}^{I-1} R_{gg}^{I+1} \right]^{-1} \left[L_{gL}^{I-1} + L_{gg}^{I-1} R_{gL}^{I+1} \right] \underset{\sim}{T}_I \Big]^{-1} \Bigg)^{\alpha\alpha} \end{aligned} \tag{2.10.6}$$

The initial scattering event occurs within the layer, and $\underset{\sim}{T}_I$ sums all possible scattering paths within the layer before emerging from the layer as a partial wave. Now consider the term within the outer square brackets. The outgoing partial wave will next scatter within one of the two half–spaces. The first term $\left[R_{LL}^{I+1} + L_{LL}^{I-1} \right] \underset{\sim}{T}_I$ sums paths in which this wave scatters within each half–space and returns immediately to layer I. This scattering is performed in the partial wave basis as it occurs between adjacent scatterers. The next term, $L_{Lg}^{I-1} \ldots\ldots \underset{\sim}{T}_I$ sums paths which first scatter within the left half–space, and then undergoes multiple scattering between the right and left half–spaces. The initial scattering in performed in the partial wave basis, as layer I is adjacent to the left half–space, but the waves leaving the left half–space emerge in the plane wave basis, as they will next scatter within the right half–space which is more distant. The multiple scattering between these two is likewise performed in the plane wave basis. Following the half–space multiple scattering the waves are re-incident upon layer I, and the terms $R_{gL}^{I+1} + R_{gg}^{I+1} L_{gL}^{I-1}$ ensure the final scattering from each half–space results in partial waves incident upon the layer, within which the final scattering occurs, since again the next scattering is between adjacent scatterers. The next term in (2.10.6) is the same as the last, but with the first scattering after leaving layer I in the right half space. Finally, taking the inverse ensures *multiple* scattering between layer I and the two half spaces, in the usual way.

2.11 Half space reflectivities for close spaced layers

In order to determine the reflectivities we consider initially the problem of adding an additional layer to an already assembled stack, and then present a similarly motivated procedure as the layer doubling algorithm for a more rapid assembly than this linear stacking technique. We need initially to obtain expressions for the single layer scattering matrices, coupling incident plane or partial waves to outgoing partial waves. In terms of the layer transition matrix $\underset{\sim}{T}$ these are

$$
\begin{aligned}
T_{gg}^{++} &= P^{+}\Gamma_{gL}^{+}\underset{\sim}{T}\Gamma_{Lg}^{+}P^{+} & T_{gg}^{+-} &= P^{+}\Gamma_{gL}^{+}\underset{\sim}{T}\Gamma_{Lg}^{-}P^{-} \\
T_{gg}^{--} &= P^{-}\Gamma_{gL}^{-}\underset{\sim}{T}\Gamma_{Lg}^{-}P^{-} & T_{gg}^{-+} &= P^{-}\Gamma_{gL}^{-}\underset{\sim}{T}\Gamma_{Lg}^{+}P^{+} \\
T_{gL}^{++} &= P^{+}\Gamma_{gL}^{+}\underset{\sim}{T}G^{+} & T_{gL}^{+-} &= P^{+}\Gamma_{gL}^{+}\underset{\sim}{T}G^{-} \\
T_{gL}^{--} &= P^{-}\Gamma_{gL}^{-}\underset{\sim}{T}G^{-} & T_{gL}^{-+} &= P^{-}\Gamma_{gL}^{-}\underset{\sim}{T}G^{+} \\
T_{Lg}^{++} &= G^{+}\underset{\sim}{T}\Gamma_{Lg}^{+}P^{+} & T_{Lg}^{+-} &= G^{+}\underset{\sim}{T}\Gamma_{Lg}^{-}P^{-} \\
T_{Lg}^{--} &= G^{-}\underset{\sim}{T}\Gamma_{Lg}^{-}P^{-} & T_{Lg}^{-+} &= G^{-}\underset{\sim}{T}\Gamma_{Lg}^{+}P^{+} \\
T_{LL}^{++} &= G^{+}\underset{\sim}{T}G^{+} & T_{LL}^{+-} &= G^{+}\underset{\sim}{T}G^{-} \\
T_{LL}^{--} &= G^{-}\underset{\sim}{T}G^{-} & T_{LL}^{-+} &= G^{-}\underset{\sim}{T}G^{+}
\end{aligned}
\qquad (2.11.1)
$$

schematically illustrated in figure 2.9. The propagators $G^{\pm}$ appearing in (2.11.1) are the angular momentum Bloch free space propagator given by

$$
\left[G_{I}^{\pm}(\mathbf{k}_{\|})\right]_{LnL'm} = \sum_{J} G_{LL'}\left(\pm(\mathbf{R}_{0m} - \mathbf{R}_{Jn} + \mathbf{c}_{I} - \mathbf{c}_{I+1})\right) e^{i\mathbf{k}_{\|}.\mathbf{R}_{J}} \qquad (2.11.2)
$$

where the summation ranges over layer unit cells. Note that the definition of the matrices (2.11.1) are such that those coupling to partial waves have site dimensions of the number of atoms within the adjacent layer. As in the case of the intralayer structure constants more suitable expressions for their evaluation may be obtained by Ewald split techniques.

The formal solution to the stacking problem is simply that of the two centre scattering problem, and is most conveniently expressed as

$$
R^{I} = R^{I+1} + \left[1 + R^{I+1}\right]\left[1 - T_{I}R^{I+1}\right]^{-1} T_{I}\left[1 + R^{i+1}\right] \qquad (2.11.3)
$$

We consider here the determination of the right half–space reflectivity only; that of the left half space follows in an exactly analogous manner. Considering the various possibilities appearing in (2.11.3) for the basis sets between which the

Figure 2.9 Schematic illustration of the 16 matrices entering the layer "tripling" algorithm. See caption to figure 2.8 for more details.

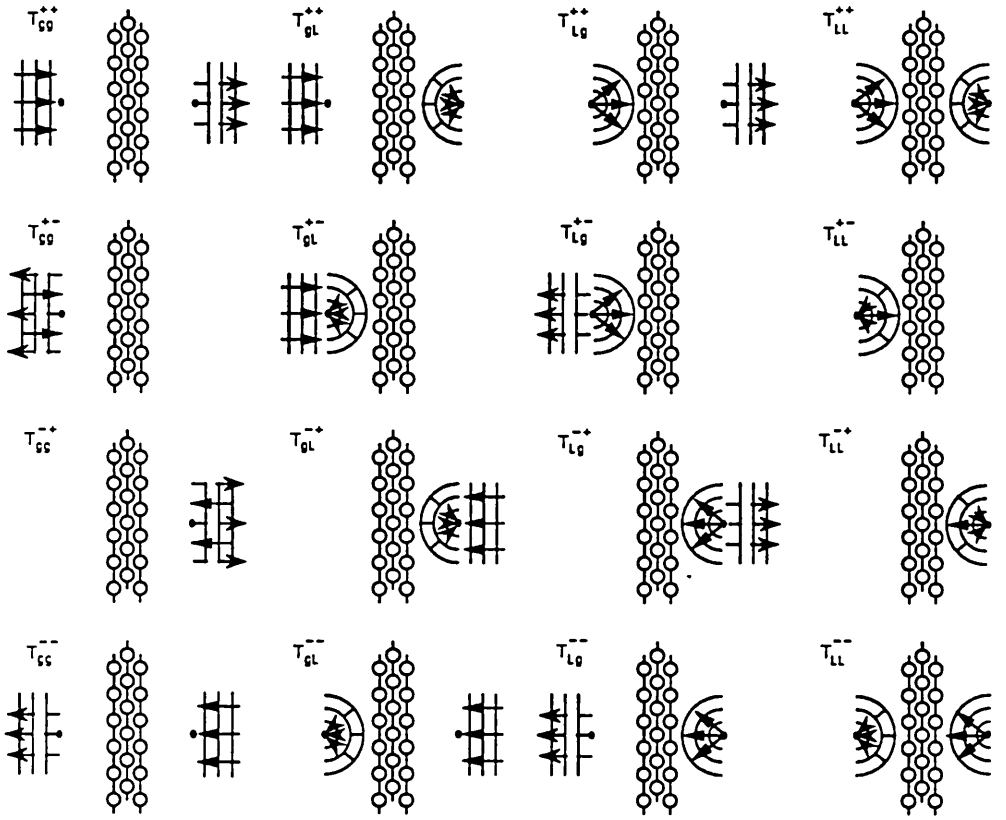

reflection matrix transforms, we obtain the following four equations which describe the relationship between the reflectivity with and without layer I.

$$R^I_{gg} = P^+_{I-1} R^{I+1}_{gg} P^-_{I-1} + P^+_{I-1} \left[\Gamma^+_{gL} + R^{I+1}_{gL}\right] \times \left[1 - \underset{\sim}{T}_I R^{I+1}_{LL}\right]^{-1} \underset{\sim}{T}_I \left[\Gamma^-_{Lg} + R^{I+1}_{Lg}\right] P^-_I \quad (2.11.4a)$$

$$R^I_{Lg} = \Gamma^+_{Lg} P^+_{I-1} R^{I+1}_{gg} P^-_{I-1} + \left[G^+_I + \Gamma^+_{Lg} P^+_{I-1} R^{I+1}_{gL}\right] \times \left[1 - \underset{\sim}{T}_I R^{I+1}_{LL}\right]^{-1} \underset{\sim}{T}_I \left[\Gamma^-_{Lg} + R^{I+1}_{Lg}\right] P^-_I \quad (2.11.4b)$$

$$R^I_{gL} = P^+_{I-1} R^{I+1}_{gg} P^-_{I-1} \Gamma^-_{gL} + P^+_{I-1} \left[\Gamma^+_{gL} + R^{I+1}_{gL}\right] \times \left[1 - \underset{\sim}{T}_I R^{I+1}_{LL}\right]^{-1} \underset{\sim}{T}_I \left[G^-_I + R^{I+1}_{Lg} P^-_I \Gamma^-_{gL}\right] \quad (2.11.4c)$$

$$R^I_{LL} = \Gamma^+_{Lg} P^+_{I-1} R^{I+1}_{gg} P^-_{I-1} \Gamma^-_{gL} + \left[G^+_I + \Gamma^+_{Lg} P^+_{I-1} R^{I+1}_{gL}\right] \times \left[1 - \underset{\sim}{T}_I R^{I+1}_{LL}\right]^{-1} \underset{\sim}{T}_I \left[G^-_I + R^{I+1}_{Lg} P^-_I \Gamma^-_{gL}\right] \quad (2.11.4d)$$

Taking (2.11.4c) as an example, we have the first term which sums all paths which do not scatter within the added layer. R^I_{gL} reflects an incident plane wave into a partial wave, and hence assumes the incident wave is more distant than one layer spacing. Thus this first term scatters in the plane wave basis, with the result projected into the spherical wave basis. In the other term the initial scattering event $P^-_{I-1}\left[\Gamma^-_{gL} + R^{I+1}_{gL}\right]$ accounts for all scattering paths initially incident upon the additional layer, so counts the direct path or those after scattering off the half-space behind, for which we return in the partial wave basis as the next scattering is on an adjacent layer. $\left[1 - \underset{\sim}{T}_I R^{I+1}_{LL}\right]^{-1} \underset{\sim}{T}_I$ counts the multiple scattering between the added layer and half-space, performed in the partial wave basis as the objects are adjacent, and the final factor $\left[G^+_I + R^{I+1}_{Lg} P^+_I \Gamma^+_{gL}\right]$ considers all possible paths out of the composite half-space, either directly off the layer in which case the propagation is performed in the angular momentum basis, or with a final scattering on the half-space, when the propagation is across the layer and hence achieved in the plane wave basis. This reflectivity illustrates the important property of this solution to the close-spaced layer problem: that all occurences of the angular momentum propagator $G^{\pm}$ are between layer scattering matrices $\underset{\sim}{T}$ and products of the form GG do not occur. Thus the angular momentum basis is truncated by the scattering properties of the atoms of the system and not through the need to converge internal summations.

These four coupled equations may be used to determine the half-space reflectivity by initially starting with R, the reflection matrix of a single layer, and repeatedly adding one more. However this procedure is too slow converging to be

of practical use. An alternative method would be to treat equations (2.11.4a-d) as a self-consistency relation by setting $R^{I}_{gg} = R^{I+1}_{gg}$ etc, which defines the reflectivity of the half–spaces, and solving the equations by standard matrix techniques, such as Newton–Raphson or a simple damped substitution (mixing) procedure. However, experience with layer doubling has demonstrated its usefulness as a technique for evaluating the reflectivities, and so we choose to develop a new layer doubling algorithm, outlined in the next Section.

2.12 Layer "tripling"

In the normal layer doubling algorithm the reflection and transmission matrices of two stacks of n layers are combined to determine the reflection and transmission matrices of the composite stack of 2n layers. Between the two stacks the scattering paths are summed within the plane wave basis used for all interlayer scattering.

In this new formulation we are assembling layers such that scattering between adjacent layers is performed in the partial wave basis, whilst that between more distant scatterers is taken into account with the plane wave basis. As a consequence we cannot use the same algorithm and stack two layers since, although the scattering between the two stacks may be performed in the angular momentum basis, we do not explicitly treat in a plane wave basis those scattering paths across the two stacks where a scattering event did not occur in one of innermost layers of the stacks. Hence we would be using products of angular momentum propagators to assemble scattering paths of significant length within our assembled stack, and the poor convergence of this basis would prevent accurate determination of the reflectivities.

To overcome this problem we assemble the scattering matrices of the half–spaces by repeatedly assembling a stack made from two copies of the previous stack sandwiching a single basic unit of the half–space. We may then treat explicitly those scattering paths between the half–spaces which include a scattering event in the sandwiched layer in the partial wave basis, whilst those across the layer not including a scattering event in the layer are treated in a plane wave basis.

The reflection and transmission matrices of the assembled stack are given by the general solution of the three–centre scattering problem. We wish to obtain various matrix elements of the transition matrix $T = \tau_L + \tau_I + \tau_R$ where the

scattering path operators are subscripted by the last object in which a scattering event occurred in, and which obey the usual EOM:

$$\begin{aligned} \tau_L &= [1 + \tau_I + \tau_R]\, L \\ \tau_I &= [\tau_L + 1 + \tau_R]\, T \\ \tau_R &= [\tau_L + \tau_I + 1]\, R \end{aligned} \tag{2.12.1}$$

L denotes the scattering matrix of the left stack, and R that of the right. In the actual tripling algorithm these two scatterers will be the same, but it is more transparent to distinguish between them for the accounting of scattering paths. A convenient procedure for the solution of these equations is to first determine the possible routes by which a wave incident upon the stack scatters and leaves (as a partial wave) with a scattering upon the central layer. We will then sum the possible paths by which this emmitted wave leaves the stack. We have in general two directions of incidence and the possibility of an originally incident plane wave or partial wave, so there are four such matrices.

The formal solution for this problem is

$$\tau_I = [1 + X]T[1 - XT]^{-1} \tag{2.12.2}$$

where X is the operator representing the scattering of waves by the two outer stacks in the absence of the central layer, and which occurred in Section 2.11.

$$X = R + L + L[1 - RL]^{-1}[R + RL] + R[1 - LR]^{-1}[L + LR] \tag{2.12.3}$$

The form of X transforming an outgoing spherical wave from layer I into an incident spherical wave after scattering between the outer stacks is

$$\begin{aligned} X_{LL} = R_{LL}^{+-} + L_{LL}^{-+} + L_{Lg}^{-+} \left[1 - R_{gg}^{+-} L_{gg}^{-+}\right]^{-1} \left[R_{gL}^{+-} + R_{gg}^{+-} L_{gL}^{-+}\right] + \\ R_{Lg}^{+-} \left[1 - L_{gg}^{-+} R_{gg}^{+-}\right]^{-1} \left[L_{gL}^{-+} + L_{gg}^{-+} R_{gL}^{+-}\right] + \end{aligned} \tag{2.12.4}$$

Thus the scattering paths connecting a plane wave incident from the right to an outgoing spherical wave from layer I is

$$\begin{aligned} \tau_{gL}^{-} = \Bigg[& R_{gg}^{--} \left[1 - L_{gg}^{-+} R_{gg}^{+-}\right]^{-1} \left[L_{gL}^{-+} + L_{gg}^{-+} R_{gL}^{+-}\right] + \\ & P^{-} L_{gg}^{-+} \left[1 - R_{gg}^{+-} L_{gg}^{-+}\right]^{-1} \left[R_{gL}^{+-} + R_{gg}^{+-} L_{gL}^{-+}\right] + \\ & P^{-} L_{gL}^{-+} + R_{gL}^{--} + P^{-} \Gamma_{gL}^{-} \Bigg] \underset{\sim}{T} \left[1 - X_{LL} \underset{\sim}{T}\right]^{-1} \end{aligned} \tag{2.12.5a}$$

that summing the scattering paths connecting a spherical wave incident from the right to an outgoing spherical wave from layer I is

$$\begin{aligned}\tau_{LL}^{-} = &\Big[R_{Lg}^{--}\left[1 - L_{gg}^{-+}R_{gg}^{+-}\right]^{-1}\left[L_{gL}^{-+} + L_{gg}^{-+}R_{gL}^{+-}\right] + \\ &\Gamma_{Lg}^{-}P^{-}L_{gg}^{-+}\left[1 - R_{gg}^{+-}L_{gg}^{-+}\right]^{-1}\left[R_{gL}^{+-} + R_{gg}^{+-}L_{gL}^{-+}\right] + \\ &\Gamma_{Lg}^{-}P^{-}L_{gL}^{-+} + R_{LL}^{--} + \Gamma_{Lg}^{-}P^{-}\Gamma_{gL}^{-}\Big]\underset{\sim}{T}\left[1 - X_{LL}\underset{\sim}{T}\right]^{-1}\end{aligned} \tag{2.12.5b}$$

that summing the scattering paths connecting a plane wave incident from the left to an outgoing spherical wave from layer I is

$$\begin{aligned}\tau_{gL}^{+} = &\Big[P^{+}R_{gg}^{+-}\left[1 - L_{gg}^{-+}R_{gg}^{+-}\right]^{-1}\left[L_{gL}^{-+} + L_{gg}^{-+}R_{gL}^{+-}\right] + \\ &L_{gg}^{++}\left[1 - R_{gg}^{+-}L_{gg}^{-+}\right]^{-1}\left[R_{gL}^{+-} + R_{gg}^{+-}L_{gL}^{-+}\right] + \\ &P^{+}R_{gL}^{+-} + L_{gL}^{++} + P^{+}\Gamma_{gL}^{-}\Big]\underset{\sim}{T}\left[1 - X_{LL}\underset{\sim}{T}\right]^{-1}\end{aligned} \tag{2.12.5c}$$

and that summing the scattering paths connecting a spherical wave incident from the right to an outgoing spherical wave from layer I is

$$\begin{aligned}\tau_{LL}^{+} = &\Big[\Gamma_{Lg}^{+}P^{+}R_{gg}^{+-}\left[1 - L_{gg}^{-+}R_{gg}^{+-}\right]^{-1}\left[L_{gL}^{-+} + L_{gg}^{-+}R_{Lg}^{+-}\right] + \\ &L_{Lg}^{++}\left[1 - R_{gg}^{+-}L_{gg}^{-+}\right]^{-1}\left[R_{gL}^{+-} + R_{gg}^{+-}L_{gL}^{-+}\right] + \\ &L_{LL}^{++} + \Gamma_{Lg}^{+}P^{+}R_{gL}^{+-} + \Gamma_{Lg}P^{+}\Gamma_{gL}^{-}\Big]\underset{\sim}{T}\left[1 - X_{LL}\underset{\sim}{T}\right]^{-1}\end{aligned} \tag{2.12.5d}$$

Finally, we now modify these waves leaving the central layer to include all possible scattering paths out of the system. We have from (2.12.1) that the full transition matrix is given by

$$T = \tau_I + [1 + \tau_I]\,X \tag{2.12.6}$$

so the sixteen matrices (2 directions of incidence/emergence and the possibility of plane wave or spherical) are explicitly

$$T_{gg}^{++} = \tau_{gL}^{+}\Gamma_{Lg}^{+}P^{+} - P^{+}P^{+} +$$
$$\left[L_{gg}^{++} + P^{+}\right]\left[1 - R_{gg}^{+-}L_{gg}^{-+}\right]^{-1}\left[R_{gg}^{++} + P^{+}\right] +$$
$$\tau_{gL}^{+}\left[R_{Lg}^{++} + \left[L_{Lg}^{-+} + R_{Lg}^{+-}L_{gg}^{-+}\right]\left[1 - R_{gg}^{+-}L_{gg}^{-+}\right]^{-1}\left[R_{gg}^{++} + P^{+}\right]\right] \qquad (2.12.7a)$$

$$T_{gg}^{--} = \tau_{gL}^{-}\Gamma_{Lg}^{-}P^{-} - P^{-}P^{-} +$$
$$\left[R_{gg}^{--} + P^{-}\right]\left[1 - L_{gg}^{-+}R_{gg}^{+-}\right]^{-1}\left[L_{gg}^{--} + P^{-}\right] +$$
$$\tau_{gL}^{-}\left[L_{Lg}^{--} + \left[R_{Lg}^{+-} + L_{Lg}^{-+}R_{gg}^{+-}\right]\left[1 - L_{gg}^{-+}R_{gg}^{+-}\right]^{-1}\left[L_{gg}^{--} + P^{-}\right]\right] \qquad (2.12.7b)$$

$$T_{gg}^{-+} = \tau_{gL}^{-}\Gamma_{Lg}^{+}P^{+} + R_{gg}^{-+}\left[R_{gg}^{--} + P^{-}\right]\left[1 - L_{gg}^{-+}R_{gg}^{+-}\right]^{-1}L_{gg}^{-+}\left[R_{gg}^{++} + P^{+}\right] +$$
$$\tau_{gL}^{-}\left[R_{Lg}^{++} + \left[L_{Lg}^{-+} + R_{Lg}^{+-}L_{gg}^{-+}\right]\left[1 - R_{gg}^{+-}L_{gg}^{-+}\right]^{-1}\left[R_{gg}^{++} + P^{+}\right]\right] \qquad (2.12.7c)$$

$$T_{gg}^{+-} = \tau_{gL}^{+}\Gamma_{Lg}^{-}P^{-} + L_{gg}^{+-}\left[L_{gg}^{++} + P^{+}\right]\left[1 - R_{gg}^{+-}L_{gg}^{-+}\right]^{-1}R_{gg}^{+-}\left[L_{gg}^{--} + P^{-}\right] +$$
$$\tau_{gL}^{+}\left[L_{Lg}^{--} + \left[R_{Lg}^{+-} + L_{Lg}^{-+}R_{gg}^{+-}\right]\left[1 - L_{gg}^{-+}R_{gg}^{+-}\right]^{-1}\left[L_{gg}^{--} + P^{-}\right]\right] \qquad (2.12.7d)$$

$$T_{gL}^{++} = \tau_{gL}^{+}\Gamma_{Lg}^{+}P^{+}\Gamma_{gL}^{+} - P^{+}P^{+}\Gamma_{gL}^{+} +$$
$$\left[L_{gg}^{++} + P^{+}\right]\left[1 - R_{gg}^{+-}L_{gg}^{-+}\right]^{-1}\left[R_{gL}^{++} + P^{+}\Gamma_{gL}^{+}\right] +$$
$$\tau_{Lg}^{+}\left[R_{LL}^{++} + \left[R_{Lg}^{+-}L_{gg}^{-+} + L_{Lg}^{-+}\right]\left[1 - R_{gg}^{+-}L_{gg}^{-+}\right]^{-1}\left[R_{gL}^{++} + P^{+}\Gamma_{gL}^{+}\right]\right] \qquad (2.12.7e)$$

$$T_{gL}^{--} = \tau_{gL}^{-}\Gamma_{Lg}^{-}P^{-}\Gamma_{gL}^{-} - P^{-}P^{-}\Gamma_{gL}^{-} +$$
$$\left[R_{gg}^{--} + P^{-}\right]\left[1 - L_{gg}^{-+}R_{gg}^{+-}\right]^{-1}\left[L_{gL}^{--} + P^{-}\Gamma_{gL}^{-}\right] +$$
$$\tau_{Lg}^{-}\left[L_{LL}^{--} + \left[L_{Lg}^{-+}R_{gg}^{+-} + R_{Lg}^{+-}\right]\left[1 - L_{gg}^{-+}R_{gg}^{+-}\right]^{-1}\left[L_{gL}^{--} + P^{-}\Gamma_{gL}^{-}\right]\right] \qquad (2.12.7f)$$

$$T_{gL}^{+-} = \tau_{gL}^{+}\Gamma_{Lg}^{-}P^{-}\Gamma_{gL}^{-} + L_{gL}^{+-} +$$
$$\left[L_{gg}^{++} + P^{+}\right]\left[1 - R_{gg}^{+-}L_{gg}^{-+}\right]^{-1}R_{gg}^{+-}\left[L_{gL}^{--} + P^{-}\Gamma_{gL}^{-}\right] +$$
$$\tau_{gL}^{+}\left[L_{LL}^{--} + \left[L_{Lg}^{-+}R_{gg}^{+-} + R_{Lg}^{+-}\right]\left[1 - L_{gg}^{-+}R_{gg}^{+-}\right]^{-1}\left[L_{gL}^{--} + P^{-}\Gamma_{gL}^{-}\right]\right] \qquad (2.12.7g)$$

$$T_{gL}^{-+} = \tau_{gL}^{-}\Gamma_{Lg}^{+}P^{+}\Gamma_{gL}^{+} + R_{gL}^{-+} +$$
$$\left[R_{gg}^{--} + P^{-}\right]\left[1 - L_{gg}^{-+}R_{gg}^{+-}\right]^{-1}L_{gg}^{-+}\left[R_{gL}^{++} + P^{+}\Gamma_{gL}^{+}\right] +$$
$$\tau_{gL}^{-}\left[R_{LL}^{++} + \left[R_{Lg}^{+-}L_{gg}^{-+} + L_{Lg}^{-+}\right]\left[1 - R_{gg}^{+-}L_{gg}^{-+}\right]^{-1}\left[R_{gL}^{++} + P^{+}\Gamma_{gL}^{+}\right]\right] \qquad (2.12.7h)$$

$$T_{Lg}^{++} = \tau_{LL}^{+}\Gamma_{Lg}^{+}P^{+} - \Gamma_{Lg}^{+}P^{+}P^{+} +$$
$$\left[L_{Lg}^{++} + \Gamma_{Lg}^{+}P^{+}\right]\left[1 - R_{gg}^{+-}L_{gg}^{-+}\right]^{-1}\left[R_{gg}^{++} + P^{+}\right] +$$
$$\tau_{LL}^{+}\left[R_{Lg}^{++} + \left[L_{Lg}^{-+} + R_{Lg}^{+-}L_{gg}^{-+}\right]\left[1 - R_{gg}^{+-}L_{gg}^{-+}\right]^{-1}\left[R_{gg}^{++} + P^{+}\right]\right] \qquad (2.12.7i)$$

$$T_{Lg}^{--} = \tau_{LL}^{-}\Gamma_{Lg}^{-}P^{-} - \Gamma_{Lg}^{-}P^{-}P^{-} +$$

$$\left[R^{--}_{Lg} + \Gamma^{-}_{Lg} P^{-}\right] \left[1 - L^{-+}_{gg} R^{+-}_{gg}\right]^{-1} \left[L^{--}_{gg} + P^{-}\right] +$$
$$\tau^{-}_{LL} \left[L^{--}_{Lg} + \left[R^{+-}_{Lg} + L^{-+}_{Lg} R^{+-}_{gg}\right] \left[1 - L^{-+}_{gg} R^{+-}_{gg}\right]^{-1} \left[L^{--}_{gg} + P^{-}\right]\right] \qquad (2.12.7j)$$

$$T^{+-}_{Lg} = \tau^{+}_{LL} \Gamma^{-}_{Lg} P^{-} + L^{+-}_{Lg} +$$
$$\left[L^{++}_{Lg} + \Gamma^{+}_{Lg} P^{+}\right] \left[1 - R^{+-}_{gg} L^{-+}_{gg}\right]^{-1} R^{+-}_{gg} \left[L^{--}_{gg} + P^{-}\right] +$$
$$\tau^{+}_{LL} \left[L^{--}_{Lg} + \left[R^{+-}_{Lg} + L^{-+}_{Lg} R^{+-}_{gg}\right] \left[1 - L^{-+}_{gg} R^{+-}_{gg}\right]^{-1} \left[L^{--}_{gg} + P^{-}\right]\right] \qquad (2.12.7k)$$

$$T^{-+}_{Lg} = \tau^{-}_{LL} \Gamma^{+}_{Lg} P^{+} + R^{-+}_{Lg} +$$
$$\left[R^{--}_{Lg} + \Gamma^{-}_{Lg} P^{-}\right] \left[1 - L^{-+}_{gg} R^{+-}_{gg}\right]^{-1} L^{-+}_{gg} \left[R^{++}_{gg} + P^{+}\right] +$$
$$\tau^{-}_{LL} \left[R^{++}_{Lg} + \left[L^{-+}_{Lg} + R^{+-}_{Lg} R^{-+}_{gg}\right] \left[1 - R^{+-}_{gg} L^{-+}_{gg}\right]^{-1} \left[R^{++}_{gg} + P^{+}\right]\right] \qquad (2.12.7l)$$

$$T^{++}_{LL} = \tau^{+}_{LL} \Gamma^{+}_{Lg} P^{+} \Gamma^{+}_{gL} - \Gamma^{+}_{Lg} P^{+} P^{+} \Gamma^{+}_{gL} +$$
$$\left[L^{++}_{Lg} + \Gamma^{+}_{Lg} P^{+}\right] \left[1 - R^{+-}_{gg} L^{-+}_{gg}\right]^{-1} \left[R^{++}_{gL} + P^{+} \Gamma^{+}_{gL}\right] +$$
$$\tau^{+}_{LL} \left[R^{++}_{LL} + \left[R^{+-}_{Lg} L^{-+}_{gg} + L^{-+}_{Lg}\right] \left[1 - R^{+-}_{gg} L^{-+}_{gg}\right]^{-1} \left[R^{++}_{gL} + P^{+} \Gamma^{+}_{gL}\right]\right] \qquad (2.12.7m)$$

$$T^{--}_{LL} = \tau^{-}_{LL} \Gamma^{-}_{Lg} P^{-} \Gamma^{-}_{gL} - \Gamma^{-}_{Lg} P^{-} P^{-} \Gamma^{-}_{gL} +$$
$$\left[R^{--}_{Lg} + \Gamma^{-}_{Lg} P^{-}\right] \left[1 - L^{-+}_{gg} R^{+-}_{gg}\right]^{-1} \left[L^{--}_{gL} + P^{-} \Gamma^{-}_{gL}\right] +$$
$$\tau^{-}_{LL} \left[L^{--}_{LL} + \left[L^{-+}_{Lg} R^{+-}_{gg} + R^{+-}_{Lg}\right] \left[1 - L^{-+}_{gg} R^{+-}_{gg}\right]^{-1} \left[L^{--}_{gL} + P^{-} \Gamma^{-}_{gL}\right]\right] \qquad (2.12.7n)$$

$$T^{+-}_{LL} = \tau^{+}_{LL} \Gamma^{-}_{Lg} P^{-} \Gamma^{-}_{gL} + L^{+-}_{LL} +$$
$$\left[L^{++}_{Lg} + \Gamma^{+}_{Lg} P^{+}\right] \left[1 - R^{+-}_{gg} L^{-+}_{gg}\right]^{-1} R^{+-}_{gg} \left[L^{--}_{gL} + P^{-} \Gamma^{-}_{gL}\right] +$$
$$\tau^{+}_{LL} \left[L^{--}_{LL} + \left[L^{-+}_{Lg} R^{+-}_{gg} + R^{+-}_{Lg}\right] \left[1 - L^{-+}_{gg} R^{+-}_{gg}\right]^{-1} \left[L^{--}_{gL} + P^{-} \Gamma^{-}_{gL}\right]\right] \qquad (2.12.7o)$$

$$T^{-+}_{LL} = \tau^{-}_{LL} \Gamma^{+}_{Lg} P^{+} \Gamma^{+}_{gL} + R^{-+}_{LL} +$$
$$\left[R^{--}_{Lg} + \Gamma^{-}_{Lg} P^{-}\right] \left[1 - L^{-+}_{gg} R^{+-}_{gg}\right]^{-1} L^{-+}_{gg} \left[R^{++}_{gL} + P^{+} \Gamma^{+}_{gL}\right] +$$
$$\tau^{=}_{LL} \left[R^{++}_{LL} + \left[R^{+-}_{Lg} L^{-+}_{gg} + L^{-+}_{Lg}\right] \left[1 - R^{+-}_{gg} L^{-+}_{gg}\right]^{-1} \left[R^{++}_{gL} + P^{+} \Gamma^{+}_{gL}\right]\right] \qquad (2.12.7p)$$

Unlike the corresponding plane wave transmission matrices, the direct path through the assembled scatterers is excluded from these relations.

This formulation is clearly a good deal more complicated than the traditional plane wave/layer doubling formulation but greatly extends the range of problems which may be treated within the layer KKR approach. It allows an optimisation of the two basis sets (plane waves/partial waves) since the partitioning of the atomic planes into layers may be accomplished in many ways. For example, when the plane wave basis becomes significantly larger than the partial wave basis, another

plane may be added to the layer to increase the layer-layer separation, increasing c_z and hence reducing the plane wave basis at the expense of an increased partial wave basis. Using the example of the (210) direction in the FCC crystal, which consists of identically spaced atomic planes schematically illustrated in figure 2.10, the use of the close–spaced layer algorithm in the simplest partitioning of one plane to each layer results in the shortest scattering path performed in the plane wave basis shown in figure 2.11a, which is already twice as long as would occur with the purely plane wave formulation. Thus, with 27 g vectors ($\exp(-g_{max}c_z) \simeq 5.33\text{x}10^{-4}$), 27–57 beams may suffice. However, the partial wave basis with atomic scattering up to $\ell = 2$ included has dimension $(2+1)^2 = 9$. We may make the dimensions more nearly equal by assigning two planes to each layer, as in figure 2.11b, so again with atomic scattering included up to $\ell = 2$ the partial wave basis size is $2 \times (2+1)^2 = 18$. Having so partitioned the structure, we have increased the minimum z separation between successive scattering events in the plane wave basis by 3, and from table (2.1) we may determine that a plane wave basis set of as few as 15 beams gives ($\exp(-g_{max}c_z) \simeq 2.18 \times 10^{-4}$), which is a reasonable attenuation. The further addition of a third plane to the layer (figure 2.11c) results in a partial wave basis of dimension 27, which greatly exceeds the plane wave dimension. Thus for the (210) direction two planes per layer is the optimal choice.

Figure 2.10 Possible partitioning of close–spaced layers to optimise the two basis sets. a). one, b). two and c). three atomic planes assigned to each layer.

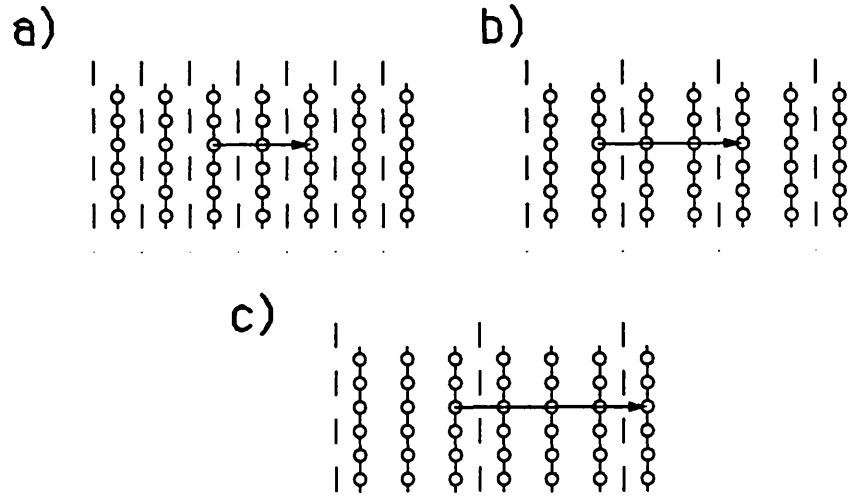

2.13 Real–space multiple scattering theory

The theory of the Sections 2.10–2.12 have described a practical method for evaluating the matrix elements of the scattering path operator necessary in evaluating the one–electron Green function in systems characterised by two dimensional periodicity, and where the layer–layer separation is sufficiently close that the use of the plane wave solution is not feasible. Using the partial wave basis to sum scattering paths between adjacent scattering units stacked along the z–direction significantly reduces the dimensions of the plane wave basis, and in fact the dimension of the two basis sets may be optimised *via* structural considerations.

There still remains a variety of systems for which the close–spaced solution will be demanding on computational resources, since extremely close layers will require a significant number of planes to be assigned to each layer before the dimensions of the two basis sets are comparable. Some recent developments in multiple scattering theory which have appeared in the literature provide a third method for evaluating the Green function in the embedded layer problem, and which could be most efficient in this regime of systems.

Zhang and Gonis (1989) have presented a real space multiple scattering theory for the electronic structure of systems with full or reduced symmetry which unifies the treatment of bulk systems, surfaces, grain boundaries and systems with impurities and substitutional disorder. The method is based upon the concepts of semi-infinite periodicity (SIP) and removal invariance, setting out to determine the Green function for the system of interest by partitioning the scatterers into subspaces characterised by SIP. These may be the left and right half spaces in the interface problem, for example, or chains of atoms at a dislocation.

The scattering properties of these subspaces are determined by utilising the removal invariance: the scattering properties of the system being invariant to within a phase (translation) under the removal of one of the scattering units whose repetition constructs the subspace. This statement may be formulated mathematically and used to obtain the scattering path operator of the subspace.

Finally the various subspace scattering operators are combined, along with those of any scatterers which cannot be assigned to regions of SIP, and the transition matrix for the whole system determined. This last step resembles a huge cluster calculation, but with various scatters, those representing regions of SIP, "dressed" to simulate the embedding medium.

Within the context of an interface calculation this formulation of the multiple scattering problem has many similarities with the theory presented in this Chapter. The concept of removal invariance, which within the theory of Zhang and Gonis is employed in the angular momentum basis, may be used to determine the reflectivities of the half-spaces through the solution of the self consistency relation

$$\underset{\sim}{\tau} = (\underset{\sim}{1} \;\; \underset{\sim}{g}(\mathbf{c})) \begin{pmatrix} (\underset{\sim}{T})^{-1} & -\underset{\sim}{G}(\mathbf{c}) \\ -\underset{\sim}{G}(-\mathbf{c}) & (\underset{\sim}{\tau})^{-1} \end{pmatrix}^{-1} \begin{pmatrix} \underset{\sim}{1} \\ \underset{\sim}{g}(-\mathbf{c}) \end{pmatrix} \qquad (2.13.1)$$

where $\underset{\sim}{T}$ is the scattering operator of the repeat unit of the half-space, $\underset{\sim}{G}$ the Bloch propagator connecting adjacent repeat units separated by $\mathbf{c}$ and $\underset{\sim}{g}$ the translation operator. The centre matrix appearing on the right hand side of (2.13.1) is simply the multi-centre scattering path operator (see equations (2.4.10) and (2.4.11)) for the combined repeat unit/half-space system, and the outer matrices fold in to a single centre representation which must be equal to the half-space scattering path operator itself.

This equation may be solved by iteration or some other numerical technique (Zhang, Gonis and MacLaren, 1989), and is directly analogous to the plane wave layer doubling problem and the plane wave/partial wave problem layer tripling

problem. The scattering path operator needed in (2.5.8) for the Green function of the embedded layer problem is then given by the expression

$$\tau = \begin{pmatrix} (\underset{\sim}{\tau}_L)^{-1} & -\underset{\sim}{G}(\mathbf{c}) & -\underset{\sim}{G}(2\mathbf{c}) \\ -\underset{\sim}{G}(-\mathbf{c}) & (\underset{\sim}{T})^{-1} & -\underset{\sim}{G}(\mathbf{c}) \\ -\underset{\sim}{G}(-2\mathbf{c}) & -\underset{\sim}{G}(-\mathbf{c}) & (\underset{\sim}{\tau}_R)^{-1} \end{pmatrix}^{-1} \qquad (2.13.2)$$

for the case of a single layer sandwiched between the half-spaces. This is the angular momentum space solution of the three centre scattering problem solved in Section 2.12 (where τ_I is the equivalent of τ here).

There are some technical details concerned with the implementation of this method (MacLaren, Zhang, Gonis and Crampin, 1989) which appear to enable an exact summation of the scatttering paths despite the exclusive use of the angular momentum basis, in the sense that no uncontrolled internal summations occur; they are all truncated by the atomic scattering factors (t-matrices). In particular the method has been shown to give identical results to the plane wave method for the density of states of an copper atom at an ideal truncated surface. Since the method is carried out entirely in real space the dimensions of the matrices involved are not affected by the separation of atomic layers and hence in the case of very close layers can provide a more efficient alternative to the plane wave or plane wave/partial wave methods.

2.14 Summary

To conclude, an outline of the implementation of the theory presented in this Chapter is given.

For a given system the atoms are partitioned into suitable layers. For each $(E, \mathbf{k}_{||})$ the scattering properties of each isolated layer are determined, *via* equations (2.6.5), along with the necessary propagators, (2.8.8) or (2.11.2). These layer scattering operators are then combined using equations (2.8.7), or (2.11.4a–d) to determine the half–space reflectivities relative to each layer. In the case of a bulk calculation this involves layer doubling/tripling the layers within the unit cell to convergence, and then the individual layers added successively to obtain the correct termination of the half–space for use in the embedded layer problem for each layer. In an interface calculation the half–space reflectivities are determined by layer doubling/tripling the layers which comprise the relevant half–space unit cell, and then adding the individual layers within the interface region to obtain the necessary half–space reflectivities for the embedded layer calculation. In this case the "bare" reflectivity, comprising just those layers within the bulk half–space, are independent of the potentials of the interface region and may be stored, to avoid re-calculation. This leads to large time savings in the context of self–consistent calculations. The propagators, being structural in nature and hence independent of the potentials, may likewise be stored for future use. Finally the embedded layer problem is solved for each layer within the bulk unit cell/interface region by combining the relevant layer and half–space scattering matrices.

The choice of which method to employ for solving the problem, be it the plane wave, plane wave/partial wave or purely angular momentum based solution may be decided through an analysis based upon the basis attenuation factor illustrated in Section 2.9 for the (210) direction, and some knowledge of the relative overheads for each approach. It is perhaps worth adding the comment that if rough calculations are being performed to look for gross trends, then the plane wave basis set can be reduced more easily than the angular momentum basis. The latter cannot, for example, be reduced below $\ell = 2$ for transition metals, whilst as few as 5–9 g vectors along the (100) direction of the fcc structure will give a reasonable description of the electronic structure. Thus the plane wave/plane wave–partial wave techniques have a certain advantage in this respect.

The theory within this Chapter has been presented from the viewpoint of an interface calculation. In the case of a surface calculation, one half–space becomes a vacuum region with a surface barrier characterised by a scattering matrix. A restricted theory for such a barrier has been given by Blake (1984) but has not yet

been implemented. The calculation time to determine the scattering properties of each layer scales as the cube of the number of atoms within it, whilst the time to combine layers is linear. Hence for some bulk systems this method may offer speed advantages when compared to other traditional codes, where the time scales typically with the cube of the total number of atoms within the system. Beyond the most obvious uses of mirror symmetry the code as developed has not, for want of generality, been symmetrised. Such a step could also offer significant savings of future computing resources.

CHAPTER 3. ELECTRONIC STRUCTURE FROM THE LKKR GREEN FUNCTION

3.0 Introduction

In this Chapter details concerning the evaluation of the electronic structure from the Green function calculated using the theory of Chapter 2 are outline. In doing so, the results of calculations on a variety of systems will be given, demonstrating the accuracy and convergence properties of the LKKR technique.

The quantity most directly related to the Green function, the charge density, is initially considered, as well as schemes for determining the full charge density which involves integrals over energy and momentum. For the former, the use of complex energies as a means of more efficient computations is demonstrated. The solution of Poisson's equation, an essential element of the self–consistent field approach defined by the Kohn–Sham equations (1.1.3–4) is described.

From the self–consistent charge densities we may evaluate total energies, and for bulk system a combination of Bloch's theorem and the multiple scattering equations allows the band structure to be determined. For interface problems the projected band structure is the two–dimensional analogue, and it's calculation by a variety of mathods is described and discussed, along with means of locating localised states permitted by the reduced periodicity.

Finally, convergence of the plane wave basis set is considered, and numerical evidence supporting the statements made in the previous Chapter concerning close–spaced layers presented.

3.1 Brillouin zone integration

The Fourier transform of the equations of motion for the scattering path operator introduced an integral over the Brillouin zone in the definition of Γ^{α}, equation (2.6.7). The method we use for the Brillouin zone integration is that of special points given by Cunningham's algorithm (Cunningham, 1974), which is a modification to two dimensions of the method of Chadi and Cohen (1973). Expanding a periodic function $f(\mathbf{k}_{||})$ as

$$f(\mathbf{k}_{||}) = f_0 + \sum_{m=1}^{\infty} f_m A_m(\mathbf{k}_{||}) \tag{3.1.1a}$$

$$A_m(\mathbf{k}_{||}) = \sum_{|\mathbf{R}|=C_m} e^{i\mathbf{k}_{||}\cdot\mathbf{R}} \tag{3.1.1b}$$

where the sum in (3.1.1b) is over those vectors of equal length, C_m, Cunningham's algorithm presents a systematic procedure for generating a set of points $\mathbf{k}_{||i}$ and weights α_i which can best estimate f_0, the average which we wish to calculate. The points generated by this algorithm satisfy

$$\sum_i \alpha_i A_m(\mathbf{k}_{||i}) = 0 \qquad m = 1, 2, \ldots\ldots N \tag{3.1.2a}$$

$$\sum_i \alpha_i = 1 \tag{3.1.2b}$$

where N is the number of functions A_m satisfying (3.1.2a), and hence

$$f_0 = \sum_i \alpha_i f(\mathbf{k}_{||i}) - \sum_{m>N}^{\infty} f_m \sum_i \alpha_i A_m(\mathbf{k}_{||i}) \tag{3.1.3}$$

The idea is to determine those sets of points and weights which maximise N, the lowest index of the Fourier series **not** included, since one may expect that for smoothly varying functions the coefficients f_m will decrease in magnitude with increasing m. Hence we approximate Γ in equation (2.6.7) with

$$\Gamma^{\alpha}(E) = \sum_i \alpha_i \Gamma(E; \mathbf{k}_{||i}) \tag{3.1.4}$$

Figure 3.1 Irreducible Brillouin zone and sampling sets for the square (upper) and hexagonal (lower) two dimensional lattices. The high symmetry points are labeled in the hexagonal case.

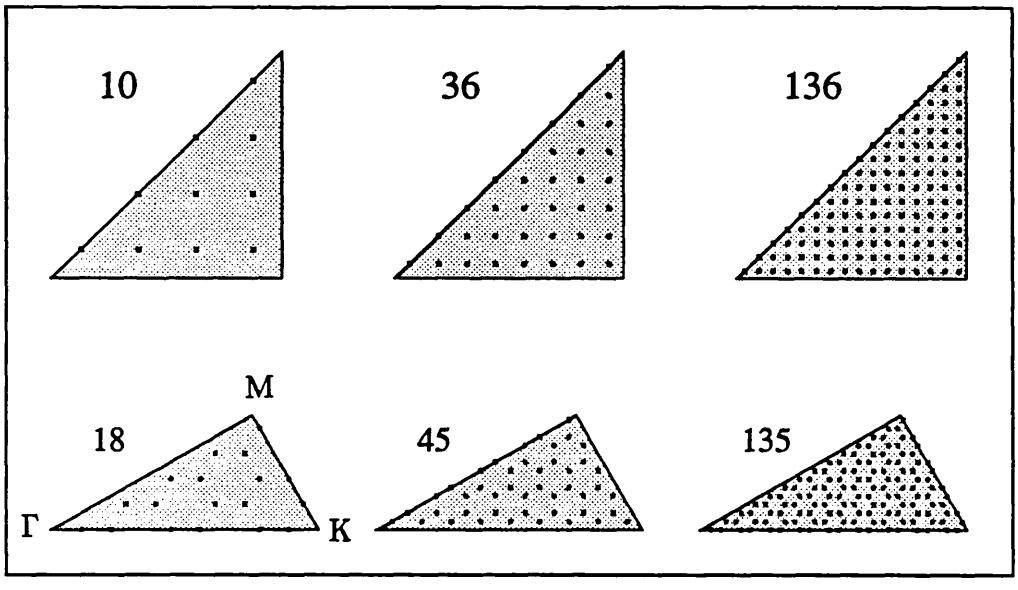

Table 3.1

Allowed values of special $\mathbf{k}_{||}$ sampling points given by Cunningham's algorithm for the square and hexagonal lattices.

Square	Hexagonal
1	1
3	3
10	6
36	18
136	45
528	135
	378

In figure 3.1 and table 3.1 are illustrated the first few sets of points for the square lattice (*e.g.* as used for the FCC (100) and BCC (100) directions) and the hexagonal lattice (*e.g.* FCC (111)). Typically only the third or fourth sets, with 10-20 sampling points have been found necessary to converge "integrated" quantities such as the Fermi level or total energies to approximately 0.001Ha. Densities of states, however, are more sensitive, particularly regions of energy characterised by *s–p* bonding. In this case the resulting parabolic bands resemble strongly the free electron bands, for which the density of states projected onto the two dimensional momentum space is given by

$$\varrho(\mathrm{E},\mathbf{k}_{||}) = \frac{\theta(2\mathrm{E} - |\mathbf{k}_{||}|^2)}{2\pi^3\sqrt{2\mathrm{E} - |\mathbf{k}_{||}|^2}} \tag{3.1.5}$$

which is illustrated in figure 3.2 (see also figure 3.9 later for a corresponding example taken from nickel). The difficulties in averaging this quantity may be seen by considering the position of the square root singularity at $|\mathbf{k}_{||}|^2 = 2\mathrm{E}$ as a function of energy. As E increases this ridge moves out in the Brillouin zone and when it just passes over a new sampling point $\mathbf{k}_{||i}$ within the set there will result a significant increase in the density of states if the weight of that point is high, that is, if only a small number of sampling points are used. As the energy increases further, the contribution diminishes before another sampling point is passed over. These erroneous oscillations can obscure true features of the density of states, and make it hard to distinguish contributions from localised states or resonances in interface or surface structures (see for example the density of states presented by Wang, Freeman, Krakauer and Posternak (1981) for their thin film calculation modelling the surface electronic structure for Al(111) for an example of this).

The flatter nature of *d*-bands across the Brillouin zone means the Brillouin zone sampling is slightly easier than for regions characteristic of *s-p* bonding (*cf* core states which require only 1 sampling point). However, localised states with *d* character present in a confined region of the two dimensional zone will not be treated correctly without sufficient sampling points.

The number of points in the sampling sets given by the Cunningham algorithm rapidly increase. It will be demonstrated later that the use of complex energies can considerably increase the efficiency of the averaging and lead to large savings in computational resources.

Figure 3.2 Free electron density of states $\varrho(E, k_{||})$ evaluated at E=0.5Ha projected onto the two dimensional momentum space $k_x, k_y > 0$. The data are truncated; $\varrho(E, k_{||}) = \min(\varrho(E, k_{||}), 0.05)$.

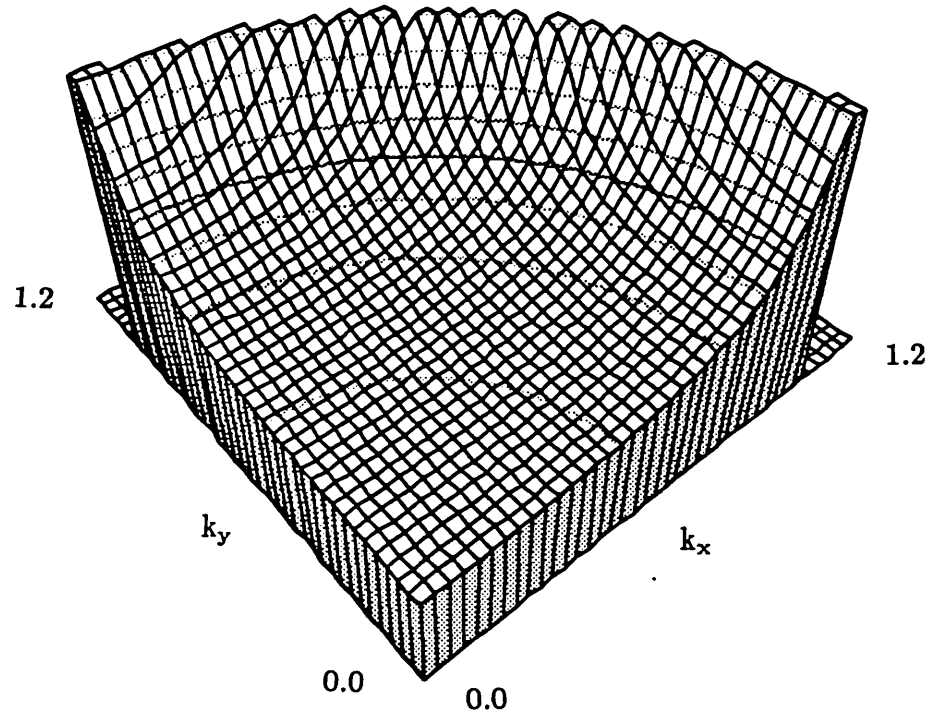

3.2 Charge density

We obtain the charge density in an expansion about each atomic from (2.5.7) and the standard relation $\varrho^\alpha(r; E) = -1/\pi \mathrm{Im} G(r, r; E)$ (Harrison, 1970)

$$\begin{aligned}\varrho^\alpha(r; E) =& \frac{4}{\pi} \mathrm{Im}\, i\kappa \sum_L Y_L^*(r) Z_\ell^\alpha(r) S_\ell^\alpha(r) Y_L(r) \\ &+ \frac{4}{\pi} \mathrm{Im}\, i\kappa \sum_{LL'} Y_L^*(r) Z_\ell^\alpha(r) \Gamma_{LL'}^\alpha Z_{\ell'}^\alpha(r) Y_{L'}(r)\end{aligned} \tag{3.2.1}$$

This may be conveniently expanded as

$$\varrho^\alpha(r; E) = \sum_L \varrho_L^\alpha(r; E) Y_L(r) \quad \text{where} \quad \varrho_L^\alpha(r; E) = \int Y_L^*(r) \varrho^\alpha(r; E) \tag{3.2.2}$$

($Y_L(r)$ is assumed to be a spherical harmonic, but may also be chosen to be a symmetrised linear combination, such as a cubic harmonic, with minor alteration to the subsequent equations) and hence

$$\begin{aligned}\varrho^{\alpha}_{L}(r;E) =& \frac{4}{\pi}\int Y^{*}_{L}(r)\mathrm{Re}\Bigg[\kappa\sum_{L'}Y^{*}_{L'}(r)Z^{\alpha}_{\ell'}(r)S^{\alpha}_{\ell'}(r)Y_{L'}(r)+ \\ &+\kappa\sum_{L'L''}Y^{*}_{L'}(r)Z^{\alpha}_{\ell'}(r)\Gamma^{\alpha}_{L'L''}Z^{\alpha}_{\ell''}(r')Y_{L''}(r')\Bigg] \\ =&\frac{4}{\pi}\sum_{L'}C^{L'}_{LL'}\mathrm{Re}\left[\kappa Z^{\alpha}_{\ell'}(r)S^{\alpha}_{\ell'}(r)\right] \\ &+\frac{2}{\pi}\sum_{L'L''}\left(C^{L''}_{LL'}+C^{L'}_{LL''}\right)\mathrm{Re}\left[\kappa Z^{\alpha}_{\ell'}(r)\Gamma^{\alpha}_{L'L''}Z^{\alpha}_{\ell''}(r)\right] \\ &+\frac{2i}{\pi}\sum_{L'L''}\left(C^{L''}_{LL'}-C^{L'}_{LL''}\right)\mathrm{Im}\left[\kappa Z^{\alpha}_{\ell'}(r)\Gamma^{\alpha}_{L'L''}Z^{\alpha}_{\ell''}(r)\right]\end{aligned} \tag{3.2.3}$$

The real coefficients $C^{L}_{L'L''} = \int Y^{*}_{L}Y_{L'}Y_{L''}d\Omega$ are related to the Gaunt coefficients, and satisfy

$$C^{L}_{L'L''} = 0 \quad \text{unless} \quad \begin{cases} \ell+\ell'+\ell'' & \text{even} \\ m = m'+m'' \\ |\ell-\ell''| \le \ell' \le \ell+\ell'' & \text{and cyclic}\end{cases} \tag{3.2.4}$$

which is of benefit in actual calculation (Pendry, 1974). The muffin-tin density of states, the spherically symmetric contribution, is given by

$$\begin{aligned}\varrho^{\alpha}_{MT}(r;E) =& \frac{1}{\sqrt{4\pi}}\varrho^{\alpha}_{00}(r;E) \\ =&\frac{1}{\pi^2}\sum_{\ell}\left[(2\ell+1)\mathrm{Re}\left[\kappa Z^{\alpha}_{\ell}(r)S^{\alpha}_{\ell}(r)\right]+\mathrm{Re}\left[\kappa\left(Z^{\alpha}_{\ell}(r)\right)^2\sum_{m=-\ell}^{\ell}\Gamma^{\alpha}_{LL}\right]\right]\end{aligned} \tag{3.2.5}$$

from which we find the total charge within the muffin-tin sphere at energy E, denoted the muffin-tin density of states (MTDOS), to be

$$\varrho^{\alpha}_{MT}(E) = \int_{S^{\alpha}}\varrho^{\alpha}(r)dr = 4\pi\int_{0}^{R^{\alpha}_{MT}} r^2 dr\varrho^{\alpha}_{MT}(r) \tag{3.2.6}$$

where S^{α} is the volume of the sphere α. The total charge density involves an energy integral over the occupied energies, which we now consider.

3.3 Energy integration

The total charge density is related to the energy resolved charge density of the previous Section *via* $\varrho(\mathbf{r},\mathrm{E})$ as

$$\varrho(\mathbf{r}) = \int_{-\infty}^{\mathrm{E_f}} \varrho(\mathbf{r},\mathrm{E})\mathrm{dE} \tag{3.3.1}$$

where the Fermi level $\mathrm{E_f}$ is defined in a bulk calculation by charge neutrality:

$$\sum_{\alpha} \mathrm{Z}^{\alpha} = \int_{\tau} \mathrm{d}\mathbf{r}\varrho(\mathbf{r}) \tag{3.3.2}$$

Z^{α} is the atomic number (nuclear charge) of the atom at site α and the sum ranges over the atoms within the unit cell.

In evaluating (3.3.1) we replace the full energy integral with a sum over the tightly bound core levels and an integral over the valence band. The core levels are those for which negligible dispersion occurs across the band, and we may determine their contribution to the charge density by direct integration of Schrödinger's equation for the isolated muffin–tin potential; negligible dispersion implies that the electrons behave as though they move in an isolated potential, not experiencing neighbouring atoms. Consequently the core charge density is necessarily spherical. Thus

$$\varrho(\mathbf{r}) = \sum_{\alpha}\sum_{\mathrm{c}_\alpha} \varrho_{\mathrm{c}_\alpha}(\mathbf{r}) + \int_{\mathrm{E_1}}^{\mathrm{E_f}} \varrho(\mathbf{r},\mathrm{E})\mathrm{dE} \tag{3.3.3}$$

where the lower limit $\mathrm{E_{min}}$ lies between the highest lying core level and the bottom of the valence band. This is illustrated schematically in figure 3.3. c_α labels the core levels for atom α. It may be the case that some higher lying core levels do display dispersion across the Brillouin zone which needs to be included for total energies or other properties. In this case the valence band integral may be split into several bands each treated as in the case of the single band considered here.

We now consider an important analytic property of the Green function which enables a very rapid evaluation of this energy integral. This is the use of complex energies. In fact, the perturbation scheme used to determine the reflectivities of the two embedding half–spaces, the layer doubling algorithm, is not guaranteed to converge on the real energy axis and we are **forced** to introduce a small imaginary component, Γ, into the energy. In practice this is not a significant restriction, since Γ may be chosen to be arbritrarily small, and indeed numerical rounding errors probably act as a finite imaginary component but cannot be relied upon to

Figure 3.3 Schematic illustration of the form of the energy integral in equation (3.3.3), and the quantities entering.

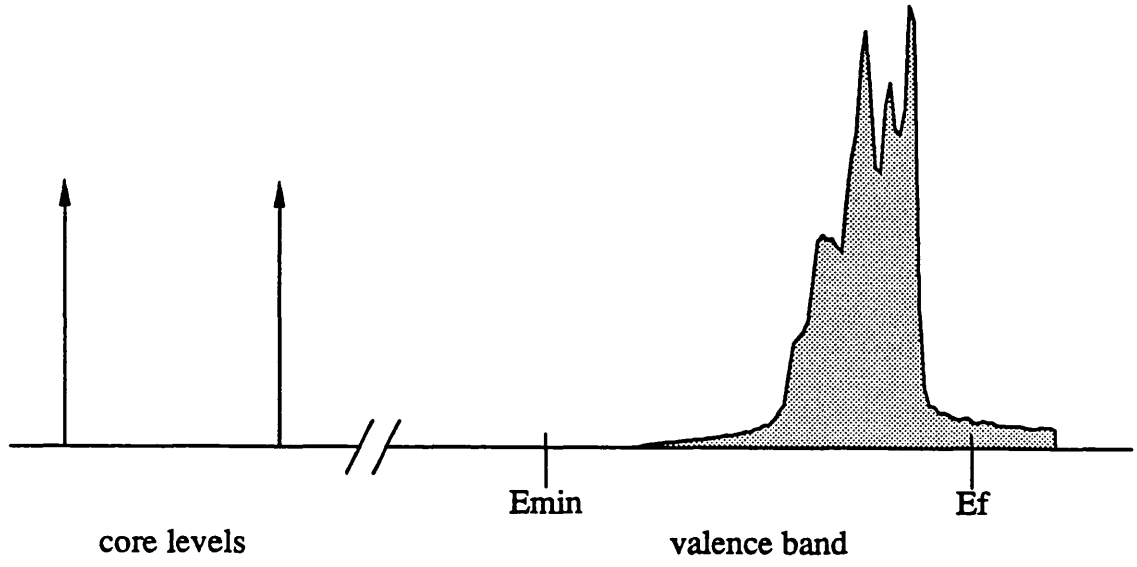

converge the reflection matrices. However, there are beneficial reasons for including a significant imaginary component in the energies, as are now illustrated.

The causal Green function at energy E, $G^+(E)$, may be defined formally as

$$G^+(E) = \frac{1}{E - H + i0^+} = P\frac{1}{E - H} - i\pi\delta(E - H) \qquad (3.3.4)$$

with H the Hamiltonian operator and P the principle part. From this we see G^+ is analytic in the upper half-plane of complex energies. Hence considering $\xi = E + i\Gamma$, $\Gamma > 0$ we see immediately from Cauchy's theorem that

$$G^+(\xi) = \frac{1}{2\pi i}\oint G^+(z)\left[\frac{1}{z - \xi} - \frac{1}{z - \xi^*}\right]dz \qquad (3.3.5a)$$

$$= \frac{1}{\pi}\int_{-\infty}^{\infty} \frac{\Gamma}{(E - E')^2 + \Gamma^2} G^+(E')dE' \qquad (3.3.5b)$$

where the semi-circular contour in (3.3.5a), illustrated in figure 3.4, extends over the whole upper half plane and encloses the point $Z = \xi$ but not $Z = \xi^*$. Hence we deduce that the charge density evaluated at complex energy Γ is related to that evaluated at real energies by

$$\varrho(r; E + i\Gamma) = -\frac{1}{\pi}\mathrm{Im}G^+(r, r; E + i\Gamma) = \frac{1}{\pi}\int_{-\infty}^{\infty} \frac{\Gamma}{(E - E')^2 + \Gamma^2}\varrho(r; E')dE' \qquad (3.3.6)$$

Figure 3.4 Contour used in evaluating equation (3.3.5a).

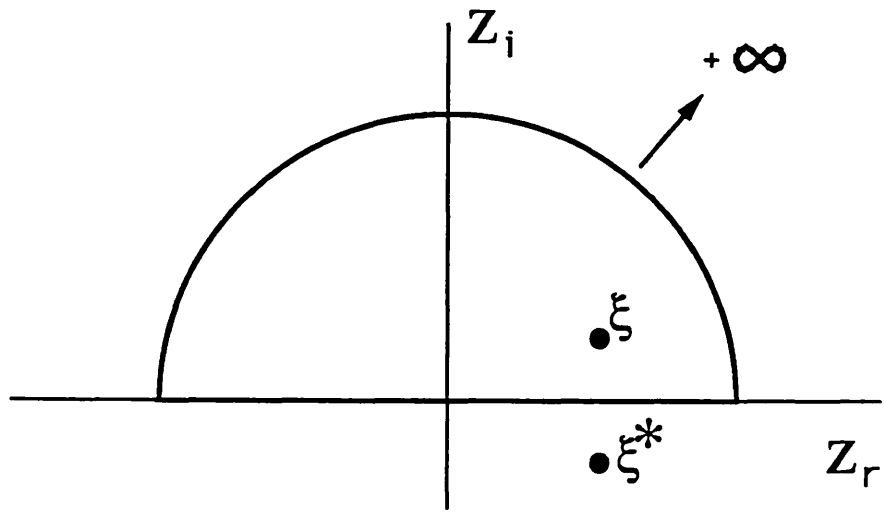

and consequently the density of states $\varrho(E + i\Gamma)$ is given by the convolution of the real energy density of states and a Lorentzian of half width Γ, the dissipative component of the energy. Structural features smaller than Γ are lost.

This effect is illustrated in figures 3.5 and 3.6. In figure 3.5 the muffin–tin density of states for the 2p core level of aluminium is plotted for various imaginary components of the energy. This level is very nearly a delta function with less than 0.01% of the weight of the electron wavefunction outside the muffin–tin. Thus we may expect the profile for various imaginary components Γ to appear Lorentzian

$$\varrho(E + i\Gamma) = \frac{1}{\pi} \frac{\Gamma}{(E - E_0)^2 + \Gamma^2} \tag{3.3.7}$$

where E_0 is the real eigenvalue, and this is clearly the case. In figure 3.6a the muffin–tin density of states for bulk copper is plotted for various imaginary componants of the energy. For Im(E)=0.010Ha (0.272eV) the MTDOS is reminiscent of density of states profiles given by photoemission experiments (Mehta and Fadley, 1977). It is largely structureless, with the bottom of the valence band extending down to about -10.0 eV (all energies relative to the Fermi level) and the narrow d-band lying between about -6.0eV and -1.0eV. Reducing the imaginary componant to 0.005Ha (0.136eV) reveals much more structure, the shoulder at -4.0eV clearly discernible along with a few peaks between -3.5eV and -2.0eV. The band minimum has risen to about -9.5eV. Finally, at an imaginary energy of 0.001Ha (0.0272eV)

Figure 3.5 Muffin-tin density of states for the 2p core level in aluminium evaluated at various imaginary energies.

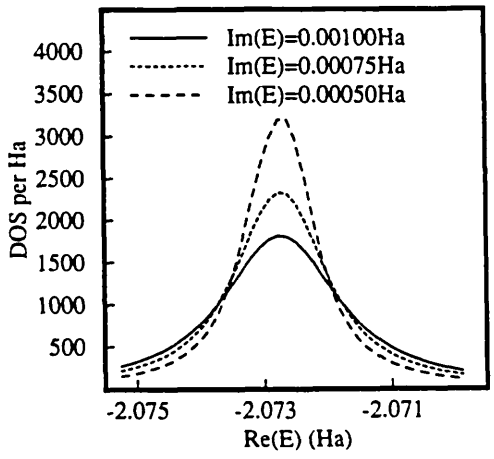

Figure 3.6 a). Valence band density of states for bulk copper evaluated at various imaginary energies. Real energies are quoted with respect to the Fermi energy. b). Valence band density of states for bulk copper taken from Moruzzi, Janak and Williams (1978).

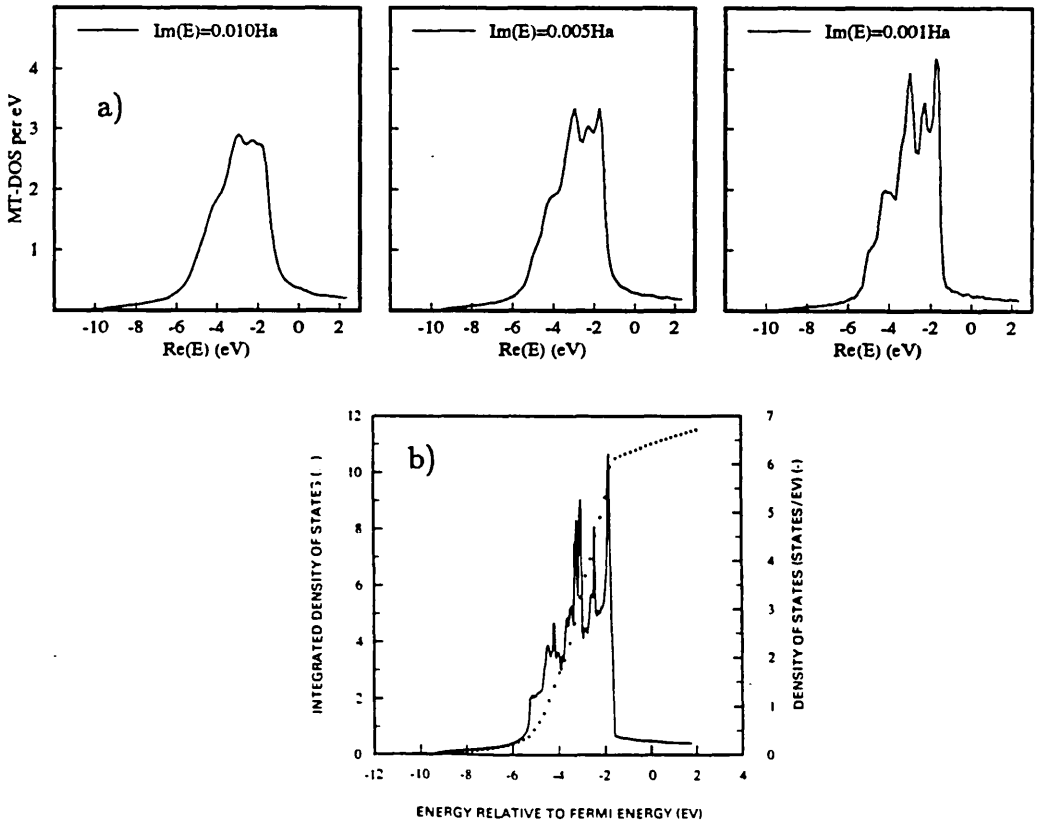

all important features of the density of states may be identified. The band minimum is still at -9.5eV, and the shoulder at -4.0eV is sharpened and accompanied by a second at slightly lower energy. Three main peaks are distinguishable within the *d*–band, which now comes down sharply at -1.75eV. The correspondance of the features and their positions with those in the density of states of copper presented by Moruzzi, Janak and Williams (1978), displayed in figure 3.6b for means of comparison, is excellent, their results being determined at zero imaginary energy. The differences in magnitude arise primarily from the results of Moruzzi *et al.* being the full cell density of states, which are necessarily larger than the muffin–tin density of states. Figure 3.7 illustrates the smoother behaviour of the muffin–tin density of states of Ni as a continuous function of the imaginary energy Γ.

Figure 3.7 Muffin–tin density of states of nickel evaluated in the complex plane out to an imaginary energy 0.06Ha.

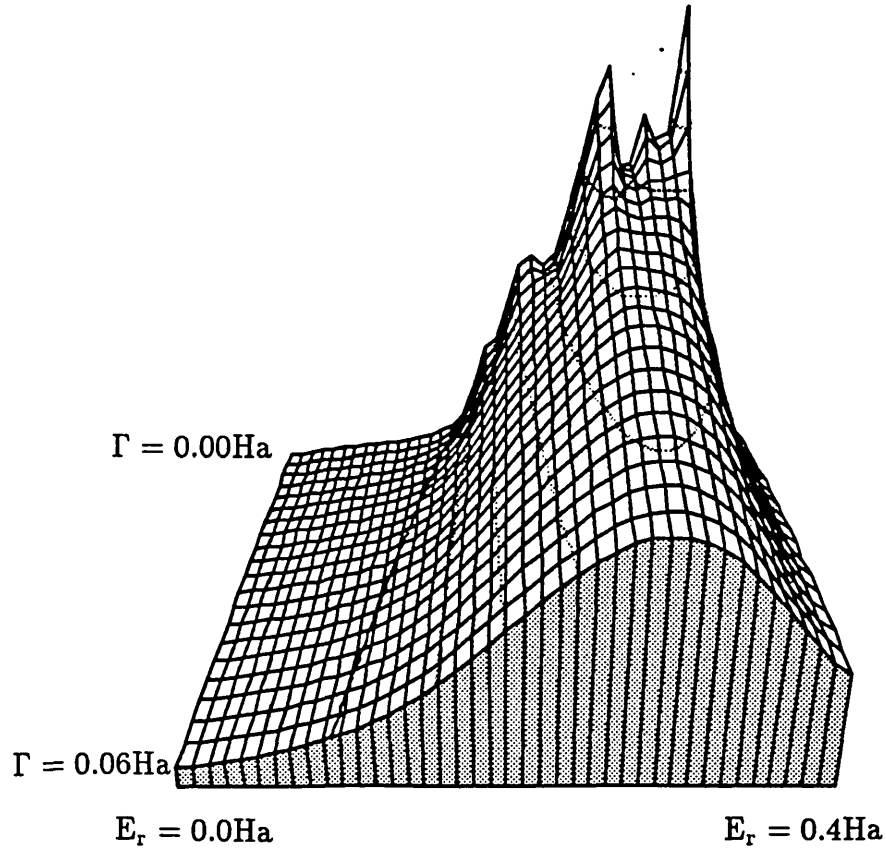

We now use the analytic behaviour of G in the upper half plane to deform the energy integral ocurring in equation (3.3.3) into the complex plane where its evaluation may be accomplished far more efficiently. From Cauchy's theorem, evaluating the integral along any contour connecting E_{min} and E_f in the upper half plane will give the same answer. In particular, for the the contour shown in figure 3.8 we may write

$$\int_{E_{min}}^{E_f} \varrho(\mathbf{r}, E)dE = \int_{c_1+c_2} \varrho(\mathbf{r}; Z)dZ$$
$$= \int_{-1}^{1} f(t)dt \qquad (3.3.8a)$$

where

$$f(t) = \begin{cases} (E_0 - E_{min} + iE_1)\,\varrho\,(\mathbf{r}, (E_0 - E_{min} + iE_1)\,t + E_0 + iE_1) & t < 0 \\ (E_f - E_0 - iE_1)\,\varrho\,(\mathbf{r}, (E_f - E_0 - iE_1)\,t + E_0 + iE_1) & t > 0 \end{cases} \qquad (3.3.8b)$$

and this may be approximated using Gaussian integration

$$\int_{E_{min}}^{E_f} \varrho(\mathbf{r}, E)dE = \sum_i w_i f(t_i) \qquad (3.3.9)$$

where the weights w_i and sampling points t_i may be taken from the tables of Abramowitz and Stegun (1970). As mentioned above, any higher lying cores having significant dispersion are best treated as separate bands, using (3.3.8,9), with E_{min} and E_f corresponding to energies straddling the mini-band.

Gaussian integration is by no means the only numerical technique which may be used for the integration, but has been found to be the most suited. When searching for the Fermi level in a bulk calculation the triangular contour has the benefit that the contribution from the upward section c_1 is independent of the endpoint, E_f, and hence need only be evaluated once, while the downward leg is repeated for different end points till the Fermi level has been located to the required precision. In the case of a semi-circular contour, the complete set of points must be re-evaluated. An alternative contour chosen by some workers for similar integrations is along the line $E_f + i\Gamma$, $0 < \Gamma < \infty$. For large imaginary components the Green function may be treated analytically, and matched closer to the real energy axis to the numerically determined function. This has advantages for certain alloy models, such as the CPA (Temmerman and Szotek, 1987), which become considerable simpler in the large Γ limit.

Figure 3.8 Energy contour used in evaluating the total charge density.

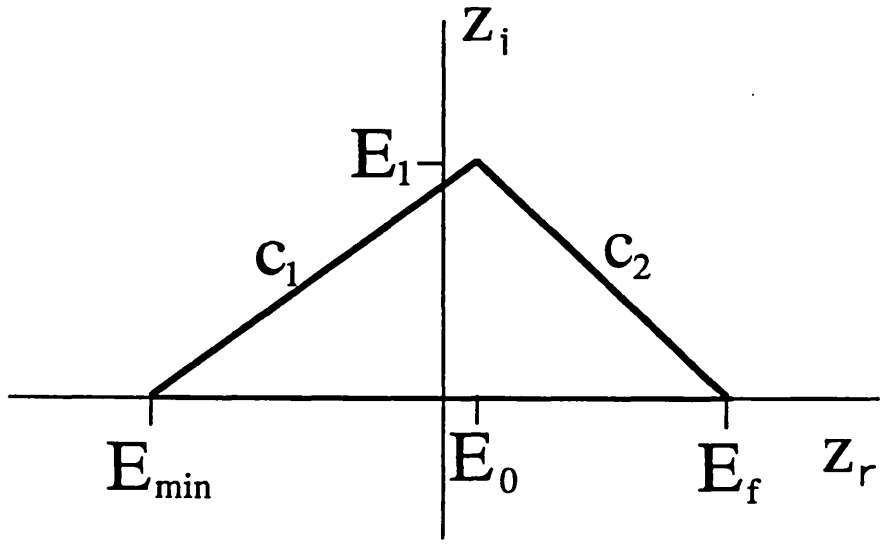

In table 3.2 the convergence of the energy integral is demonstrated for two different situations. In the first column the number of sampling points used in (3.3.9) are given. The second and third columns are integrals of the muffin–tin charge for the Ni 3s and 3p core levels respectively, using a contour between $E_0 \pm 0.005$ Ha, E_0 being the the real eigenvalue. The integral converges rapidly, especially for the 3s level. Deviations from an integral number of electrons within the muffin–tin are indicative of a small amount of dispersion. The last column tabulates the valence band charge within the muffin–tin between -0.100Ha and 0.314 Ha for copper. The convergence in this case is even more marked than for the core levels since the density of states across the band is rather more uniform, and thus more amenable to the Gaussian integration method.

The smoother behaviour of the density of states also allows a more rapid determination of the Brillouin zone integrations. Typical examples of the behaviour of the density of states as a function of the momenta $\mathbf{k}_{||}$ are illustrated in figure 3.9a-d, for the particular case of the Ni (100) direction. Although the actual averaging is performed upon $\Gamma(\mathbf{k}_{||})$ (2.6.7), this is a complex function and so difficult to illustrate. For the muffin–tin potentials both the atomic wavefunctions $Z_\ell(r), S_\ell(r)$ and transition matrix t_ℓ are independent of $\mathbf{k}_{||}$ and hence the variations in $\varrho(E + i\Gamma; \mathbf{k}_{||})$ are directly related to physically important variations in $\Gamma(\mathbf{k}_{||})$. Figure 3.9a and 3.9b are evaluated at the real energy E=0.01Ha, an energy at which the states are largely *s-p* like and without significant *d* hybridisation. The

Table 3.2

Convergence of energy integrals using the Gaussian integration technique with the number of sampling points N_E, for core level and valence band muffin–tin charges. The core level calculations were performed with a contour of width 0.01Ha centred on the real eigenvalue, and the valence band integral extended from -0.100Ha to 0.314Ha relative to the muffin–tin zero.

	muffin tin charge		
N_E	Ni 3s core	Ni 3p core	Cu valence band
8	2.00361	6.00443	10.36535
16	2.00076	5.99726	10.36349
32	2.00003	5.99541	10.36356
64	1.99993	5.99497	10.36357

similarity of figure 3.9a with the free–electron density of states illustrated in figure 3.2 is marked, the only significant differences arising from the finite imaginary energy component Γ. The difficulties in evaluating the Brillouin zone average is obvious. This is in sharp contrast with the analogous quantity evaluated at 0.1 Ha above the real energy axis. The Lorentzian broadening has produced a much more smoothly varying function across the Brillouin zone, and one which may be determined much more accurately with fewer sampling points. Figures 3.9c-d reiterate this behaviour, at the real energy E=0.25Ha, where significant *d* character is present.

We can conclude from these observations that quantities which involve integrations over energy, such as the charge density, Fermi level and total energies, when evaluated along contours which move out into the complex plane, are significantly more accurate than if the same quantities were evaluated at real energies with an identical number of E and $\mathbf{k}_{||}$ sampling points. Indeed, the number of k points may be varied as a function of the dissipative component of the energy to achieve maximum accuracy for minimum resources, far more being employed near to the real energy axis.

Figure 3.9 Density of states across the Brillouin zone for Ni (100) **a**).E = 0.1 + 0.01i **b**). E = 0.1 + 0.1i **c**). E = 0.25 + 0.1i **d**).E = 0.25 + 0.01i. (all energies in Ha)

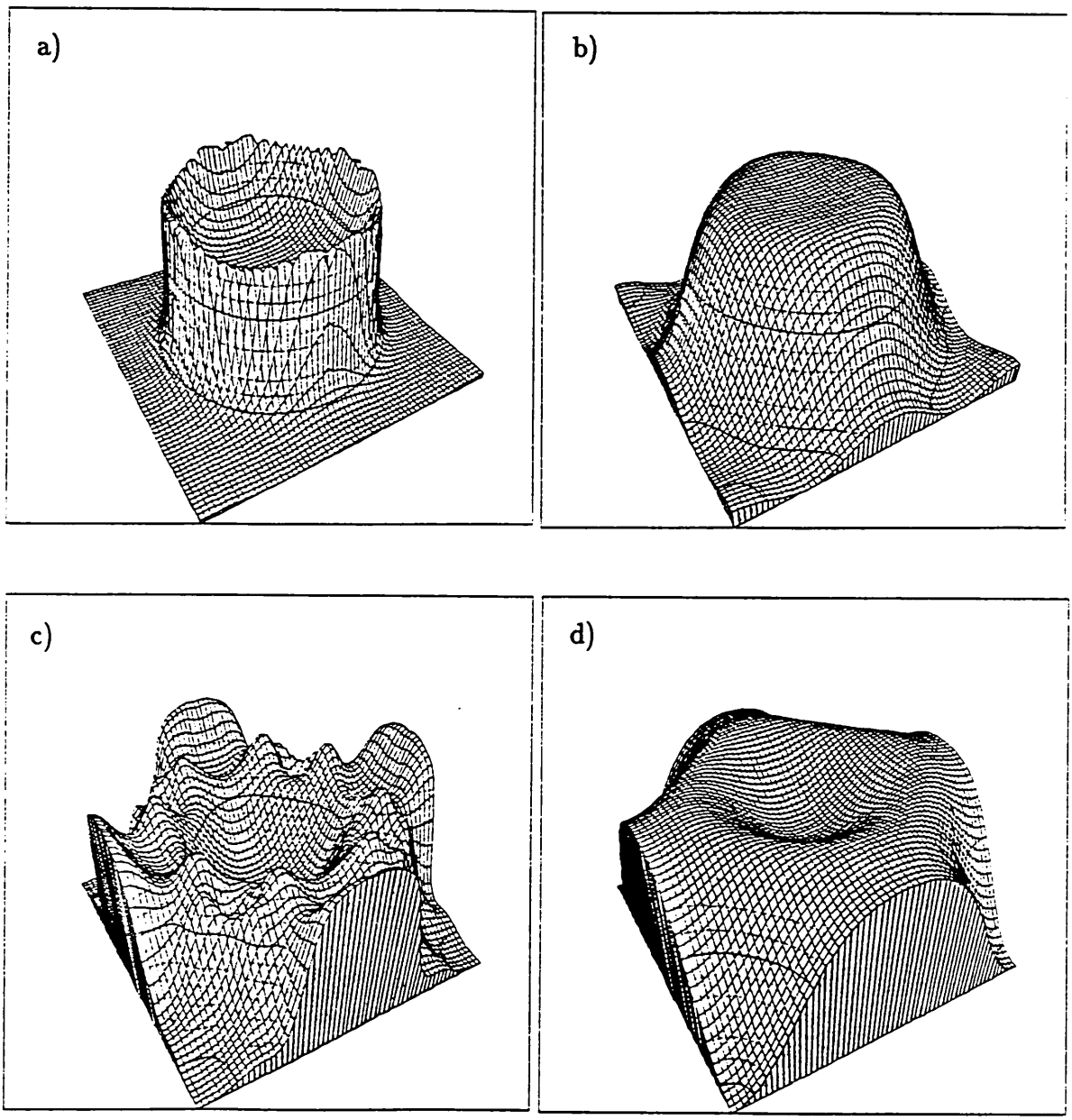

An additional consequence is that not only may one determine integrated quantities more efficiently with complex energies, but one may evaluate the density of states in the complex plane and extrapolate closer to the real real energy axis (Hass, Velicky and Ehrenreich, 1984; Eschrig, Richter and Velicky, 1986). Fitting the density of states evaluated at the imaginary energy Γ_1 to a complex rational function we may determine the corresponding density of states at the imaginary energy Γ_2 by extrapolation (Press, Flannery, Teukolsky and Vetterling, 1986); a rational function has the distinct advantage over a simple polynomial of being capable of reproducing the singular pole structure typical of Green functions near the real energy axis. In figure 3.10a are illustrated the real and imaginary components of the diagonal elements of the Green function evaluated at $\Gamma = 0.003$Ha integrated throughout the muffin–tin sphere

$$G(E) = \int_0^{R_{MT}} r^2 dr \int d\Omega G(\mathbf{r}, \mathbf{r}; E) \tag{3.3.10}$$

so $-\text{Im } G(E)/\pi$ is the normal muffin–tin density of states. The function is largely structureless, and typical of the resonant behaviour of the density of states within the *d* band. In figure 3.10b the muffin–tin density of states resulting from a high order rational extrapolation of this data to just 0.003Ha above the real energy axis is given, along with the original curve. At this imaginary energy all significant features of the $\Gamma = 0$ density of states as calculated by Moruzzi Janak and Williams (1978), and shown in figure 3.10c, may be identified. The benefit of this approach in calculating the density of states is that only 45 Brillouin zone sampling points were required in the evaluation of the results in figure 3.10a, which is an order of magnitude fewer than are normally required at 0.003Ha. Of course, the larger imaginary component of the energy has the effect that at any given energy the electron "experiences" less of the crystal structure, particularly long–range structure, since the wavefunction will decay with distance. Thus, typically more energy points are required if the extrapolation is to be accurate and not contain spurious details. Since the number of sampling points in the sets generated by Cunningham's algorithm escalate very rapidly, though, the play–off between more energy points and fewer $\mathbf{k}_{||}$ points usually leads to more rapid calculations. As a general rule if ΔE is the (real) separation of energy points in the original calculation, one should not extrapolate closer than ΔE to the real energy axis.

Figure 3.10 a). Energy dependence of the diagonal elements of the Green function integrated over the muffin–tin sphere, evaluated with imaginary energy 0.03Ha. b). Muffin–tin density of states for nickel at imaginary energy 0.003Ha, obtained by extrapolation *via* a rational polynomial fit, with the original data evaluated at 0.03Ha. c). Muffin–tin density of states for bulk nickel taken from Moruzzi, Janak and Williams (1978).

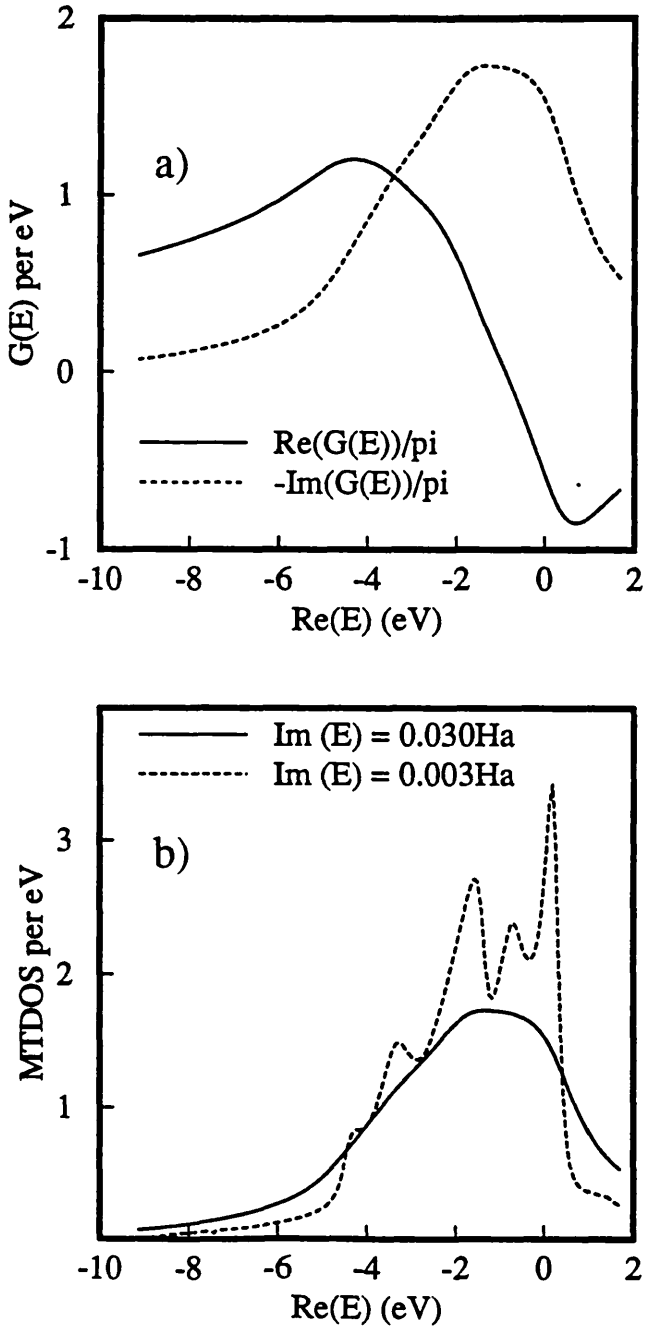

3.4 Solution of Poisson's equation for the muffin–tin potential

The charge within the muffin–tin sphere is given by

$$q^{\alpha}_{MT} = \int_{S^{\alpha}} \varrho^{\alpha}(r)dr = 4\pi \int_{0}^{R^{\alpha}_{MT}} r^2 dr \varrho^{\alpha}_{MT}(r) \tag{3.4.1}$$

The determination of the Fermi level requires an integral over the unit cell of the full charge density (3.3.2). Partitioning this volume into Wigner–Seitz polyhedra τ^{α}_{WS} centred upon each atomic site and consisting of the set of points closer to the atomic site than any other, we have $q^{total} = \sum_{\alpha} q^{\alpha}$ and

$$\begin{aligned} q^{\alpha} &= \int_{\tau^{\alpha}_{WS}} \varrho^{\alpha}(r)dr \\ &= \sum_{L} \int_{0}^{R_{max}} r^2 dr \varrho^{\alpha}_{L}(r) w^{\alpha}_{L}(r) \quad w^{\alpha}_{L}(r) = \int_{\Omega} Y_{L}(r)\theta(r \in \tau^{\alpha}_{WS})d\Omega(r) \end{aligned} \tag{3.4.2}$$

R_{max} represents the largest radii within the polyhedra. The integral for the weight function $w^{\alpha}_{L}(r)$ is over the solid angle for which r is within the Wigner–Seitz polyhedra. It may be evaluated by sampling many directions (Pindor, Temmerman and Györffy, 1983) and since it is purely structural, need only be determined once for each system. For close–packed materials, and also in many other cases, the atomic sphere approximation may be made in which the full cell integral (3.4.2) is replaced by one over the Wigner–Seitz sphere

$$q^{\alpha} \approx q^{\alpha}_{WS} = 4\pi \int_{0}^{R^{\alpha}_{WS}} r^2 dr \varrho^{\alpha}_{MT}(r) \tag{3.4.3}$$

The Wigner–Seitz radii are chosen so that all volume is occupied

$$\tau = \sum_{\alpha} \frac{4}{3}\pi \left(R^{\alpha}_{WS}\right)^3 \tag{3.4.4}$$

which is a unique prescription for elemental solids (1 unique atom) but not for poly-atomic crystals, in which case the Wigner–Seitz radii may be chosen in proportion to the muffin–tin radii. The accuracy of this approximation for close–packed crystals may be judged by comparison of the self–consistent results of Moruzzi, Janak and Williams (1978), in which a full cell integral was effected, and those given in this thesis (*e.g.* figures 3.6a,b), which used the Wigner Seitz sphere approximation. In particular, the position of the Fermi level may be expected to reflect any inaccuracy in this approximation.

The electrostatic potential arising from the charge density $\varrho(\mathbf{r})$ is given by the solution of Poisson's equation

$$-\nabla^2 V(\mathbf{r}) = 4\pi\varrho(\mathbf{r}) \tag{3.4.5}$$

The spherically–symmetric solution, when expanded about site α, is thus determined by the one dimensional problem

$$\frac{1}{r^2}\frac{d}{dr}\left(r^2\frac{d}{dr}V^\alpha(r)\right) = Z^\alpha\frac{\delta(r)}{r^2} - 4\pi\varrho^\alpha_{MT}(r) \tag{3.4.6}$$

which has the general solution

$$V^\alpha(r) = \frac{-Z^\alpha}{r} + \frac{4\pi}{r}\int_0^r r'^2\varrho^\alpha_{MT}(r')dr' + 4\pi\int_r^{R^\alpha_{MT}} r'\varrho^\alpha_{MT}(r')dr' + C^\alpha \tag{3.4.7}$$

The first term arises from the nucleus, atomic number Z^α. The second is due to the charge within the sphere of radius r, and the third from the spherical charge distribution within the muffin–tin but outside radius r. The last constant is a boundary condition on the potential within the sphere, and which depends upon the other atoms of the system. Two methods have been used for the determination of this constant in the work presented in this thesis.

3.5 Fourier solution

Atoms within the system are assigned to the three regions illustrated in figure 3.11a; bulk+ and bulk−, within which the atoms display semi-infinite periodicity (in position and charge), and an interface region of sufficient dimension to be charge neutral. Extending the bulk half-space charge densities through all space we have the Fourier expansions

$$\varrho^{\pm}(z,\mathbf{r}_{\|}) = \frac{1}{a^{\pm}\Omega}\sum_{\mathbf{G}^{\pm}}\varrho^{\pm}(\mathbf{G}^{\pm})e^{i\mathbf{g}.\mathbf{r}_{\|}}e^{ig_z^{\pm}(z\mp L)} \tag{3.5.1}$$

with $\mathbf{G}^{\pm} = (g_z^{\pm},\mathbf{g})$, $g_z^{\pm} = \frac{2n\pi}{a^{\pm}}$, $n = 0,\pm1,\pm2,\ldots$ and likewise for the interface region extended *ad infinitum*

$$\varrho^{0}(z,\mathbf{r}_{\|}) = \frac{1}{a^{0}\Omega}\sum_{\mathbf{G}^{0}}\varrho^{\pm}(\mathbf{G}^{0})e^{i\mathbf{g}.\mathbf{r}_{\|}}e^{ig_z^{0}z} \tag{3.5.2}$$

with $\mathbf{G}^{0} = (g_z^{0},\mathbf{g})$, $g_z^{0} = \frac{2n\pi}{a^{0}}$, $n = 0,\pm1,\pm2,\ldots$. The origins of the bulk+ and bulk− Fourier expansions are assumed to be at $z = +L$ and $z = -L$, respectively, whilst the interface Fourier expansion has origin at $z = 0$. $a^{\pm}$ and a^{0} are the repeat z spacings of the respective unit cells. A Fourier representation of the charge density, which possesses two-dimensional periodicity,

$$\varrho(k_z,\mathbf{g}) = \int_{-\infty}^{\infty}dz\varrho(z,\mathbf{g})e^{-ik_z z} \tag{3.5.3}$$

may be found using the step function

$$\Theta(x) = \lim_{\varepsilon\to0}\int_{-\infty}^{\infty}\frac{dk}{2\pi i}\frac{e^{ikx}}{k-i\varepsilon} = \begin{cases} 1 & x>0 \\ 0 & x<0 \end{cases} \tag{3.5.4}$$

along with the convolution theorem

$$\int_{-\infty}^{\infty}e^{-ik_z z}f(z)g(z)dz = \int_{-\infty}^{\infty}\frac{dk}{2\pi}f(k_z-k)g(k) \tag{3.5.5}$$

to extend the contributions from the three regions over all space. Hence we may write the full expansions as $\varrho(k_z,\mathbf{g}) = \varrho^{+}(k_z,\mathbf{g}) + \varrho^{0}(k_z,\mathbf{g}) + \varrho^{-}(k_z,\mathbf{g})$ where

$$\begin{aligned}
\varrho^{+}(k_z,\mathbf{g}) =& \int_{L}^{\infty}dz\varrho^{+}(z,\mathbf{g})e^{ik_z z} = \int_{-\infty}^{\infty}dz\Theta(z-L)\varrho^{+}(z,\mathbf{g})e^{-ik_z z} \\
=& \frac{-ie^{-ik_z L}}{a^{+}}\sum_{g_z^{+}}\frac{\varrho^{+}(\mathbf{G}^{+})}{k_z-g_z^{+}-i\varepsilon} \\
\varrho^{0}(k_z,\mathbf{g}) =& -\frac{i}{a^{0}}\sum_{g_z^{0}}\frac{\varrho^{0}(\mathbf{G}^{0})}{k_z-g_z^{0}-i\varepsilon}\left[e^{i(g_z^{0}-k_z)L} - e^{-i(g_z^{0}-k_z)L}\right] \\
\varrho^{-}(k_z,\mathbf{g}) =& \frac{ie^{ik_z L}}{a^{-}}\sum_{g_z^{-}}\frac{\varrho^{-}(\mathbf{G}^{-})}{k_z-g_z^{-}+i\varepsilon}
\end{aligned} \tag{3.5.6}$$

Figure 3.11 a). Schematic illustration of the geometry as used in solving Poisson's equation, showing repeat lengths and expansion origins. The darker atoms are those whose potentials would be allowed to change during a self–consistent interface calculation. **b).** "Dressing" the interface with bulk layers.

a)

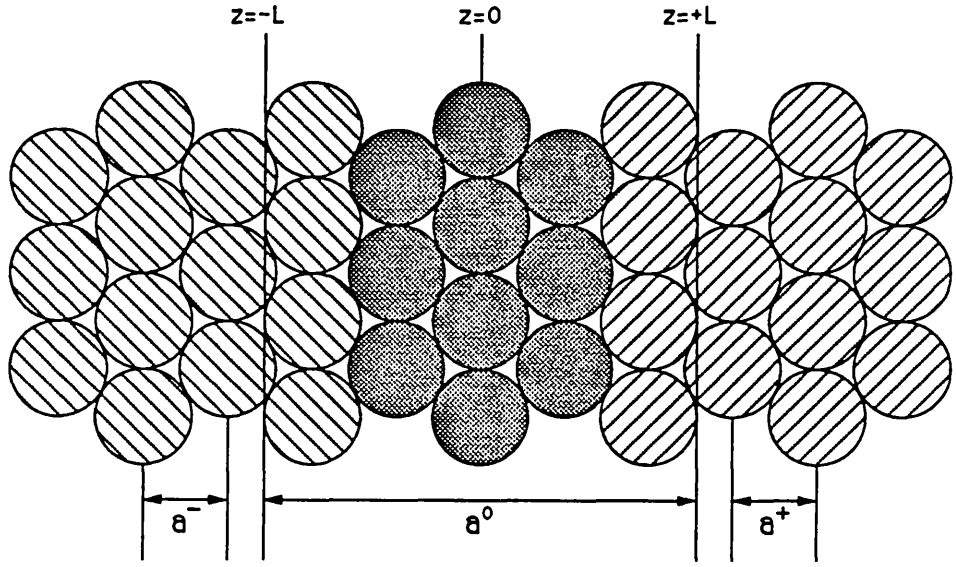

b)

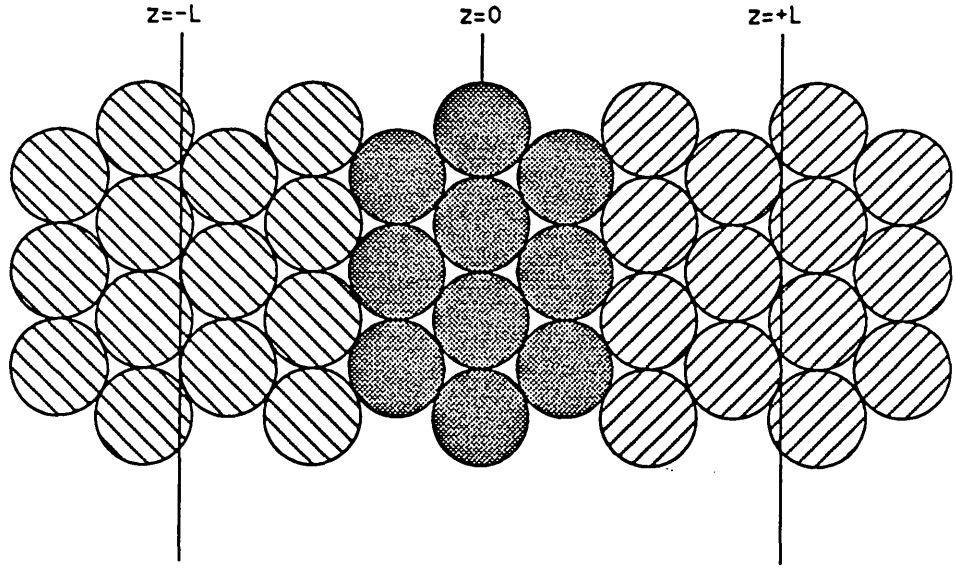

The potential follows immediately from Poisson's equation

$$\frac{V(r)}{4\pi} = \frac{1}{\Omega}\int \frac{dk_z}{2\pi}\sum_{g}\frac{\varrho(k_z,g)e^{ik_z z}e^{ig.r_{\|}}}{(k_z^2+g^2)} \tag{3.5.7}$$

Substituting in the contributions from the three regions we obtain *via* contour integration the following solution valid within the interface region $-L < z < L$. Writing $V(r) = V^+(r) + V^0(r) + V^-(r)$, we have

$$\begin{aligned}
\frac{V^+(r)}{4\pi} &= \sum_{g_z^+,g}\frac{\varrho^+(G^+)}{a^+\Omega}\left[\frac{e^{g(z-L)}e^{ig.r_{\|}}}{2g(g-ig_z^+ +\varepsilon)}\right] \\
\frac{V^0(r)}{4\pi} &= \sum_{g_z^0,g}\frac{\varrho^0(G^0)}{a^0\Omega}\left[\frac{e^{ig_z^0 z}}{(G^0)^2} - \left[\frac{e^{-ig_z^0 L}e^{-g(z+L)}}{2g(g+ig_z^0-\varepsilon)} + \frac{e^{ig_z^0 L}e^{g(z-L)}}{2g(g-ig_z^0+\varepsilon)}\right]\right]e^{ig.r_{\|}} \\
\frac{V^-(r)}{4\pi} &= \sum_{g_z^-,g}\frac{\varrho^-(G^-)}{a^-\Omega}\left[\frac{e^{-g(z+L)}e^{ig.r_{\|}}}{2g(g+ig_z^- +\varepsilon)}\right]
\end{aligned} \tag{3.5.8}$$

We choose the muffin–tin zero to be defined such that the average interstitial potential is zero as $z \to +\infty$. The potential in this limit is given by the bulk solution for the atoms in the + half space and in this region may be shown to be

$$V(r) = \frac{4\pi}{\Omega a^+}\sum_{G^+}\frac{\varrho^+(G^+)}{(G^+)^2}e^{iG.r}e^{-ig_z L} \tag{3.5.9}$$

Thus the constant added to the potential in all space is given by

$$\begin{aligned}
V_{mtz} &= -\frac{1}{\tau^{int}}\int_{\tau^{int}} V(r)dr \\
&= \frac{4\pi}{\Omega}\sum_{G^+,\alpha}\frac{\varrho^+(G^+)}{(G^+)^3}\frac{4\pi(R_{MT}^{\alpha})^2 j_1(G^+R_{MT}^{\alpha})}{a^+\tau^{int}}e^{iG^+.R_\alpha}e^{-ig_z L}
\end{aligned} \tag{3.5.10}$$

The sum is over all atoms α, located at $\mathbf{R}_\alpha$ (relative to an origin at $z = L$) within the bulk+ unit cell. Using equation (3.5.8) and expanding the solution about atomic site α within the interface region in an angular momentum basis, and evaluating the spherically symmetric term at the muffin–tin radius we get

$$\begin{aligned}
V_{00}^{\alpha} &= \frac{4\pi}{\Omega}\sum_{g}\left[\chi_\alpha^+(g) + \chi_\alpha^-(g)\right] \\
&\quad + \frac{4\pi}{\Omega}\left[\sum_{G_0} j_0(G^0R_{MT}^{\alpha})\frac{\varrho^0(G^0)e^{iG^0.r_\alpha}}{a^0(G^0)^2}\right] + V_{mtz}
\end{aligned} \tag{3.5.11}$$

with

$$\chi_{\alpha}^{\pm} = \left[\sum_{g_z^{\pm}} \frac{\varrho^{\pm}(G^{\pm})}{2ga^{\pm}(g \mp ig_z^{\pm})} - \sum_{g_z^0} \frac{\varrho^0(G^0)e^{\pm ig_z^0 L}}{2ga^0(g \mp ig_z^0)} \right] e^{-g(L \mp z_\alpha)} e^{ig.R_\alpha} \qquad (3.5.12)$$

This is to be compared with equation (3.4.7) evaluated at the muffin–tin radius, and thus

$$C^{\alpha} = V_{00}^{\alpha} + \frac{Z^{\alpha}}{R_{MT}^{\alpha}} - \frac{q_{MT}^{\alpha}}{R_{MT}^{\alpha}} \qquad (3.5.13)$$

The solution represented by equation (3.5.8) is a generalised full–potential solution of Poisson's equation in the interface/surface geometry with two dimensional translational periodicity (MacLaren, Vvedensky and Crampin, 1989). Using the ideas of Weinert (1981) the true charge density within each muffin–tin sphere is replaced by a smoother pseudocharge density, possessing a much more rapidly convergent Fourier expansion but which is characterised by the same multipole moments

$$q_L^{\alpha} = \int_0^{R_{MT}^{\alpha}} r^2 dr \int d\Omega Y_L^*(\Omega) r^{\ell} \varrho^{\alpha}(\mathbf{r}) \qquad (3.5.14)$$

This latter property ensures the solution of Poisson's equation within the interface region is the same as for the true charge density (Jackson, 1975), and this then acts as a boundary condition upon the surface of the muffin–tin, within which Poisson's equation may be easily solved for numerically using the true charge density. Hence the full solution is obtained over all space.

The muffin–tin components of the pseudo charge density required for evaluating (3.5.11–12) are given by (Weinert, 1981)

$$\varrho(G) = \sqrt{4\pi} \sum_{\alpha} \frac{(2n+3)!\,!\; j_{n+1}(GR_{MT}^{\alpha})}{(GR_{MT}^{\alpha})^{n+1}} q_{00}^{\alpha} e^{-iG.R_\alpha} \qquad (3.5.15)$$

where the sum extends over those atoms within the relevant half space unit cell or interface region and n is an arbritrary integer which controls the rate of convergence (5 has been found suitable).

3.6 Green function solution

The potential due to a spherical charge distribution is the same outside the region of charge as that of a point charge located at the centre, the value of the charge that of the total charge within the sphere. Hence, in the interstitial region, the muffin-tin solution to Poisson's equation is the same as that given by the Ewald problem (Ewald, 1921) with a background charge density $\langle\varrho\rangle$ and point charges q^α

$$\begin{aligned}\langle\varrho\rangle &= \frac{1}{\tau^{\text{int}}}\sum_\alpha [Z^\alpha - q^\alpha_{MT}] \\ q^\alpha &= Z^\alpha - q^\alpha_{MT} + \frac{4}{3}\pi(R^\alpha_{MT})^3\langle\varrho\rangle\end{aligned} \tag{3.6.1}$$

The spherically symmetric solution to this problem expanded about site α has been given by Slater and DeCicco (1963)

$$V^\alpha(r) = -\frac{q^\alpha}{r} - \frac{2}{3}\pi\langle\varrho\rangle r^2 + A^\alpha \tag{3.6.2}$$

In the interface problem we take the interstitial charge density to be that of the system as $z \to +\infty$. The charge density for the whole system (in the Ewald problem) may be expanded as

$$\varrho(r) = \frac{1}{\Omega}\int \sum_g \varrho(g, k_z) e^{ig\cdot r} e^{ik_z z}\frac{dk_z}{2\pi} \tag{3.6.3}$$

so that

$$\varrho(g, k_z) = \sum_\alpha q^\alpha e^{-ik_z z^\alpha} e^{-ig\cdot R^\alpha} \tag{3.6.4}$$

The potential may then be determined from

$$V(r) = \frac{2\pi}{\Omega}\int dk_z \sum_g \frac{\varrho(g, k_z)}{g^2 + k_z^2} e^{ig\cdot r} e^{ik_z z} \tag{3.6.5}$$

When $g \neq 0$ this expression may be evaluated by contour integration to give

$$V_1(r) = \frac{2\pi}{\Omega}\sum_{g\neq 0}\sum_\alpha q^\alpha e^{ig\cdot(r-R^\alpha)} e^{-g|z-z^\alpha|} \tag{3.6.6}$$

which may be evaluated in real space or by the usual Ewald split techniques when the convergence factor is small. The $g = 0$ solution can be determined from the differential equation

$$\frac{d^2}{dz^2}V_2(z) = -\frac{4\pi}{\Omega}[\varrho(z) - \langle\varrho\rangle\Omega] \tag{3.6.7}$$

where $\varrho(z)$ is the $g = 0$ Fourier coefficient of the charge density. The general solution of the equation is

$$V_2(z) = -\frac{4\pi}{\Omega}\left[\sum_\alpha q^\alpha \frac{|z - z^\alpha|}{2} - \Omega\langle\varrho\rangle\frac{z^2}{2} + Az + B\right] \tag{3.6.8}$$

where the summation is only over the interfacial atoms, and where A and B are constants fixed by the boundary conditions which we take to be that the solution evaluated on the atoms in the layers on either side of the interface are bulk like. The constant A^α in (3.6.2) then follows by taking the limit $\mathbf{r} \rightarrow \mathbf{R}_\alpha$ in (3.6.6) and (3.6.8) (MacLaren, 1989), and then matching (3.6.2) and (3.4.7) we have

$$C^\alpha = \frac{Z^\alpha}{R^\alpha_{MT}} - \frac{q^\alpha_{MT}}{R^\alpha_{MT}} - \frac{q^\alpha}{R^\alpha_{MT}} - \frac{2}{3}\pi\langle\varrho\rangle(R^\alpha_{MT})^2 + A^\alpha \tag{3.6.9}$$

The bulk solution may be obtained for matching by this method. The Ewald solution averages to zero over the unit cell and so the constant, V_{mtz}, added to the solution to make the average interstitial potential zero can be shown to be

$$V_{mtz} = \frac{2\pi}{3\tau^{int}}\sum_\alpha\left[3(R^\alpha_{MT})^2 q^\alpha + \frac{4}{5}(R^\alpha_{MT})^5\langle\varrho\rangle + 2(R^\alpha_{MT})^3 A^\alpha\right] \tag{3.6.10}$$

For the bulk problem periodicity allows us to solve for $V_2(z)$ (MacLaren, 1989)

$$V_2(z) = \frac{\pi}{\Omega}\sum_\alpha q_\alpha\left[\frac{(z - z_\alpha)^2}{2} - 2|z - z_\alpha| + \frac{c}{3}\right] \tag{3.6.11}$$

with c the repeat z spacing of unit cells.

3.7 Discussion

Both solutions have been found to give reasonable answers in a variety of interface problems. The two solutions differ slightly, in that the boundary condition upon the interface atoms within the Fourier solution are found by matching to bulk values at $\pm\infty$, whilst the Green function solution matches to bulk values on the first bulk atoms outside the chosen interfacial region. The Fourier solution is much more cumbersome to evaluate, with the convergence of the many nested summations awkward to monitor, whilst the Green function solution is much more rapid. Largely for this reason, and because the interfacial region for the solution of Poisson's equation may always be "dressed" by several bulk layers so the difference between matching at infinity or just outside the interface region is largely immaterial (figure 3.11b), the Green function solution is preferred.

A second point worthy of comment is the necessity of charge neutrality within the interface region. An implicit assumption within the two solutions is that the $\mathbf{G} = \mathbf{0}$ Fourier coefficient for the interface region is zero, which is equivalent to the statement that the net charge of the interface region, given by

$$dq = \sum_{\alpha} [Z^{\alpha} - q^{\alpha}_{MT}] - \langle \varrho \rangle \tau^{int} \tag{3.7.1}$$

is zero. In an interface calculation between similar materials (stacking fault, grain boundary), the Fermi energy is pinned to the value of the bulk half spaces, and charge neutrality is not guaranteed. Experience has shown that the solution of Poisson's equation is stable under small charge excess/deficit, and indeed the potential appears to move toward neutralising any charge imbalance. Within a muffin–tin formulation true charge neutrality is difficult to obtain since it requires the interstitial charge density for both the interface region and the two bulk half spaces to be identical, in general an unlikely event. Consequently it is necessary to ensure that the interfacial region is sufficiently large for dq to be reasonably small, and in the case of calculations in which there is a large increase in the interstitial volume (*e.g.* grain–boundary or cleavage problem) it is probably advisable to include empty spheres (muffin–tin spheres without a nucleus at the centre) to redress the balance. A measure of the required charge neutrality within the context of total energy calculations can be judged by considering the product of the charge imbalance and the Fermi energy, $dq \times E_f$, which is approximately the error to the band contribution to the total energy assuming the excess/deficit of states are taken from near the Fermi level. If this quantity is significant in relation to the

energy differences within the problem, then care must be taken in the interpretation of results. Two possible schemes to account for the lack of charge neutrality are to scale the charge density uniformly to remove the charge imbalance

$$\varrho^{\text{scaled}}(\mathbf{r}) = \varrho(\mathbf{r}) \times \left\{ \sum_{\alpha} Z^{\alpha} / \int_{\tau} \varrho(\mathbf{r}) d\mathbf{r} \right\} \tag{3.7.2}$$

which re–distributes states across the whole valence band, or alternatively to "float" the Fermi level within the interface region to ensure charge neutrality by the manipulation of the states at the Fermi level. Both methods are somewhat unsatisfactory, and at present it is not possible to state which gives the best results. The development of a full potential version of the layer code will hopefully go some way to removing any such problems.

To be added to the Coulomb potential found from the solution of Poisson's equation is the exchange–correlation potential (equation (1.1.5)) for which the Slater Xα approximation and the Hedin–Lundquist (Hedin and Lundquist, 1971) forms have been used. The new potential may not be directly used as input to the following iteration, the strong Coulomb forces tending to overcorrect for charge imbalance and leading to huge charge oscillations and numerical instability if such a philosophy is followed. Instead, a simple mixing scheme is employed,

$$V_{\text{new}}(\mathbf{r}) = V_{\text{old}}(\mathbf{r})(1 - \beta) + \beta V_{\text{calc}}(\mathbf{r}) \tag{3.7.3}$$

where V_{calc} is the calculated potential, and V_{old} (V_{new}) the previous (next) potentials used to determine the charge density. β is a mixing parameter of the order of 30–50% for bulk systems but 1% or even lower for interface calculations, where charge neutrality is not guaranteed. It is noted that more elaborate schemes have been proposed for the acceleration of the self–consistent convergence cycle (*e.g.* Srivastava, 1984, and references therein), which, although requiring the storage of several previously generated potentials or charge densities and thus increasing memory requirements, offer the possibility of significant savings in run time.

3.8 Total energy

The total energy of the solid consisting of interacting electons and (frozen) ions is given by

$$E = T + U + E_{xc} \tag{3.8.1}$$

where

$$T = \sum_i \int \psi_i^*(r) \left(-\frac{1}{2}\nabla_r^2\right) \psi_i(r) dr \tag{3.8.2a}$$

$$U = \int\int \frac{\varrho(r)\varrho(r')}{|r-r'|} dr dr' - \sum_R Z_R \int \frac{\varrho(r)}{|r-R|} r' + \sum_{\substack{R,R' \\ R \neq R'}} \frac{Z_R Z'_R}{|R-R'|} \tag{3.8.2b}$$

$$E_{xc} = \int \varrho(r)\epsilon_{xc}(\varrho(r)) dr \tag{3.8.2c}$$

The sum over levels in (3.8.2a) is over the occupied states; the integrals extend over all space and the summations in (3.8.2b) over atomic sites. The local density approximation has been used in (3.8.2c), the exchange correlation energy, which is actually *defined* as the difference between the exact energy and the sum of (3.8.2a) and (3.8.2b).

Within the muffin–tin model and the atomic sphere approximation these terms may be evaluated from (Janak, 1974; Skriver, 1984)

$$\begin{aligned} T &= \int_{-\infty}^{E_f} E\varrho(E) dE - \int_\tau V(r)\varrho(r) dr \\ &= \sum_\alpha \left[\sum_{c_\alpha} 2(2\ell_{c_\alpha}+1) E_{c_\alpha} - \frac{1}{\pi} \sum_i \mathrm{Im} \left\{ w_i \int_{\tau_\alpha} G(r,r';E_i) d\tau_\alpha \right\} \right. \\ &\quad \left. - 4\pi \int_0^{R^\alpha_{MT}} r^2 \varrho^\alpha_{MT}(r) V^\alpha(r) dr \right] \end{aligned} \tag{3.8.3a}$$

$$\begin{aligned} U = \sum_\alpha \left[(4\pi)^2 \int_0^{R^\alpha_{MT}} \left\{ \varrho^\alpha_{MT}(r) \int_0^r dr' r'^2 \varrho^\alpha_{MT}(r') \right\} r dr \right. \\ \left. - 4\pi Z^\alpha \int_0^{R^\alpha_{MT}} r\varrho^\alpha_{MT}(r) dr - \frac{1}{2}(Z^\alpha - q^\alpha_{MT}) C^\alpha \right] \end{aligned} \tag{3.8.3b}$$

$$E_{xc} = \sum_\alpha 4\pi \int_0^{R^\alpha_{MT}} \varrho^\alpha_{MT}(r)\epsilon_{xc}(\varrho(r)) r^2 dr + \Omega^{int} \langle\varrho\rangle \epsilon_{xc}(\langle\varrho\rangle) \tag{3.8.3c}$$

whilst the pressure, P, may be evaluated from (Janak, 1974)

$$3\tau P = 2\sum_{\alpha}\left[-\frac{1}{\pi}\sum_{i}\mathrm{Im}\left\{w_i\int_{\tau_\alpha} G(\mathbf{r},\mathbf{r}';E_i)d\tau_\alpha\right\} - 4\pi\int_0^{R^\alpha_{MT}} dr\, r\varrho_v(r)\frac{d}{dr}\left(r^2V(r)\right)\right.$$
$$-\frac{1}{2}\left(Z^\alpha - q^\alpha_{MT}\right)C^\alpha - 3\tau^{int}\langle\varrho\rangle\left[\varepsilon_{xc}(\langle\varrho\rangle) - \mu_{xc}(\langle\varrho\rangle)\right]$$
$$\left.-4\pi(R^\alpha_{MT})^3\varrho(R^\alpha_{MT})\left[\varepsilon_{xc}\left(\varrho(R^\alpha_{MT})\right) - \mu_{xc}\left(\varrho(R^\alpha_{MT})\right)\right]\right] \qquad (3.8.4)$$

$\varrho_v(r)$ is the muffin–tin radial charge density due to the valence electrons.

Figure 3.12 shows the variation of energy and pressure under a symmetry–preserving expansion/contraction of the face–centred cubic lattice for aluminium, and is typical of a variety of lattice–constant tests which have been performed on face–centred cubic metals to monitor the accuracy of the LKKR code. This calculation used 13 g vectors in the plane wave basis set, phase shifts up to $\ell = 2$ and the muffin–tin radii were scaled to touch in each calculation. These parameters are the same as those used in the stacking fault calculations presented in Chapter 4. In this particular case the energy is minimised when $2 \times R_{MT} = 5.36$ au, in very good agreement with the bulk KKR result of Moruzzi, Janak and Williams (1978), who get a result of 5.37. The pressure at this lattice constant is about -9Kbar, reasonable close to zero. This level of agreement, considering very different expressions for the energy and pressure, is very encouraging, illustrating that the LKKR technique is as accurate as the bulk counterpart.

Figure 3.12 Lattice constant test for aluminium, with changes in energy and pressure monitored under a symmetry preserving scaling of the bulk unit cell.

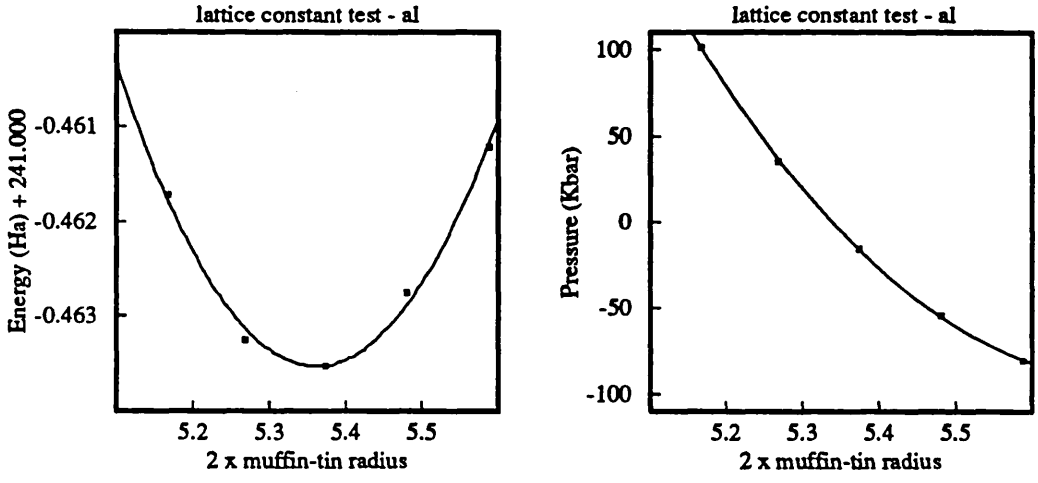

3.9 Band structure

Partitioning the system into layers provides a natural method for the calculation of the bulk band structure $\mathbf{K}(E)$ both on the real $\mathbf{K}$ axis of conventional calculations *and* into the complex plane, where information regarding the nature of localised states may be found (Heine, 1963).

The band structure is determined by applying the Bloch condition across the repeat unit of the system. If $T^{\pm\pm}$ represents the (plane wave) scattering matrices of the repeat unit, formed from the scattering matrices of the atomic layers *via* repeated use of the layer coupling equations (2.8.7), then we may write the following two conditions relating the amplitudes of the wavefunctions across the i^{th} unit (figure 3.13)

$$\begin{aligned}\Psi_{i+1}^{+} &= \Psi_i^{+} P_i^{+} T^{++} + \Psi_{i+1}^{-} T^{-+} \\ \Psi_i^{-} &= \Psi_i^{+} P_i^{+} T^{+-} P_i^{-} + \Psi_{I+1}^{-} T^{--} P_i^{-}\end{aligned} \tag{3.9.1}$$

with $\Psi_i^{\pm}(\mathbf{r}) = \sum_{\mathbf{g}} a_{\mathbf{g}}^{i\pm} \exp \imath \mathbf{K}_{\mathbf{g}}^{\pm} \cdot (\mathbf{r} - \mathbf{c}_i)$, the plane wave expansion valid in the interstitial region. Applying the Bloch condition to relate $\Psi_i^{\pm}$ and $\Psi_{i+1}^{\pm}$ the following generalised eigenvalue problem may be formulated, where $\mathbf{c}$ is the repeat

Figure 3.13 Schematic illustration of the wavefields in the band structure problem.

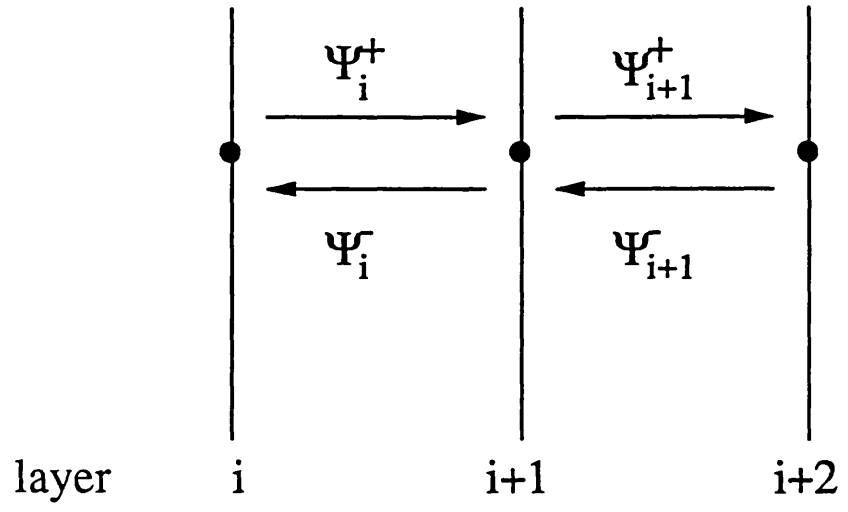

vector across the repeat unit of scatterers, and from which the band structure $\mathbf{K}(E)$ may be determined (Wood and Pendry, 1973)

$$(\Psi^+ \quad \Psi^-)\begin{pmatrix} P^+T^{++} & -P^+T^{+-}P^- \\ 0 & 1 \end{pmatrix} = e^{i\mathbf{K}\cdot\mathbf{c}}(\Psi^+ \quad \Psi^-)\begin{pmatrix} 1 & 0 \\ -T^{-+} & T^{--}P^- \end{pmatrix} \tag{3.9.2}$$

Unlike conventional calculations, the problem is solved at fixed $E, \mathbf{k}_{||}$ and the resulting k_z evaluated. The conventional band structure is given by the real k_z solutions. At a planar defect, states within the interface region will be matched to the complete set of states within the bulk half spaces with the same $E, \mathbf{k}_{||}$. The k_z will in general be complex, and correspond to the solutions of the eigenvalue problem, (3.9.2). The analytic structure of the real–energy bands has been discussed in some detail by Heine (1963). Of particular note is the observation that the spatial decay of the wavefunction when no real k_z solutions exist will be governed by the magnitude of the the imaginary component of the complex k_z eigenvalues.

As well as providing important information with regard to the electronic structure of bulk and interface systems, the band structure provides a stringent test of the calculation of the layer scattering matrices. Figure 3.14 illustrates a small section of the band structure for Ni calculated using the equations above.

Figure 3.14 A small part of the nickel band structure calculated from the eigenvalue problem (3.9.2).

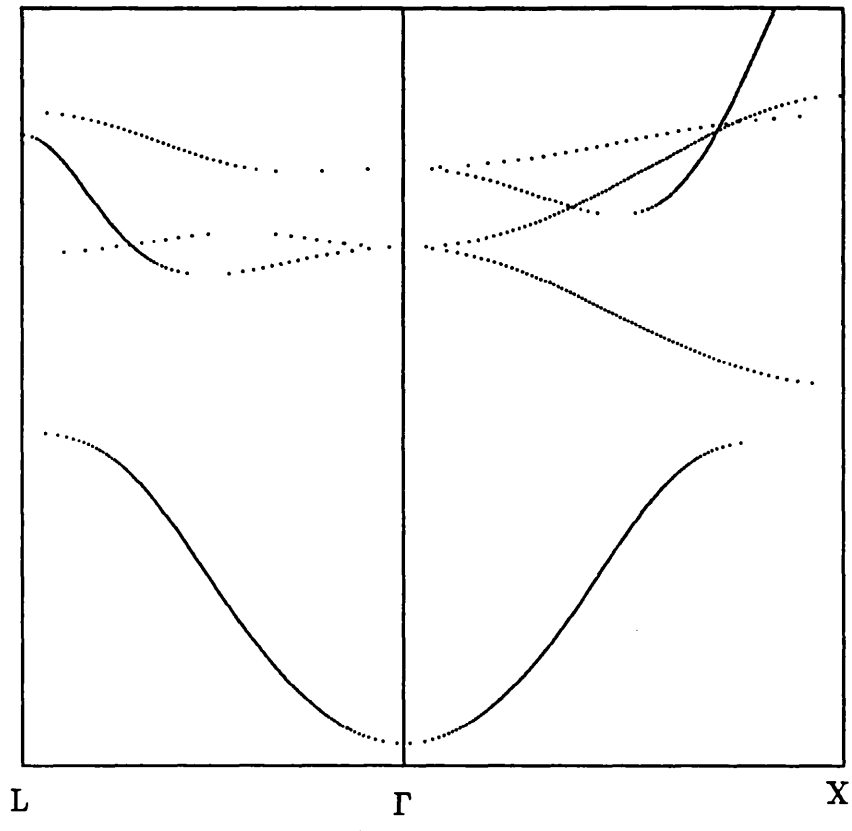

3.10 Projected band structure

For systems of reduced symmetry, for which the layer KKR approach has been developed, the normal band structure becomes projected onto a two-dimensional analogue, with the effectively infinite repeat distance in the **z** direction resulting in a Brillouin zone with no k_z dimension. This projected band structure is, like the conventional band structure, normally illustrated by displaying the projected bands along high symmetry lines within the irreducible two dimensional Brillouin zone. Its importance for the electronic description of both surfaces and interfaces lies in the possibility of the identification of regions of E-**K** space where extended states exist and hence pointing out pockets where localised states may be present. It is an intrinsic property of the bulk material.

Within the formalism presented here this projected band structure may be obtained by solving the eigenvalue problem stated above for various $E, \mathbf{k}_{||}$ throughout the two dimensional Brillouin zone and searching for any Bloch solutions with a real k_z component, corresponding to extended electron states. Regions where only complex k_z exist are regions of $(E, \mathbf{k}_{||})$ space where electrons within an interface or at a surface will be unable to couple to solutions in the bulk half space which extend over any great distance. Any such electrons will be localised, the wavefunction amplitude decaying off with distance. In fact, even within regions where extended states do exist electron states may be localised due to the surface or interface, if they correspond to a different symmetry than the extended states and hence are unable to couple. An example is the Δ_1 surface state found on the (100) face of molybdenum, which occurs in the hybridisation gap where only states of Δ_2, $\Delta_{2'}$ and Δ_5 symmetry exist (Inglesfield, 1982). Localised states may extend into regions of $(E, \mathbf{k}_{||})$ space where extended states exist, and still show up strongly as resonances. The symmetrised projected band structure may be obtained by classifying the wavefunctions corresponding to the extended states with real k_z determined from the eigenvalue problem by their point groups within the two dimensional Brillouin zone.

An alternative method of determining the projected band structure is to evaluate the density of states for the bulk crystal along lines of constant $\mathbf{k}_{||}$ on the faces of the irreducible Brillouin zone. The absence of extended states implies zero density of states in the bulk problem. In order to resolve the band edges sharply only a small imaginary component is used (typically 1×10^{-5}Ha; zero imaginary energy cannot be used with the layer doubling algorithm), since the imaginary energy will broaden the states into regions forbidden on the real energy axis. As there is no Brillouin zone sampling the projected band structure may be determined rapidly. Figure 3.15 illustrates the density of states so determined for the $\Gamma - K$ face of the irreducible Brillouin zone of the (111) crystal orientation of Al. The symmetrised band structure may be determined by decomposing the density of states into its irreducible components.

Both methods outlined above may be used to evaluate the projected band structure, but a third method has been found most rapid. The perturbation scheme used to evaluate the reflectivities does not converge on the real energy axis in the presence of extended states, since an incident wavefield may be decomposed into a "travelling" component, linear combinations of the eigenstates of the bulk repeat system of layers with real k_z, and a "decaying" component, containing the rest. For any finite slab of layers the travelling componant will pass

Figure 3.15 Muffin–tin density of states evaluated at various constant $\mathbf{k}_{||}$ between the Γ and K points of the irreducible Brillouin zone of the (111) face of aluminium, illustrating the projected band structure.

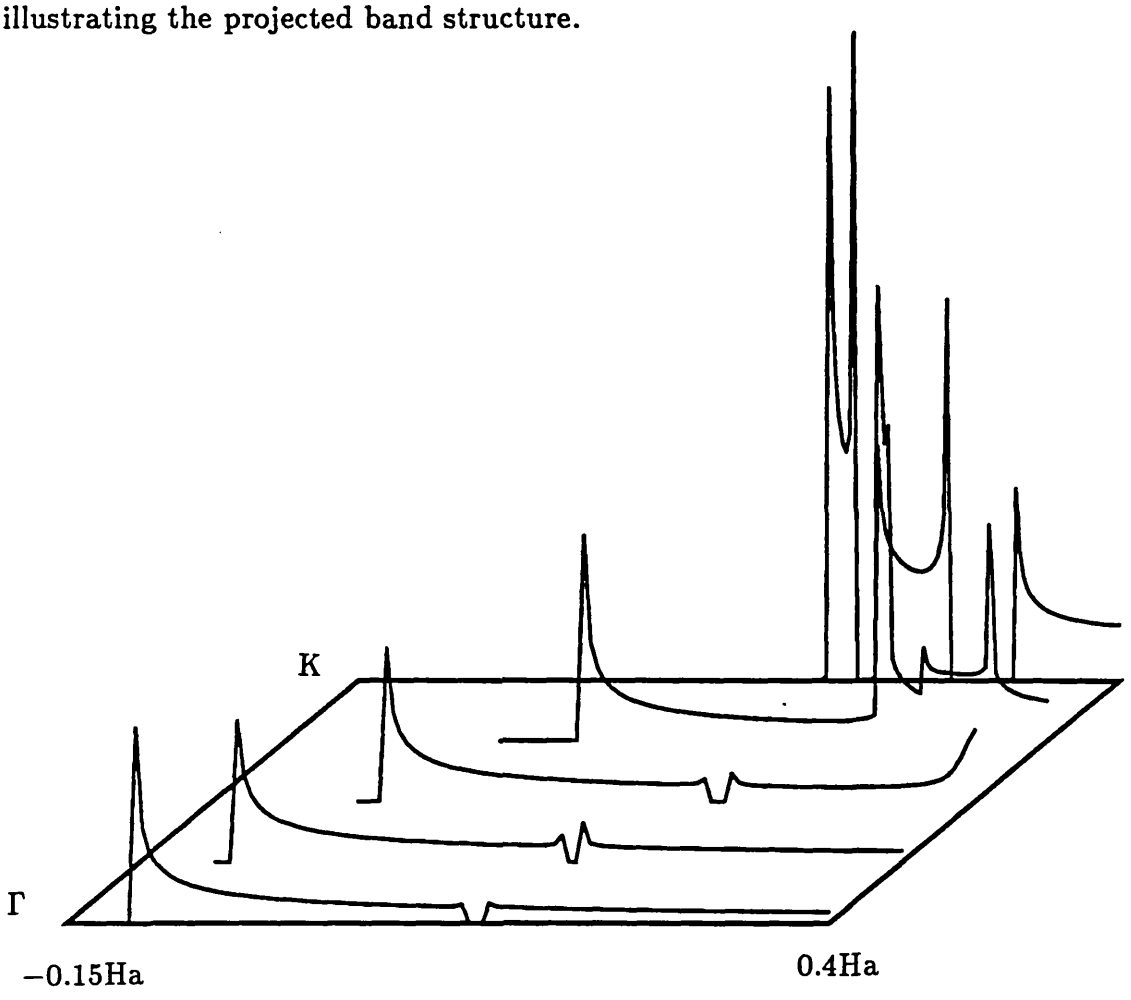

through undamped, and hence may scatter off any additional layers on the far side into a travelling wave with opposite k_z which then propagate back. Thus the contribution from this furthest layer is non zero and the reflectivity of the finite slab is not independent of the last layer added, which is the condition used for its determination. The convergence of the layer doubling or "tripling" algorithm may be monitored by evaluating the largest relative change in the matrix elements of the reflection matrix after each pass. For example, for the plane wave case we may monitor

$$S_n = \max\left[\frac{R^n_{gg'} - R^{n-1}_{gg'}}{R^{n-1}_{gg'}}\right] \qquad (3.10.1)$$

Figure 3.16 Convergence of the elements of the reflection matrix with the number of passes through the layer doubling algorithm for nickel. Continuous line E = $0.1+0.0i$ (all energies in Ha) where extended states exist. Long dash E = $0.1+1\times 10^{-5}i$ showing convergence. Short dash E = $0.2+0.0i$ where no extended states exist.

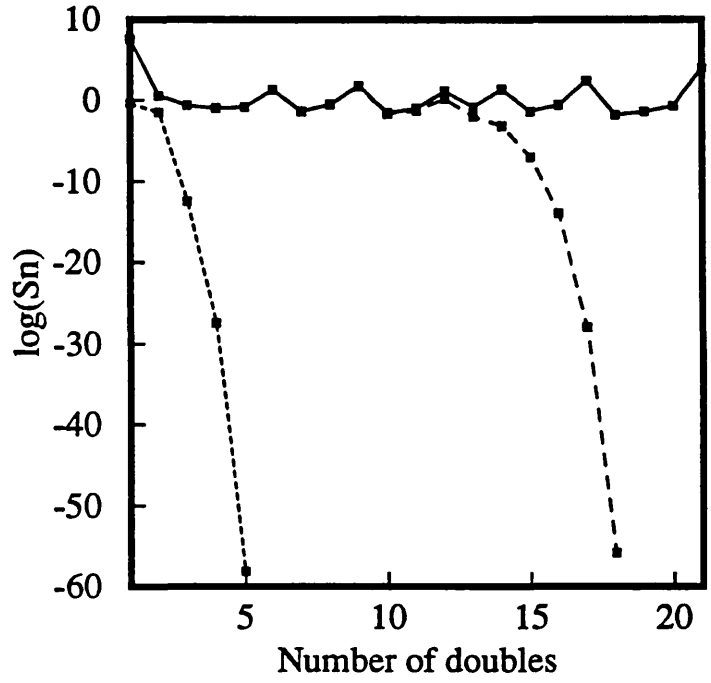

where R^n is the reflection matrix after n doublings. Figure 3.16 charts this quantity for the (111) face of Ni, at the Γ point of the two dimensional Brillouin zone with $k_{||} = (0,0)$. The short dashed line is $\log S_n$ evaluated at E = $0.2+0.0i$Ha, an energy at which no extended states exist. The reflection matrix has converged after only 5 doubles, or when 32 layer have been stacked. The solid dashed line is evaluated at E = $0.1+0.0i$Ha. Extended states occur at this energy, and it is evident that the reflection matrix is not converging. Even after 21 doubles or 2×10^6 layers there is no indication of convergence starting. However, adding a small imaginary part so E = $0.1+1\times 10^{-5}i$Ha results in the reflection matrix converging after 18 passes through the doubling algorithm. The number of doubles that will be required in the presence of extended states may be determined approximately by assuming the wavefunction decays as $\exp -(\Gamma n\Delta z)$, with Γ the dissipative component of the energy, Δz the layer–layer z separation and n the number of layers.

We may therefore determine the projected band structure by attempting to converge the half space reflection matrices on the real energy axis, those energies at which S_n falls to zero corresponding to gaps in the projected band structure. The symmetrised band structure may be determined by checking linear combinations of the elements of the reflection matrix transforming as the various irreducible representations of the full point group.

In figure 3.17a the projected band structure determined for the (111) face of aluminium by this method is illustrated. This is is excellent agreement with various other calculations which have presented this information, such as that taken from Caruthers, Kleinman and Alldredge (1974) in figure 3.17b.

3.11 Localised states

The existence of regions of $(E, k_{||})$ space within which no extended states of a given symmetry exist allows for the presence of localised states which decay with distance into the bulk half spaces. Surface states have been found to be a common occurrence, and the agreement between theory and experiment in their location and description provides strong support for the validity of theoretical calculations of surface electronic structure. Their importance in determining the structural properties of the surface has been emphasized by various authors. Interfacial states have been less well studied both theoretically and experimentally, although their importance to electronic and mechanical properties have also been noted.

The presence of interface states within the layer KKR formalism may be identified by searching $(E, k_{||})$ space till the following condition is satisfied

$$\det\left[1 - R^{I+1}L^{I-1}\right] = 0 \qquad (3.11.1)$$

which is obtained by requiring a non trivial solution of the self–consistent requirement

$$\Psi_I^+ = \Psi_I^- L^{I-1} \qquad \Psi_I^- = \Psi_I^+ R^{I+1} \qquad (3.11.2)$$

(all propagators have been ignored) which must be satisfied by the wavefunction of the localised state within the interface region. A similar line of argument may be used to obtain the condition for surface states (Pendry, 1974). Equation (3.11.1) is a complex determinantal equation, the zeros of which are difficult to locate. An alternative method which has proved more suitable for determining the presence of localised states is to evaluate the density of states within the gap of the projected band structure, first with a reasonably large dissipative component so that the localised states are not missed with the energy grid used, and then with a smaller imaginary energy to more precisely determine their location. The localised state

Figure 3.17 a). Two dimensional projected band structure for Al(111) evaluated by attempting to converge the bulk reflection matrix on the real energy axis. A square indicates the layer doubling procedure failed to converge at that $(E,k_{||})$. b). Two–dimensional projected band structure for Al(111) from Caruthers, Kleinman, and Alldredge, 1974.

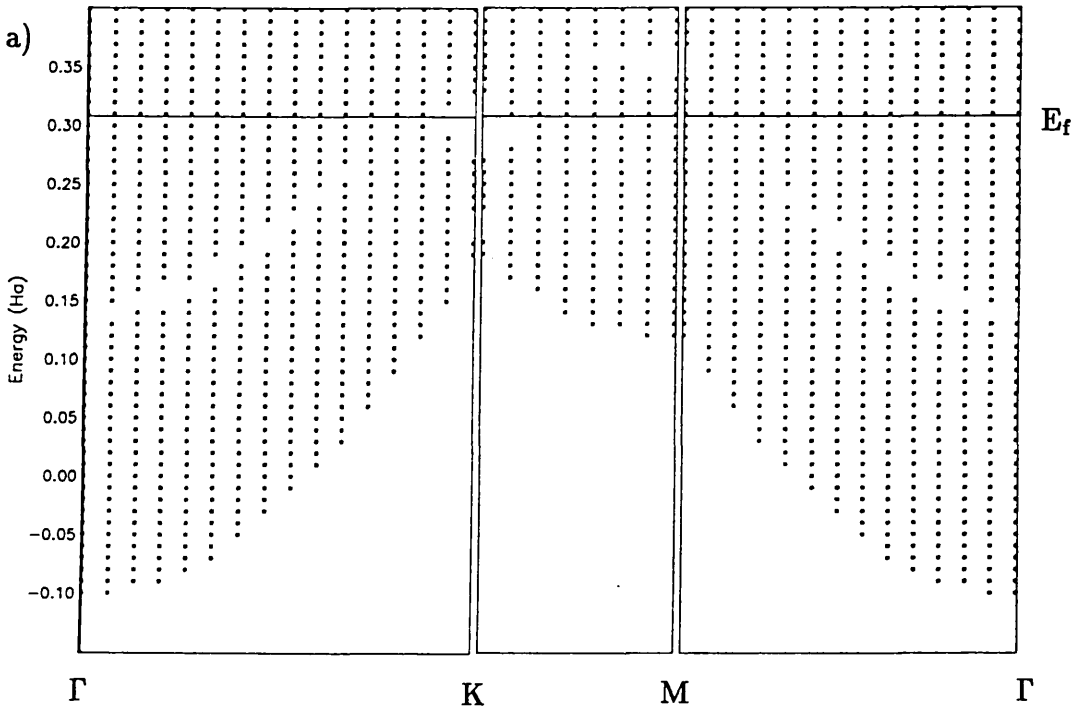

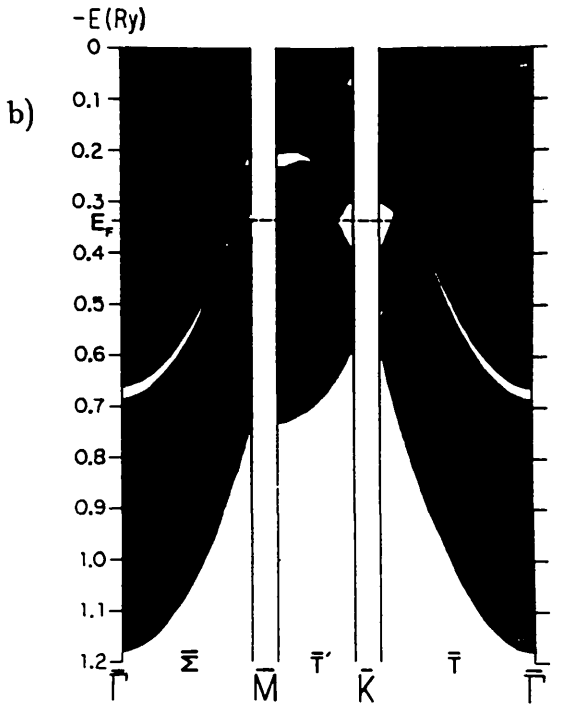

is characterised by a very sharp peak in the density of states, illustrated in figure 3.18. This shows the muffin-tin density of states at the K point of the Brillouin zone (figure 3.1) of a copper twin fault (see next Chapter for the structure) and contains two localised states at E=0.2193Ha and E=0.2365Ha, within gaps in the bulk density of states. Figure 1.1 also illustrates localised states for an intrinsic fault in copper, the locations of all these states corresponding well in *relative* position with those found for similar faults in nickel by Grise, Kleinman and Mednick (1980). The imaginary energy necessary to resolve the presence of the state for a given grid of energy points may be estimated by assuming the state is broadened in a similar fashion to the core level in figure 3.5.

Figure 3.18 Localised states at the K point of a twin fault in copper appearing as singular peaks in the density of states at E=0.2193Ha and E=0.2365Ha.

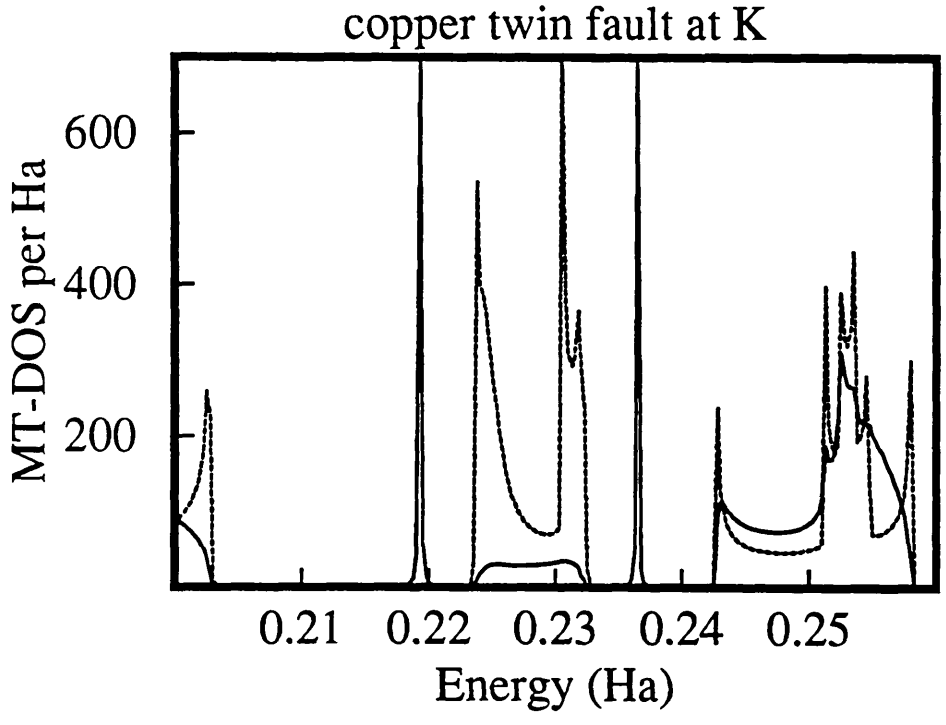

3.11 Basis set convergence

Of crucial importance in the practical use of the layer KKR formalism is the question of the basis set convergence, and in particular the size of the plane wave basis set necessary, since the angular momentum basis in both the plane wave and combined plane wave/partial wave formulations of Chapter 2 is truncated by the atomic scattering properties of the muffin-tin potential. This convergence is now illustrated, and numerical data demonstrating the need for the close spaced layer formulation.

For a given choice of crystal direction in which the stacking of layers is performed, we have a set of reciprocal lattice vectors $\{\mathbf{g}\}$ which forms the plane wave basis through the interlayer expansion vectors $\exp i\mathbf{K}_{\mathbf{g}}^{\pm} \cdot \mathbf{r}$. In solving the band structure problem, to preserve symmetry (eigenvalue degeneracy) it is necessary that the basis set chosen contain complete sets of symmetry related $\mathbf{g}$ vectors. This is also true for the determining the charge density, and since the basis set attenuation depends upon $|\mathbf{g}|$ it is consistent to include all $\mathbf{g}$ vectors with $|\mathbf{g}| \leq g_{max}$, g_{max} being the cutoff used. Thus for the (111) direction in FCC crystals we are restricted to a choice of basis set sizes 1,7,13,19,31,..., and for FCC or BCC (100) the sizes 1,5,9,13,17,21,25,...

Figure 3.19 Muffin-tin density of states for bulk copper evaluated with a plane wave basis set of 7, 13 and 19 g vectors.

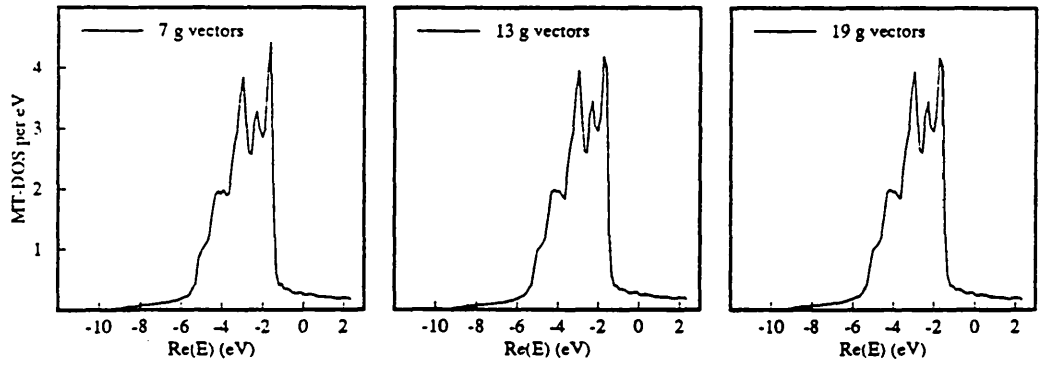

In practice a remarkably small number of vectors are required. Using just the $g = (0,0)$ component is not practical since, being rotationally invariant, coupling with the intralayer basis is severely restricted. However, as illustrated in figure 3.19, the density of states for Cu evaluated with the layers stacked along the (111) direction shows only minor differences when calculated with 7 and 13 g vectors, slightly different structure being present at about -4.0eV and the peak at the top of the d band, at -1.75eV, being shifted and as a consequence of a fairly course energy grid appears much sharper with 7 g vectors. The agreement between 13 and 19 g vectors is excellent.

Figure 3.20 displays the convergence of particular values of the density of states as a function of plane wave basis set size, the values being plotted as the ratio to the value calculated with the largest basis set size. Figures 3.20a and 3.20b were determined along the FCC (111) direction where the z spacing of adjacent layers is large, and the purely plane wave basis suitable for treating the interlayer scattering. 13 g vectors have converged the density of states to about 0.1%. Figures 3.20c and 3.20d are likewise calculated with the plane wave formulation, but correspond to the FCC (210) direction which comes under the classification of close–spaced. As many as 47 g vectors are insufficient to converge the density of states, and which shows no sign of converging. This is the behaviour alluded to in the previous Chapter. To be contrasted with this are the results shown in 3.20e and 3.20f, which are calculated using the close–spaced formulation for the same structure. We now find the density of states is sufficiently converged with only 15–20 g vectors in the plane wave basis.

To accompany the density of states results, figure 3.21 contrasts the relative calculation time for the two codes as the plane wave basis set dimensions increase. Although the close–spaced theory takes significantly longer than the purely plane wave treatment for a given number of plane wave vectors, the important point to note is that the time taken with 15–20 g vectors for the converged close–spaced solution is comparable to the calculation time using 30–35 g vectors with the plane wave solution, and which is clearly an inadequate number from the results shown in figure 3.20. Hence the close spaced formulation has greatly increased the ability to study systems with closely spaced layers.

A final comment is required with regard to the calculation of interface energies by the layer KKR method, which depends upon a large cancellation of errors. The absolute energies determined for a given system contain errors from a variety of sources, including the local density approximation, the muffin–tin approximation, Brillouin zone integrals and basis set truncation. In general it is to be expected

Figure 3.20 Convergence of the density of states with the dimension of the plane wave basis. See text for explanation of a)–f).

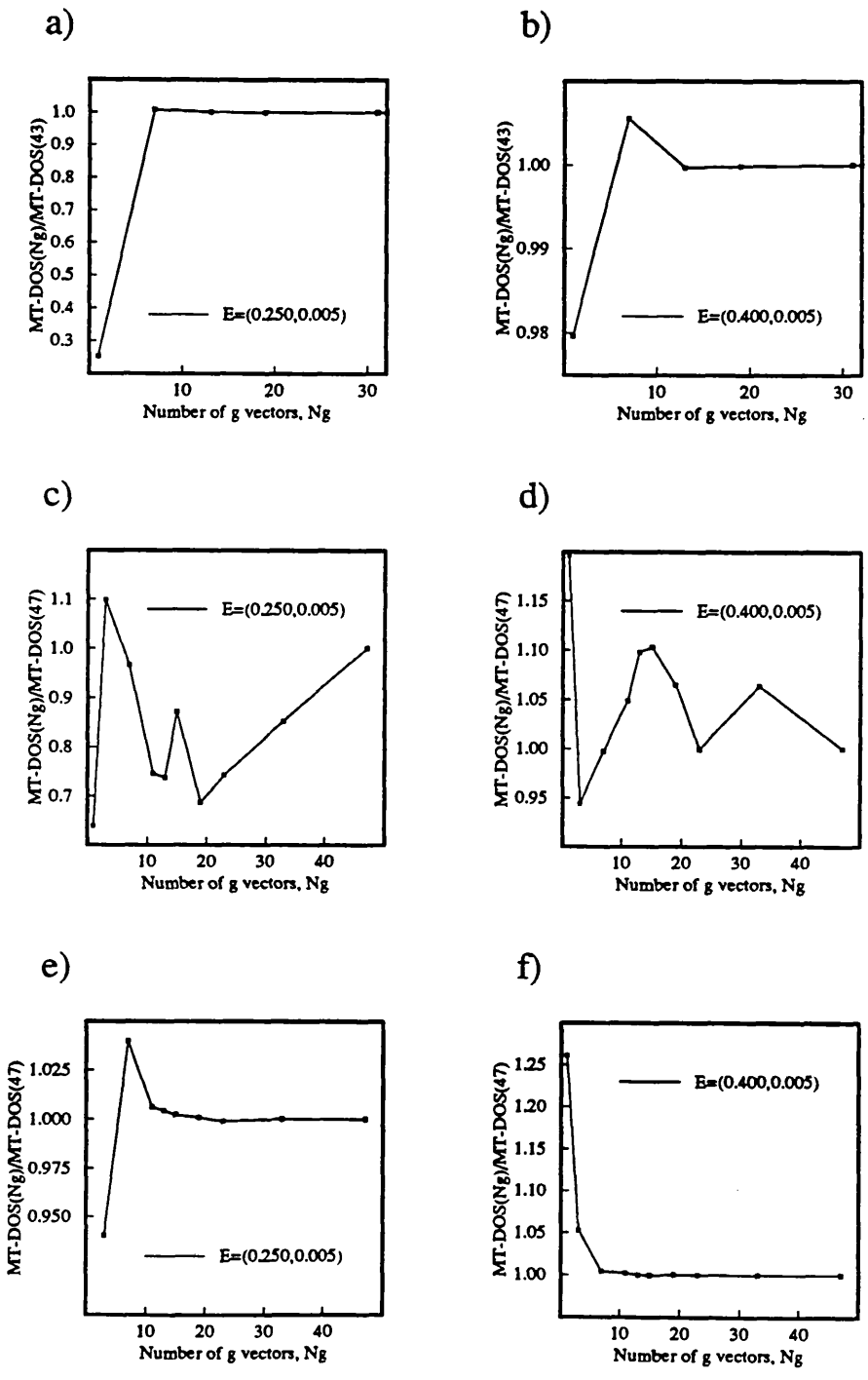

Figure 3.21 Relative calculation times using the plane wave (normal) and plane wave/ partial wave (close–spaced) codes along the (210) direction of nickel.

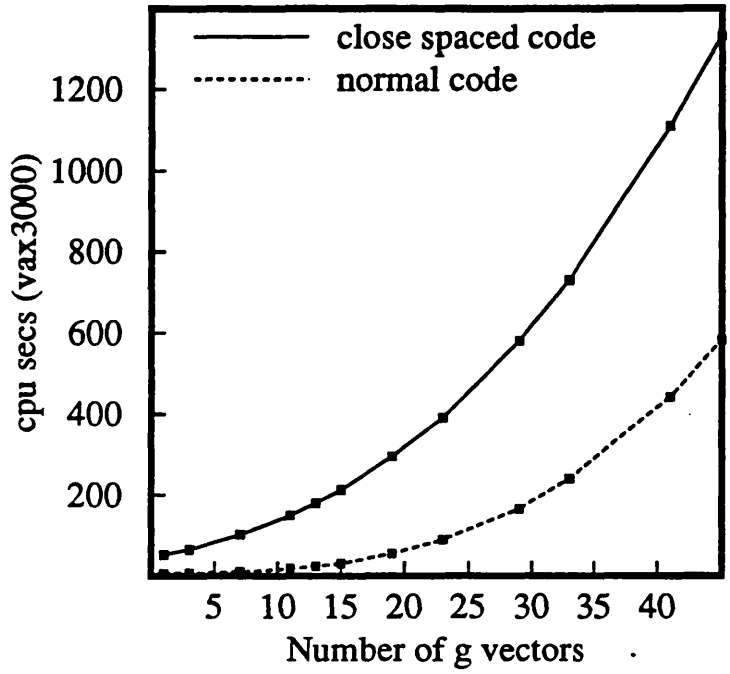

that in absolute terms these errors exceed structural energy differences. However, we may hope that **relative** differences in energy between two calculations will be accurate if the same approximations are made in performing them, that is, if the same approximation is made to the exchange–correlation functional, corresponding points in the Brillouin zone sampling used and the same size basis set chosen. A similar philosophy has been applied to the calculation of cohesive energies (e.g. Moruzzi, Janak and Williams, 1978) and structural phase diagrams (e.g. Chang and Cohen, 1986), with a success suggesting the belief in the cancellation of errors is well–placed. Of the various errors entering the calculations, all but the local density approximation may be corrected systematically; the muffin–tin approximation may be checked by perturbation theory, or through the use of full–potential techniques (e.g. Wimmer, Krakauer, Weinert and Freeman, 1981).

In this respect, it should be noted that the self consistent bulk–potentials generated by the layer KKR method and subsequently to be used in the bulk half spaces of an interface calculation must be determined along corresponding directions with the same basis set, Brillouin zone sampling and energy ordinates.

CHAPTER 4: STACKING FAULTS IN FCC METALS

4.0 Introduction

A regular crystal may be considered as a stacking of atomic planes, the actual composition of the planes and the relative displacements determining the precise structure. Stacking faults may be viewed as an interruption to the regular stacking sequence of the atomic planes. As a geometrical exercise any number of possible stacking faults may be visualised, but with each fault there is an associated energy, and the actual occurrence of each fault depends crucially upon this energy. The energy itself depends upon many properties of the host material, such as the types of atoms and the nature of the bonding, and also upon structural factors. The retention of normal coordination and bond lengths has, as may be expected, been found to crucially affect the energy and subsequent occurrence of the stacking faults (Saada, 1966). Only faults in the stacking sequence along the [111] direction have been observed in FCC crystals, being the only ones preserving nearest neighbour relations, whilst direct observation of stacking faults in the BCC crystal structure, for which no faults exist which retain nearest neighbour bond length and coordination, are speculative and at best rare (Saada, 1966). In comparison with surface and grain boundary energies, those for stacking faults are typically an order of magnitude smaller (see table 4.1), again a consequence of the retention of nearest neighbour coordination and bond lengths.

Interest in stacking faults rests primarily in their influence upon the mechanical properties of materials. For example, in the FCC crystal the dissociation of a perfect dislocation $\frac{1}{2}[\bar{1}0\bar{1}]$ into an extended dislocation results in two Shockley partial dislocations $\frac{1}{6}[\bar{1}\bar{1}2]$ and $\frac{1}{6}[\bar{2}11]$ bounding a stacking fault. The energy required for the formation of this fault affects the ease by which the dislocation splits into partials and consequently the dislocation mobility. Materials with low stacking fault energies are characterised by planar slip and twin formation, whilst

Table 4.1

Selected interface energies γ (in ergs/cm^2) for various metals (sf = stacking fault, gb = grain boundary and s = surface). Data taken from Appendix 2 of Hirth and Lothe, 1982.

Metal	γ_{sf}	γ_{gb}	γ_s
Ag	16	790	1140
Au	32	364	1485
Ni	125	866	2280
Pt	322	1000	3000

those with high stacking fault enegies are characterised by more homogeneous deformation and dislocation cell formation due to easy cross slip. Dislocations split into partials are restricted to a single glide plane and can cross slip only if they recombine, and with the equilibrium separation of the partials going as the inverse of the stacking fault energy, cross slip is increasingly difficult as the energy decreases. Stacking faults also provide barriers to the movement of dislocations, and the energy γ plays a role in the physics of a variety of other defect structure (Hirth and Lothe, 1982).

On a wider front, stacking faults are of interest to the question of phase stability, and polytypes in general (Zangwill and Bruinsma, 1987). Again considering the FCC crystal, the local atomic environment in the vicinity of a stacking fault is HCP, and indeed the "hard-ball" central forces model predicts the twin fault energy to be equal to the FCC–HCP transformation energy per layer (note, however, the variation in c/a ratios for HCP crystals points to certain inadequacies of the central force model). The accumulation of solute atoms at a stacking fault resulting in a decrease in the interfacial energy is a phenomena predicted by Suzuki (1952, 1962) and provides a means for controlling the plastic properties of metals. Furthermore, those segregants tending to reduce the stacking fault energy would also promote the FCC-HCP phase transition, and modify the elastic properties of the crystal. Finally, stacking faults have been shown to contribute to electrical

resistivity (Howie, 1960; Cotterill, 1961) and corrosion, when the faults extend to the surface.

In this Chapter experimental studies are outlined, and previous theoretical studies on silicon and metals described, to put into context the new results presented on twin faults in copper, aluminium and iridium. Finally, preliminary results looking at the possible mechanisms by which impurities modify the properites of the stacking fault are presented.

4.1 Experimental results

The experimental determination of the stacking fault energy in FCC metals and alloys has been reviewed by Gallagher (1970), who concludes that no single method of determination combines all the desirable attributes such as a wide range of applicability, and a direct and preferably strong dependence of the energy upon the experimental measurement. Of the many techniques used, the extended node method is close to being ideal when applicable. This technique looks at the equilibrium structure of dislocation arrays; the material between the partials is a stacking fault and so the magnitude of the fault energy controls the dislocation separation, and the radius of curvature, R, of the faulted area in triple nodes (Saada, 1966). Simple analysis gives $\gamma \propto R^{-1}$ and so only in materials with low stacking fault energies (typically < 30 ergs/cm^2; note 1 erg/cm^2 = 1 mJ/m^2) may nodes be resolved and hence the energy determined. The agreement between various determinations of the fault energy using the method of extended nodes is remarkably good, especially compared to the general standard of agreement between determinations by other techniques, which reflects to some degree the difficulty in performing the experiments and the problems in applying linear continuum elasticity theory to describe the atomic scale changes (table 4.2). However, other than silver, the elemental FCC metals have stacking fault energies too high for the use of the extended nodes method for their determination, and consequently their energies are more uncertain.

Since most real applications of metals are at room temperature or higher, and theoretical calculations are performed at T = 0, the temperature dependence of the stacking fault energy is of great importance. Again Gallagher (1970) has reviewed the published investigations of this dependence, and concluded that the variation in stacking fault energy with temperature is weak, with a number of additional influences, such as changes in segregation behaviour, change in elastic constants and a reduction in the solute pinning forces on the dislocations, also affecting the size of the faulted areas, usually taken to be indicative of a change

Table 4.2

Stacking fault energy of silver as determined in a variety of studies using the techniques listed (compiled from Gallagher, 1970). Energies in ergs/cm^2.

Method	Energy determined
Extended nodes	$21, 20 \pm 7, 21.9 \pm 3.5, 27 \pm 7, 22.8 \pm 4$
Faulted dipoles	$30.7, \leq 21 \pm 6$
τ_3, stress at onset of dynamical recovery	$43, 65 \pm 8, \sim 40, 15 \pm 3$
tetrahedra stability	$< 43, 17 \pm 4, 15.4$

in stacking fault energy. For copper and aluminium, the stacking fault energy is estimated to change by only about -0.04ergs/cm^2/°C.

The conclusions drawn by Gallagher in his review of experimental studies of the FCC metals and alloys are applicable to metals in general. The uncertainties in experimental values for the HCP metals have been addressed by Fleischer (1986), and similar factors affect the antiphase boundary energies in ordered alloys (Murr, 1975). Overall, the conclusion to be drawn from the experimental studies is that accurate theoretical determinations of the energy are very useful and can greatly aid experiment.

4.2 Theoretical studies of stacking faults in silicon

Silicon is probably the most studied and best understood material, both because of its importance to the electronics industry, and because its electronic properties may be well represented within the local pseudopotential approximation. The latter has enabled the material to be comprehensively studied by the self–consistent pseudopotential, which is fast and accurate even to the extent of allowing the validity of the local density approximation and the nature of the one–electron states to be considered in some detail (Godby and Needs, 1989). A huge amount of time has been devoted to understanding a whole spectrum of properties, and in particular a large number of studies have been directed toward the characterisation of the silicon stacking fault. Much can be learned from these investigations when studying stacking faults in metals, such as accuracy of calculation techniques, relaxation effects and the nature of localised states.

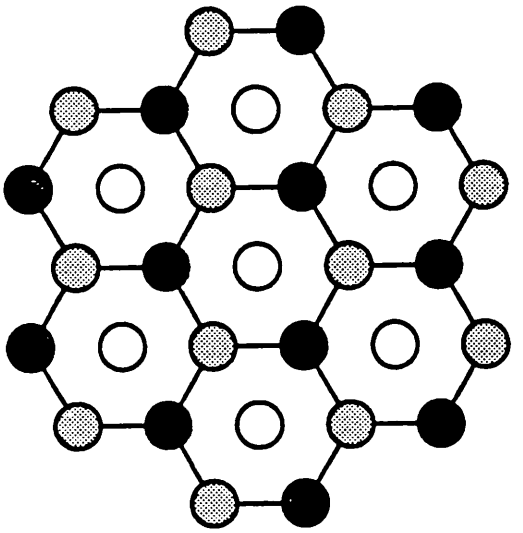

Figure 4.1 Atomic positions of AA' (unshaded), BB' (shaded) and CC' (black) sites of the silicon lattice projected onto the (111) plane.

The silicon lattice has the diamond structure, which may be viewed as two inter–penetrating FCC lattices displaced relative to one another by one–quarter of the cube diagonal. Along the [111] direction of the cubic lattice the stacking sequence of (111) hexagonal planes for the perfect crystal follow a ...AA'BB'CC'AA' BB'CC'... pattern, with the plane A' (B' or C') directly above A (B or C), the separation being the nearest neighbour distance,. A' and B (B' and C or C' and A) are separated by one–third the nearest neighbour distance, and with an in–plane shift of one–third the usual hexagonal lattice basis vectors (figure 4.1). Three stacking faults are known to occur. The intrinsic stacking fault (ISF) results when a double plane AA' is removed from the sequence, and the extrinsic faults (ESF) may be viewed as the addition of an extra double plane. The twin fault is a complete reversal of the stacking sequence.

ISF	...AA'BB'CC'BB'CC'AA'BB'...
ESF	...AA'BB'CC'BB'AA'BB'CC'...
TSF	...AA'BB'CC'AA'CC'BB'AA'...

Theoretical studies have focussed upon determining the stacking fault energy and the presence of localised states induced by the disruption to the symmetry. Guiding and prompting these investigations are experimental studies which have determined the stacking fault energy to be 50–70 ergs/cm^2 by a variety of techniques, such as the separation of partials (e.g. Ray and Cockayne, 1970), the radii of curvature in extended nodes of dislocation networks (e.g. Ray and Cockayne, 1971) and the width of double ribbons (Föll and Carter, 1979). Furthermore, there have been reports of localised states 0.1eV below the conduction band, found by Kimmerling, Leamy and Patel (1977) using charge collection scanning electron microscopy, and 0.15eV above the valence band maximum observed by Weber and Alexander (1983) by photoluminescence spectra.

Chen and Falicov (1974), using pseudopotential theory and the second order perturbation theory developed by Hodges (1967), obtained an energy of 55 ergs/cm^2 for the ISF. This calculation used empirically fitted form factors, and is surprisingly accurate in light of the approximations made (Krause, 1976), including neglect of self–consistency and exchange-correlation effects, and the use of perturbation theory. Indeed second order perturbation theory predicts the stable phase of silicon to be HCP (Harrison, 1965). Weigel, Alexander and Corbett (1975) used the semi–empirical extended Hückel theory (EHT) within the slab approximation to look at all three faults, the energies being determined by comparison with a

slab of perfect crystal to remove the effects of the free surfaces. The EHT parameters gave a good band structure and reasonable elastic properties, and gave fault energies $\gamma_{ISF} = 86.0$ ergs/cm^2, $\gamma_{ESF} = 85.5$ ergs/cm^2 and $\gamma_{TSF} = 43.0$ ergs/cm^2. These energies and inspection of the charge distributions suggested the ISF and ESF could be regarded to some degree as a superposition of twin faults, separated by one double plane in the ISF and two in the ESF. Thus, at least for the silicon stacking faults, the connection between the stacking fault energy and phase stability appears strong. Altmann, Lapiccirella, Lodge and Tomassini (1982) used a valence force field model beyond the harmonic approximation fitted to experimental phonon dispersion data and obtained $\gamma_{ISF} = 44$ ergs/cm^2.

Marklund (1981) examined the electron energy levels using supercells of 10–20 atomic planes with an empirical local pseudopotential scheme and predicted the localised level 0.11eV above the valence band maxima found experimentally by Weber and Alexander (1983). The same level was found by Mattheiss and Patel (1981) using a non–orthogonal tight–binding method with parameters determined *via* a non-linear least squares fit to an accurate non–local pseudopotential band structure. They also employed supercells and located localised states by observation of the charge distribution of the eigenfunctions. Other defect states were found, but none below the conduction band minimum which would correspond to that observed by Kimmerling, Leamy and Patel (1977), and which could therefore to be due to either impurities or disorder arising from the surrounding dislocation. Mattheiss and Patel (1981) determined the fault energies and minimised them by allowing relaxation in the interplanar spacing. The energies, $\gamma_{ISF} = 64$ ergs/cm^2, $\gamma_{ESF} = 44$ ergs/cm^2 and $\gamma_{TSF} = 19$ ergs/cm^2, were approximately halved through the inclusion of relaxation, which involved changes of the order of 1% in the interplanar spacings. Qualitative agreement with these results was given by Sánchez-Dehesa, Vergés and Tejedor (1981) using generalised Wannier functions. They determined relaxations of up to 4% in interplanar spacings and energies $\gamma_{ISF} = 145 \pm 30$ ergs/cm^2 and $\gamma_{ESF} = 50 \pm 30$ ergs/cm^2, but their method involved large cancellations of absolute energies.

The only first–principles calculation of the stacking fault electronic structure of silicon is due to Chou, Cohen and Louie (1985). Using norm–conserving pseudopotentials within the self–consistent supercell approach they determined the fault energies to be $\gamma_{ISF} = 33$ ergs/cm^2 and $\gamma_{ESF} = 26$ ergs/cm^2, with an uncertainty of about 20%. Interestingly, the ratio of energies $\gamma_{ISF}/\gamma_{ESF}$, which may be expected to be more accurate experimentally than the individual energies, since it applies to a particular sample and avoids systematic uncertainties, agrees very

well (Föll and Carter, 1979). Localised states were observed, in agreement with the previous theoretical calculations, and the authors suggest a possible reason for the absence of the state observed by Kimmerling, Leamy and Patel (1977) may be the local density approximation, which significantly under–estimates the band gap in silicon. Thus, features in the vicinity of the conduction band may be in error. In support of this, localised states were identified that were pulled from the conduction band, but **not** below the absolute minimum. Structural relaxations, which were determined *via* the Hellmann–Feynman forces (Hellman, 1937; Feynman, 1939; Slater, 1972) as they were found to contain less noise than the energy, revealed an expansion of the order of 1% in the interplanar spacing. The resulting energy change was less than the 20% calculation uncertainty. Table 4.3 summarises some of the theoretical determinations of the stacking fault energy in silicon.

4.3 Theoretical studies of stacking faults in metals

Low energy stacking faults (due to the preserving of nearest neighbour coordination, and thus likely to exist) have been found in the close–packed FCC and HCP crystal structures. Viewed as a stacking of (111) hexagonal planes along the [111] direction, the stacking sequence in the FCC structure is analogous to the diamond crystal but with single and not double planes. The intrinsic, extrinsic and twin faults may likewise be viewed (Hirth and Lothe, 1982) as resulting from the subtraction, addition and reversal of the stacking sequence (figure 4.2).

FCC

ISF	...ABCBCAB...
ESF	...ABCBABC...
TSF	...ABCACBA...

The HCP lattice is given by the stacking sequence ...ABABABAB... of hexagonal planes, and the possible faults are two intrinsic (I_1 and I_2) and an extrinsic fault (Hirth and Lothe, 1982) (figure 4.2).

HCP

I_1SF	...ABABACACACA...
I_2SF	...ABABABCACAC...
ESF	...ABABACBABAB...

Table 4.3

Estimates of the stacking fault energy (in ergs/cm^2) of silicon.

Energy			Method (reference)
ISF	ESF	TSF	
$33 \pm 20\%$	$26 \pm 20\%$		ab – initio pseudopotential theory (Chou *et al*, 1985)
86.0	85.5	43.0	extended Huckel theory (Weigel *et al*, 1975)
145 ± 30	50 ± 30		generalised Wannier functions (Sanchez – Dehesa *et al*, 1981)
64	44	19	non – orthogonal tight binding (Mattheiss and Patel, 1981)
44			valence force field (Altmann *et al*, 1982)
55			2nd order perturbation theory (Chen and Falicov, 1974)
$50 - 70$	$50 - 70$		experiment (see text)

The perturbation method within the pseudopotential theory used by Chen and Falicov (1974) on silicon was originally developed by Hodges (1967) to study the stacking fault energies of various close–packed metals. His results demonstrated the trends in the energies (Al high, Pb low) but were not accurate. Indeed, Pb and Zn were found to have negative stacking fault energies, indicating instability to fault formation and thus predicting the wrong crystal structure. Simon (1979) has reviewed subsequent applications of the pair–potential approach (derived from pseudopotential theory or orthogonalised plane wave methods). He notes that applications to noble metals have not achieved much success, and concludes that, in the case of normal metals, the energies derived are very sensitive to the actual form of the interionic potential, but are of the correct order of magnitude. Despite the

Figure 4.2 Bulk and stacking fault structures of the FCC and HCP lattices. The view is edge on to the (111) planes and taken in a [211] direction. Shaded atoms occupy positions one row back.

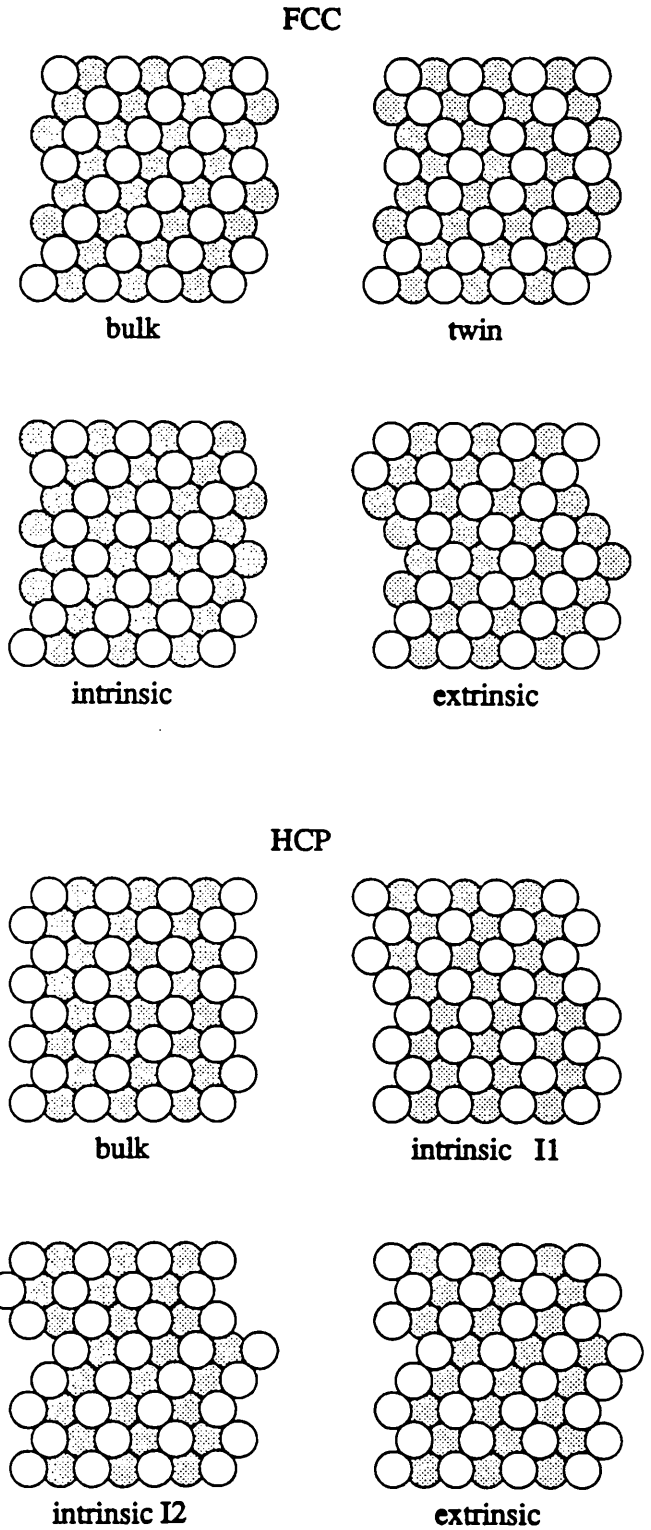

presence of long–range terms in the energy expressions, the stacking fault energies are generally proportional to the number of faults, $\gamma_{TSF} \sim \gamma_{ISF}/2 \sim \gamma_{ESF}/2$, with the intrinsic fault systematically higher (by $\sim$ 16 %) in energy than the extrinsic fault. These conclusions supported the studies of Beissner (1973) who used the real space summation technique of Blandin, Friedel and Saada (1966) to compare a variety of model potentials. In polyvalent metals, trends and phase stability were well described, but in monovalent metals there was tremendous sensitivity to small changes in energy–wave number characteristics of the potential; in general energies were lower than found in experiment. Beissner also noted that exchange–correlation effects were not so important as in the case of other defect calculations. This could be due to the rather smaller changes in charge distribution and volume (as compared to surface, grain–boundary or dislocations), which might alter the validity of the application of the local density approximation when compared to the perfect crystal. Beissner also noted a systematic underestimation of the theoretical energies when compared to experiment.

Harrison (1973) has employed the pair potential formalism to aluminium and examined the effects of lattice relaxations. Using 10 atomic layers and constant total volume, his results (using an empirical pseudopotential) indicated lattice displacements of the order of 2%, analogous to those found in silicon, and accompanying reduction in the fault energies of up to 10%.

Calculations probing the electronic structure at stacking faults have primarily focussed upon nickel. Yndurain and Falicov (1976) applied their transfer matrix approach (Falicov and Yndurain, 1975b) to the intrinsic and extrinsic faults of the FCC lattice, using tight–binding parameters determined by fitting to established band–structures. Evaluating the density of states $\rho(E, \mathbf{k}_{||})$ at high symmetry points within the two–dimensional Brillouin zone they identified the presence of localised states throughout the Brillouin zone, including one at the Γ point in both the ISF and ESF about 1eV below the Fermi energy, between the bulk bands of t_{2g} and e_g symmetry. Pointing out the absence of surface states in this vicinity of $(E, \mathbf{k})$ space, and noting that the state is well removed from the bulk bands, so should be easily resolved by photoemission, they suggested experimental verification should be possible. Grise, Kleinman and Mednick (1980) disputed this possibility, their calculation using the linear–combination–of–atomic–orbitals method applied to large supercells containing ISF's, ESF's or TSF's, which revealed many more localised states, including those of Yndurain and Falicov (1976). These states, however, occured largely in gaps which were also predicted to include surface states (Dempsey, Grise and Kleinman 1978), although experimentally these have not been found,

possibly due to resolution problems, as the gaps in which they reside are rather narrow. Furthermore, studies of the density of states and charge distributions (and magnetisation) at the various faults indicated relatively small deviations from bulk behaviour, offering little hope that experimental probes may be able to resolve the effects of the stacking faults. The need for the stacking fault to be located near the surface (within 5–10 atomic planes), in order that electronic probes may experience it and the subsequent scattered electrons to escape, would also introduce a surface–stacking fault interaction which would have to be taken into account; Grise, Kleinman and Mednick determined the localised electrons to reside largely within 1–2 atomic planes of the fault, although some present within narrow gaps were rather more de–localised.

4.4 Twin faults in aluminium, copper, and iridium

Results are now presented for the electronic structure of twin faults in the FCC metals aluminium, copper and iridium. As discussed in the introduction to this Chapter and as supported by both experimental data and theoretical calculations, the twin fault may be viewed to some degree as the fundamental building block of the intrinsic and extrinsic stacking faults, and so the results obtained in these studies should also be applicable to those faults. The stacking fault structure is an ideal problem to be studied by the layer KKR method. The perturbations induced by the structural changes are evidently small and subtle, and may be poorly represented by supercell calculations (see figure 1.1). The materials studied here are well described by the muffin–tin approximation to the crystal potential, being close packed, and at the fault area itself the change in structure retains this packing. As a first approximation the stacking sequence of the atomic planes is simply reversed and relaxation of the interplanar spacings have been neglected. Such relaxations would alter the interstitial volume and it is not certain that the muffin–tin approximation, with its sharp distinction between the interstitial and intrasphere regions, can accurately describe relaxation effects of such a nature.

The three metals studied have distinctly different electronic structure. In figure 4.3-5 the muffin–tin density of states (MTDOS) for the bulk structures are displayed. Figure 4.3 is for aluminium, evaluated by the layer KKR method with partial waves included up to $\ell = 2$, $N_{\mathbf{g}} = 13$, 378 special $\mathbf{k}_{||}$ sampling points in the one-twelfth irreducible Brillouin zone and an imaginary offset to the energy contour of 0.0025Ha (~0.068eV). The self–consistent potential was calculated with 6 Brillouin zone sampling points and 8 energy points on the triangular energy contour. The profile is in excellent agreement with other muffin–tin calculations

(Moruzzi, Janak and Williams, 1978), and also full potential pseudopotential results (Ashcroft, 1979). Below about -4.0eV (all energies are quoted relative to the Fermi energy) the MTDOS has a parabolic $E^{1/2}$ free–electron like profile, the slight rippling being an artifact of the finite number of Brillouin zone sampling points used, as descibed in Chapter 3. Moving up in energy the MTDOS deviates from the free–electron like profile and displays a number of peaks and troughs associated with critical points in the band structure and which occur as a result of backscattering and subsequent constructive/destructive interference off the principle planes of the crystal lattice. These features have been examined in detail by Ashcroft (1979). Aluminium is trivalent and the Fermi energy passes through a region where there is significant hybridisation and where bands meeting the zone boundaries. From the *s*,*p*, and *d* decomposition of the MTDOS also given in figure 4.3 it is clear that the *d* contribution is significant and must be included for accurate calculations. The stacking fault energy for aluminium is high, about 166 ergs/cm^2 (Murr, 1975), and consequently experimentally only indirect methods may be used for its determination.

Figure 4.3 Muffin–tin density of states for bulk aluminium, and *s*, *p* and *d* decomposition.

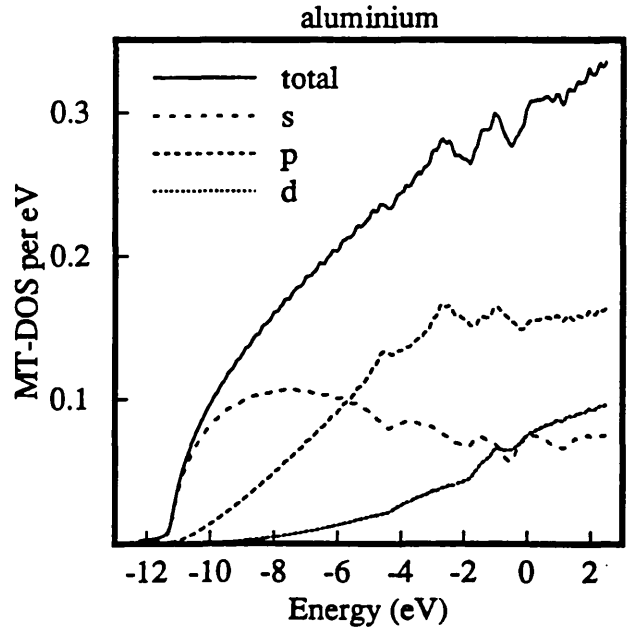

Figure 4.4 Muffin–tin density of states for bulk copper, and s, p and d decomposition.

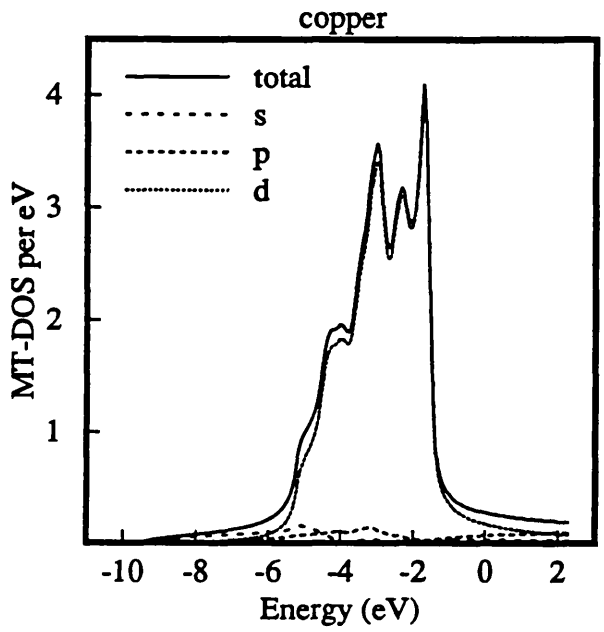

Figure 4.5 Muffin–tin density of states for bulk iridium, and s, p and d decomposition.

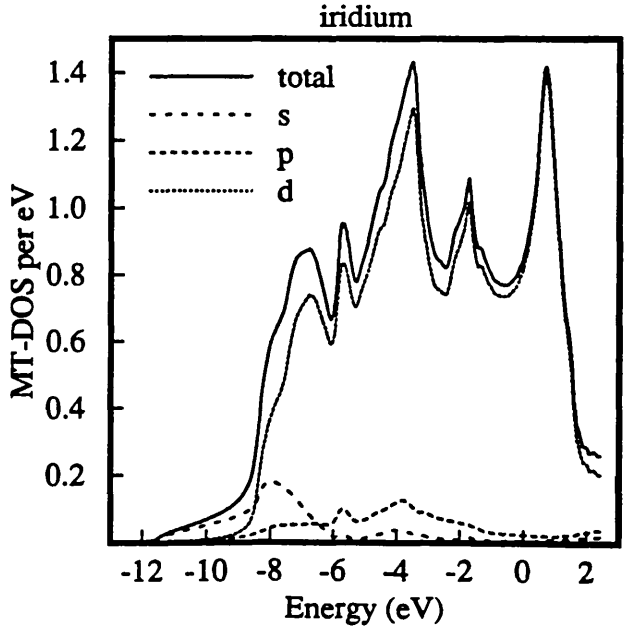

In figure 4.4 the MTDOS for the noble metal copper is plotted, calculated with the same parameters as were used for aluminium. Again there is excellent agreement with other muffin–tin calculations (Moruzzi, Janak and Williams, 1978), taking into account the Lorentzian broadening due to the finite imaginary energy. The copper MTDOS is dominated by the *d*-band extending approximately from -5.5eV to -1.75eV within the *s–p* band and results in significant hybridisation of the states within this region. Copper has 29 electrons, 11 of which are present in the valence band. Of these, approximately 10 occupy the *d*–band and the remaining electrons fill up the *s–p* band so that the Fermi energy lies approximately 1.75eV above the top of the *d*–band, in a region characterised by isotropic bonding. Consequently copper is an extremely ductile metal. Its stacking fault energy is lower than aluminium, with experimental determinations falling in the range 40–80 ergs/cm^2 (Gallagher, 1970; Murr, 1975; Carter and Ray, 1977), but which is still to be considered relatively high by comparison with some alloys.

In figure 4.5 the corresponding MTDOS for iridium is presented. For iridium, atomic number 77, relativistic effects are important and were included *via* the method of Koelling and Harmon (1977) described in Chapter 2. The effect on the valence band of treating the electrons relativistically is to broaden the *sp* band and lower it with respect to the *d* band. Thus the lowest peak in the MTDOS, due to strong *sp-d* hybridisation, is significantly reduced in amplitude in comparison with, for example, rhodium, which is one row above iridium in the periodic table in the same column. However, changes in the vicinity of the Fermi level are small. Parameters identical to those used for aluminum were employed in the calculation of the MTDOS and self–consistent potentials for iridium. The agreement with the results of Noffke and Fritsche (1982) is good. They employed partial waves up to $\ell = 3$ in their calculations but the *f*–component of the density of states is minimal and has been neglected here. The atomic $4f$ electrons were treated as core levels as described in Chapter 3, for which scattering phase shifts are not required. The iridium MTDOS is dominated by an extremely wide *d*–band (about 10eV wide compared to 4eV for copper). There are 9 electrons available for occupying the valence band states, and the Fermi level lies within the *d*–band near a minimum of the MTDOS. The very wide *d*–band of iridium is indicative of directional bonding with strong orbital overlap, and has been suggested to be the cause of its anomolous mechanical behaviour (Hecker, Rohr and Stein, 1978; Rohr, Murr and Hecker, 1979) — iridium is known to fail by brittle cleavage in single crystals and in polycrystalline form has a tendency to fail by brittle intergranulare fracture, both properties being intrinsic and not due to impurities

(Reid and Roubort, 1972). This behaviour is in contrast to the usual properties of FCC crystals which fail in a ductile manner as a result of the large number of slip systems available. In this respect copper is a classic FCC material. The directionality of the bonding in iridium is also evidenced by its elastic constants, with a negative Cauchy discrepancy, $C_{12} - C_{44} < 0$, atypical of FCC materials but in line with BCC metals, which are usually associated with more covalent bonding (Johnson, 1989). The stacking fault energy of iridium is in some dispute (Darling 1973). Ahlers (1970) quotes a value of $2960 \pm 560 ergs/cm^2$ whilst Murr (1975) gives $300 ergs/cm^2$ and reports the observation of deformation twinning, which favours a lower value.

Figure 4.6 Twin fault structure as viewed in figure 4.2, with shading to indicate atoms whose potentials were allowed to relax.

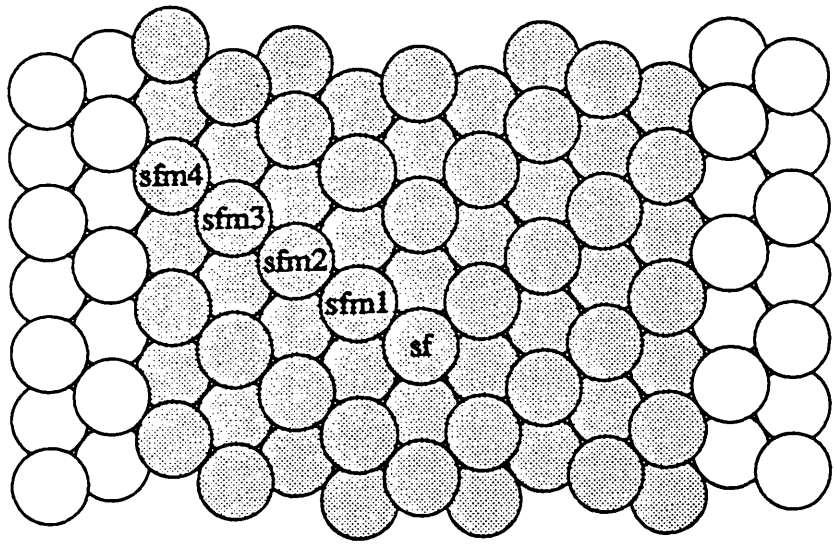

The twin faults in these materials were modelled with a nine layer symmetric interface region illustrated in figure 4.6, which also contains the notation used to label the atoms within the various atomic planes. Only those potentials within this 9 layer region were permitted to relax. In comparison with bulk calculations, in going to self–consistency only a small amount of the new potential may be mixed in with the old to generate a new starting potential, to retain stability of the iterative procedure, and for the stacking fault calculations a mixing parameter of the order of 5% was found to be best. The potentials were iterated till fractional changes in

the charge density were less than 10^{-5}, which required 10–15 iterations — most of the induced changes are purely a consequence of the structural modifications, and do not involve great rearrangement of charge, as will be seen below.

In figures 4.7–9 are summarised the density of states obtained for various atoms in the vicinity of the copper fault. Figure 4.7 compares the MTDOS of the central fault atom, *sf*, and that of the atom in the adjacent atomic plane *sfm1*, with that of a bulk copper atom. The changes induced by the reversal of the stacking sequence are evidently small, and reside primarily within the narrow *d*–band. The minor peak at between -2 and -3eV is absent on the central atom and greatly diminished on the adjacent atom. The peak between -3 and -4eV is split on atom *sf* and there is a slight change in structure below about -4eV. Particularly noticeable is the retention of the *d*–band width. Within a tight binding picture this width is determined to a first approximation by the nearest neighbour coordination, and the HCP structure also has the 12–fold coordination of the FCC lattice but with an angular redistribution of nearest neighbour atoms. There is a similar number of second nearest neighbours, at the same distance, and the first difference appears with the introduction of 2 atoms half way between second and third FCC nearest neighbours. Thus the band width remains. The range of the induced perturbations is small for copper. Figure 4.8 compares the MTDOS of an atom two atomic layers from the fault plane (labelled *sfm2* in figure 4.6) with a bulk atom. The deviations from the bulk–like MTDOS are small for this atom, and even more so for the two other atoms included in the interface region. Thus the interface region is clearly large enough in size. Finally figure 4.9 highlights the energy region within 1eV on either side of the Fermi level. As mentioned above, the bonding in this energy range is isotropic, with spatially diffuse *s* and *p* contributions and which are largely unaffected by the changes in local structure.

Figures 4.10–12 show the corresponding results for aluminium. The perturbations induced upon atoms within the two central planes of the fault, *sf* and *sfm1*, are visible in the comparison with the bulk MTDOS presented in figure 4.10. These changes occur predominantly around the Fermi energy. Below -4eV the MTDOS of the fault atoms displays the free–electron like $E^{1/2}$ parabolic behaviour. The first deviations occur at about -3eV, when the energy bands begin to experience the edges of the Brillouin zone and therefore begin to experience the crystal structure. The conditions for Bragg scattering, constructive/destructive scattering off the principle planes of the crystal lattice, are upset by the presence of the twin fault and consequently the peaks and troughs in the density of states are greatly diminished — the MTDOS of the atom *sf* displays a much more free–electron like

Figure 4.7 Comparison of the muffin–tin density of states of the central two atoms at a twin fault in copper with the bulk.

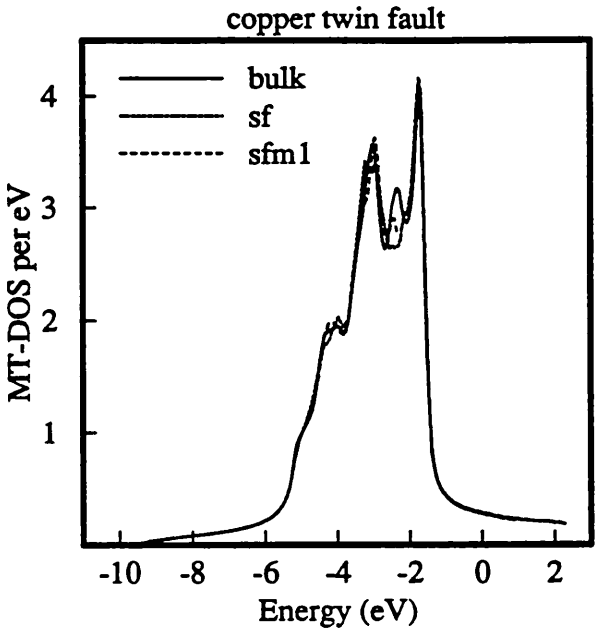

profile than do the bulk atoms. The perturbations decay with distance from the fault, being largest upon the atom *sf*. Aluminium is a weak scatterer of electrons, resulting in a longer electron mean free path, and consequently the perturbations induced by the fault are less localised than for copper, where the *d* levels are more effective at screening the perturbations. Figure 4.11 compares the MTDOS of the atom *sfm4*, the most distant atom from the fault included in the interface region, with that of the bulk. There are still small differences between the two curves, but they are of little significance. Finally, figure 4.12 focusses on the changes in the MTDOS near the Fermi energy. The perturbations are clearly more significant than for copper, with the Fermi energy in aluminium in a region of energy where the energy bands meet the zone boundaries.

Finally, figures 4.13–15 summarise the corresponding results for iridium. In figure 4.13 are plotted the MTDOS for the two central atoms at the twin fault and for comparison that of a bulk atom. The changes induced are significantly larger than for copper and aluminium, extending across the *d*-band. There is some redistribution of states between -8 and -6eV and the major peak centred on -4eV

Figure 4.8 Comparison of the muffin–tin density of states of the atom two layers from the twin fault plane in copper with the bulk.

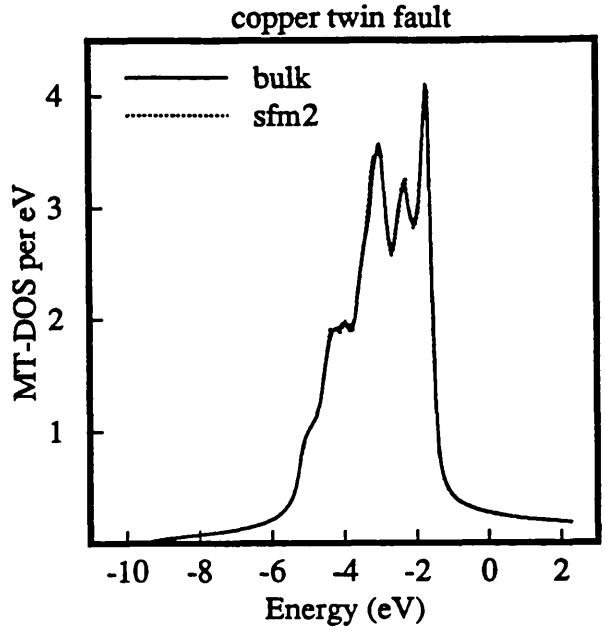

Figure 4.9 The muffin–tin density of states within 1eV of the Fermi energy for the central atom in a twin fault in copper, and the bulk.

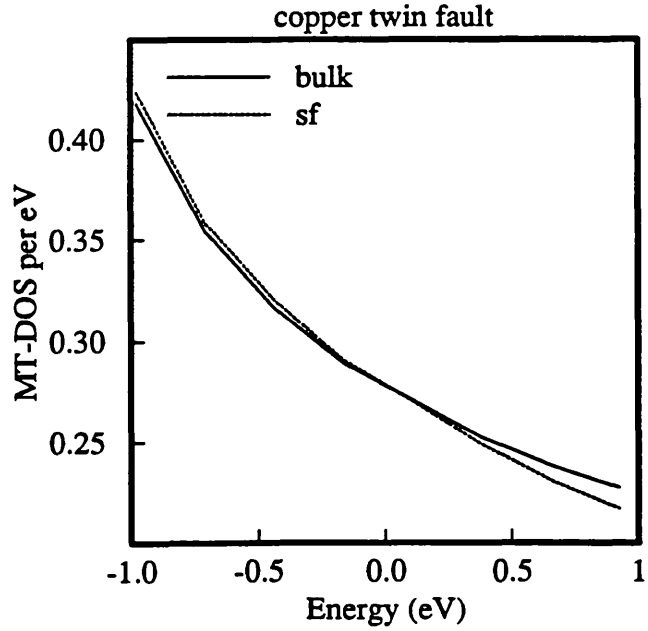

Figure 4.10 Comparison of the muffin-tin density of states of the central two atoms at a twin fault in aluminium with the bulk.

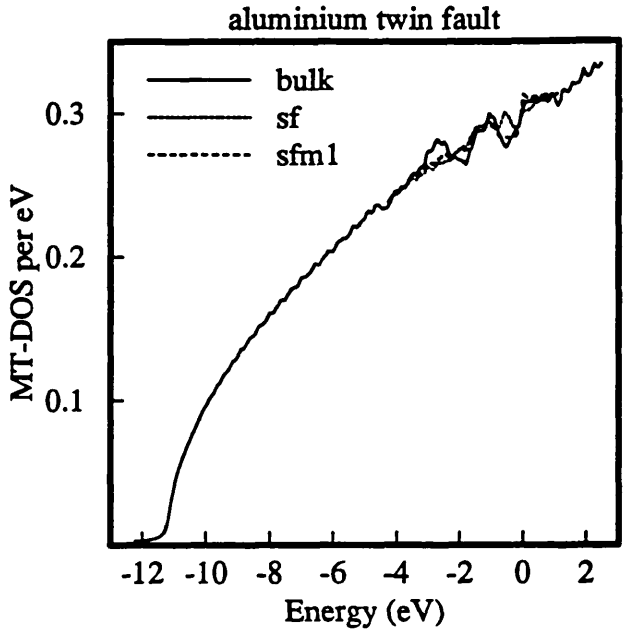

is split on atom *sf*, but not on atom *sfm1* one layer out. Again on the central atom there is a complete loss of the peak at -2eV, with atom *sfm1* recovering about half the loss of weight. In the minimum between the peaks at -2eV and +1eV there is an enhancement in the density of states which decays with distance from the fault plane. On the next layer out, *sfm2*, there is a deficit of states in this region (figure 4.14), but almost all structure is recovered, and on atom *sfm3* the MTDOS is virtually indistinguishable from bulk. Figure 4.15 highlights the changes in the vicinity of the fermi energy, where the central fault plane has an enhancement of about 0.07 states/eV, or approximately 7% .

The changes induced by the stacking fault in iridium mirror those found in copper, taking into account the much broader *d*-band, and support the idea that the changes are largely structural in origin arising from the modification in symmetry at the twin fault. In figure 4.16 are the MTDOS corresponding to the three metals but evaluated for the HCP structure, using self-consistent bulk potentials from the FCC lattice. Features in the curves for copper and iridium are immediately identifiable as those occuring on the twin fault atom, illustrating how the local atomic environment determines the MTDOS. The peak just above

Figure 4.11 Comparison of the muffin–tin density of states of the atom four layers from the twin fault plane in aluminium with the bulk.

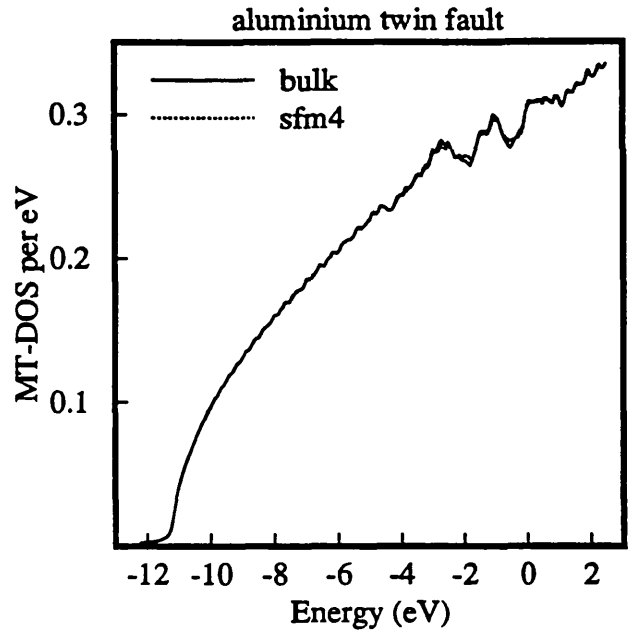

Figure 4.12 The muffin–tin density of states within 1eV of the Fermi energy for the central atom in a twin fault in aluminium, and the bulk.

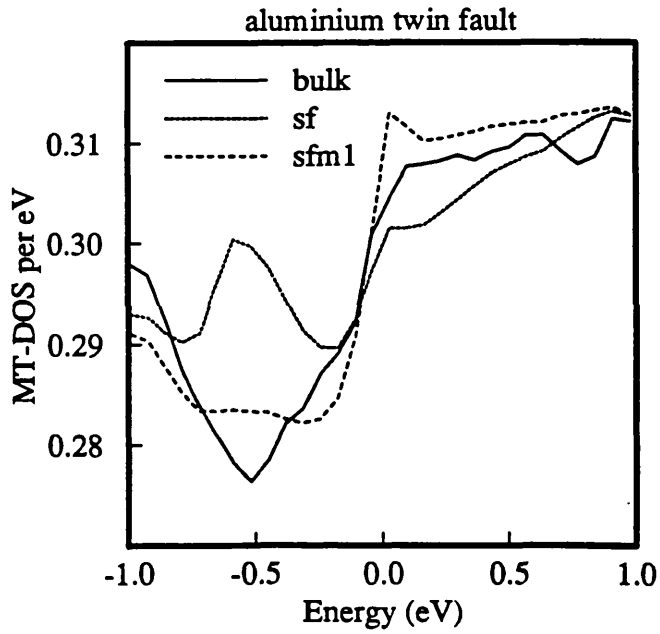

Figure 4.13 Comparison of the muffin-tin density of states of the central two atoms at a twin fault in iridium with the bulk.

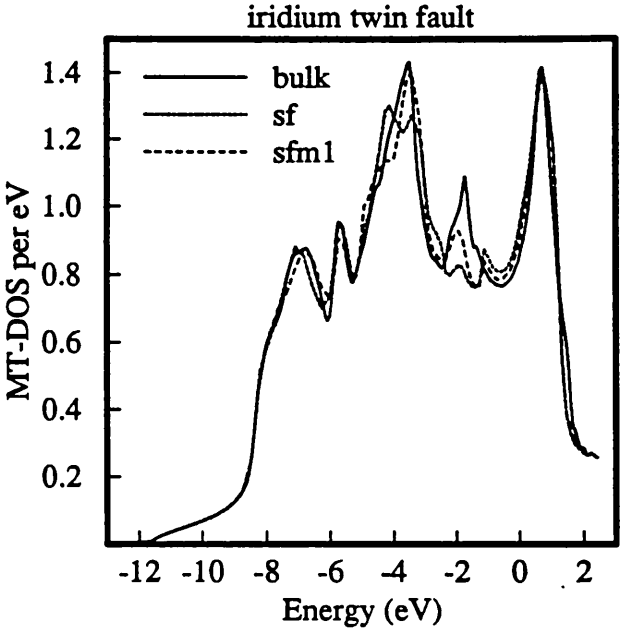

-4eV in iridium is split into two and for both copper and iridium there is no sign of the small peak between the two main ones. An atomic d level is split in a cubic environment into t_{2g} (xy, xz, yz) and e_g $(3z^2 - r^2, x^2 - y^2)$ components, whilst in the HCP lattice it is split into e_{2g} $(x^2 - y^2, xy)$, e_{1g} (xz, yz) and a_{1g} $(3z^2 - r^2)$ components. Thus the reduced symmetry of the HCP lattice results in changes in band ordering and hybridisation splitting and removing structure in the MTDOS. A "local-environment" point of view is significantly more useful for transition metals with their short-ranged d-bands than for free-electron like aluminium, and although it appears that in the HCP structure there is significantly less structure in the MTDOS in the vicinity of the Fermi energy, as was found for the twin fault, there also appears the typical signature of a Van Hove singularity at about -4eV, which was not present in the twin fault MTDOS, and which is clearly due to the long range coherent scattering off the lattice planes and thus specific to the HCP crystal.

Figure 4.14 Comparison of the muffin-tin density of states of the atom two layers from the twin fault plane in iridium with the bulk.

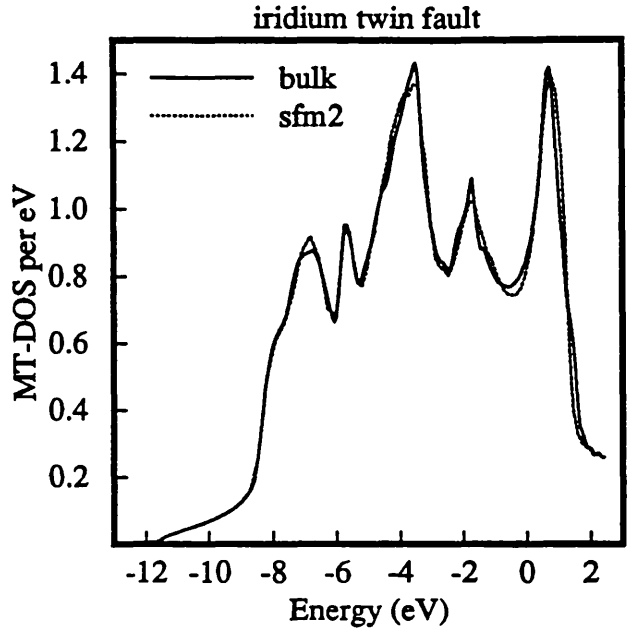

Figure 4.15 The muffin-tin density of states within 1eV of the Fermi energy for the central atom in a twin fault in iridium, and the bulk.

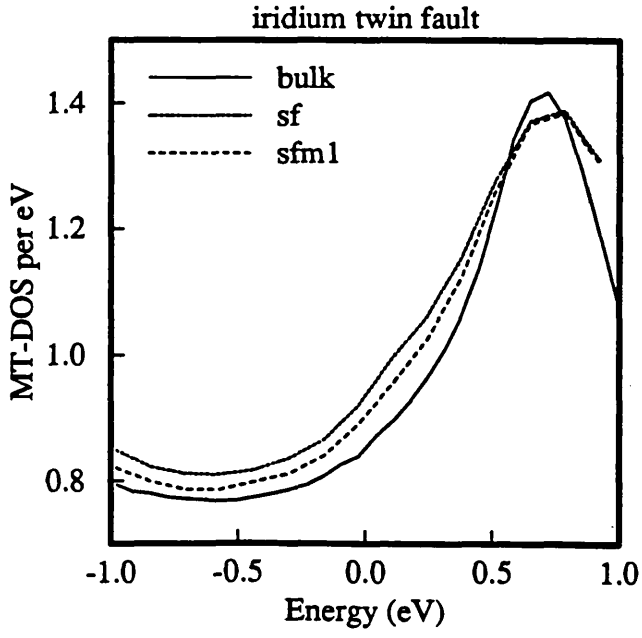

Figure 4.16 Muffin–tin density of states for copper, iridium and aluminium evaluated in the HCP cystal structure using bulk FCC potentials (dotted line). The shaded region is the corresponding bulk FCC MTDOS.

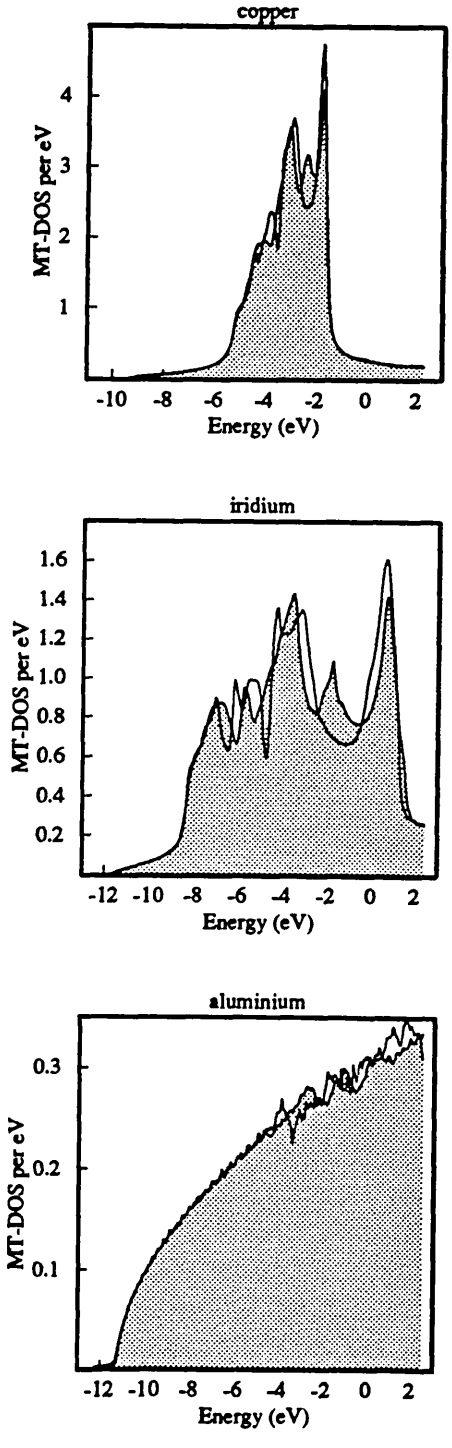

The twin fault energies were calculated (MacLaren, Crampin, Vvedensky and Eberhart, 1989) by evaluating the total energy of the atoms in the interface region using equation (3.8.3) and subtracting off the energy of a similar sized region of bulk crystal. Implicit in this procedure is the assumption that both the interface region is large enough in size and that the parameters used in the numerical determinations are sufficient. These requirements have not been fully checked, but from the density of states it is fairly apparent that the major changes are well localised within the interface region, and from other calculations the parameters have been found to give good results. The energies are given in table 4.4 and the twin fault values have been doubled for comparison with the experimentally determined energies which are applicable to the intrinsic fault. There is good agreement between the calculated and experimental values, in particular the ordering Ir > Al > Cu, and considering the uncertainty that exists for the experimental values, the use of the muffin–tin approximation and neglect of structural relaxations the results are encouraging. The findings in the calculations of stacking faults in silicon and Harrison's (1973) pair–potentials calculations on aluminium would imply the relaxation effects are minimal. The trend in values mirrors to some degree the perturbations induced in the vicinity of the Fermi energy, which are largest in iridium and smallest in copper, and which are a consequence of the degree to which the change in symmetry at the twin fault affects the hybridisation of electrons at those energies. On the whole the re–arrangement of electron states averages out to zero over the valence band, as witnessed by the relative charges upon the atoms in the fault region which are found to retain their bulk values very closely (as also reported in the calculations of Weigel, Alexander and Corbett (1975) and Grise, Kleinman and Mednick (1980)), and thus changes at the Fermi level are most significant in determining any band contribution to the energy. This is in some way supported by tight–binding calculations using full d–bands which give negligible energies for the faults (Pei, 1978; Ducastelle and Cyrot–Lackmann, 1970,1971), and for several other close–packed metals one may understand the relative stacking fault energies by considering the hybridisation in the vicinity of the Fermi energy. Thus in silver, $\gamma \simeq 16$ ergs/cm^2 and the Fermi energy is several eV above the d–band and characterised by free–electron like states, whilst for both nickel, $\gamma \simeq 125$ergs/cm^2 and rhodium $\gamma \simeq 300$ ergs/cm^2 with the Fermi energy passing through the d-band a high value for the fault energy results. However, as witnessed by the reasonably high fault energy in copper, where there are no changes in the vicinity of the Fermi energy, the band energy is not responsible for the total fault energy, nor necessarily dominant. It is hoped in the future to calculate the fault energies of other FCC and HCP metals, and also APB energies in ordered alloys.

Table 4.4

Calculated stacking fault energies and corresponding experimental values, taken from Gallagher (1970) and Murr (1975) (in ergs/cm^2)

Metal	Calculated	Experiment
Cu	58	40 – 80
Al	118	166
Ir	341	300

4.5 Localised states

Localised states were looked for at selected values of $\mathbf{k}_{||}$ within the two–dimensional Brillouin zone for both the copper and aluminium twin faults. In the case of copper the states found agreed very closely in location (in terms of relative position with respect to the projected band edges) with those found for the nickel twin fault by Grise, Kleinman and Mednick (1980). Figure 3.18 is typical. For aluminum we find states in both gaps of the projected band structure occuring below 0.4Ha (relative to the muffin–tin zero; the Fermi energy is at 0.309Ha) at the K point of the Brillouin zone. These may be seen in figure 4.17, and are the first stacking fault states found in a non–transition metal. As in the case of surface states, it therefore appears that with the exception of the monovalent metals (Li, Na, ...), which do not have any gaps in the projected band structure below the Fermi energy, occupied stacking fault states will be present in all metals. The lower gap between 0.205Ha and 0.220Ha has two states, at 0.2085Ha and 0.2154Ha, clearly visible as almost singular peaks between the two band edges, and there are also two states in the higher gap, also shown in figure 4.17, at energies 0.2854Ha and 0.3103Ha, the latter interestingly very close to the Fermi level. Table 4.5 contains the relative weight of each state upon the various atoms within the interface region and moving away from the fault, the weight taken to be equal to the relative MTDOS's obtained for each atom. Due to the Lorentzian broadening the absolute values of the MTDOS depend upon the imaginary energy used in the evaluation, which in this case was 10^{-5} Ha, and so for convenience the central atom is given a weight of 1.0 and all others expressed relative to this. To be perfectly correct one should integrate over the lineshape for each atom, but the relative magnitudes at the peak energy should not differ significantly. It is apparent from this table that all the localised states

extend many atomic planes into the crystal on either side of the fault, and that the amplitude oscillates to some degree with distance. This behaviour is consistent with the surface states found on the (111) face of the aluminium crystal (Mednick and Kleinman, 1984), which are observed at both the Γ and K points below the Fermi energy, and which decay in some cases by less than 10% in the centre of an 18 layer thin film. This weak localisation also explains the insensitivity of the fault states to the self–consistency process, that is, they may also be detected in almost identical positions using bulk potentials in the interface region. This is presumably because such a large fraction of the wavefunction is moving in regions where the potential is negligibly altered by self–consistency. Although the extended nature of the localised stacking fault states would suggest that they might be detected by some surface probe, the very fact that localised surface states also occur in the same energy region would present difficulties in interpreting the experimental results. The dispersion of these states across the Brillouin zone has not been studied, and no states were found in the band gaps below the Fermi energy at either the Γ or M points of the two–dimensional Brillouin zone.

Table 4.5

The relative weights of the localised states at the twin fault in aluminium on the atoms in the interface region.

			atom		
Energy (Ha)	sf	sfm1	sfm2	sfm3	sfm4
0.3103	1.000	3.262	1.054	0.339	1.054
0.2854	1.000	0.331	0.480	0.283	0.095
0.2154	1.000	13.803	9.796	0.433	6.068
0.2085	1.000	0.310	0.154	0.476	0.147

Figure 4.17 Localised states visible in the MTDOS evaluated at the K point at the aluminium twin fault.

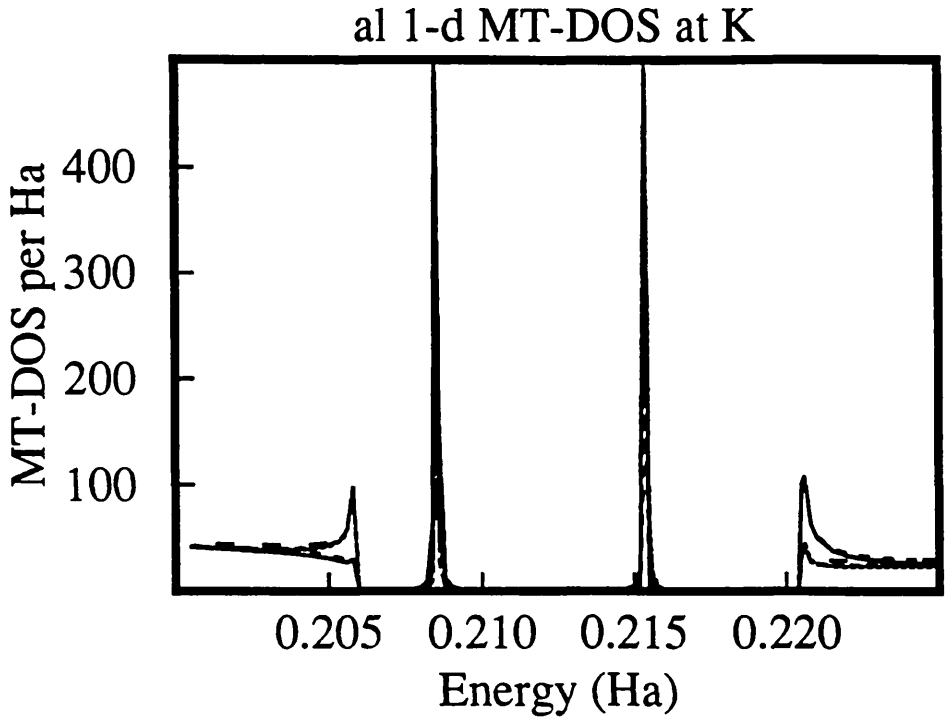

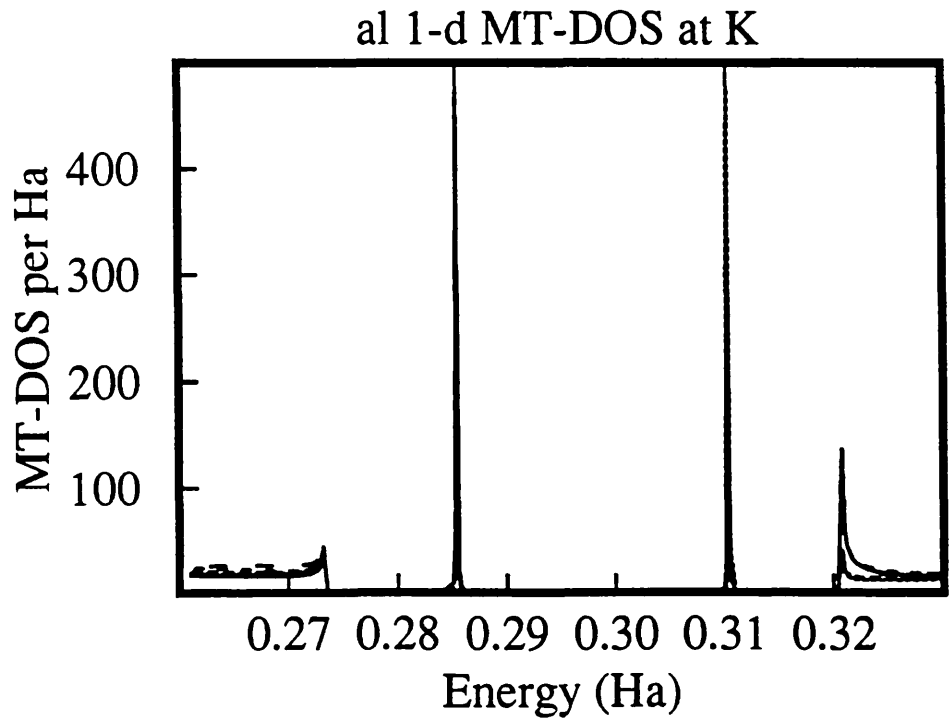

4.6 Impurities at stacking faults

The inhibition of the hybridisation of electron states at the twin fault as a consequence of the mirror symmetry introduced suggests a possible mechanism by which impurities may alter the stacking fault energy. First suggested by Suzuki (1952, 1962), experiment has shown that the addition of small concentrations of a secondary element can considerably modify γ_{sf}, and as a direct consequence the observed mechanical behaviour of the material (Murr, 1975). For example, in the case of aluminium, copper impurities significantly lower the fault energy (Gray, 1988a) whilst magnesium has little or no effect (Gray, 1988b). A reduction in the energy suggests segregation of the solute at the fault, whilst an increase in energy would favour desegregation. The effect of solute atoms upon stacking fault electronic structure has not been previously addressed, presumably due to the complexity of the calculations, and since chemical/band structure effects are likely to be important and hence invalidate pair–potential approaches. In these calculations (Crampin, Vvedensky, MacLaren and Eberhart, 1989a) an idealised geometry was chosen and rather than attempting to determine the change in energy of the addition of an impurity atom, we look for possible mechanisms for the observed behaviour in the MTDOS. Determinations of the fault energy almost certainly require the inclusion of relaxation effects, and also a search for the optimum site in the vicinity of the stacking fault.

Figure 4.18 Structure and unit cell used in the impurity calculations.

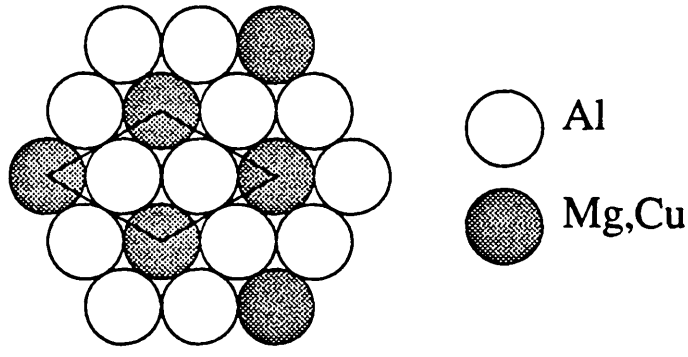

In order to model the impurity at the twin fault we use a three layer interface region and within the fault plane employ the two–dimensional supercell geometry shown in figure 4.18. It should also be possible to perform truly isolated impurity calculations along the lines of the magnetic impurity calculations of Podloucky, Zeller and Dederichs (1980). In the present calculation we restrict the impurity to the central fault plane, so that each impurity atom is surrounded by a shell of aluminium atoms whose potentials are allowed to relax.

In figure 4.19 along with the bulk MTDOS are presented the corresponding results for the magnesium impurity and aluminium atoms in the central and adjacent planes, labelled Al1 and Al2 respectively. These were calculated at an imaginary offset of 0.005Ha ($\simeq$ 0.136eV) and consequently the MTDOS contains rather less structure and the peaks and troughs are less pronounced. However, all important features may be resolved. The presence of the electronically similar magnesium atom clearly has little effect upon the aluminium atoms in the vicinity of the fault, which still possess the featureless profile found in the pure fault. This is in sharp contrast to the effect of copper seen in figure 4.20. Here we see the *d* resonance strongly interacting with the higher lying aluminium states both in the plane and to a lesser degree with the aluminium in the adjacent layer. The position of this peak is slightly lower than that found in the KKR–Green function calculations of Deutz, Dederichs and Zeller (1981), and the line shape is slightly broader, probably indicative of a slight interaction between the copper atoms in adjacent supercells, although in their calculations Deutz *et al.* did not allow for the relaxation of the surrounding aluminium potentials which may therefore account for the former difference. The presence of the copper atoms at the fault clearly enhances the hybridisation of the aluminium states near and below the Fermi level and pushes weight from above to below the *d* resonance on the central Al1 atoms. This would be expected to lower the band contribution to the total energy. The reappearance of structure at the critical energies demonstrates that the copper atom is clearly able to provide more states to which the aluminium *s* and *p* electrons can couple within the restrictions imposed by the mirror symmetry, hence enabling hybridisation more in line with that present in the bulk. It is tempting to suggest this apparent "relaxation" of the inhibited hybridisation accounts for the observed reduction in the fault energy, in which case the position of the *d* resonance may be expected to play an important role in determining the influence of the solute. Further studies are intended to persue this question.

Figure 4.19 Muffin–tin density of states for the aluminium stacking fault with magnesium impurity.

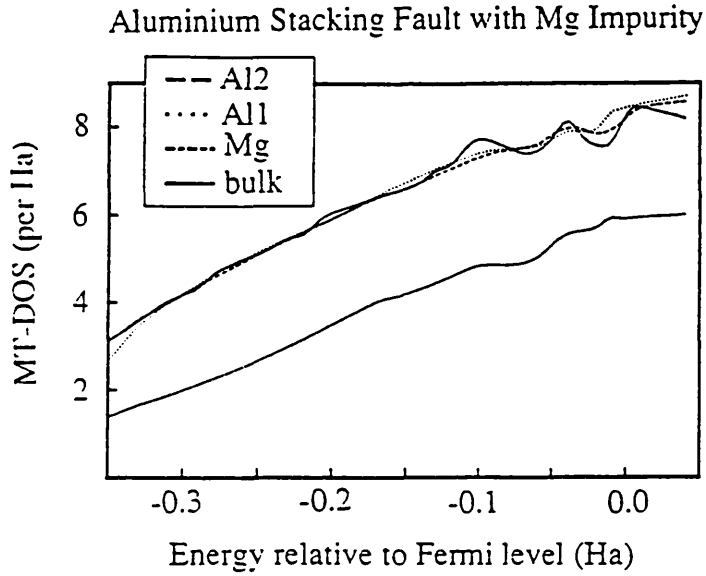

Figure 4.20 Muffin–tin density of states for the aluminium stacking fault with copper impurity.

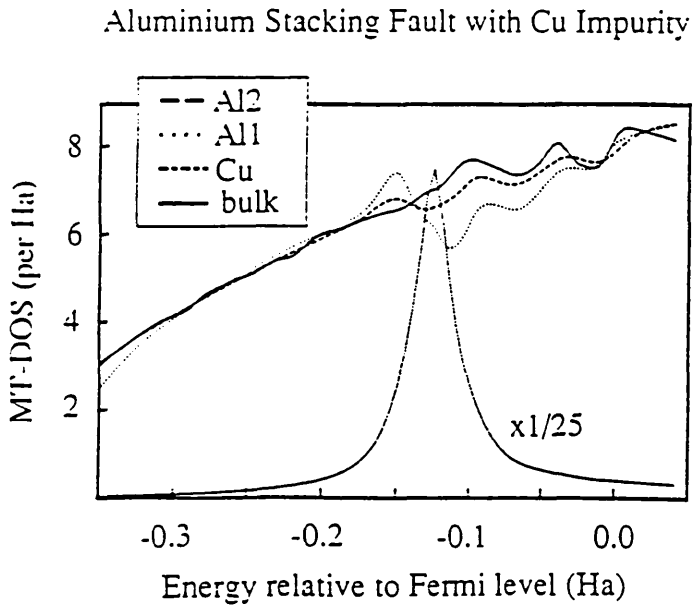

CHAPTER 5: NICKEL Σ5 (210) GRAIN–BOUNDARY

5.0 Introduction

In this Chapter the results of the first self–consistent electronic structure calculation on an isolated transition metal grain–boundary will be presented. It is not for lack of importance that the electronic structure of grain–boundaries have received, as of yet, little attention from a theoretical standpoint. They are known to play a fundamentally important role in the mechanical properties of materials, as well as influencing electronic, chemical and corrosion behaviour. Rather, their poorly characterised structure, reduced symmetry compared to the bulk and the major perturbations to the atomic and electronic structures have all inhibited the application of standard techniques which depend heavily upon symmetry and Bloch's theorem to reduce the complexity of the problem to be solved. It has been established, experimentally both indirectly (Gleiter, 1971) and directly (*e.g.* Fitzsimmons and Sass, 1989) and also through atomistic computer simulation, that the atomic structure of many grain–boundaries is ordered, rather that amorphous, and consequently the LKKR technique represents a viable and efficient approach to the study of these defects.

Recently, the technological importance of grain–boundaries in their influence upon the mechanical properties of materials have prompted a number of investigations. The observations by Aoki and Izumi (1979) of the increased ductility of boron–doped polycrystalline Ni_3Al, a possible candidate material for high–temperature aerospace applications but for a tendancy to fail intergranularly in a brittle fashion, and subsequent studies on numerous intermetallic compounds (*e.g.* Takasugi and Izumi, 1985) and of the influence of ternary additions on their fracture behaviour (*e.g.* Takasugi, Izumi and Masahashi, 1985), have highlighted the beneficial consequences to material development that a complete and predictive understanding of the underlying mechanisms responsible for intergranular

embrittlement and ductility enhancement would provide. The first applications of quantum–mechanical calculations in this direction appeared in the pioneering work of Briant and Messmer (1980, 1982a,b, 1984) and Messmer and Briant (1982), who applied the self–consistent multiple–scattering Xα cluster technique to small configurations of atoms in representative grain–boundary geometries. The phenomena of temper embrittlement of steel was studied by modeling a variety of metal–impurity (M–I) systems, with M taken from Fe, Ni, Mn or Cr and I from P, S, Sb, B, or C. On the basis of these calculations, it was concluded that embrittlement was a consequence of the weakening of M–M bonds following the withdrawl of charge to form strong M–I bonds, and the degree to which a given element embrittled was related to the relative electronegativity of the impurity and metal. For the case of M being nickel, the tendancy to withdraw charge from the M–M bonds decreased as S > P > C > B, with boron actually acting as a cohesive enhancer, by not withdrawing charge. This inferred decohesion results in metal fracture along a path winding along the grain–boundary, breaking M–M bonds weakened by adjacent M–I interactions.

These results complemented suggestions by Losch (1979), who first proposed that a basis for understanding may exist in a local bonding picture, and who also emphasised the link between the problem of catalysis and grain–boundary embrittlement. He suggested a decohesion mechanism arising from weakened M–M bonding, and also suggested the possibility of I–I bonding weakening M–I bonding, leading to a weakened grain–boundary region. The importance of I–I interactions was addressed in work by Eberhart, Johnson and Latanision (1984), who noted that experimentally the brittleness of nickel was a complicated function of sulfur concentration. Low concentrations cause little change in ductility but above 60ppm bulk concentration there exist a direct relationship between sulfur concentration and the decrease in stress and strain to fracture (Loier and Boos, 1981). Using the multiple–scattering Xα cluster method they deduced the sulfur–sulfur interaction to be covalent, interpreting the resulting anisotropy in local elasticity as the cause of the increasing propensity to brittle fracture as the sulfur concentration rises.

The *intrinsic* brittleness of many polycrystalline materials has been addressed by Eberhart and Vvedensky (1987) in a model in which the existence of localised states at grain–boundaries is taken as a signature of brittle behaviour. In such materials the inability to enhance s hybridisation when deviations from bulk geometry introduce new bond angles was found to result in localised electronic states near the Fermi energy, significantly reducing the energy barriers to bond rearrangement within the grain–boundary region. As a consequence this region may

more easily accommodate strain than the surrounding metal, leading to strain build–up and subsequently to fracture. In ductile materials such localised states were not found. As a measure of the degree to which *s* hydridisation is achieved, the relative *s* orbital electronegativities of the constituent species were employed in a graphical plot which distinguished ductile from brittle materials (Vvedensky and Eberhart, 1987), giving an analogous partitioning as the structure–property maps using the Mendeleev numbers of Pettifor (1986). However, the orbital electronegativities are environmentally specific, and in some cases the use of purely atomic parameters has been found to lead to an incorrect partitioning of ductile–brittle materials (Eberhart and Vvedensky, 1988a), whilst studying the *effective* negativities in the solid–state environment gave correct behaviour. On the basis of electronegativities, ductility–enhancement by impurities could also be accounted for, and predicted (Eberhart and Vvedensky, 1988b). Another general explanation for embrittlement was proposed by Haydock (1981), who suggested the effect of segregated impurities was to introduce transgranular covalent bonds, thus localising electrons, making bonds less mobile and consequently reducing ductility. Even though such bonds may increase the cohesive energy of the boundary, they reduce the available low–energy electronic excitations which are involved in charge rearrangement, and by inhibiting smooth transfer of bonds they will cause discontinuous response to stress.

None of these investigations considered the energetics of the systems being studied, but instead relied upon a local orbital picture, which has successfully explained a variety of phenomena in the field of magnetism and catalysis, and which, indeed, underpins much of the theoretical chemistry performed today. Such as approach is justifiable for the study of qualitative behaviour and trends, but unlikely to yield quantitative behaviour. However, the phenomenon of grain–boundary embrittlement is general indeed, apparently independent upon the specifics of grain–boundary. There is some reason to believe, on the basis of atomistic studies (Foiles, 1989) and simple energy models (Takasugi and Izumi, 1987), that a great deal of multiplicity exists in the atomic structure of the boundaries. That is, several structural configurations possess very similar energies, and, consequently, may be expected to co–exist. This, and the insensitivity of the embrittlement upon the actual grain–boundary (*e.g.* it appears not to matter whether it be $\Sigma 5$, $\Sigma 3$, tilt, or twist etc.) suggests the underlying mechanisms are general, and local, and hence probably accessible to cluster studies interpreted correctly. Some workers (see Chen, Srolovitz and Voter, 1988) have suggested that the behaviour of dislocations is a *sine qua non* to an understanding of the embrittlement process. Thus,

although ultimately these investigations must be supported by accurate calculations capable of determining fracture energies, stresses and the like, they are very much at the limits of current capabilities and in many cases beyond. It is likely that for some time yet we will have to depend heavily upon the insight simplified treatments such as the cluster models provide.

Accurate total–energy calculations *have* actually been applied to a grain–boundary system of pertinence to mechanical properties. Embedded atom studies such as those of Chen, Srolovitz and Voter (1989) have yielded boundary energies in reasonable agreement with experiment, as well as Griffith cohesive energies, which ignore plastic deformation. Chen, Voter, Albers, Boring and Hay (1989) have employed the results of linearized muffin–tin–orbital calculations on a number of hypothetical nickel–boron and aluminium–boron compounds to determine embedded atom potentials for subsequent studies of segregated boron at nickel and Ni_3Al grain–boundaries, and likewise for segregated sulfur. Painter and Averill (1987) have combined the cluster approach for modelling low symmetry structures with total energy calculations in studying the binding–energy and forces within a nickel octahedra with and without a centrally located interstitial boron or sulfur atom. These results suggested the presence of boron *increased* the sustainable strain at the grain–boundary, whilst sulfur *induced* strain, thereby weakening bonds across the boundary, and could be interpreted in terms of the larger core size of the sulfur atom. Experimentally, boron acts as a cohesive enhancer in nickel–rich alloys, whilst sulfur embrittles nickel, in agreement with the findings of Painter and Averill. In a more recent paper (Painter and Averill, 1989), this approach has been applied to the study of lithium–row atoms in the same nickel octahedra. Quantum size effects were again deduced to be important, with the observed trends attributed to the competition between atomic size and impurity–host covalent bonding. Larger orbital radii were found to induce strain whilst affecting covalent bond formation, which was also influenced by the relative positions of the impurity *sp* valence levels and *d* band of the host. The Painter and Averill approach is necessarily incomplete, ignoring a number of important factors such as the role of impurity–impurity interactions, the effects of bond–angle distortions (they employed a homogeneous deformation of the octahedral cluster), and the obvious fact that segregants will occupy preferential sites at grain–boundaries, including substitutional. Goodwin, Needs and Heine (1988) applied the self–consistent pseudopotential technique to a simplified grain–boundary model of aluminium, and considered the effects of impurity atoms arsenic and germanium. The drawback of the pseudopotential approach lies in the restricted materials to which it may

be applied, preventing application to materials such as nickel. Indeed, experimentally, neither arsenic or germanium have been reported to induce intergranular brittleness in aluminium. Furthermore, the complexity of the problem required the adoption of a particularly simplified geometry, with the grain–boundary fracture modelled by simply cleaving (111) planes of the face–centered cubic crystal within a small supercell. However, as has been demonstrated in numerous calculations, the pseudopotential technique is capable of an accurate and meaningful description of the energetics of solids. These studies indicated the effect of the impurity was to *increase* the fracture energy, both for fracture adjacent to the layer of impurities and also for fracture one layer further into the solid (between aluminium–aluminium layers with the impurity one layer from one of the resulting surfaces). Thus, unlike other models such as Briant and Messmer (1980), the effect of the impurity was increased cohesion. The question of embrittlement in this system was further addressed by Goodwin *et al.* (1989) when the grain–boundary model with impurity arsenic atoms was distorted to determine the ideal cleavage stress, and hence the implications for fracture examined within the model of Kelly, Tyson and Cottrell (1967). The results suggested the effect of the impurity was to slightly reduce the cleavage stress, whilst greatly increasing the ideal shear stress. These were deduced to be a consequence of the arsenic atoms forming directional covalent bonds with the aluminium host producing local rigidity, encouraging bond breaking but making bond rearrangement less favourable (Haydock, 1981). The choice of materials, simplified geometry (no volume mismatch, unlike real grain–boundaries) and deformations studied prevent the adoption of these results to other systems *per se*, but give direction to subsequent studies. Both the studies of Goodwin *et al.* and Painter and Averill highlight the numerous complications and imposing problems inherent to the accurate and realistic modelling of grain–boundary electronic structure, including the tremendous difficulties of extending the calculations as they stand. In the case of the cluster calculations, for example, the application of an inhomogeneous deformation to the octahedral cluster, to mimic bond–angle strain, would be likely to worsen to realism of the cluster as a model for grain–boundary environment, more poorly representing the coordination typical within a solid.

The following sections report a calculation of the electronic structure of the $\Sigma 5$ (210) grain–boundary in nickel, and the effects of segregated sulfur. This study employs the layer KKR theory of Chapters 2 and 3, and considers an isolated fault embedded in an infinite crystal. The calculations do not include total–energies, since the muffin–tin approximation at present used within the method cannot be

expected to give accurate results for situations of volume mismatch typical of grain–boundary geometries. Instead, the effects of changes in the local density of states are understood as consequences of the change in local environment, and features of the electronic structure of the boundary with segregated sulfur which might bear upon the sulfur–induced embrittlement of nickel are identified. The importance of self–consistency and embedding are examined. We start by considering the choice of grain–boundary structure, of importance to any calculation which does not determine the minimum energy atomic structure.

5.1 Grain–boundary structure

The atomic structure in the vicinity of grain–boundaries is not easily accessible to experimental probes and, consequently, detailed information regarding the location of atoms is not readily available. This is in sharp contrast to surface structure determination, where a number of techniques, most notably low–energy electron diffraction (LEED), have been used to characterise the relaxations, reconstructions and adsorbate sites of numerous crystal faces (MacLaren *et al.*, 1987). Recently, however, the availability of artificially fabricated bicrystal grain–boundaries and the application of new X–ray diffraction techniques have enabled the accurate structural determination of a few relatively simple metal grain–boundaries (Fitzsimmons and Sass, 1988,1989; Taylor, Majid, Bristowe and Balluffi, 1989), promising much for the future. These methods rely upon a cancellation of unknown factors by the observation of *relative* intensities obtained from thin–film bicrystals containing an interface and the adjoining perfect crystal, and at present have a resolution of approximately 0.05Å.

The recent structural determinations of simple grain–boundaries by X–ray diffraction techniques have enabled a direct assessment of the predictions of simulations which have attempted to obtain the atomic coordinates of the grain–boundary *via* energy–minimisation. Empirical pair–potentials have always struggled with grain–boundary geometries, due primarily to the neglect of volume–dependent contributions to the cohesive energy which are significant at metallic grain–boundaries, where the close–packing is disrupted and a resulting volume expansion occurs. Attempts at constant–volume simulations to overcome the inherent deficiencies in the model are therefore physically unreasonable. The embedded–atom method (EAM) (Daw and Baskes, 1983, 1984) accounts for these volume–dependent contributions through the inclusion, of an electron–density dependent embedding function, usually fitted to reproduce experimentally known bulk and point–defect properties. The electron density varies with volume changes

and consequently the EAM better accounts for variations in local environment as found at grain–boundaries. As an example, EAM simulations of [001] twist boundaries in gold (Majid, Bristowe and Balluffi, 1989) and experimentally determined structures (Taylor, Majid, Bristowe and Balluffi, 1989) indicate an extremely satisfactory level of agreement, and suggest the EAM may usefully be employed in the future for the determination of relaxed atomic coordinates of metallic grain–boundaries to be subsequently used in first–principles electronic structure determinations.

For the current study we have not used the relaxed atomic coordinates, but generated the $\Sigma 5$ (210) symmetric tilt boundary structure illustrated in figure 5.1 in the following manner. Reflecting a half–crystal of stacked (210) planes of the face–centred cubic nickel crystal, the separation of the two grains was adjusted to prevent overlap of the atoms in layer 1 with those directly across the boundary. Secondly, the atoms within the central layer labelled 0 were relaxed within the plane parallel to the interface to maximise the number of nearest neighbours. This prescription yields a structure in good agreement with the results of simulations by Chen, Srolovitz and Voter (1989). Employing a "local volume" potential essentially identical to the EAM technique, they determined a potential for Ni by exactly fitting to the experimental cohesive energy, lattice constant and bulk modulus and optimising the agreement between predicted and known elastic constants, vacancy formation energy, diatomic molecule bond length and energy and phase stabilities. Similarly, a potential for aluminium was determined, and as well as surface and grain–boundary studies of these two metals, the potentials were employed in studies of Ni_3Al, with surface rippling and relaxations found which corresponded with experiment. In the case of the Ni $\Sigma 5$ (210) / [001] symmetric tilt boundary structure, they determined the layer spacing 0–1 to be $0.322a_0$ (a_0 the cubic lattice constant; normal layer–layer spacing $a_0/\sqrt{20} = 0.224a_0$) and a very slight further expansion of more distant layers, whilst the above prescription yields $a_0/\sqrt{8} = 0.354a_0$ with other expansions neglected. Chen, Srolovitz and Voter (1989) provide no information regarding lateral displacements, but their studies deduced a symmetric geometry with no relative displacement of the two grains parallel to the boundary, as employed in this study.

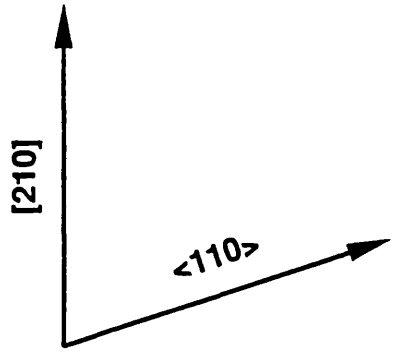

Figure 5.1 Atomic structure of the Σ5 (210) / [001] symmetric tilt boundary used in the calculations, with the atoms closest to the fault labeled. The dotted line indicates the conventional face-centred cubic cell, with shaded atoms lying one plane back. **Below.** Plan view of the interface layer (labeled 0 in main diagram) with one of the two adjacent layers (shaded).

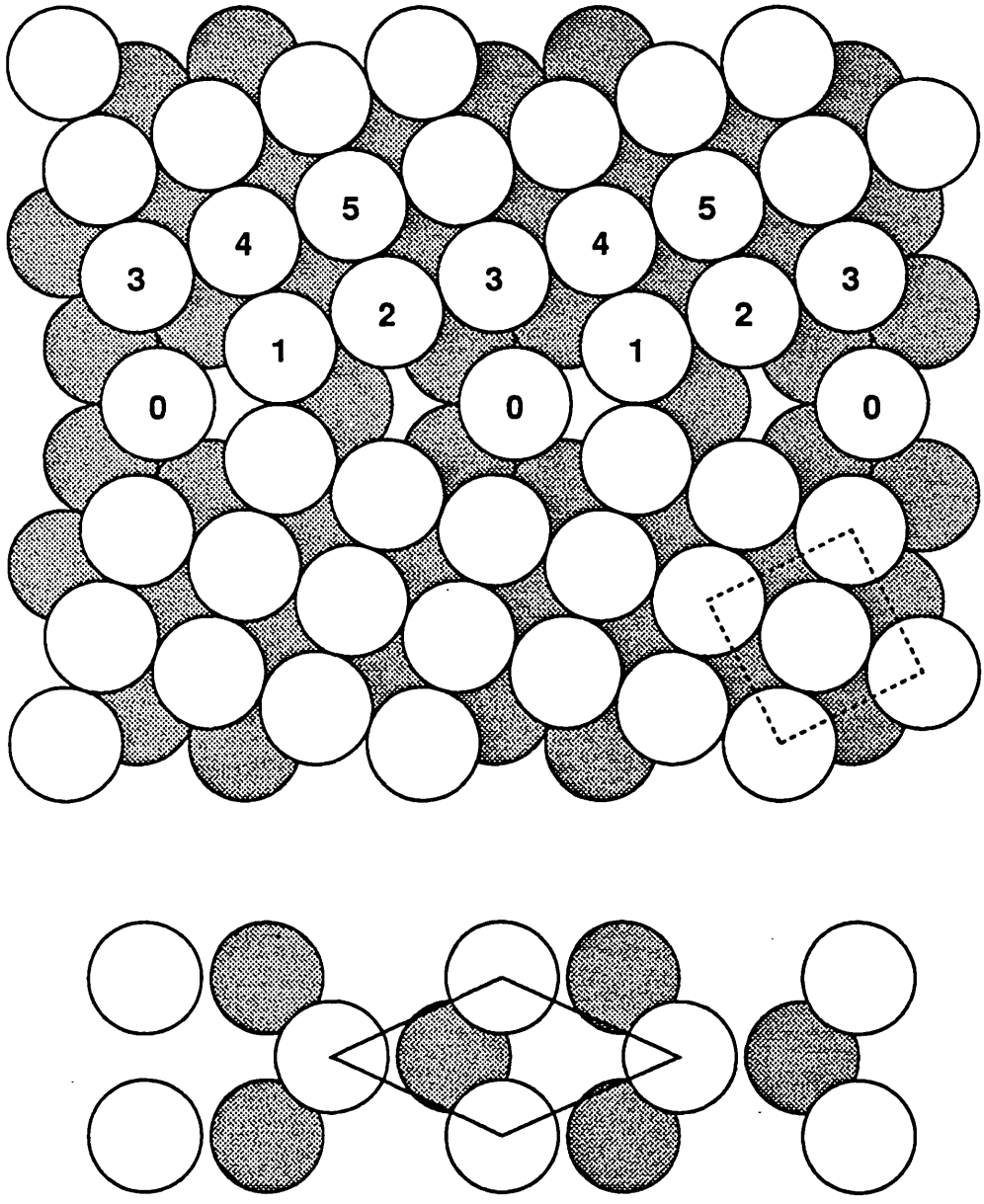

5.2 Calculation details

The small perpendicular displacement of the (210) planes in nickel require the use of the modified algorithm presented in Chapter 2 for the coupling of the layer scattering matrices, evaluation of the reflectivities and solution of the embedded layer problem. The (210) direction was chosen in Section 2.12 as an example to illustrate how the dimensions of the plane wave and partial wave basis sets may be optimised, and from which it was concluded that assigning two atomic planes to each layer with a resulting plane wave basis with $N_{\mathbf{g}} = 15$ and partial wave basis of dimension $2 \times (\ell + 1)^2 = 18$ was optimal. These are the basis sets used in this calculation, with the central 3 planes of the boundary (containing atoms of type 0 and 1 as labeled in figure 5.1) assigned to a single layer. A significant number of iterations, of the order of 50, were required to converge the density of states, which forms the basis of our interpretation, to within 0.1%. This is significantly larger than may be required in a bulk calculation due to the small mixing parameter ($\beta \simeq 0.005$ in equation (3.7.3)), which was necessary to prevent charge oscillations and numerical instabilities in the self–consistent iterations. The half space reflectivities, independent of the potential within the interface region, were written out after the first iteration and subsequently read when required, resulting in significant time savings.

The interface region within which the potentials were permitted to relax included a total of 11 atomic planes symmetrically placed about the fault. This size was determined by preliminary studies. The most distant atom treated self–consistently, labeled 5 in figure 5.1, has a full complement of first– and second–nearest neighbour nickel atoms at bulk distances. During the self–consistency cycle energy integrations were approximated by an eight–point Gaussian quadrature scheme along a triangular contour in the complex plane, and Brillouin zone averaging achieved with 4 special $\mathbf{k}$ points. Due to the use of complex energies, these parameters are found to suffice, as may be seens from the bulk muffin–tin density of states (MTDOS) profiles appearing in figure 5.2 which were evaluated from a potential generated with these parameters. The corresponding fully converged results of Moruzzi, Janak and Williams (1978) were given in figure 3.10c. The MTDOS was evaluated along a contour 0.027eV above the real energy axis with 32 $\mathbf{k}$ points.

An important consideration, when performing calculations within the muffin–tin approximation, is the degree to which the results are affected by the adoption of this form of the potential. No full–potential calculations on grain–boundary structures exist for means of comparison, and so in the present study the differences

between calculations with and without "empty" spheres in the voids of the grain–boundary structure (figure 5.1) were considered. The resulting MTDOS were virtually indistinguishable, therefore providing some justification for the use of the muffin–tin approximation — at least in the present study, where energies are not calculated.

5.3 Nickel grain–boundary

Figure 5.2 illustrates the MTDOS obtained for the atoms in the vicinity of the $\Sigma 5$ grain–boundary (Crampin, Vvedensky, MacLaren and Eberhart, 1989b), and are compared with that of bulk nickel. The zero of energy is taken to be the Fermi level. Most pronounced deviations from the bulk profile occur within the interface layer 0, where the largest differences in coordination and bond angles are found. The reduced coordination results in a significantly reduced band width, also a noticable effect on layers 1, 2 and slightly on 3. Layer 4 is the first to have a full complement of nearest neighbours (*i.e.*, 12 as in bulk nickel) and the band width is fully recovered. By layer 5 all features of the MTDOS of bulk nickel are recovered, supporting the choice of 11 interface layers, although a slight enhancement of states between -3eV and -5eV is visible. Also, on layers 2–5, the peak in the MTDOS at the Fermi level is diminished. This peak is attributable to Van Hove singularities occuring where the top of the *d*–band meets Brillouin zone boundaries, and results from the long range periodicity of the lattice. Thus, it is not surprising that the structure is lost (cf. figure 3.18, where the disruption of long range order due to the presence of a twin fault results in a much smoother one–dimensional density of states). At about -1eV the loss of resolution in the MTDOS of layer 0 (structure arising from states with e_g–type symmetry) may be attributed to the absence of a full complement of second–nearest neighbours along the [100] directions of the cubic crystal. The contribution from nearest–neighbour bonding states (t_{2g}–type) is visible at -2eV, shifted slightly upward in energy, but below this energy the MTDOS is severely reduced, a consequence of there only being 4 surrounding atoms at bulk nearest–neighbour spacing.

The significantly enhanced density of states in the vicinity of the Fermi energy may have several important consequences. Chemically, the grain–boundary may be more active, which might account for some segregation behaviour. Furthermore, it is to be expected that the magnetisation of the boundary layer will differ significantly from the bulk, which might be an experimentally observable property. Increased magnetic moments are traditionally associated with reduced coordination, when the atomic magnetisation is significantly greater than in the

Figure 5.2 MTDOS near a Ni (210) / [001] symmetric tilt boundary (shaded), compared with the MTDOS of bulk Ni (dashed line).

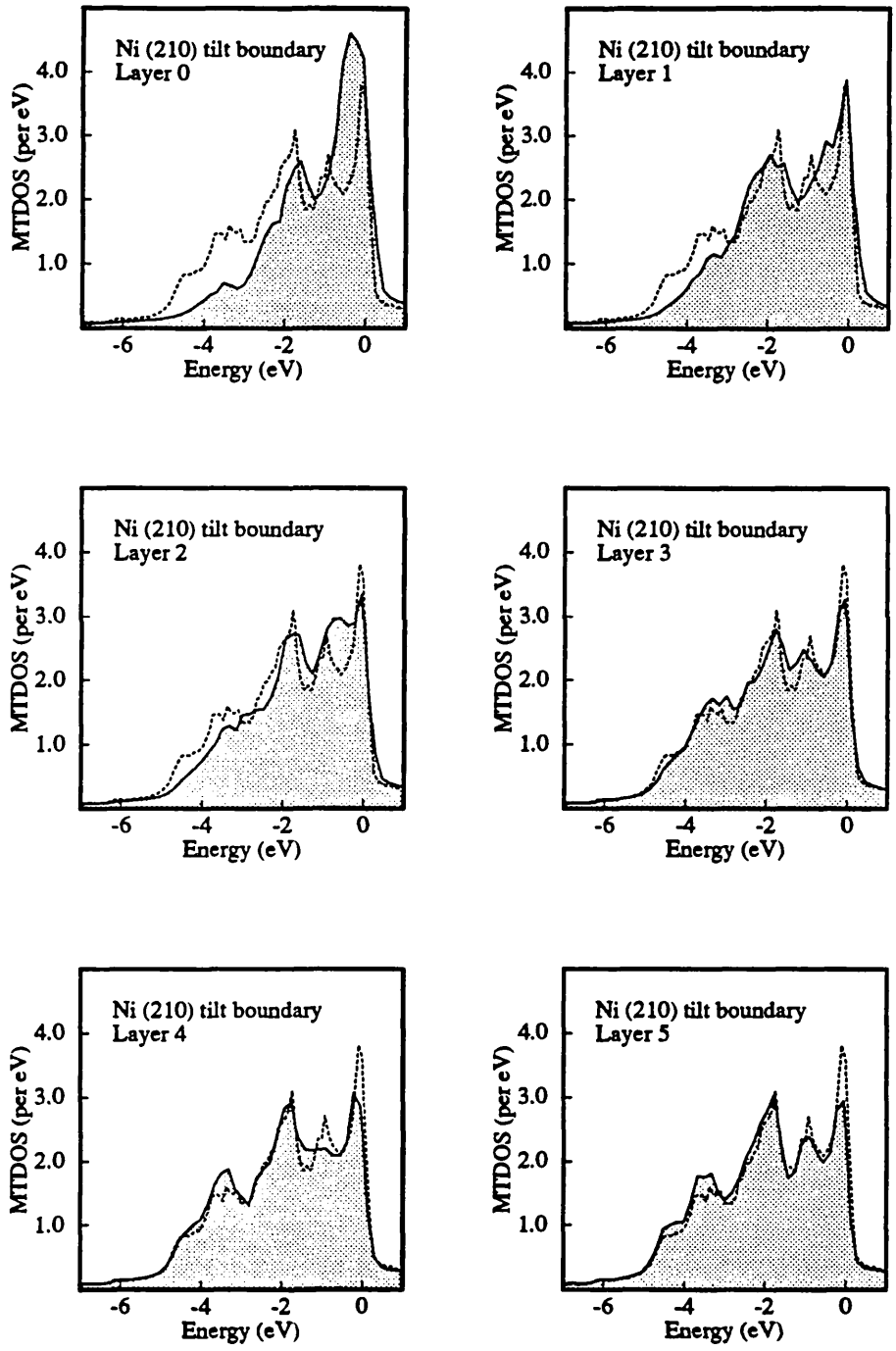

Figure 5.3 Comparison of the MTDOS calculated at the Ni (210) / [001] symmetric tilt boundary with the LKKR technique (dashed line), and a multiple–scattering Xα cluster calculation (shaded). The cluster results have been rescaled to the LKKR peak height. The inset shows the cluster geometry in cross–section.

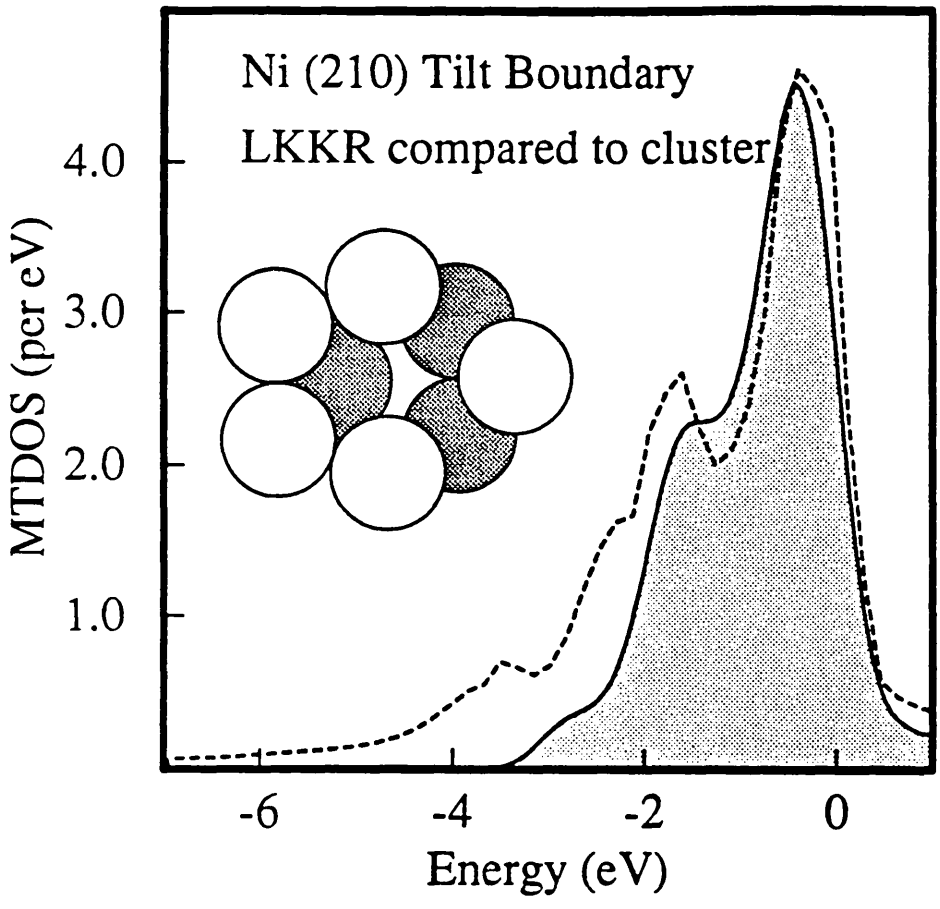

bulk, and to a first approximation may be attributed to a reduced band width and thus increased Fermi level density of states (*e.g.* surface studies, such as Ni (100) by Jepsen, Madsen and Andersen (1982)). These are precisely the conditions found at the grain–boundary. It seems certain that an accurate study of the energy of a nickel grain–boundary must consider the magnetic contribution to the total energy. The magnetic properties of grain–boundaries would be an interesting research area on its own, with the possibility of magnetically induced atomic reconstructions and a different Curie temperature from the bulk. Experimentally there may be an observable temperature dependence in the fault energy arising from the magnetisation.

One of the aims of performing LKKR calculations on grain–boundary structures is that comparison with the results of more simplified treatments of the problem will allow the evaluation of their accuracy and the consequences of the approximations. Ultimately it is hoped that this will include the comparison of grain–boundary energies with, for example, the predictions of atomistic simulations such as the embedded–atom method. At present we may compare the MTDOS of the true isolated grain–boundary embedded in an infinite crystal, with the corresponding results from cluster calculations. Figure 5.3 is just that, with the dotted line the MTDOS calculated with the LKKR method, for atom 0 in the grain–boundary structure illustrated in figure 5.1, whilst the shaded region is the MTDOS from a multiple–scattering Xα cluster calculation (Vvedensky, Crampin, Eberhart and MacLaren, 1989). The cluster used to represent the grain–boundary structure is also illustrated in figure 5.3 in cross–section. The cluster results have been Gaussian broadened and are rescaled so that the peak heights are similar. The correspondence between the results of these two calculations is very good, lending credence to the claims that calculations on small clusters may give insight into such problems. The most noticeable deviations occur in the lower energies, where features due more diffuse orbital behaviour, and therefore not well approximated within the cluster, occur.

We may also evaluate the importance of self–consistency to a description of the electronic structure of the grain–boundary. Figure 5.4 shows the MTDOS of atoms 0, 1, and 5 calculated with bulk potentials at the atomic sites within the interface region, rather than those generated self–consistently. There are most notable differences between these results and the self–consistent results of figure 5.2. On layer 0, the general features of the MTDOS resemble those of bulk nickel (not shown in the figure, but very similar to layer 5), but with a *symmetric* contraction of the *d*–band. In contrast, the self–consistent results show an *asymmetric* contraction of the *d*–band, with an upward shift in the weight of states, particularly those at lower energies. This difference may easily be understood, reflecting the reduced effectiveness of the bonding in the grain–boundary geometry. As a consequence of the increased bond–lengths and reduced coordination, orbitals directed toward both nearest and second–nearest neighbours are less able to maximise overlap with those on nearby atoms, and consequently rise in energy. The t_{2g}-type states are most affected, with the nearest neighbour relations being perturbed most from the reference solid. The e_g states in the bulk are directed into the interstitial volumes *between* atoms, which in the boundary are roughly preserved. The self–consistency procedure allows the full consequences of the charge redistribution into the interstitial regions to be reflected in the potential. It is clear that non self–consistent

Figure 5.4 Non self-consistent MTDOS for the Ni (210) / [001] symmetric tilt boundary.

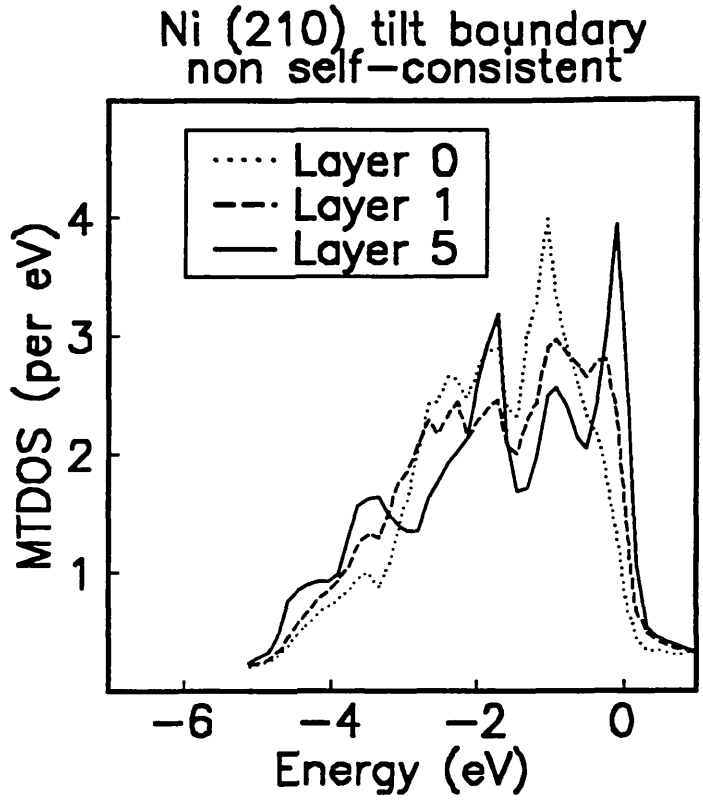

results of grain-boundary electronic structure (*e.g.* Zhang and Gonis, 1989; Sowa, 1989) must be interpreted with great care.

5.4 Effects of segregated sulfur

The discussion at the start of this Chapter contained frequent reference to studies aimed at elucidating the mechanism for sulfur induced embrittlement of nickel. There are many features of the embrittlement which are unresolved, such as the importance of sulfur–sulfur interactions, the effects of combined impurities, and the favoured distribution of sulfur in the grain–boundary environment. Using the embedded–atom method, Chen, Voter, Albers, Boring and Hay (1989) determined the optimum site for sulfur at the $\Sigma 5$ (210) grain–boundary was substitutional, which is also supported by the work of Painter and Averill (1987) showing interstitial sulfur induces significant strain due to its large core size and may therefore be considered unstable relative to the substitutional site. In the boundary structure of figure 5.1, the largest interstitial region, without including the facility for atomic relaxation, may only support an atom of radius 1.67 au. A substitutional site, however, results in a nickel–sulfur bond length of 4.6 au, in agreement with those found in nickel–sulfur crystals (at surfaces, typically 4.2 au (MacLaren *et al.*, 1987); NiS 4.5 au; Ni_3S_2 4.3 au; NiS_2 4.3 au (all from Wyckoff, 1963)).

Actual concentrations of segregated impurities at grain–boundaries are difficult to determine accurately, especially for sulfur due to a propensity for the occupation of surface sites which causes uncertainty in interpreting concentrations found on fracture surfaces. Experimentally, Loier and Boos (1981) have shown the embrittlement of nickel by sulfur depends sensitively upon the sulfur concentration. For bulk concentrations approaching 60ppm (corresponding to $\sim$ 9 at% intergranular concentration), little change in ductility occurs compared to pure nickel. In a nickel alloy, below a sulfur content approaching 80ppm, the pure system was even found to be most brittle. However, above 60 ppm sulfur concentration in nickel, an increase in sulfur content is found to systematically decrease the stress and strain to fracture, increasing intergranular brittleness. There are also some suggestions that embrittlement by low concentrations of sulfur ($<$ 10ppm) are not just a consequence of the presence of sulfur.

We choose as our model the structure resulting from the substitution of nickel atoms labeled 0 in figure 5.1 with sulfur. The use of a monolayer of segregated sulfur enables the study of sulfur–sulfur interactions which, on the basis on the observed concentration dependence, appear to play a role in the embrittlement. The calculations were performed with the same parameters as the pure boundary results, and again the potentials were allowed to relax within an 11 layer interface region. Figure 5.5 displays the MTDOS of the sulfur atom and surrounding nickel atoms (Crampin, Vvedensky, MacLaren and Eberhart, 1989b). Noticeable is the

Figure 5.5 MTDOS of the indicated atoms near a Ni (210) / [001] symmetric tilt boundary (shaded), with sulfur substituted for the atom 0. For comparison the associated MTDOS from figure 5.2 are given (dashed line), except for the sulfur atom, where the comparison is with bulk nickel.

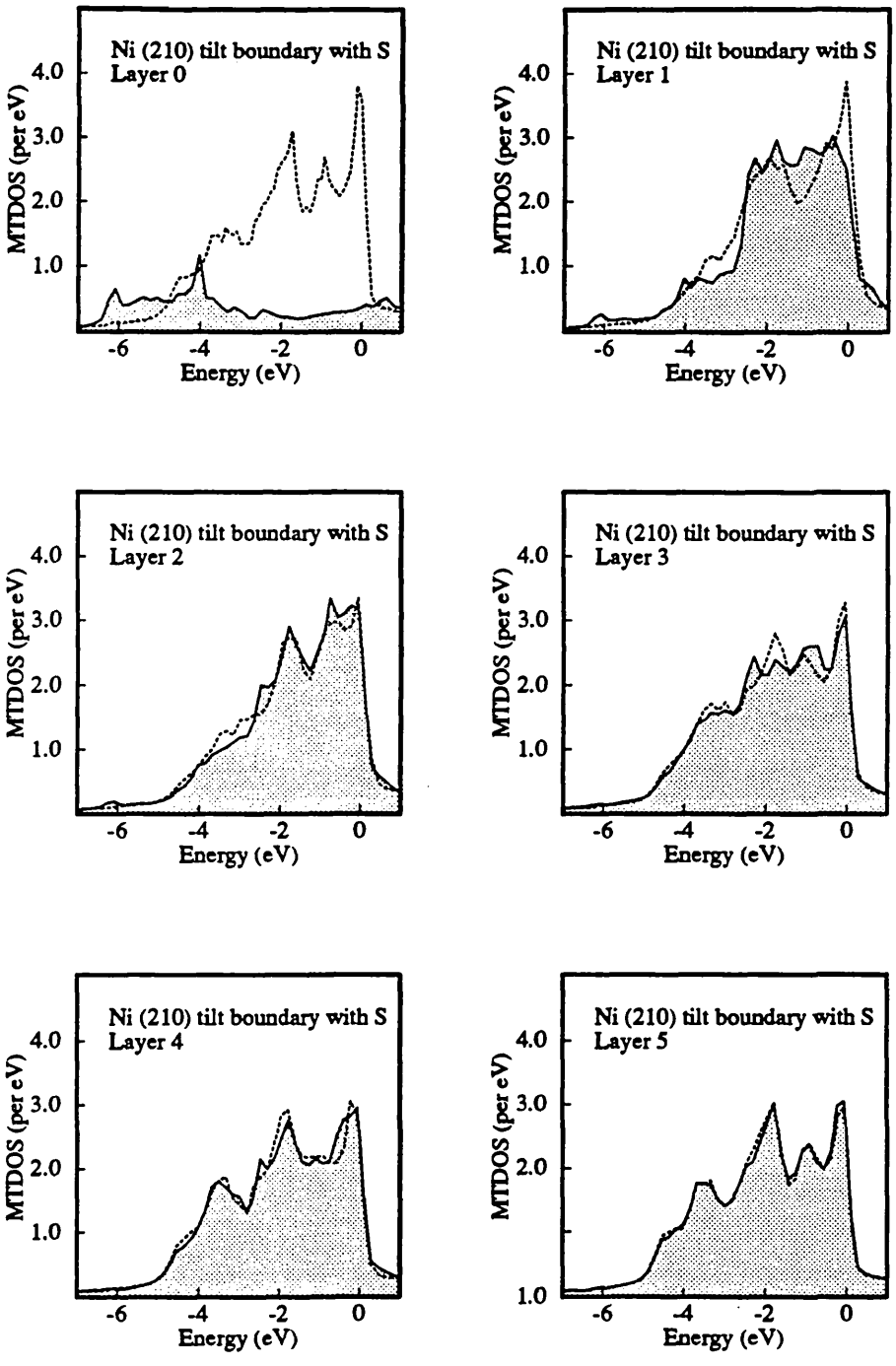

formation of a band on the sulfur atom between -4 and -6 eV. The nickel atom labeled 1, and to a slightly lesser degree atom 2, are seen to suffer a depletion in bonding states at about -3eV, whilst there is a significant loss of states at the Fermi energy on the nickel adjacent to the sulfur (the energy sampling grid in the vicinity of the Fermi energy was refined to ensure this is a real phenomenon). The former effect is probably to be expected as a consequence of the nickel atom having one of its nickel neighbours replaced by sulfur, whilst the latter is an effect also observed on transition metal surfaces, where sulfur is known to act as a poison to certain types of chemical reactions (*e.g.* MacLaren, Vvedensky, Pendry and Joyner, 1987). This highlights the correspondance between the problems of catalysis and embrittlement pointed out by Losch (1979) and Haydock (1980). Perturbations to the MTDOS of the nickel atoms are primarily restricted to these two atoms, although minor changes are found on atoms 3 and 4 which are more distant but still see the sulfur atom directly. This also agrees with the behaviour of sulfur on nickel surfaces found by MacLaren, Pendry and Joyner (1986) using a non self–consistent cluster technique, where the effects induced in the nickel atoms by the presence of sulfur extend little beyond nearest neighbours. The MTDOS of atom 5 is practically indistinguishable from the clean boundary, this particular atom being completely screened from the sulfur by its neighbours. There is rather less structure within the *d*–bands of the nickel atoms surrounding the sulfur than for the pure nickel boundary.

The energetics of this system have not been considered, for reasons accounted above, and so it is not possible to say anything definite with regard to the effects of the segregated sulfur upon the cohesive energy and fracture properties of the boundary. Indeed, a calculation of the cohesive energy of the boundary would involve the determination of the energetically favoured sulfur site and would not be meaningful without including local relaxations of the nickel atoms. However, there are certain features of these results which may have a bearing upon the sulfur induced embrittlement of nickel. The presence of neighbouring sulfur atoms in the grain–boundary is clearly seen to result in significant sulfur–sulfur covalent bonding. Note there appears to be little contribution from this bond on the neighbouring nickel atom. The sulfur *p* orbitals have drawn charge from the nickel bonding states and rehybridised nickel states down from the Fermi energy. Eberhart, Johnson and Latanision (1984) have commented upon the importance of nickel mediated sulfur–sulfur bonding, and these results confirm their cluster calculations, and despite an absence of calculated energies allow conjecture as to the possible origin of sulfur induced embrittlement of nickel. Within the model

of Kelly, Tyson and Cottrell (1967) the distinction between brittle and ductile fracture arises from a competition between cohesive and shear stresses at a crack tip, with ductility a result of the spontaneous blunting of the crack through shear at the tip. This shear process in the case of a crack propagating along the grain-boundary, as is expected from the reduced cohesion compared to bulk arising from the volume expansion, involves the breaking of bonds and re-formation of *new* bonds. The bonds broken will be strong sulfur-sulfur bonds, whilst those formed will be weaker sulfur-nickel bonds. Hence compared to the clean grain-boundary, the effect of sulfur is to increase the shear stress and possibly decrease the cohesive stress, thus increasing the tendancy for brittle fracture.

There is also an alternative explanation for the sulfur induced embrittlement of nickel. It is clear that within this model for the sulfided grain-boundary, the strong sulfur-sulfur bonding *parallel* to the boundary and concomitant weakening of the nickel-nickel bonds *across* the boundary will effect a significant modification in the elastic properties, introducing considerable anisotropy. Covalent crystals are typically hard and brittle, with localised orbitals producing rigid bonds inhibiting atomic rearrangment during deformation. The removal of Fermi level states from the first layer nickel will also significantly inhibit charge polarisation and consequently bond mobility will be severely reduced. The presence of interacting sulfur atoms may therefore be expected to hinder the progress of dislocations through the boundary region, the resulting pileup causing a localisation of strain and subsequent fracture. It is perhaps worth mentioning that no first-principles technique is currently capable of providing a description of the interaction between dislocations and grain-boundaries. Furthermore, it is possible, and even likely, that embrittlement is a result of two or more underlying mechanisms.

A full explanation of the effects of impurities at grain boundaries will require many more calculations, varying structure and geometry, and drawing correlations with well characterised systems. These will include the effects of more dilute concentrations and also combined impurity effects, studying grain boundary chemistry and its influence upon fracture behaviour. Extension of the layer KKR technique to full potential will allow a realistic calculation of cohesive energies, cleavage and shear stresses and fracture energies, whilst magnetic studies may allow a direct experimental verification of the results of calculations. It is hoped in the near future to apply the layer KKR technique for calculating the electronic properties of relaxed grain-boundary structures as determined with atomistic simulation by the embedded-atom, and answer some of the overriding questions which remain.

REFERENCES

Abramowitz, M., and Stegun, I.A., 1970, **Handbook of Mathematical Functions**, (Dover, New York).

Adams, J.B. and Foiles, S.M., 1989, preprint.

Altmann, S.L., Lapiccirella, A., Lodge, K.W. and Tomassini, N., 1982, J. Phys. C **15**, 5581.

Andersen, O.K., 1975, Phys. Rev. B**12**, 3060.

Aoki, K. and Izumi, O., 1979, J. Japan Inst. Metals, **43**, 1190.

Appelbaum, J.A., and Hamann, D.R., 1972, Phys. Rev. B**6**, 2166.

Ashby, M.F., Spaepen, F. and Williams, S., 1978, Acta Metall. **26**, 1647.

Ashcroft, N.W., Phys. Rev. B**10**, 4906.

Banerjea, A. and Smith, J.R., 1988, Phys. Rev. B**37**, 6632.

Baskes, M.I., 1989, Course notes, Sandia EAM workshop (Aug. 22-23).

Beeby, J.L., 1968, J. Phys. C **1**, 82.

Beissner,R.E., 1973, Phys. Rev. B**8**, 5432.

Benesh, G.A., and Inglesfield, J.E., 1984, J. Phys. C **17**, 1595.

Blake, R.J., 1984, Computer Phys. Commun. **33**, 425.

Blandin, A., Friedel, J. and Saada, G., 1966, J. Phys. C **3**, 128.

Brennan, S., Stöhr, J., Jaeger, R. and Rowe, J.E., 1980, Phys. Rev. Lett. **45**, 1414.

Briant, C.L. and Messmer, R.P., 1980, Philos. Mag. **42**, 569.

Briant, C.L. and Messmer, R.P., 1982a, Acta Metall. **30**, 1811.

Briant, C.L. and Messmer, R.P., 1982b, J. Phys. Coll. C**6**, 255.

Briant, C.L. and Messmer, R.P., 1984, Acta Metall. **32**, 2043.

Bullett, D.W., 1980, Solid St. Phys. **35**, 129.

Carr, R. and Parrinello, M., 1985, Phys. Rev. Lett. **55**, 2471.

Carter, C.B. and Ray, I.L.F., 1977, Philos. Mag. **35**, 1161.

Caruthers, E., Kleinman, L. and Alldredge, G.P., 1974, Phys. Rev. B**9**, 3330.

Chadi, D.J., and Cohen, M.L., 1973, Phys. Rev. B**8**, 5747.

Chang, K.J., and Cohen, M.L., 1986, Phys. Rev. B**34**, 8581.

Chen, L.J. and Falicov, L.M., 1974, Philos. Mag. **29**, 1.

Chen, S.P., Srolovitz, D.J. and Voter, A.F., 1989, J. Mater. Res. **4**, 62.

Chen, S.P., Voter, A.F., Albers, R.C., Boring, A.M. and Hay, P.J., 1989, Scripta Metall. **23**, 217.

Chou, M.Y., Cohen, M.L. and Louie, S.G., 1985, Phys. Rev. B**32**, 7979.

Christodoulou, L., Parrish, P.A. and Crowe, C.R., 1988, Mat. Res. Soc. Symp. Proc. (in press).
Chubb, S.R., Papaconstantopoulos, D.A. and Klein, B.M., 1988, Phys. Rev. B**38**, 12120.
Cohen, M.L., 1985, Physica, **T1**, 5.
Cotterill, R.M.J., Philos. Mag. **6**, 1351.
Crampin, S., Vvedensky, D.D., MacLaren, J.M. and Eberhart, M.E., 1989, Mat. Res. Soc. Symp. Proc. **141**, 373.
Crampin, S., Vvedensky, D.D., MacLaren, J.M. and Eberhart, M.E., 1989b, Phys. Rev. B**40**, 3413.
Cunningham, S.L., 1974, Phys. Rev. B**10**, 1988.
Cyrot-Lackmann, F., 1969, Surf. Sci. **15**, 535.
Darling, A.S., 1973, Intern. Met. Rev. **18**, 91.
Daw, M.S., 1986, Surf. Sci. **166**, L161.
Daw, M.S., 1989, Phys. Rev. B**39**, 7441.
Daw, M.S. and Baskes, M.I., 1983, Phys. Rev. Lett. **50**, 1285.
Daw, M.S. and Baskes, M.I., 1984, Phys. Rev. B**29**, 6443.
Daw, M.S., Baskes, M.I., Bisson, C.L. and Wolfer, W.G., 1985, in **Modelling Environmental Effects on Crack Growth Processes**, Ed. Jones, R.H. and Gerberich, W.W., (Metallurgical Society Fall Meeting, Toronto Canada).
Daw, M.S. and Hatcher, R.D., 1985, Solid State Commun. **56**, 687.
Dempsey, D.G., Grise, W.R. and Kleinman, L., 1978, Phys. Rev. B**22**, 1729.
Deutz, J., Dederichs, P.H. and Zeller, R., 1981, J. Phys. F **11**, 1787.
DiVincenzo, D.P., Alerhand, O.L., Schlüter, M. and Wilkins, J.W., 1986, Phys. Rev. Lett. **56**, 1925.
Ducastelle, F. and Cyrot–Lackmann, F., 1970, J. Phys. Chem. Solids **31**, 1295.
Ducastelle, F. and Cyrot–Lackmann, F., 1971, J. Phys. Chem. Solids **32**, 285.
Durham, P.J., Pendry, J.B., and Hodges, C.H., 1982, Computer Phys. Commun. **25**, 193.
Eberhart, M.E., Johnson, K.H. and Latanision, R.M., 1984, Acta Metall. **32**, 955.
Eberhart, M.E. and Vvedensky, D.D., 1987, Phys. Rev. Lett. **58**, 61.
Eberhart, M.E. and Vvedensky, D.D., 1988a, Phys. Rev. B**37**, 8488.
Eberhart, M.E. and Vvedensky, D.D., 1988b, Scripta Metall. **22**, 1183.
Eckelt, P., 1967, Phys. Stat. Sol. **23**, 307.
Eschrig, H., Richter, R. and Velicky, B., 1986, J. Phys. C **19**, 7173.
Evans, R., and Keller, J., 1971, J. Phys. C **4**, 3155.
Ewald, P.P., 1921, Ann. Physik **64**, 253.

Falicov, L.M., and Yndurain, F., 1975a, J. Phys. C **8**, 147.
Falicov, L.M., and Yndurain, F., 1975b, J. Phys. C **8**, 1563.
Faulkner, J.S., and Stocks, G.M., 1980, Phys. Rev. B**21**, 3222.
Feibelman, P.J., 1985, Phys. Rev. Lett. **54**, 2627.
Feibelman, P.J. and Hamann, D.R., 1984, Phys. Rev. Lett. **52**, 61.
Feuerbacher, B., Fitton, B. and Willis, R.F. (eds), 1978, **Photoemission and the Electronic Properties of Surfaces**, (Wiley, New York).
Feynman, R.P., 1939, Phys. Rev. **56**, 340.
Fitzsimmons, M.R. and Sass, S.L., 1988, Acta Metall. **36**, 3103.
Fitzsimmons, M.R. and Sass, S.L., 1989, Acta Metall. **37**, 1009.
Fleischer, R.L., 1986, Scripta Metall. , **20**, 223.
Foiles, S.M., 1988, MRS Fall Meeting, Boston MA.
Foiles, S.M., 1989, Course notes, Sandia EAM workshop (Aug. 22-23).
Föll, H. and Carter, C.B., 1979, Philos. Mag. A**40**, 497.
Gallagher, P.C.J., 1970, Metall. Trans. , **1**, 2429.
García-Moliner, F., and Rubio, J., 1969, J. Phys. C **2**, 1789.
Gleiter, H., 1971, Phys. Stat. Sol. , B**45**, 9.
Godby, R.W. and Needs, R.J., 1989, Phys. Rev. Lett. **62**, 1169.
Gonis, A., 1986, Phys. Rev. B**33**, 5914.
Gonis, A., 1989, Bull. Am. Phys. Soc., **34**, 825.
Gonis, A., Zhang, X.-G., and Nicholson, D.M., 1988, Phys. Rev. B**38**, 3564.
Goodwin, L., Needs, R.J., and Heine, V., 1988, Phys. Rev. Lett. **60**, 2050.
Goodwin, L., Needs, R.J., and Heine, V., 1989, Europhys. Lett. **9**, 551.
Gray III, G.T., 1988a, (private communication)
Gray III, G.T., 1988b, Acta Metall. **36**, 1745.
Grise, W.R. , Kleinman, L. and Mednick, K., 1980, Phys. Rev. B**22**, 1729.
Gurman, S.J., and Pendry, J.B., 1973, Phys. Rev. Lett. **31**, 637.
Györffy, B.L., 1972, Phys. Rev. B**5**, 2382.
Györffy, B.L., and Stott, M.J., in **Band Structure Spectroscopy of Metals and Alloys**, edited by D.J. Fabian and L.M. Watson (Academic, New York) p385.
Ham, F.S. and Segall, B., 1961, Phys. Rev. **124**, 1786.
Harrison, E.A., 1973, Phys. Stat. Sol. **19**, 487.
Harrison, W.A., 1970, **Solid State Theory**, (McGraw–Hill, New York).
Harrison, W.A., 1965, Physica **31**, 1692.
Hass, K.C., Velicky, B. and Ehrenreich, H., 1984, Phys. Rev. B**29**, 1984.
Haydock, R., 1980, Solid St. Phys. **35**, 215.
Haydock, R., 1981, J. Phys. C **14**, 3807.

Hecker, S.S., Rohr, D.L. and Stein, D.F., 1978, Metall. Trans. **9A**, 481.
Hedin, L. and Lundquist, B.I., 1971, J. Phys. C **4**, 2064.
Heine, V., 1963, Proc. Phys. Soc. **81**, 300.
Heine, V., 1980, Solid St. Phys. **35**, 1.
Hellmann, H., 1937, **Einführung in die Quanten Theorie**, (Deuticke, Leipzig)
Hirth, J.P. and Lothe, J., 1982, **Theory of Dislocations**, (McGraw–Hill, New York).
Hodges, C.H., 1967, Philos. Mag. **15**, 371.
Hohenberg, P. and Kohn, W., 1964, Phys. Rev. **136**, B864.
Holzwarth, N.A.W. and Lee, M.J.G., 1978a, Phys. Rev. **B18**, 5350.
Holzwarth, N.A.W. and Lee, M.J.G., 1978b, Phys. Rev. **B18**, 5365.
Hong, T. and Freeman, A.J., 1989, Mat. Res. Soc. Symp. Proc., (in press).
Howie, A., 1960, Philos. Mag. **5**, 251.
Inglesfield, J.E., 1971, J. Phys. C **4**, L14.
Inglesfield, J.E., 1978, Surf. Sci. **76**, 355.
Inglesfield, J.E., 1981, J. Phys. C **14**, 3795.
Inglesfield, J.E., 1982, Rep. Prog. Phys. **45**, 223.
Inglesfield, J.E. and Benesh, G.A., 1988, Phys. Rev. **B37**, 6682.
Jackson, J.D., 1975, **Classical Electrodynamics**, 2nd Edition (Wiley, New York).
Janak, J.F., 1974, Phys. Rev. **B9**, 3985.
Jepsen, O., Madsen, J. and Andersen, O.K., Phys. Rev. **B26**, 2790.
Johnson, R.A., 1989, Course notes, Sandia EAM workshop (Aug. 22-23).
Kambe, K., 1967a, Z. Naturforsch. **22a**, 322.
Kambe, K., 1967b, Z. Naturforsch. **22a**, 422.
Kambe, K., 1968, Z. Naturforsch. **23a**, 1280.
Kambe, K., 1969, Z. Naturforsch. **24c**, 1432.
Kelly, A., Tyson, W.R. and Cottrell, A.H., 1967, Philos. Mag. **15**, 567.
Kimmerling, L.C., Leamy, H.J. and Patel, J.R., 1977, Appl. Phys. Letters **30**, 217.
Koelling, D.D., 1981, Rep. Prog. Phys. **44**, 139.
Koelling, D.D. and Arbman, G.O., 1975, J. Phys. F **5**, 2041.
Koelling, D.D., Freeman, A.J. and Mueller, F.M., 1970, Phys. Rev. **B1**, 1318, 1970.
Koelling, D.D., and Harmon, B.N., 1977, J. Phys. C **10**, 3107.
Kohn, W. and Sham, L.J., 1965, Phys. Rev. **140**, A1133.
Krause, C.W., 1976, Philos. Mag. **33**, 207.

Lambrecht, W.R.L and Andersen, O.K., 1986, Surf. Sci. , **178**, 256.
Lang, N.D., and Kohn, W., 1970, Phys. Rev. B**1**, 4555.
Lassila, D.H. and Birnbaum, H.K., 1987, Acta Metall. **35**, 1815.
Lee, D.H. and Joannopoulos, J.D., 1981a, Phys. Rev. B**23**, 4988.
Lee, D.H. and Joannopoulos, J.D., 1981b, Phys. Rev. B**23**, 4997.
Loier, C. and Boos, J., 1981, Metall. Trans. **12A**, 1223.
Losch, W., 1979, Acta Metall. **27**, 1885.
Loucks, T., 1967, **Augmented Plane Wave Method**, (W.A. Benjamin, Reading, MA).
Màca, F. and Scheffler, M., 1985, Computer Phys. Commun. **38**, 403.
MacLaren, J.M., 1989, private notes.
MacLaren, J.M., Crampin, S. and Vvedensky, D.D., 1989, Phys. Rev. B(in press).
MacLaren, J.M., Crampin, S., Vvedensky, D.D., and Eberhart, M.E., 1989, submitted to Phys. Rev. Lett. .
MacLaren, J.M., Crampin, S., Vvedensky, D.D., and Pendry, J.B., 1989, Phys. Rev. B(in press).
MacLaren, J.M., Pendry, J.B. and Joyner, R.W., 1986, Surf. Sci. **178**, 856.
MacLaren, J.M., Pendry, J.B., Rous, P.J., Saldin, D.K., Somorjai, G.A., Van Hove, M.A. and Vvedensky, D.D., 1987, **Surface Crystallographic Information Service**, (Reidel, Dordrecht)
MacLaren, J.M., Vvedensky, D.D., and Crampin, S., 1989, unpublished.
MacLaren, J.M., Vvedensky, D.D., Pendry, J.B. and Joyner, R.W., 1987, J. Chem. Soc. Faraday Trans. 1 **83**, 1945.
MacLaren, J.M., Zhang, X.-G., Gonis, A. and Crampin, S., 1989, to be published in Phys. Rev. B.
Majid, I., Bristowe, P.D. and Balluffi, R.W., 1989, Phys. Rev. B**40**, 2779.
Marklund, S., 1981, Phys. Stat. Sol. **108**, 97.
Masuda-Jindo, K. and Terakura, K., 1989, Phys. Rev. B**39**, 7509.
Mattheiss, L.F., and Patel, J.R., 1981, Phys. Rev. B**23**, 5384.
Mednick, K. and Kleinman, L., 1984, Phys. Rev. B**22**, 5768.
Mehta, M., and Fadley, C.S., 1977, Phys. Rev. Lett. **39**, 1569.
Mele, E.J., and Joannopoulos, J.D., 1978, Phys. Rev. B**17**, 1816.
Messmer, R.P. and Briant, C.L., 1982, Acta Metall. **30**, 457.
Molenaar, J., 1988, J. Phys. C **21**, 1455.
Moruzzi, V.L., Janak, J.F. and Williams, A.R., 1978, **Calculated Electronic Properties of Metals**, (Pergamon, New York)
Murr, L.E., 1975, **Interfacial Phenomena in Metals and Alloys**, (Addison-Wesley, Reading MA).

Noffke, J. and Fritsche, L., 1982, J. Phys. F **12**, 921.
Noguerra, C., Spanjaard, D., and Jepsen, D.W., 1978, Phys. Rev. B**17**, 607.
Nørskov, J.K. and Lang, N.D., 1980, Phys. Rev. B**21**, 2131.
Painter, G.S. and Averill, F.W., 1987, Phys. Rev. Lett. **58**, 234.
Painter, G.S. and Averill, F.W., 1989, Phys. Rev. B**39**, 7522.
Papaconstantopoulos, D.A., 1986, Handbook of the Band Structure of Elemental Solids, (Plenum, New York).
Paxton, A.T. and Sutton, A.P., 1988, J. Phys. C **21**, L481.
Payne, M.C., Bristowe, P.D. and Joannopoulos, J.D., 1987, Phys. Rev. Lett. **58**, 1348.
Pei, C-C., 1978, Phys. Rev. B**18**, 2583.
Pendry, J.B., 1974, **Low Energy Electron Diffraction**, (Academic Press, London).
Pettifor, D.G., 1986, J. Phys. C **19**, 285.
Pindor, A.J., Temmerman, W.M. and Györffy, B.L., 1983, J. Phys. F **13**, 1627.
Pinkava, P., 1989, Private communication.
Plummer, E.W. and Gadzuk, J.W., 1970, Phys. Rev. Lett. **25**, 1493.
Podloucky, R., Zeller, R. and Dederichs, P.H., 1980, Phys. Rev. B**22**, 5777.
Pollmann, J. and Pantelides, S.T., 1978, Phys. Rev. B**18**, 5524.
Press, W.H., Flanneery, B.P., Teukolsky, S.A. and Vetterling, W.T., 1986, **Numerical Recipes**, (Cambridge University Press, Cambridge), p83.
Ray, I.L.F. and Cockayne, D.J.H., 1970, Philos. Mag. **22**, 853.
Ray, I.L.F. and Cockayne, D.J.H., 1971, Proc. Roy. Soc. London A**325**, 543.
Reid, C.N. and Roubort, J.L., 1972, Metall. Trans. **3**, 2257.
Rohr, D.L., Murr, L.E. and Hecker, S.S., 1979, Metall. Trans. **10a**, 399.
Saada, G., 1966, in **Theory of Crystal Defects**, edited by B. Gruber, (Academic, New York).
Sánchez-Dehesa, J., Vergés, J.A. and Tejedor, C., 1981, Phys. Rev. B**24**, 1006.
Schmeits, M., Mazur, A. and Pollmann, J., 1983, Phys. Rev. B**27**, 5012.
Schwarz, K., 1971, Phys. Rev. B**5**, 2466.
Simon, J.P., 1979, J. Phys. F **9**, 425.
Skriver, H.L., 1984, **The LMTO Method**, Springer Series in Solid-State Sciences 41, (Springer-Verlag, Berlin)
Slater, J.C., 1972, J. Chem. Phys. **57**, 2289.
Slater, J.C. and P. DeCicco, 1963, Quarterly Progress Report No. **50**, Solid State and Molecular Theory Group, M.I.T., 46.
Slater, J.C. and Johnson, K.H., 1972, Phys. Rev. **5**, 844.

Slater, J.C. and Koster, K.F., 1954, Phys. Rev. **94**, 1498.
Sowa, E.C., 1989, Bull. Am. Phys. Soc., **34**, 825.
Srivastava, G.P., 1984, J. Phys. A **17**, L317.
Stott, M.J. and Zaremba, E., 1980, Phys. Rev. B**22**, 1564.
Suzuki, H., 1952, Sci. Reports Tokohu Univ., **A4**, 455.
Suzuki, H., 1962, J. Phys. Soc. (Japan), **17**, 322.
Takagugi, T. and Izumi, O., 1985, Acta Metall. **33**, 1247.
Takagugi, T. and Izumi, O., 1987, Acta Metall. **35**, 823.
Takagugi, T., Izumi, O. and Masahashi, N., 1985, Acta Metall. **33**, 1259.
Taylor, M.S., Majid, I., Bristowe, P.D. and Balluffi, R.W., 1989, Phys. Rev. B**40**, 2772.
Temmerman, W.M. and Szotek, Z., 1987, Computer Phys. Reports. **5**, 173.
Tersoff, J. and Falicov, L.M., 1982, Phys. Rev. B**26**, 6186.
Thiry, P., Chandesris, D., Lecante, J., Guillot, C., Pinchaux, R. and Pétroff, Y., 1979, Phys. Rev. Lett. **43**, 82.
Treusch, J. and Sandrock, R., 1966, Phys. Stat. Sol. **16**, 487.
Van Hove, M.A., and Tong, S.Y., 1979, **Surface Crystallography by LEED**, Springer Series in Chemical Physics 2, (Springer-Verlag, Berlin).
Vvedensky, D.D. and Eberhart, M.E., 1987, Philos. Mag. **55**, 157.
Vvedensky, D.D., Crampin, S., Eberhart, M.E. and MacLaren, J.M., 1989, to be published in Contemporary Physics.
Wachutka, G., 1987, Phys. Rev. B**36**, 4275.
Wang, D-S, Freeman, A.J., Krakauer, H., and Posternak, M., 1981, Phys. Rev. B**23**, 1685.
Weber, E.R. and Alexander, H., 1983, J. Phys. Coll. C**4**, 319.
Weigel, C., Alexander, H. and Corbett, J.W., 1975, Phys. Stat. Sol. **71**, 701.
Weinert, M., 1981, J. Math. Phys. **22**, 2433.
Weyrich, K.H., 1988, Phys. Rev. B**37**, 10269.
Williams, A.R. and Morgan, J. van W., 1974, J. Phys. C **7**, 37.
Wimmer, E., Krakauer, H., Weinert, M. and Freeman, A.J., 1981, Phys. Rev. B**24**, 864.
Wood, K. and Pendry, J.B., 1973, Phys. Rev. Lett. **31**, 1400.
Wyckoff, R.G., 1963, **Crystal Structures** (Interscience, New York).
Yndurain, F. and Falicov, L.M., 1976, Phys. Rev. Lett. **37**, 928.
Zangwill, A., and Bruinsma, R., 1987, Comments Cond. Mat. Phys. **13**, 1.
Zhang, X.–G. and Gonis, A., 1989, Phys. Rev. Lett. **62**, 1161.
Zhang, X.–G. Gonis, A. and MacLaren, 1989, submitted to Phys. Rev. B.